PROCESS INTENSIFICATION FOR ACID HYDROLYSIS OF STARCH AND CELLULOSE FOR THE NANOPARTICLE PRODUCTION AND ITS APPLICATION

A Thesis submitted in the partial fulfillment of the requirements for the award of the degree of

DOCTOR OF PHILOSOPHY

IN

CHEMICAL ENGINEERING

By

Mr. VIKAS SADASHIV HAKKE

(ROLL NO: 718055)

Under the guidance of

Prof. SHIRISH H. SONAWANE

Professor

and

PROF. G. UDAY BHASKAR BABU

Associate Professor

DEPARTMENT OF CHEMICAL ENGINEERING

NATIONAL INSTITUTE OF TECHNOLOGY

WARANGAL-506 004 (T.S), INDIA

January 2023

Dedicated

to

- **My beloved Mother and Father, without them it was not possible to be at this platform.**
- **To my lovely wife, without whom I could not imagine the path of research. She is always a pillar of strength for me to do all my research work.**
- **All of my teachers and professors who educated me and pushed me to think positively.**

DECLARATION

This is to certify that the work presented in the thesis entitled **"Process Intensification for Acid Hydrolysis of Starch and Cellulose for The Nanoparticle Production and Its Application"**, is a bonafied work done by me under the supervision of Prof. Shirish H. Sonawane, and Prof. G. Uday Bhaskar Babu was not submitted elsewhere for the award of any degree.

I declare that this written submission represents my idea in my own words and where other's ideas or words have not been included. I have adequately cited and referenced the original sources. I also declare that I have adhered to all principles of academic honesty and integrity and have not misinterpreted or fabricated or falsified any idea / data / fact / source in my submission. I understand that any violation of the above will be a cause for disciplinary action by the Institute and can also evoke penal action from the sources which have thus not been properly cited or from whom proper permission has not taken when needed.

Date: **(Mr. Vikas Sadashiv Hakke)**

Place: Warangal Research Scholar,

Roll No.718055

CERTIFICATE

This is to certify that the thesis entitled **"Process Intensification for Acid Hydrolysis of Starch and Cellulose for The Nanoparticle Production and Its Application"** that is being submitted by **Mr. Vikas Sadashiv Hakke,** in partial fulfillment for the award of Doctor of Philosophy (**Ph.D)** in the Department of Chemical Engineering, National Institute of Technology, Warangal, is a record of bonafide work carried out by him under my guidance and supervision. The results of embodied in this thesis have not been submitted to any other Universities or Institutes for the award of any degree or diploma.

Dr. Shirish Hari Sonawane
Professor
Department of Chemical Engineering
National Institute of Technology, Warangal.
Warangal.

Dr. G. Uday Bhaskar Babu
Associate Professor
Department of Chemical Engineering
National Institute of Technology,

ACKNOWLEDGEMENT

I take the opportunity to express my heartfelt adulation and gratitude to my supervisor, **Dr. SHIRISH H. SONAWANE**, Professor, and **Dr. G. UDAY BHASKAR BABU** Chemical Engineering Department, National Institute of Technology, Warangal for his unreserved guidance, constructive suggestions, thought provoking discussions and unabashed inspiration in nurturing this research work. It has been a benediction for me to spend many opportune moments under the guidance of the perfectionist at the acme of professionalism. The present work is a testimony to his alacrity, inspiration, and ardent personal interest, taken by him during the course of this thesis work in its present form.

I wish to sincerely thank university authorities, **Prof. N. V. RAMANA RAO**, Director, National Institute of Technology, Warangal and other top officials who gave me an opportunity to carry out research work.

I also sincerely thank **Dr. P. V. Suresh**, Professor, Head, Chemical Engineering Department, National Institute of Technology, Warangal for his continuous support towards carrying out research work, timely suggestions, support and providing the necessary departmental facilities and services during successful completion of research work.

I wish to express my sincere and whole hearted thanks and gratitude to my doctoral scrutiny committee (DSC) members, **Dr. Prakash Saudagar**, Associate Professor, Department of Biotechnology, **Dr. Vidyasagar Shilapuram**, Associate professor, **Dr. Raghu Raja Pandiyan K**, Assistant Professor, Department of Chemical Engineering, National Institute of Technology, Warangal for their kind help, encouragement and valuable suggestions for successful completion of research work.

I would like to extent my tanks to **Prof. Seshagiri Rao Ambati**, Associate professor, Indian Institute of Petroleum and Energy (IIPE), Visakhapatnam. (Former DSC member) for his valuable suggestion and support during the course of work.

I would like to extend my thanks to all the faculty members in Department of Chemical Engineering for their valuable suggestions and encouragement. I am also thankful to all the supporting and technical staff of Department of Chemical Engineering who has directly or indirectly helped during the course of my work.

I am thankful to all my fellow research scholars and colleagues specially from sonoprocess facility, **Dr. M. Suresh Kumar, Dr. Shabana Shaik, Dr. Prashanth Suryawanshi, Dr. Uday D. Bagale, Dr. Rajesh Kumar, Dr. M. Yadagiri, Dr. D. Srinivasa**

Rao, Dr. P. Narasimha, Dr. Swapnil Adsul, Mrs. Vividha K. Landge, Dr. Shital B. Podtar, Mr. P. Dilipkumar, Mr. Yogesh Patil, Mr. Surya Teja, Mr. Sivaprakash S., Mrs. Suvarna Khelkar, Mr. Shashi Gupta, Ms. Ritwija Panda, Dr. Ganesh R Gawale, Dr. Gajanan Surywanshi, Dr. Harshal Patil, Dr. Abhay Lingayat, Dr. Upendra Murya, Dr. Sandip Khobragade, Dr. Roshan Bodhile, Dr. Kishor, Mrs. Anita Zade, Mrs. Sneha Korpe, and many other friends, for always standing by my side and sharing a great relationship as compassionate friends. I will always cherish the warmth shown by them.

I take this opportunity to sincerely acknowledge the **Ministry of Education, Department of Science & Technology (DST), (International Bilateral Cooperation Division) for the funding of my research work under the Indo-Tunisia International collaboration, No. DST/INT/TUNISIA/P-06/2017, 2017** for providing the financial assistance.

I would like to thank my late grandmother, **Smt. Jamunabai Mashnaji Hakke**, and my late grandpa, **Sri. Mashnaji Tukaram Hakke**, for their unwavering encouragement, assistance, unending love and belief in me.

Words are inadequate to express my thanks to all my family members for their constant support, co-operation, love and affection whose blessings made my journey worth effort. My special appreciation is to my father **Sri. Sadashiv Mashnaji Hakke**, mother **Smt. Malti Sadashiv Hakke**, who has been a constant source of encouragement for my higher studies. The support of my beautiful wife, **Mrs. Vividha V. Hakke**, and my beautiful daughter, **Ms. Medhanshi V. Hakke**, has been invaluable to me while I have carried out this study.

I express my gratitude towards my sister **Dr. (Mrs.) Ashwini Shrikant Balwande**, and brother in law **Dr. Shrikant B. Balwande**, my uncle **Mr. Suresh M. Hakke**, **Mr. Sanjay M. Hakke** and all family members for their love and support.

(Mr. Vikas Sadashiv Hakke)

Process Intensification for Acid Hydrolysis of Starch and Cellulose for the Nanoparticle Production and its Application

Abstract:

The process intensification of conventional acid hydrolysis was attempted for the production of starch and cellulose nanoparticles. The conventional acid hydrolysis consumes the higher time with lower yield of nanoparticles are the motivation for the consideration for the modification. The study investigates an intensified approach to the production of starch and cellulose nanoparticles. The batch and continuous acid hydrolysis with cavitation assistance delivers a better yield of nanoparticles while requiring less time for hydrolysis. With an acid concentration of 0.5 M, the ultrasonic aided acid hydrolysis of starch granules takes 40 minutes to transform the micron scale starch granules in the nanoscale below 100 nm which is required 48 h in conventional approach. The technique is robust, and the produced starch nanoparticles (SNP) exhibit superior thermal and mechanical characteristics. Cellulose nanofibers (CNFs) were created using a similar method. The synthesized CNF are confirmed with the analytical methods. The synthesized CNFs are within range of 9-11 nm width and 20 nm in length. The hydrodynamic cavitation aided acid hydrolysis technique was used to accomplish continuous synthesis of cellulose nanocrystals (CNC). The procedure uses less solvent (acid medium) and is safer to deal with. The CNC below 50 nm was created using microcrystalline cellulose with an initial size of 8-14 µm. The CNC produced has superior mechanical and thermal resistance. The produced bio-nanoparticles (SNP/CNC) were used as a nanofiller in a commercially available polyurethane (PU) solution to develop bionanocomposite thin films for packaging applications. SNP-PU and CNC-PU nanocomposite films have superior thermomechanical characteristics to plan PU thin films. The CNC-PU nanocomposite observed to be have higher mechanical and thermal resistance than SNP-PU nanocomposite. These films also have stronger barrier qualities against the transfer of oxygen, microorganisms, and water vapour through the film. Nanoparticles (SNP) are also employed as a bio-adsorbent to remove harmful heavy metal ions (Cu) from synthetic wastewater. At a lower dose value of 20 mg/mL, the procedure removes 93 % of Cu (II) ions. The wastewater treatment work using these manufactured nanoparticles might be further explored for industrial wastewater removal of harmful heavy metal ions in a cost-effective method.

The present research work divided into three major systems. In the first system intensification of conventional acid hydrolysis were studied. CNCs and SNPs are developed through the conventional and intensified acid hydrolysis.

In the second system, the synthesized nanoparticles of CNCs and SNPs where used as nanofiller in the polyurethane (PU) for the production of nanocomposites. The synthesized nanocomposite thin films where analysed for the thermal and mechanical properties. The synthesized nanocomposite thin films shows higher resistance to the transmission of oxygen, water vapour and bacterial mass across the thin film. Synthesized nanocomposite films can be used for the packaging applications.

In third system synthesized SNPs was exploit for the heavy metal ions extraction from the synthetic wastewater. The attempt was made for utilization of charged surface SNPs as nanoadsorbent. The SNPs shows significant adsorption capacity for the Cu (II) ions from the wastewater.

List of Figures

List of Table

Table of Contents

Chapter 1. Introduction

1.1 Process Intensification

In the present state of industrial sustainability, standard industrial processes are both energy intensive and time consuming. Proper resource use, such as raw material, utility, space, and conversion time, is much more vital for the success of the chemical businesses. The sustainability of chemical processes for effective and efficient conversion has been a key issue in the previous decade [1]. Chemical processes were accelerated in order to obtain maximal intramolecular and intermolecular activity. These activities are based on fluid dynamics. The fluid's variant dynamics will be unable to progress with all molecules in a comparable reaction environment [2]. The notion of process intensification (PI) is critical for meeting the sustainability challenges in the next years. This is because a shift in the design paradigm is expected to result in radical innovation. The primary goal of the PI method was to maintain a homogeneous environment for all fluid molecules. With this strategy, resource optimization with optimal use of available resources leads in maximum conversion [2,3]. The separation and purification operations are the most costly portion of the manufacturing process in the process industries. Reducing the number of separation and purification stages may have a significant influence on the total cost of the operations. Industry requires long-term transformation to transform old processes into ones that are both lucrative and environmentally safe. Intensifying processes is an effective way to increase operational efficiency. It may increase operability and safety while minimizing costs and environmental effect. Despite the fact that the PI concept and methodology have been around for a long in the scientific world, its essential principles are very relevant to contemporary discussions about sustainability and the circular economy. These discussions center on reducing resource consumption, reducing waste, and maintaining and reusing raw resources. Sustainable biofuel purification is dependent on the development of methods with little environmental impact, which might be accomplished via enhanced technology [4,5].

The PI is a rapidly growing field of research and industrial development that has already created many innovations in the chemical process industry. Reactive distillation, rotating packed beds, and microreactors are three of the most prominent PI applications. A distillation column is packed with a catalyst in a process called reactive distillation, which removes vapor products from a boiling liquid while also allowing for the reaction to proceed. As a result, the equilibrium is shifted toward more conversions [6], which boosts response rates and selectivity generally

while slashing energy consumption by 80% and capital expenditures by 20% [2,7]. Figure 1.1 illustrates the reactive distillation process as an intensive approach for the catalytic reaction and separation process.

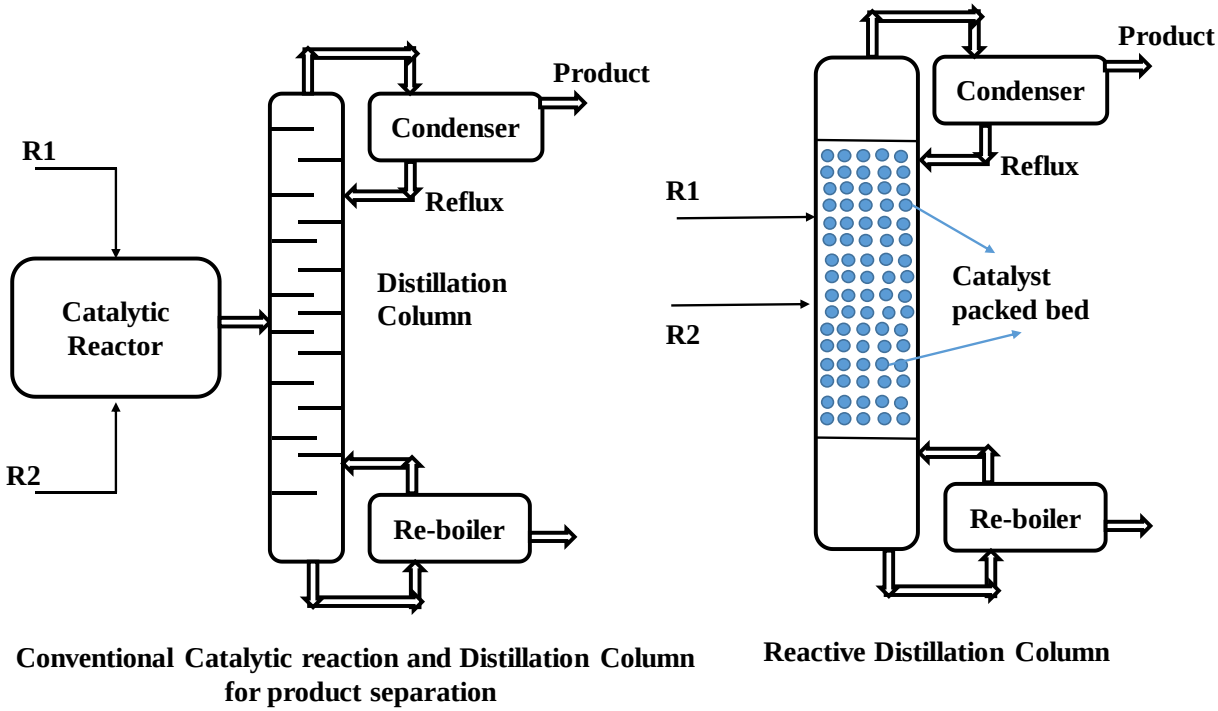

Figure 1.1 Process intensification of catalytic reaction and distillation process.

The rotating packed bed, on the other hand, eliminates the limits on mass transfer activities such as dead pockets and non-uniform concentration throughout the reactor. The uniform distribution and increased turbulence coexist in the reactor, causing the mass transfer coefficient to rise [8]. The possible use of microreactors in lower dimensions for chemical transformations is not a new concept. The increased turbulence at lower velocities in the reactants is caused by the smaller size. The pressure created by increased turbulence causes radial and axial mixing in the surrounding environment [9-11]. Microreactors have many benefits over larger reactors, including increased energy efficiency, shorter reaction times, and higher overall product yields, as well as the most simple methods for regulating these properties.

Improved productivity in the PI method often resulted from a process of evolution that included both process understanding and expert knowledge into the use of process engineering techniques. The concern with PI is that the search space used in trial-and-error, experiment-based methodologies is often too small to uncover novel, inventive, and more sustainable

process designs [12]. Van Gerven and Stankiewicz [13] first try the PI approach and describe the basic requirements for increasing process productivity. However, the chemical industries did not initially recognise these efforts. Van Gerven and Stankiewicz [13] describe that, on the molecular scale, modified chemical conversion methods, advanced chemical kinetics, and the topological geometry of the catalyst support such features as shape-selective structures, functionalized surfaces, optimised pore radii distributions, and pore connectivity. In the PI approach major concern was not focused on the development of new equipment design or new composition of the catalyst for the maximum conversion rather than, it has major concern with performance of new design of equipment or combination of the catalyst for the selectivity and yield of the conversion [14]. The combination of two unit operations to achieve the higher selectivity serves the objective of implementing the PI technique in the process. Thus the PI approach divided in the two major categories. One follows the modification in the conventional design of reactors and second follows the development of unconventional process modifications to achieve the target conversions. The structural modification leads to the intensification of unit operation to achieve the minimum unit size, unit hold up and maximize the throughput of the operation. The selective yield of the conversion, maximum mass and heat transfer associated with the process for the same unit size and space [15]. Another approach of process intensification focus on the finding the possibilities for combination of conventional unit operations to optimize the process requirement and maximize the yield of desired product. One of these class is to find the utilization the alternative energy source for the intensification of the process. The use of ultrasound cavitation was one of the significant approaches through which the intensification of conventional processes could be achieved. The intensification of conventional acid hydrolysis process was reported in the present work.

1.2 Cavitation and its potential applications

The cavitation is not new to the world of fluid dynamics and its effects. The phenomenon of cavitation provides the promising alternative dynamic source of energy to intensification of the process. The formation of cavities are form from the gas molecules entrapped on the rough surface of metal sheet. These cavities has huge potential to create the massive destructive impact on even thick metal plates and was discovered and reported in 19th century. The phenomenon of cavitation, or the formation of vapour cavities within a homogeneous liquid medium, may occur under a number of circumstances. Depending on the flow configuration and physical conditions, the liquid may exhibit a wide range of properties. At very low

pressures, it is possible to break down a liquid phase to the gaseous phase, a process known as cavitation. It is not necessary that fluid or liquid medium is required in flowing condition for the cavitation phenomenon to be occur. In the static liquid when the oscillating pressure field is applied over the free surface of a liquid, at higher amplitude the cavities are produced with in the nearly homogeneous liquid phase [16]. The physical, chemical, and biological processes that may benefit from the cavitation method have been researched extensively. This unique method is proven to be more energy efficient than several standard methods while simultaneously reducing the overall processing cost and producing the desired transformation. Intensifying many kinds of physical and chemical processes with less energy use is one of the many promising applications of cavitation.

Cavitation is the rapid release of a substantial amount of energy through the production, expansion, and collapse of microbubbles or cavities at different points in the reactor in a matter of milliseconds to microseconds [17]. When liquid first reaches the low-pressure area, vapor cavities (bubbles or voids) are formed, and during isothermal expansion, these cavities grow to their maximum size. A supercritical condition of high local temperature and pressure, known as a hot spot, is formed in the following compression cycle as a consequence of an instantaneous adiabatic collapse of cavities. Chemical and physical changes necessary for the process are facilitated by the high temperatures and pressures created at these local points. The enhancement of physical processes including nano-emulsion synthesis, nanoparticle production, microbial disruption, and disinfection may be attributed mostly to the mechanical or physical impacts of cavitation, such as micro-jet streaming and high intensity local turbulence. Rather, the acceleration of chemical processes including chemical synthesis and breakdown of water pollutants is mostly attributable to its chemical impacts, such as the production of highly reactive free radicals in the aquatic environment [17,18].

1.2.1 Types of cavitation

The cavitation technology is classified in the four major types when considered the mode of the cavities generated inside the homogeneous liquid medium. The bubbles in the liquid medium developed due to the physic-chemical variations in the liquid phase. The variation in the temperature, and local pressure are responsible for the development of gas bubble inside the uniform liquid phase. The vapour pressure of liquid solution is best example to explain this phenomenon more clearly. The roughness of metal surface always carries the entrapped gas molecules. These gas molecules play a role for the initial present nuclei for the bubble formation. Different ways are used to induce variations in the temperature and pressure around

liquid molecules. One of the most common was ultrasonic irradiation, in which sound waves were utilized to create a high pressure compressed zone and a low pressure rarefaction zone. This physical shift in the pressure around molecules is responsible for the formation of gas nuclei and bubbles inside homogenous liquid mediums. In another way, a rapid decrease in the flow area of the flowing fluid in a close conduit causes a considerable pressure differential in the flowing liquid. When the general pressure of the liquid phase goes below the vapour pressure of the moving liquid, the molecules from the liquid phase beat the activation energy needed for the phase change from liquid phase to vapour phase. This will result in quantifiable phase charge of liquid molecules to vapour phase.

As process of liquid molecules detached from liquid phase and get attached to gas phase, it increases the size of the bubble this phenomenon will called as growth of the bubble. At the maximum size of the bubble, it gets collapse. The phenomenon of development of cavities inside the nearly homogeneous liquid medium is divided into two types.

In the first approach cavitation are developed through sound wave irradiation call acoustic cavitation and second one is cavitation due to the obstacle or due to design of conduit in the flowing fluid known as hydrodynamic cavitation. The initiation of cavitation is a significant phenomenon since it requires precise circumstances. The critical point at which cavitation becomes possible is known as the cavitation threshold. It has been determined that, depending on water temperature, a sound pressure of 1-8 bar is necessary to cause water to undergo cavitation. The probability of cavitation occurring in a flow regime is estimated by determining the ratio of forces collapsing cavities to those beginning their creation. The collapse of the cavity leads in the formation of local hot spots at very high temperatures and pressures of up to 10,000 K and 1000 atm, respectively [18,19].

1.2.2 Ultrasound cavitation

Typically ultrasound (> 20 kHz) is used for this method because to its ability to impact the liquids inherent pressure changes. Ultrasound waves, which are made up of rarefaction and compression cycles, are transmitted through a liquid medium and create acoustical energy as they do so. Because of the significant negative acoustic pressure generated during the rarefaction (expansion) cycle, intermolecular distances are pushed farther apart than is strictly necessary, giving rise to holes at the points where these distances surpass the essential molecular distance. A cycle of compression and rapid collapse occurs when the cavities are compressed by the positive acoustic pressure. Because of its adiabatic nature, the last phase of collapse results in very high temperatures and pressures in a small region [20].

1.2.3 Hydrodynamic cavitation

The term hydrodynamic cavitation (HC) becomes very common and well known after well explore by Pandit and Joshi [21]. Before this paper's release, the vast majority of research on cavitation in hydraulic systems focused on ways to prevent the formation of cavities and cavitating situations. The basic idea was to convert the negative energy given out by cavities into useful mechanical and chemical work. Constriction of the flow and the pressure-velocity conditions are monitored in HC to ensure that the cavitating parameters necessary to produce hot spots are met. The cavitating conditions may be generated locally, allowing the process as a whole to run at room temperature and pressure. The passage of a fluid through a constriction in a pipe causes pressure fluctuations in the fluid, resulting in cavitation. Cavities are formed when pressure varies via a constriction channel (venturi, orifice, etc.) of varying geometry [22]. The mechanical spinning of an item inside a liquid may also result in the production of HC. While other HC devices, such as a high-pressure homogenizer or a high-speed rotor, are capable of creating cavitation conditions, their use is limited by the substantial amount of energy required to do so. Typically, cavitating devices like orifices and venturi are employed to create HC.

The cavitation approach for the intensification of acid hydrolysis in biomass will add the driving force for the uniform mass transfer of the acid from the bulk to the surface of the biomass. The ease with which acidic ions can contact the active sites of biomass can increase the rate of reaction in some cases. Though this claim is not always correct, in some cases the rate could decrease due to non-interactive intermediate synthesis during the hydrolysis reaction. For the purpose of this research, it was decided to use cavitation to help speed up the normal acid hydrolysis process.

1.2.3 Role of PI through cavitation assistance for biomass particle size reduction

The conventional approach for the bio-mass particle size reduction was through the acid hydrolysis and physical destruction using high pressure homogeniser. The biomass generally consists of glucose based polymeric structures for the energy storage, plasma, proteins and other small ingredients. The cell was of biomass consists of lignocellulose, cellulose and protein in variable proportions depending up on the source of biomass [23]. The biomass conversion through the conventional approaches required energy (in high pressure homogeniser) and more time (acid hydrolysis) was the major problem for its commercial applications widely. The nanoscale biomass could be used for the various applications such as carrier materials biomedical applications, food packaging, and emulsification process.

High intensity ultrasonic (US) irradiation of chemical processes for the intensification of the chemical reaction by raising the mass transfer rate and radicals in the solution is a unique strategy for improving the process's efficiency, yield, and energy requirement. The use of US in material synthesis has proven to be advantageous and can be combined with other techniques to create a synergistic effect that improves the overall synthesis process. The ultrasonic radiation may mix and heat the precursor, resulting in concentrated small hot energy patches that are powerful enough to cause high-energy implosive bubble collapse. The US approach is notably beneficial in the synthesis of hollow micro- or nano-spherical and other new materials. This is owing to the complicated and broad range of activities triggered by the US, which results in nanobiomaterials with diverse architectures and alterations tailored for medication delivery and diagnostics applications. Extreme conditions (5000 K and 1000 bar) may be produced in a short period of time, which stimulates chemical processes and resulting in the formation of nanomaterials.

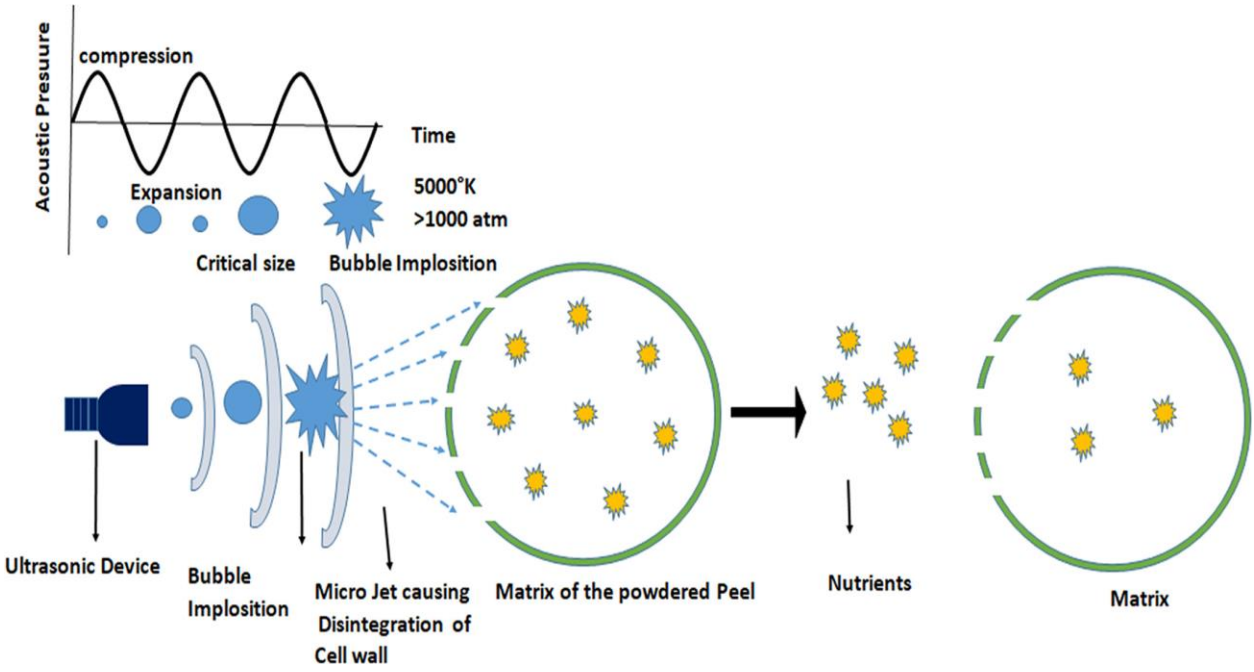

Figure 1.2 Schematic representation of ultrasound cavitation physical process. [Reprinted [24] with permission from Elsevier, 2021]

Controlled structure and size are benefits of US-synthesised bionanomaterial. When compared to traditional synthesis processes, US- synthesis is more ecologically friendly and uses a fraction of the energy. The mechanism of US assisted processes was illustrated in figure 1.2. Improvement of chemical reactivity is related to physical effects of the ultrasound in

heterogeneous sonochemical systems, such as heat and mass transfer, activation of the surface and interference of the solid due to jetting. The chemical reactions shows improved yield with the lower energy consumptions with cavitation assistance [24].

1.3 Biomass Nanoparticles

Biomass is abundant in an agriculturally based country like India. These biomass are divided into two categories: useful and waste. The majority of the waste biomass was converted into useful energy. The various methods such as pyrolysis, hydrothermal carbonization, other thermochemical methods, and activation procedures involving physical and chemical interactions are used to convert the biomass into a useful form. These methods, however, are either prohibitively expensive or disproportionately harmful to the environment. For this reason, there is a pressing need for more long-term strategies for recovering value from biomass that has been deemed trash. For alternative biomass applications, wiser approaches must be developed. The biomass nanoparticles are utilized as nanofiller in the compatible polymer for the development packing tin films. The rising need for greener and biodegradable materials, which leads to societal satisfaction, necessitates a strong push for the growth of nanomaterials research. With the right filler, improved filler/matrix interaction, and cutting-edge techniques, polymeric composites may be developed with promising future uses in construction, building, transportation, aircraft, and packaging. Natural fibres biodegradability is seen as the most crucial and intriguing aspect of their use in polymeric materials. Nanocomposites have intriguing features, a high surface-to-volume ratio, and several potential uses. In addition to reducing environmental impact, the aerospace, automotive, electrical, and biotechnology industries may all benefit from the use of such nanocomposites [25–27]. The current study focuses on the synthesis of bio-material nanoparticles, specifically starch and cellulose, using an intensified acid hydrolysis process. These biomaterial nanoparticles could be a good replacement for the synthetic polymeric fillers in the polymeric matrix to achieve higher mechanical and thermal resistance [28].

1.3.1 Starch and its specifications.

Starch consists of a highly ordered and dense packing of glucan chains organized within large, insoluble granules. They are a semicrystalline substance with alternating layers of amorphous and crystalline phases. They have wide applications in the food products and other industries due to their unique thermal and surface functionality. The polysaccharide starch is a naturally occurring biopolymer. It shows higher bio-adhesive properties as well as biodegradability,

making it a suitable base material. The semi-crystalline polysaccharide starch structure looks like an onion. An alternative layer of amorphous and crystalline portions balances the starch structure. The starch contains two macromolecular α-1, 4-d-glucopyranose. The average length of these molecular structures is about 5-7 Å. The linear chain of α-1, 4-d-glucopyranose is known as amylose, whereas the breached macromolecule is called amylopectin [29]. The branched structure of amylopectin consists of alternative semi-crystalline and amorphous layers. The interlayer distance between repetitive patterns was observed to be 9–10 nm. The branched point was specifically found in the amorphous regime of amylopectin. The α-1, 6-d will be the common breaching point found in amylopectin. The packaging of the amylose and amylopectin in the amorphous regime is in a disordered pattern, whereas in the crystalline regime it is in ordered layers. The amylopectin breached structure shows higher affinity towards the acid, and shows higher dissociation in the acidic environment [30]. The acid hydrolysis of starch granules shows different morphology at the nanoscale structure. A plate-like morphology may be found in the semi-crystalline regime due to the presence of layers, whereas an oval or spherical morphology may be found if external force is applied during hydrolysis. These nanoscale starch granules are termed starch nanocrystals [31].

The extraction of starch from potatoes, wheat, rice, and cassava is most common. All these sources of starch show different compositions of amylose and amylopectin in the starch granules.

Table 1.1 Characteristics of starch from different sources

Sr. no	Botanical source	Maize [34]	Wheat [35]	Potato [36]	Waxy [37]	Cassava [38]
1	Granular Size (μm)	30	30	40-100	15	3-30
2	Amylose %	25-28	25-29	20-25	0.5	28
3	Crystallinity	39	36	25	39	-
4	Crystalline type	A	A	B	A	B

The retrogradation classification of starch granules plays an essential role in their film-forming property. At a higher temperature, starch shows gelatinization properties. In water at higher temperatures, starch granules break down into smaller segments of biopolymers. This polymer in solution has randomness in the structure and functional activity. On cooling, the disordered segment of starch will not be able to form the structure again. Thus, this is a completely

irreversible process. The hydroxyl functional group of starch is combined through the structure after gelatinization [32]. This combination develops the new hydrogen and oxygen bonds, which are strong enough for the development of a film-like structure. The crystalline structure of starch granules gets diminished, and a film with a different crystalline index develops after the gelatinization temperature [33]. Depending up on the source of starch granules some of commonly used starch specification was compared in the Table 1.1

1.3.2 Cellulose and its specifications.

Cellulose has emerged as the most abundant renewable polymer resource. Plant cell walls are made up of cellulose, hemicellulose, and lignin. Hemicelluloses are cell wall polysaccharides. Hemicelluloses are polysaccharides with low molecular weight that are unrelated to cellulose. They are amorphous, branching polymers with lower polymerization degrees (150-200) than cellulose. They dissolve and hydrolyze quickly in alkaline water. Lignin is a three-dimensional network of phenylpropane monomers [39,40].

Cellulose, also known as poly (anhydro-1,4-glucopyranose), is a naturally occurring polydisperse, linear, crystalline (polysaccharide) macromolecule with a high molecular weight and high degree of polymerization, often ranging from 10,000 to 15,000 glucose residues [39]. Cellulose may also develop from bacterial sources, and the best-known example is Acetobacter xylinum which creates additional cellular cellulose as a tiny pellicle extending from its cell. It is unknown why bacteria biosynthesize extracellular cellulose, however it seems to serve a structural role similar to that of plants [41]. Cellulose is very chemically resistant. Before deterioration may occur, quite extreme conditions of acidity, alkalinity, or temperature are normally necessary. In nature, cellulose occurs as varying-sized microfibrils, which are aggregation of parallel chains of cellulose macromolecules bound together by hydrogen bonding. However, like with other crystalline polymers, cellulose has amorphous sections that form when the chains are not orientated parallel to one another [42].

The messily available biomass was utilized with effective modification in applications such as nanofiller, surface active entities, base material for the new generation of Janus catalysts, and emulsifiers in the suspension. The most effective modification method with a viable economy is required to explore more and more applications of biomass. The nanoscale biomass, with its higher density and larger volume to surface area ratio, is effectively utilized in various applications. In the present research work, cavitation-assisted acid hydrolysis was employed to get the nanoscale starch and cellulose nanoparticles. These nanoparticles were used as

nanofiller in the polymer suspension, and packaging films were casted. The synthesized packaging films were analysed for their mechanical and thermal resistance, water vapor and bacterial transmission across the film, and oxygen barrier. The aim and objective of the work are defined as below:

1.4 Aim and Objectives of research work

The aim of the present research work is to develop the cavitation based intensified acid hydrolysis method for the production of starch and cellulose nanoparticles and study their effective utilization as nanofiller and nano-adsorbent.

To achieve the aim of the research following objectives were attempted.

- Synthesis of starch nanoparticles through ultrasound assisted acid hydrolysis approach.
- Synthesis of cellulose nanocrystals through hydrodynamic cavitation (continuous) process.
- Investigate the performance of starch and cellulose nanoparticles as nanofillers in polyurethane-based films for the improvement in mechanical properties, thermal properties, and barrier to water vapor permeability, oxygen permeability, and bacterial transmission.
- Study the performance of starch nanoparticles as nano-adsorbent for the removal of Cu (II) ions from synthetic wastewater.

1.5 Thesis outline

The detailed introduction to the present work is described in the present chapter. The intensified approach was utilised for the synthesis of starch and cellulose nanoparticles. The conventional acid hydrolysis process was hybridised with a cavitation approach to improve production yield and reduce process time consumption for nanoparticle synthesis. The basics of the process intensification (PI) approach, along with the fundamentals of cavitation, were described in the present chapter 1. The polysaccharides such as starch and cellulose are natural polymers that show higher mechanical and thermal strengths in their smallest form, the monomer cluster. Through the acid hydrolysis approach, the synthesis of starch and cellulose nanoparticles is a time-consuming process. Also, due to the slower hydrolysis rate, the synthesised granules have a wider particle size distribution (PSD). The current chapter provides a detailed description of the application of these nanoparticles.

Chapter 2 presents a detailed literature overview for the different techniques used for the synthesis of nanoparticles of starch and cellulose. The techniques explored for the synthesis of starch and cellulose nanoparticles were evaluated for their energy and cost effectiveness. The methods for the preparation of nanocomposite films and their applications were discussed in the chapter. The various polymer solutions and their commercial applications are noted. The overall comparison included a detailed discussion of gap identification and solution requirements. The exploitation of the intensified acid hydrolysis process for the synthesis of starch and cellulose nanoparticles was finalised and will proceed in the next stage of research work.

Chapter 3. In this chapter, the synthesis of starch nanocrystals (SNC) is described. The conventional acid hydrolysis process was intensified with ultrasound sonication assistance. The hydrolysis rate of the starch granules was enhanced due to the shock wave impact of the cavity collapses in the suspension. The rate of mass transfer of acid molecules on the surface of starch granules is found to be significantly increased, which induces the higher hydrolysis rate at the outer surface of the granules. The hydrolysis rate increases as the sonication exposure time increases for the starch granules, resulting in a meaningful reduction in the overall time for the conversion. The conventional acid hydrolysis process required 48 h for the conversion of starch granules from micron scale to nanoscale with higher acid concentrations; with the intensified acid hydrolysis, the conversion time is 50 min. The particle size distribution (PSD) of the synthesised SNP with intensified acid hydrolysis is narrower and more stable. The synthesised SNP was utilised as a nanofiller in a polyurethane polymer solution to prepare the nanocomposite thin film. These nanocomposite films are observed to have higher mechanical and thermal resistance. In chapter 5, we discussed the preparation of nanocomposite films along with their characterization. SNPs are also utilised as biosorbents for the separation of heavy metal ions from synthetic wastewater; in chapter 8, a detailed discussion of this has been given.

Chapter 4 describes the synthesis of cellulose nanoparticles using two alternative cavitation techniques. The experimental approach for producing cellulose nanofibers (CNF) from raw cotton using an enhanced acid hydrolysis process was detailed, and CNF production was validated using several analytical methods. The hydrodynamic cavitation method is used to create cellulose nanocrystals (CNCs) from microcrystalline cellulose. The experimental approach was thoroughly explained, and the synthesised CNC were validated using the analytical method. When contemplating prospective applications for nanoscale items, the shape of both nanoparticles is a crucial problem. During the investigation, the main concerns were

the mechanical and thermal performance of both the geometry and the cellulose nanoparticles. The operational parameters of the experiments during CNC and CNF synthesis are optimised and reported in this chapter.

Chapter 5 presents the synthesis of starch nanoparticles (SNPs)-based polyurethane (PU) nanocomposite thin films. The chapter described the experimental procedure for the synthesis of SNP-PU nanocomposite thin films and its corresponding performance analysis. The thermal and mechanical resistance of the plain PU film shows significant enhancement with the addition of the SNP nanoparticles. The bacterial, oxygen, and water vapour permeabilities were also reported in the chapter for the SNP-PU nanocomposite thin film.

Chapter 6 deals with the ultrasound assisted synthesis of CNC-based polyurethane nanocomposite thin film. The chapter described the experimental procedure for the synthesis of CNC-PU nanocomposite thin film and its corresponding performance analysis. The thermal and mechanical resistance of the plain PU film shows significant enhancement with the addition of the CNC nanoparticles. The bacterial, oxygen, and water vapour permeabilities were also reported in the chapter for the CNC-PU nanocomposite thin film. The comparative study of thin films based on starch and cellulose nanoparticles individually in a polyurethane polymer solution. The overall effective performance of SNP and CNC quantities in the polymer matrix was compared for the thermal and mechanical resistance of the film. Both films' water vapour and bacterial barriers are critical in terms of packaging application. Both films exhibit adequate bacterial and water vapour barriers at lower nanoparticle concentrations in the polymer matrix.

Chapter 7 discusses the use of starch nanoparticles (SNPs) to separate heavy metal ions (Cu^{+2}) from synthetic wastewater. The intensified acid hydrolysis process synthesised surface-activated SNPs, which have the ability to interact with species of the opposite charge. The experimental observations described in Chapter 7 indicate that SNP could be a valuable bio-adsorbent for the removal of heavy metal ions from wastewater.

Chapter 8 gives the overall conclusion and suggestions at what more research could be done to make the studies more useful in the industrial commercialization.

List the references used in the present thesis.

Outcomes for the present research work.

References

[1] A.A. Kiss, M. Jobson, X. Gao, Reactive Distillation: Stepping Up to the Next Level of Process Intensification, Ind. Eng. Chem. Res. 58 (2019) 5909–5918. https://doi.org/10.1021/acs.iecr.8b05450.

[2] G.J. Harmsen, Reactive distillation: The front-runner of industrial process intensification, Chem. Eng. Process. Process Intensif. 46 (2007) 774–780. https://doi.org/10.1016/j.cep. 2007.06.005.

[3] S. Sitter, Q. Chen, I.E. Grossmann, An overview of process intensification methods, Curr. Opin. Chem. Eng. 25 (2019) 87–94. https://doi.org/10.1016/j.coche.2018.12.006.

[4] D. Reay, C. Ramshaw, A. Harvey, A Brief History of Process Intensification, Process Intensif. (2013) 1–25. https://doi.org/10.1016/b978-0-08-098304-2.00001-8.

[5] J.A. Glaser, Process intensification, Clean Technol. Environ. Policy. 14 (2012) 155–160. https://doi.org/10.1007/s10098-012-0466-5.

[6] F. Kim, L.J. Cote, J. Huang, Graphene oxide: Surface activity and two-dimensional assembly, Adv. Mater. 22 (2010) 1954–1958. https://doi.org/10.1002/adma.200903932.

[7] A.I. Stankiewicz, J.A. Moulijn, Process Intensification: Transforming Chemical Engineering, Chem. Eng. Prog. 96(1) (2000) 22–34.

[8] Z. Qian, Q. Chen, I.E. Grossmann, Optimal synthesis of rotating packed bed reactor, Comput. Chem. Eng. 105 (2017) 152–160. https://doi.org/10.1016/j.compchemeng. 2017.02.026.

[9] O. Worz, K.P. Jackel, T. Richter, A. Wolf, Microreactors, a new efficient tool for optimum reactor design, Chem. Eng. Sci. 56 (2001) 1029–1033. https://doi.org/10.1016/S0009-2509(00)00318-3.

[10] S. Appalakutti, S. Sonawane, B.A. Bhanvase, V. Mittal, M. Ashokkumar, Process intensification of copper chromite ($CuCr_2O_4$) nanoparticle production using continuous flow microreactor, Chem. Eng. Process. - Process Intensif. 89 (2015) 28–34. https://doi.org/10.1016/j.cep.2014.12.012.

[11] A.A. Bojang, H.S. Wu, Design, fundamental principles of fabrication and applications of microreactors, Processes. 8 (2020). https://doi.org/10.3390/PR8080891.

[12] J.G. Segovia-Hernandez, A. Bonilla-Petriciolet, Process intensification in chemical engineering: Design optimization and control, 2016. https://doi.org/10.1007/978-3-319-28392-0.

[13] T. Van Gerven, A. Stankiewicz, Structure, Energy, Synergy, Time-The Fundamentals

of Process Intensification, Ind. Eng. Chem. Res. 48 (2009) 2465–2474. https://doi.org/10.1021/ie801501y.

[14] N. Garg, G.M. Kontogeorgis, R. Gani, J.M. Woodley, A process synthesis-intensification method for generation of novel and intensified solutions, Chem. Eng. Process.-Process Intensif. 156 (2020) 108103. https://doi.org/10.1016/j.cep.2020.108103.

[15] B.-G. Rong, E. Kolehmainen, I. Turunen, Methodology of conceptual process synthesis for process intensification, in: B. Braunschweig, X. Joulia (Eds.), 18th Eur. Symp. Comput. Aided Process Eng., Elsevier, 2008: pp. 283–288. https://doi.org/10.1016/S1570-7946(08)80052-1.

[16] P.R. Gogate, V.S. Sutkar, A.B. Pandit, Sonochemical reactors: Important design and scale up considerations with a special emphasis on heterogeneous systems, Chem. Eng. J. 166 (2011) 1066–1082. https://doi.org/10.1016/j.cej.2010.11.069.

[17] V.S. Moholkar, A.B. Pandit, Bubble behavior in hydrodynamic cavitation: Effect of turbulence, AIChE J. 43 (1997) 1641–1648. https://doi.org/10.1002/aic.690430628.

[18] P.R. Gogate, A.B. Pandit, Engineering design methods for cavitation reactors II: Hydrodynamic cavitation, AIChE J. 46 (2000) 1641–1649. https://doi.org/10.1002/aic.690460815.

[19] V.S. Hakke, M.M. Seepana, S.H. Sonawane, A.K. Kola, R. Vooradi, Hybrid Treatment Technologies for the Treatment of Industrial Wastewater, in: Inamuddin, M.I. Ahamed, E. Lichtfouse (Eds.), Water Pollut. Remediat. Heavy Met., Vol 53., Springer International Publishing, Cham, 2021: pp. 211–241. https://doi.org/10.1007/978-3-030-52421-0_8.

[20] J. Wu, W.L. Nyborg, Ultrasound, cavitation bubbles and their interaction with cells, Adv. Drug Deliv. Rev. 60 (2008) 1103–1116. https://doi.org/10.1016/j.addr.2008.03.00.

[21] A.B. Pandit, J.B. Joshi, hydrolysis of fatty oils: effect of cavitation, Chem. Eng. Sci. 48 (1993) 3440–3442. https://doi.org/10.1016/0009-2509(93)80164-L.

[22] P.R. Gogate, A.M. Kabadi, A review of applications of cavitation in biochemical engineering/biotechnology, Biochem. Eng. J. 44 (2009) 60–72. https://doi.org/10.1016/j.bej.2008.10.006.

[23] C. Calvino, N. Macke, R. Kato, S.J. Rowan, Development, processing and applications of bio-sourced cellulose nanocrystal composites, Prog. Polym. Sci. 103 (2020). https://doi.org/10.1016/j.progpolymsci.2020.101221.

[24] D.R. Dash, S.S. Pathak, R.C. Pradhan, Improvement in novel ultrasound-assisted extraction technology of high value-added components from fruit and vegetable peels, J. Food Process Eng. 44 (2021) e13658. https://doi.org/10.1111/jfpe.13658.

[25] S.M. Emadian, T.T. Onay, B. Demirel, Biodegradation of bioplastics in natural environments, Waste Manag. 59 (2017) 526–536. https://doi.org/10.1016/j.wasman. 2016.10.006.

[26] J.W. Rhim, P.K.W. Ng, Natural biopolymer-based nanocomposite films for packaging applications, Crit. Rev. Food Sci. Nutr. 47 (2007) 411–433. https://doi.org/10.1080/104 08390600846366.

[27] E. Fortunati, I. Armentano, Q. Zhou, A. Iannoni, E. Saino, L. Visai, L.A. Berglund, Multifunctional bionanocomposite films of poly (lactic acid), cellulose nanocrystals and silver nanoparticles, 87 (2012) 1596–1605. https://doi.org/10.1016/j.carbpol.2011. 09.066.

[28] J. Lorcks, Properties and applications of compostable starch-based plastic material, Polym. Degrad. Stab. 59 (1998) 245–249. https://doi.org/10.1016/S0141-3910(97)001 68-7.

[29] A. Buleon, P. Colonna, V. Planchot, S. Ball, Starch granules: Structure and biosynthesis, Int. J. Biol. Macromol. 23 (1998) 85–112. https://doi.org/10.1016/S0141-8130(98)000 40-3.

[30] D. Le Corre, J. Bras, A. Dufresne, Starch nanoparticles: A review, Biomacromolecules. 11 (2010) 1139–1153. https://doi.org/10.1021/bm901428y.

[31] H.-Y. Kim, J.H. Lee, J.-Y. Kim, W.-J. Lim, S.-T. Lim, Characterization of nanoparticles prepared by acid hydrolysis of various starches, Starch - Starke. 64 (2012) 367–373. https://doi.org/10.1002/star.201100105.

[32] K.F. Gotlieb, A. Capelle, Starch derivatization: Fascinating and unique industrial opportunities, 2005. https://doi.org/10.3920/978-90-8686-541-3.

[33] F. Hu, S. Fu, J. Huang, D.P. Anderson, P.R. Chang, Structure and Properties of Polysaccharide Nanocrystals, 2015. https://doi.org/10.1002/9783527689378.ch2.

[34] M. Perez Herrera, T. Vasanthan, Rheological characterization of gum and starch nanoparticle blends, Food Chem. 243 (2018) 43–49. https://doi.org/10.1016/j.foodchem .2017.09.011.

[35] M. Jamalabadi, S. Saremnezhad, A. Bahrami, S.M. Jafari, The influence of bath and probe sonication on the physicochemical and microstructural properties of wheat starch,

Food Sci. Nutr. 7 (2019) 2427–2435. https://doi.org/10.1002/fsn3.1111.

[36] R. Chang, N. Ji, M. Li, L. Qiu, C. Sun, X. Bian, H. Qiu, L. Xiong, Q. Sun, Green preparation and characterization of starch nanoparticles using a vacuum cold plasma process combined with ultrasonication treatment, Ultrason. Sonochem. 58 (2019) 104660. https://doi.org/10.1016/j.ultsonch.2019.104660.

[37] Q. Sun, H. Fan, L. Xiong, Preparation and characterization of starch nanoparticles through ultrasonic-assisted oxidation methods, Carbohydr. Polym. 106 (2014) 359–364. https://doi.org/10.1016/j.carbpol.2014.02.067.

[38] M. Guimaraes, V.R. Botaro, K.M. Novack, F.G. Teixeira, G.H.D. Tonoli, Starch/PVA-based nanocomposites reinforced with bamboo nanofibrils, Ind. Crops Prod. 70 (2015) 72–83. https://doi.org/10.1016/j.indcrop.2015.03.014.

[39] M. Poletto, H.L. Ornaghi Junior, A.J. Zattera, Native cellulose: Structure, characterization and thermal properties, Materials (Basel). 7 (2014) 6105–6119. https://doi.org/10.3390/ ma7096105.

[40] N. Lin, A. Dufresne, Nanocellulose in biomedicine: Current status and future prospect, Eur. Polym. J. 59 (2014) 302–325. https://doi.org/10.1016/j.eurpolymj.2014.07.025.

[41] S.-P. Lin, I. Loira Calvar, J.M. Catchmark, J.-R. Liu, A. Demirci, K.-C. Cheng, Biosynthesis, production and applications of bacterial cellulose, Cellulose. 20 (2013) 2191–2219. https://doi.org/10.1007/s10570-013-9994-3.

[42] K. Fleming, D.G. Gray, S. Matthews, Cellulose Crystallites, Chem. – A Eur. J. 7 (2001) 1831–1836. https://doi.org/10.1002/1521-3765(20010504)7:9<1831::AID-CHEM1831>3. 0.CO;2-S.

Chapter 2 Literature Study

The aim of the present study is to develop a cost effective method for the synthesis of starch and cellulose nanoparticles and their effective utilization in packaging and nanoadsorbent applications. In this regard, a literature review was conducted to better understand the current state-of-the-art process for the synthesis of starch and cellulose nanoparticles. The current chapter covers the fundamentals of starch and cellulose, such as their chemical structure, composition, and current process for the production of nanoscale starch and cellulose particles. The acid hydrolysis was employed for the production of starch or cellulose nanoparticles; an overview of the conventional of hydrolysis is also included in this chapter. The recent literature was used to discuss the specifics of bio-nanocomposite polymer production and their practical use. The chapter concludes with a indentification of the research gaps in the reported literature. The highlighted gaps in the provided work will be very useful in defining the problem statement and motivating the current research endeavor.

2.1 Synthesis of starch nanoparticles

All most all the plants generates the starch to store the energy; which is renewable, and biodegradable polymer. After the cellulose it is the second most common kind of biomass in the natural world. The staple foods including rice, maize, wheat, tapioca, and potatoes, in addition to their roots, stalks, and crop seeds, contain this substance. The starch extraction industries uses wet grinding, sieving, and drying to extract and refine starches [1]. Starch is a polysaccharide that has a variety of possible applications, including as a biopolymer synthesis and a food additive. Native starch is made up of two homopolymers called amylose and amylopectin. It is not soluble in water and has a semi-crystalline structure. The complicated structure of native starch is made up of a basic monomer: glucose, the modification in the geometry of which, results in the homopolymer components of starch grain, amylose and amylopectin. They own long chains of the modified glucose structured monomers. The number of glucose molecules and their orientation in the polymer chain have significant effects on the functionality and characterization of the starch granule, even though they are from the same or similar sources. Figure 2.1 depicts the chemical configurations of a) amylose and, b) amylopectin. The polymeric configuration of amylose is normally linear in terms of geometry and complexity, whereas amylopectin shows the specific limbs attached with other glucose monomers. The average number of straight chains as branch associated with amylopectin is at

least 20-25 [2]. Different shapes, sizes, and crystallinity of starch particle are caused by interactions and complex bonding patterns between amylose and amylopectin.

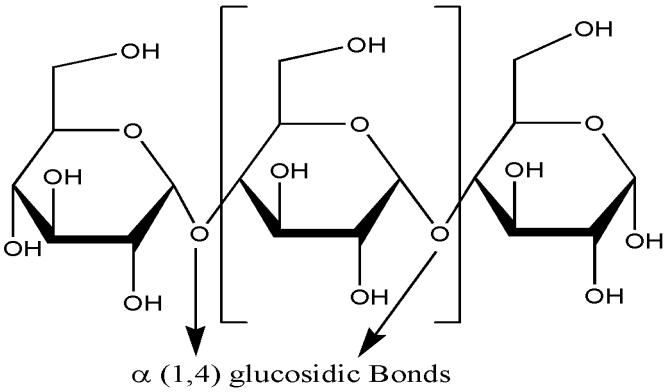

a) Structure of Amylose

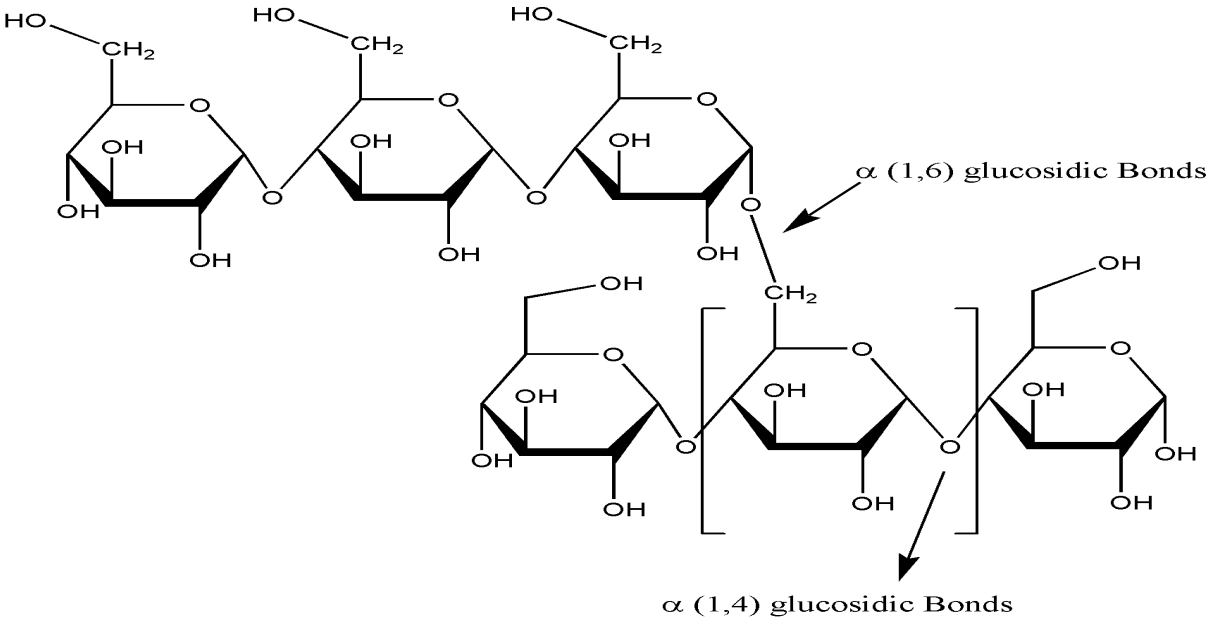

B) Structure of Amylopectin

Figure 2.1 Chemical structure of starch components a) amylose and b) amylopectin.

The straight chain of glucose units lightly linked with each other by α-(1,4)-D-glycoside bonds, in small fractions they also possess small branches with α-(1,6) kind of linkages. However, the counter part of the starch amylopectin is highly branched polymer. It consist of short chain branches of α-(1,4)-D-glycopyranose, linked with α-D-(1,6)-glucosidic linkages roughly after 20 number of associate glucose monomers [3,4]. The onion-like structure of starch consists of alternative layers of amorphous and crystalline phases. The growth ring structure made up of the alternative crystalline and amorphous lamellae is significant in the granular structure of starch. The thickness of randomly packed amorphous lamellae consists of both amylose and amylopectin. The number and thickness of alternative crystalline and amorphous regions inside

the starch structure are dependent on the origin of the starch. However, the crystalline and amorphous regions show a combined thickness of 9 nm, irrespective of starch source; this is a significant characteristic of the starch granule. The crystalline region of the granule was built by the intertwining of linear chains of glucose monomer units with α-(1,4)-D-glycoside bonds. The amylopectin molecules possess the branches which help in the intertwining process, thus higher the percentage of amylopectin in the starch granule higher will be the degree of crystallinity [3,5,6] This will lead to close and compact binding of the crystalline region. The amorphous region, on the other hand, was caused by the intertwining of short branched polymeric chains of amylose. The short length of branching hindered the extent of intertwining of linkages and compact orientations of molecules. [4,7]. Depending up on these linkages the starch granules classified with three different category as A, B, and C-Type. The A-Type structure of starch shows higher concentration of water molecules inside the starch granules. The B-Type of structure shows lower concentration of water molecules interacted with the starch granule. The C-Type shows the intermediate properties of water molecular linkages in the granular structure [8,9].

There are three different kinds of minor elements present in association with starch granules: I fragments of the cell wall, (ii) components found on the surface, and (iii) components found inside the granules themselves. Proteins, enzymes, amino acids, and nucleic acids make up most of the surface components, whereas lipids are the primary building block of the inside. Thus, proteins, lipids, and minerals are often cited as trace components of starch. The ratio of these components is determined by the plant from which the starch originated (species and varieties). Root and tuber starch may include as little as 0.05 % protein and 0.05-0.1 % lipids, whereas cereal starch typically has 0.3% protein and up to 1.0 % lipids. Although starch includes a variety of elements, phosphorus is the most crucial [10]. Compared to its macro sized counterparts, nanosized particles of a material exhibit unusual characteristics, such as a greater surface area to volume ratio. Starch is converted into nanoparticles via a number of different documented processes which includes enzymatic hydrolysis, acid hydrolysis, precipitation, electro-spraying, gamma irradiation, and high pressure homogenization. The conventional acid hydrolysis is more efficient because it produces smaller starch particles with zero by-products generation [11–13].

2.1.1 Conventional acid hydrolysis

The size of native starch particles and the period of acid contact affected the formation of SNPs during the breakdown of starch. During the acid interaction of starch granules, either with

hydrochloric acid or sulfuric acid, the crystalline region of the starch granules gets isolated. The strong belief in the starch hydrolysis process is that, the amorphous region (randomly packed amylose and amylopectin) loses its identity first in the interaction with acid [14]. The dissolution of the loosely packed amorphous region in acid hydrolysis results in the separation of the crystalline region of the starch granule. As a result, the starch granules' resulting structure has higher crystallinity and resistance to mechanical and thermal impacts. The structure becomes more stable and strong enough to withstand higher stress and temperature with respect to native starch [15]. The hydrolysis of starch follows two stages. The first stage is fast hydrolysis, followed by slower hydrolysis. During the fast step of the hydrolysis, the amorphous region interacts with the acid molecules. However, the hydrolysis rate reduces due to the resistance offered by the compact structure bonding amylose and amylopectin in the crystalline region of the starch granule. The onion-like structure of starch offered different resistances layer by layer for the penetration of acid molecules towards the core of the granule [16,17]. The figure 2.2 shows the TEM image for the starch nanocrystals.

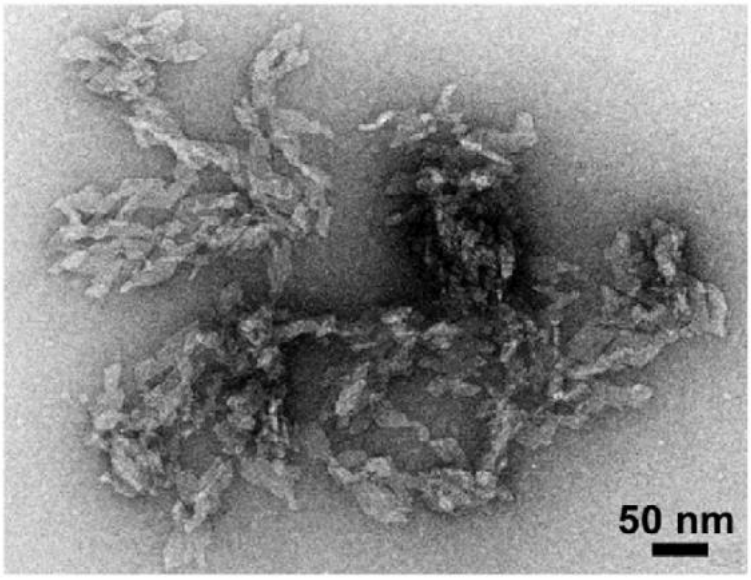

Figure 2.2 TEM image of starch nanocrystals through conventional acid hydrolysis approach [reprinted from [18] with permission from American Chemical Society]

The hydrolysis rate of starch granule will dependent on the number or quantity of amorphous and crystalline regions in the structure which dependent on the source of the starch, crystallinity of the native starch granule, acid used for the hydrolysis, concentration of acid, acid interaction time of starch granule and the surrounding condition during the hydrolysis such as pressure and temperature of surroundings. All these parameters directly or indirectly effects on the

degree of hydrolysis that is on the yield of the hydrolysis or quantity of SNP produced from the native starch [19,20]. The addition of a sulfate functional group on the surface of the nanoscale starch granules is induced by sulfuric acid (H_2SO_4) during hydrolysis. These additional functional groups provide additional stability to the SNPs in the solution; however, these benefits are lacking in the case of hydrolysis with hydrochloric acid (HCl). But the drawback of these additional functional groups is that at higher temperature exposure, the sulfate-ester bond reduces stability, and coarser nanoparticles are rapidly developed. These interactions are also not very suitable for starch granules when they are intended to be used in the formation of nanocomposite material complexes. [21]. During the acid interaction with the starch granule the surface protein and enzymes were react first and offered very minute resistance to the hydrolysis. The inner layer of the starch which is helix type structure of alternative crystalline and amorphous lamellas. The size of original starch granule will effect on the rate of hydrolysis as well as duration of hydrolysis. As with lower size starch granules surface proteins and enzymes are also lower and penetration of acidic media inside the starch granule is in the higher extent as compared with the larger size starch granule [22]. Thus, the overall acid hydrolysis rate of starch granules shows dramatic variations it depends up on the size of starch granule as well as contact of acid. The polymeric structure of amylose and amylopectin gets segmented during the hydrolysis leading to produce the smaller chains of these polymer [23]. However, acid hydrolysis has the drawbacks of being a slow process and, more significantly, a poor yield (less than 15 %) [24] .

Selvaraju et al. [25] reported the study of the acid hydrolysis of starch granule with individual both sulfuric acid as well as hydrochloric acid. The author reported that, with different acid the hydrolysis rate of starch granule was different for the same time (7 days), as well as the shape, surface morphology, particles size distribution (PSD) and yield of SNP are different. The spherical shape with yield of 10 % of SNP was reported with HCl acid were as random shape or oval geometry with yield of 8 % of SNP with H_2SO_4 acid. It can be concluded that for the different source starch granules, the degree of acid hydrolysis is different, irrespective of whether the same acid type, concentration, and contact time were maintained during the hydrolysis process [23]. The study of acid hydrolysis using sulfuric acid for waxy maize starch [17,21,23,26], for maize starch [23], for potato starch, corn starch, mungbean starch [23] was reported. However with HCl hydrolysis of waxy maize starch [27], potato starch [28], Canavalia ensiformis Starch [29] was explore at lower extent. In this concern it can be conclude that, the time requirement to achieve the similar SNP particle size HCL hydrolysis (15 days)

required significant more time than that of H_2SO_4 hydrolysis (5-7 days). The yield of SNP with sulfuric acid is much higher than that of HCl hydrolysis. [25,30].

2.1.2 Precipitation approach for the SNP synthesis.

The precipitation of a starch dispersion in a suitable solvent is a well-known method for the synthesis of starch nanoparticles after acid hydrolysis. In the precipitation of starch nanoparticles from starch dispersed solution, organic solvents such as alcohols, urea, and the alkaline solution of NaOH are commonly used. The controlled size and morphology of the synthesized nanoparticles are the primary requirements to be achieved through the anti-solvent nanoprecipitation method [31]. The source of the starch, its composition of amylose and amylopectin, lipids, and proteins, all these will not have an effect on the particle size of SNP produced through the precipitation method. Controlling the ratio of starch-dissolved solution to organic solvent used in the method allowed for a wide range of SNP to be produced. However, the large amount of organic solvent required by this method is a major concern, limiting its commercial application. Though the precipitation method produced a controlled-size SNP, the overall efficiency and yield of the process are much lower than those of the conventional acid hydrolysis process.

In the phenomenon of precipitation, when the dispersed polymers of amylose and amylopectin are added to the solvent, a change in the orientation of the polymer linkages takes place along with the solvent displacement from the lipophilic solution [32]. The ratio of starch-dissolved solution to precipitation solvent has a significant effect on the size and yield of SNP synthesized in the process, as do other process parameters such as the effect of solvent temperature on SNP synthesis [33]. Tan et al. [34] demonstrate the effect of various parameter such as concentration of solvent and starch in the process on the size and yield of the synthesized starch-based nanospheres through nanoprecipitation approach. The meaningful enhancement was observed in the size of the SNP nanospheres as the concentration of starch in the precipitation solution increases. In the similar context Juna et al. [35,36] reported the decreases in the size of SNP in precipitation method as the temperature of system increases. The precipitation process was conducted by the Juna et al. [35,36] in the microwave controlled environment where the temperature variation was considered to be uniform and constant for every experimentations.

The preheated native starch shows higher possibility towards the preparation of SNP through precipitation approach. The high rate of SNP synthesis was observed with pre-heated native starch in association with commonly used solvents individually (such as methanol) or in combination (two or more solvents such as urea and NaOH) was observed by chin et al. [37].

In another approach of micro emulsion Chin et al. [38] reported the synthesis of SNP with mean particle size of 83 nm which is smaller than the precipitation approach (109 nm). The simple water in oil microemulsion was exploited for the synthesis of SNP. The particle size of synthesized SNP was affected by the process parameters such as surfactant, concentration of surfactant, ratio of water to oil, oil to surfactant, and oil phase. The process generate lower interfacial tension, it is thermally stable and synthesized nanoparticles shows monodispersed conditions all these improvements shown by the microemulsion over the precipitation method [37,38]. The effect of surfactant concentration on the shape and size of SNP granules was also reported.

The synthesized SNP with the precipitation method was in the range of 300 nm to 400 nm [39]. The process of synthesizing nanoparticles with the proposed precipitation method requires less assistance for the product separation, and it is also easier to operate as compared with the acid hydrolysis method [35]. Microemulsion-based precipitation was used well to regulate SNP particle sizes in a stable environment [38]. The spherical shape of SNPs has been discovered to be more common than other forms with a narrower size distribution between 80 and 90 nm [40]. It was also developed for the synthesis of SNPs in the 110-140 nm size range [31]. The size distribution of SNPs was similarly affected by the rate of mechanical agitation. The requirement of large quantity of solvent, lower overall conversion of starch in to SNP, and the precise operations makes the process difficult for the industrial scale implementations. However the process develops size controlled SNPs with minimal separation operations.

2.1.3 Ultrasound Irradiation: an approach for SNP synthesis

Like acid hydrolysis, ultrasound irradiation is a top-down method; however, it will not consume the chemicals for the treatment, and the overall time requirement is much lower to achieve the conversion. It enforces high physical shear stress on the external surface of starch granules during high-intensity sound exposure. The intensity of the shear stress will be dependent on many process parameters, such as the density, viscosity, and temperature of the solution in which starch is suspended, the power input to the ultrasound generator (the type of horn, transducer used in sonication equipment), and the cavitating conditions. The high-energy vibrations are created by piezoelectric or magnetostrictive transducers to produce ultrasound. A sonotrode or probe that is in direct touch with the fluid receives and amplifies these vibrations. Extraction (plant material release), emulsification, homogenization, crystallization (smaller ice crystal formation during freezing), filtration, separation, viscosity alteration, anti-foaming, and extrusion are just some of the known applications of high power ultrasound in

the food processing industry. Cavitation and the subsequent production of free radicals are responsible for ultrasound ability to inactivate enzymes and bacteria by rupturing their cell membranes [41]. The figure 2.3 shows the SNP synthesized with ultrasound assistance.

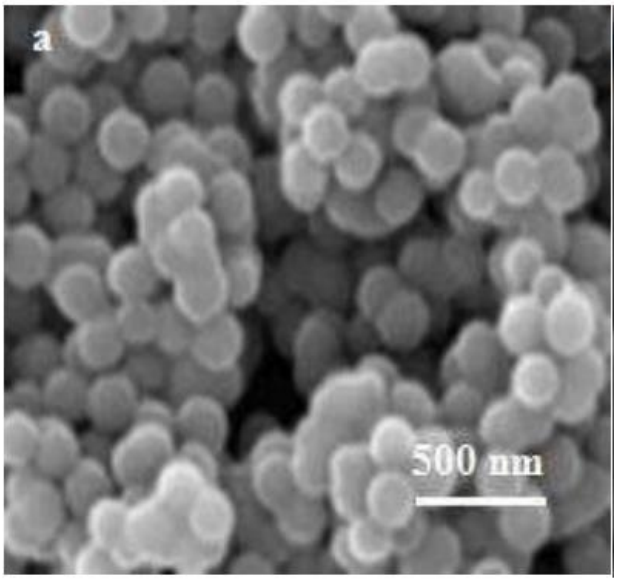

Figure 2.3 SNP synthesized with ultrasound irradiation. [reprinted from [40] with permission from Elsevier].

The higher the frequency of the sonicating device, the lower the physical impact; and the lower the frequency, the greater the physical impact. The study reported that at lower frequencies, from 20 to 30 kHz, the cavitation effect is significant to achieve the physical destruction of starch granules into smaller fractions or segments. The alternate compression and rarefaction region of the sound wave is the basic cause of the development of the pressure gradient inside the liquid medium, as a result of which the cavities are produced, nurtured, and collapse. The mechanical impact on the starch granules will be caused by the shock wave generated during the intense collapse of the cavities. The reduction in particle size was achieved by reducing the length of amylose and amylopectin polymers in the granules. The only drawback associated with ultrasound irradiation is the localized shockwaves generated after collapses of the cavities will produces the mechanical impact which is random in the application. The randomness in the mechanical impact of cavitation brings the irregular breakdown of the starch granule, thus the wide particle size distribution for synthesized nanoparticles is observed. The different configuration of amylose and amylopectin will effects different morphology of SNP. Due to the random breakdown of the starch granules the overall yield of the conversion is lower. The energy required to generate the high frequency sound waves is another constrain on the process to be applicable on the large scale [42]. The benefits of the ultrasound irradiation is the process

does not required additional chemical for the particle size reduction of starch granules, no byproducts were generated during the conversion except different particle size starch granules. The process required minimal amount of solvent and same solvent can be reused in reparative cycles [40,43].

The another parameters such as the native starch granular size, solvent used for the dispersion of native starch, type of sonication devices (horn or bath), and process parameter such as temperature and pressure of the system are directly or indirectly effect on particle size of SNPs synthesized. The localized hot spot generated during the cavities collapses in the suspension of native starch granule, induces rise in the temperature of suspension which increases the possibility of gelatinization of starch in the suspension. The glucose monomer polymers (amylose and amylopectin) get dissociated at higher temperature and different orientation of the glucoside bonds will takes place. Thus, it is required to be operate the process at lower temperature to avoid the phenomenon of gelatinization of starch. The starch structure get completely destructed in the gel phase which is irreversible process [44,45]. Unlike other methods, ultrasound irradiation results in the physical destruction of granules, which significantly disturbs the original granule orientation of starch. In the fragmented starch granules, the crystalline layer breaks, i.e., the intertwining of branched amylopectin and amylose loosens up, leading to the enhancement of the amorphous region of the granules. However, the crystallinity of the SNP synthesized in acid hydrolysis increased significantly due to acid interactions between glycose-based polymers [43,46]. The morphology of the synthesized SNP with the ultrasound irradiation method was observed to be random. This randomness in the morphology was due to the randomness of the mechanical impact during the cavitation effect. The surface of SNP shows the presence of the hydroxyl functional group. The energy requirement for the particle size reduction is minimal in the ultrasound irradiation approach [47]. The physical destruction of starch granules leads to the breaking of the strongly tight crystalline phases of amylose and amylopectin, due to which the resistance offered by the starch granules for the penetration of the solvent molecules reduces. The enhancement in the water absorption capacity of SNP was observed by Ahmad et al. [48].

The detrimental impact of ultrasonic irradiation on food material was documented by Jambraket et al. [49], who found that the free radicals produced by the ultrasound had an adverse effect on the food. When the granular structure of starch particles is disrupted by sonic cavitation, the amorphous phase of the particle comes into direct contact with the acid solution. However, the ultrasound effect in combination with the heat treatment call thermo-sonication

will be beneficial and effective to the food processing units. In the similar context the sonication in combination with the high pressure is more significant and energy efficient process for food industry [50].

The time of ultrasound irradiation on the suspension of starch particles has effects on the mean size and geometry of the SNPs synthesized. A significant decrease in particle size is associated with a decrease in the crystallinity of the SNP as the irradiation time increases [46]. Moreover, the energy requirement for the conversion gets significantly higher as the time for exposure to irradiation increases. The mode in which the irradiation was provided is also important. The reported study recommended irradiation in pulse mode. The pulse mode is a discontinuous mode in which an intermediate interval for irradiation is provided to allow enough time for the temperature and pressure inside the suspension to be restored. In the continuous mode of exposure, the energy dissipated during the collapses of the cavities gets accumulated in the suspension, and the suspension temperature gets significantly higher. The break-down of amylose and amylopectin polymer chains in the smaller segments only generates the SNP, whereas at higher temperatures, gelatinization could cause the complete destruction of starch structure [51].

2.1.4 Other significant approaches for the synthesis of SNPs.

LeCorre et al. [52] reported that, the enzymatic pretreatment on the native starch granules was beneficial for the second stage acid hydrolysis of starch. They abundantly found enzymes perform the first stage hydrolysis on the starch granule. The commonly found enzymes such as α-amylase, β-amylase, and pullulanase can strongly interact with the native starch granules resulting in the easier penetration of acid molecules interior of starch granule. The higher the rate of diffusion of acid molecules inside of starch granule higher will be the rate of hydrolysis and time consumed by the conversion is significantly reduces from 5 days to 45 h [52]. The enzyme interact with the α-1, 4 bonds cause the cleavage in the amylose or amylopectin polymeric chains, due to which the acid molecules could penetrate and transferred to the interior regions of starch granule. The enzymes β-amylase is co-amylose which induces the split between the amylose straight polymer chains. Kim & Lim [53] reported the effective utilization of α-amylase for the pretreatment of waxy rice starch before the acid hydrolysis treatment. The enhancement in the acid hydrolysis rate was observed to be significant. The split has developed in the amylose and amylopectin polymers during enzymatic hydrolysis, resulting in the formation of holes in the intertwined compact structure of the crystalline region of the starch. The debranching of amylopectin is due to enzymatic interaction; thus, in the

enzymatic hydrolysis, the overall crystallinity of the SNPs decreases [53]. The enzymatic pretreatment optimizes the acid hydrolysis process. It consumes less time with the added cost of additional enzymatic hydrolysis of SNP, due to which the cost of the process increases. Only the enzymatic process is faster, and the yield of the process is about 50%, which is much better than that of acid hydrolysis.

Another approach for the synthesis of starch nanoparticles was through high pressure applications, such as the high pressure homogenization process [54,55]. In the high-pressure homogenization process, shear stress is applied to the starch granular surface by the high-velocity fluid flowing through the close-flowing channels. The liquid is made up of native starch granules and flows through small diameter channels at high pressure and velocity. A high-pressure fluid flows from an external source, such as a hydraulic pump or high-pressure pump. Under the mechanical force impact, the shear stress applied by liquid streams on the surface of starch granules breaks the hydroxyl bonds and processes with particle size reduction. When applied to a starch granule, shear stresses cause physical destruction of the compact crystalline structure as well as size reduction. As like in the ultrasound irradiation for the physical destruction of starch granules, the complete destruction of the starch structure also observed in the high pressure homogenization process [56,57]. Tester et al. [58] reported the structural analysis of starch. The slurry of starch which could be homogenized in the equipment is quantitatively very less to obtained SNP with particle size distribution in the lower values. Ding and Kun [59] reported the experimental results for the synthesis of SNPs through high pressure homogenization with average particle size of 300 nm. The produced SNP reported to be have lower value of crystallinity due to direct rupture of starch granules during shear stress application.

Glucose based polymers (amylose and amylopectin) could be modified by gamma irradiation in a number of ways, including by grafting, cross-linking, and degradation. There is evidence that gamma irradiation may effectively shrink starch molecules [60]. Singh et al. [61] reported that the gamma rays have the ability to quickly split big molecules into smaller ones, and as a result, glycosidic bonds are likewise broken by gamma rays [61]. The process begins with the creation of a homogeneous paste of the starch, followed by its exposure with gamma rays that create active free radicals encouraging the hydrolysis of starch by breaking the branched amylopectin and short branched amylose exclusively from the amorphous region of starch granules. As a result, this process is somewhat similar to acid hydrolysis. In most cases, however, the generated nanoparticles have a size of less than 100 nm. As a result of their

diminutive size, nanoparticles are more likely to coalesce into thermally unstable nanocrystal aggregates [30]. It has been observed that gamma rays alter the geometrical and physical characteristics of starch, with disintegration occurring in the amorphous areas rather than the crystalline ones [62]. Lamanna et al. [63] successfully produces the SNPs with 30 nm and 20 nm in size from waxy maize and cassava starch, respectively, by applying a gamma radiation dosage of 20 kGy; these SNPs have been shown to be more susceptible to heat deterioration than native starch particles. Irradiating a polymeric solution also results in the formation of nanogels. Binh et al. [64] reported use of gamma radiation at doses of 10-16 kGy to cross-link carboxymethyl starch, resulting in nanogels with sizes below 50 nm.

Under the impact of relatively high temperature, pressure, and shear forces, starch granules undergo significant structural changes in the extrusion process. Since there is not enough water to cause full gelatinization, the starch granules soften and melt during the extrusion process, and the nanosize particles that arise allow water to travel more quickly inside the starch granules. High shear pressures disrupt molecular connections during extrusion, which may also lead to the starch granules losing their crystallinity [65]. SNPs formed by reactive extrusion are also regarded as "regenerated starch nanoparticles" because to the cross-linking of the fragmented starch molecules that occurs throughout the process [66]. Reactive extrusion with or without glyoxal as cross-linkers has been used to create SNPs from maize starch (Song, Thioc, & Deng, 2011). It was shown that, without the use of cross-linkers, SNPs could grow to a size of 300 nm at 100°C, but SNPs grown with cross-linkers shrank to 160 nm at 75°C. When cross-linkers were introduced, shear forces and torque were amplified, allowing for a considerable decrease in nanoparticle size to occur even at low temperatures. Without a cross-linker, the authors of this study found that when the extrusion temperature rose, the starch particles shrank in size and the torque dropped as a result of the starch's softer consistency [67]. However, extrusion with the addition of cross-linker resulted in a cross-linked starch network requiring greater torque and, therefore, higher shear forces, leading to smaller starch particles at a relatively lower temperature. This indicated that the thermal effect of increasing temperature was likely to influence the reduction of size of the starch particles during extrusion without the cross-linker under small torque, whereas in the case of cross-linker assisted extrusion, a higher value of torque was influential to decrease the size of the starch particles. SNPs with a size of 160 nm were achieved at a temperature of 75°C, compared to 300 nm at a temperature of 100°C without cross-linker [68].

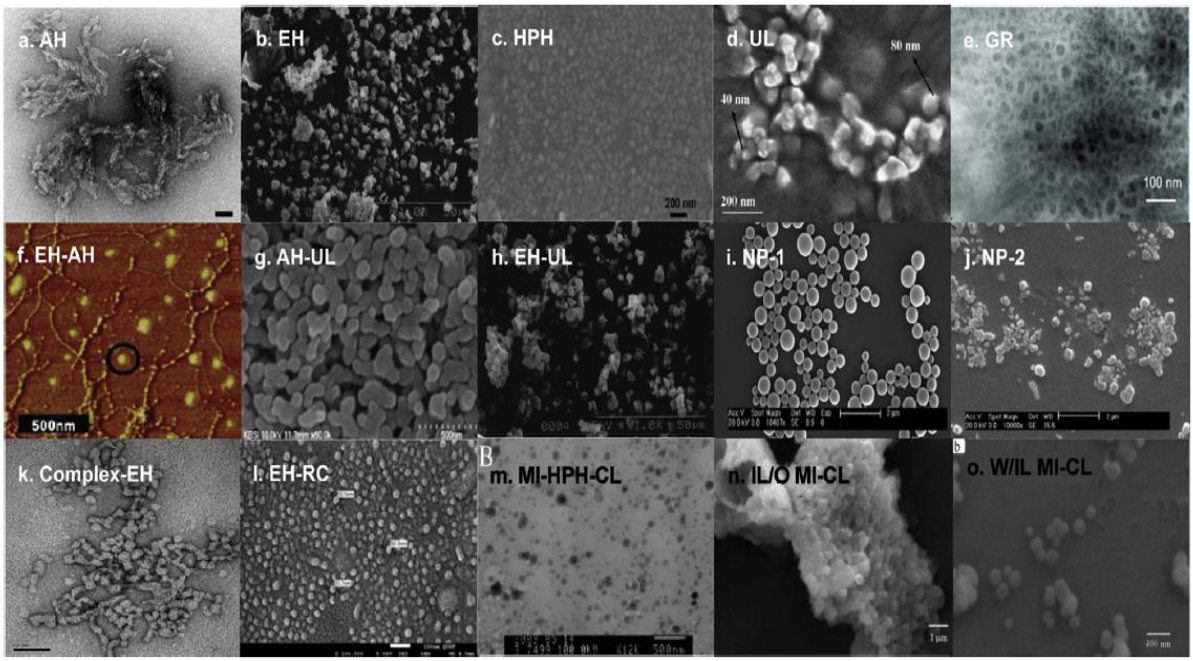

Figure 2.4 Morphology of starch nanoparticles (SNPs) obtained by various preparation methods. (a) TEM micrograph of waxy maize SNPs obtained by acid hydrolysis. (b) SEM micrograph of waxy rice SNPs obtained by enzymatic hydrolysis. (c) SEM micrograph of high amylose corn SNPs obtained by high-pressure homogenization. (d)SEM micrograph of waxy maize SNPs obtained by ultrasonication. (e) TEM micrographs of waxy maize SNPs obtained by gamma radiation. (f) AFM micrographof waxy maize SNPs obtained by enzymatic hydrolysis and acid hydrolysis. (g) SEM micrograph of waxy maize SNPs obtained by combination of acid hydrolysis and ultrasonication. (h) SEM micrograph of waxy rice SNPs obtained by enzymatic hydrolysis followed by ultrasonication. (i and j) SEM micrograph of waxy maize starch acetate (SA) nanospheres and corn SNPs obtained by nanoprecipitation, respectively. (k) TEM micrograph of amylomaize starch–butanol complexes isolatedby enzymatic hydrolysis. (l) SEM micrograph of proso millet SNPs obtained by combination of enzymatic hydrolysis and recrystallization. (m) TEM micrograph of soluble SNPs obtained by high-pressure homogenization of water-in-oil (W/O) microemulsion followed by cros-linking through sodium trimetaphosphate (STMP). (n)SEM micrograph of normal maize SNPS obtained by combination of ionic-in-oil (IL/O) microemulsion preparation and its cross-linking through epichlorohydrin. (o)SEM micrograph of SNPs obtained by combination of water-in-ionic liquid (W/IL) microemulsion preparation using a acid treated starch followed by cross-linking throughepichlorohydrin [reprinted from [69] with permission from Elsevier]

Table 2.1 SNPs synthesized methods and their characteristics (yield and crystallinity)

S. No.	Method	Yield	Crystallinity	Applications	Ref.
1	Acid hydrolysis 3.16 M H_2SO_4 at 40 ^oC, 5 Days	15 %	No change with respective to native starch	Corrugated and Paper making	[70]
2	enzymatic treatment α-Amylase hydrolysis at 37 ^oC for 3 h	33 %	No change	Food & cosmetic industry	[15]
3	Physical treatment Ultra-sonication (80% power, 8 ^oC, 75 min)	22 %	decreases	Food ingredient	[46]
4	Precipitation preparation by precipitating starch solution with ethanol as the precipitant	16%	Transformed to V type Lower crystallinity	Paint additives	[59]
5.	Gamma radiation at a dose of 20 kGy (14 kG/h)	21 %	Decreases	confectionery	[63]

The figure 2.4 gives an illustration of different size and shape of SNPs synthesized with the different methods. The physical and chemical disintegration of starch granules with different methods produces the SNP with different morphology and physico-chemical characteristics; each method has its benefits and drawbacks associated with it. The conventional acid hydrolysis methods have a huge possibility for modification in combination with other methods. The enzymatic hydrolysis as pre-treatment for the starch leads to a significant reduction in the time for the acid hydrolysis in the second stage. Thus, for the next stage of work, acid hydrolysis in combination with the cavitation effect was decided to be explored for the development of an economical, sustainable SNP synthesis process. Table 2.1 discussed about the methods for the synthesis of SNP with their yield, crystallinity and applications.

2.2 Synthesis of cellulose nanofibers / nanoparticles

Like as starch, Cellulose is the most common natural polymer on Earth and a crucial structural component of plant cell walls. Aside from plants, cellulose may also be found in algae, fungi, bacteria, and even some marine species such as tunicates. Cellulose is a polysaccharide that is fibrous, stiff, and insoluble in water, which helps to maintain plant cell walls rigid and undamaged. Cellulose is a natural polymer that is biocompatible with human cells and can be renewed, making it a possible substitute for non-biodegradable polymers derived from fossil fuels. The semi-crystalline structure of cellulose composed like starch by two regions. The

crystalline region of the cellulose is highly compact and orderly arranged. Whereas, the amorphous phase is completely disordered. The compactness of the structure is major function of hydroxyl bond between and outside of the monomer units. The chemical composition of cellulose illustrated in Figure 2.2. The monomers in the cellulose structure are linked with glycosidic oxygen molecule bond. The overall polymer resulting from the condensation of monomers to prepare the long chain of cellulose. The β-1,4-linked glucopyranose unites are connected with each other by the oxygen bond bridge, which are 180° corkscrewed with respect to their neighbors. These are heavy molecular weight natural polymer. The combination of two glucopyranose monomer forms a monomer unit of cellulose polymer monomer is known as cellobiose [71]. The condensate water molecules were ejaculate from the combination and the both the monomers are connected across the oxygen molecule. Due to the similar electronic configuration both the monomers are connected with mirror alike orientation in 180^{o} to each other, as illustrate in figure 2.5. This naturally occurring polymer is produced from the cellobiose dimer. Cellulose polymerization levels vary from roughly 10,000 glucopyranose units for wood cellulose to over 15,000 units for cotton cellulose. The high reactivity of the hydroxyl groups contained in each glucopyranose unit is the starting point for hydrophilicity, chirality, biodegradability, and other cellulose-specific properties. Some properties, such as a multiscale microfibrillated structure, a hierarchical organization (crystalline and amorphous fractions), and a highly cohesive nature, may be attributed to these hydroxyl group ability to form strong hydrogen bonds [72].

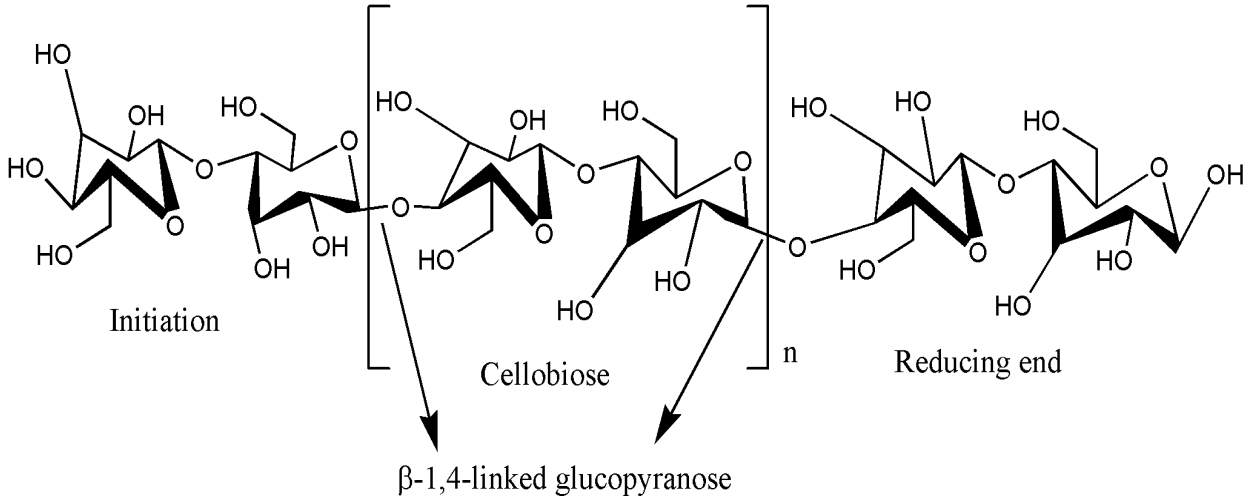

Figure 2.5 Chemical structure of cellulose, which is a linear polymer made up of β-D-glucopyranose units covalently linked with β-(1–4) glycosidic bonds.

The algae, bacteria, and other marine creatures may also produce enormous amounts of cellulose along with the plants [73]. Plants are plentiful and affordable cellulose sources. Wood pulp and cotton fibers provide most cellulose. For harvesting, processing, and extraction, large-scale industrial infrastructures are available. Jute, ramie, sisal, flax, hemp, etc. are additional well-known cellulose sources [74].

Water plants, grasses, and plant components including leaves, stems, and fruits produce cellulose. Wheat and rice straw, sugarcane bagasse, sawdust, cotton stalls, etc. are used to make cellulose. The crystalline algal cell walls contain native cellulose. Green algae are recommended for cellulose extraction over red and yellow algae. Cladophorales (Cladophora, Chaetomorpha, Rhizoclonium, and Microdyction) and Siphonocladales include cellulose-producing algae (Valonia, Dictyosphaeria, Siphonocladus, and Boergesenia) [75]. Valonia or Cladophora cellulose may be 95% crystalline. 8 Depending on the species production process, cellulose microfibril characteristics may vary. Komagataeibacter xylinus, a vinegar fermentation contaminant, produces cellulose from a number of nitrogen and carbon sources [76]. K. xylinus generates cellulose microfibrils in the form of transparent, flat, thick pellicles [77,78]. These cellulose pellicles include cellulose, water, and other medium components. Dilute alkaline solutions hydrolyze cellulose pellicle impurities [79]. The cellulose pellicles may be processed into pure cellulose membranes after alkali treatment and washing. Microbially produced cellulose offers various benefits over plant-derived cellulose, including a unique nanostructure, purity, higher-dimensional stability, stronger mechanical strength, and increased water-holding capacity [80]. Microbial cellulose has the same molecular formula and polymeric structure as plant cellulose, but its glycosyl units are arranged differently inside crystallite unit cells, leading to increased crystallinity. Microbial cellulose has greater polymerization and characteristics compared to plant cellulose [81]. Tunicates are marine invertebrates that produce cellulose. Cellulose works as a skeleton in tunic tissues, which coat the tunicates epidermis [82]. Animals make cellulose utilizing epidermal enzyme complexes. Tunicate species abound in nature, and their cellulose characteristics differ. Structure and characteristics of cellulose microfibrils from various species are frequently equivalent, although tiny changes in production might alter final attributes [83].

The proportion of crystalline regions relative to amorphous regions in natural cellulose bulk may vary depending on where it originates from [84]. The highly crystalline sections of cellulose microfibrils may be removed via a succession of mechanical, chemical, and enzyme processes, resulting in the formation of cellulose nanocrystals (CNCs). CNCs are stiff, rod-

shaped particles consisting of virtually perfect crystalline cellulose chain segments. When compared to bulk cellulose, which includes more amorphous fractions, these nanocrystals exhibit greater specific strength, modulus, surface area, and unique liquid crystalline properties [85].

As, like starch nanoparticle synthesis method, a number of mechanical, and chemical techniques have been used to leached out the crystalline cellulose. The physical destruction of the cellulose to achieve the size reduction of cellulose includes the methods such as high-pressure homogenizations, high-intensity ultrasonic treatments, microfluidization operations, cryocrushing, and others. The physical destruction of cellulose through shear pressure in the mechanical approach facilitate to cellulose microfibrils to get separate from the structure and longitudinal axis cut produces the particle size reduction of cellulose. As like in the starch cellulose did not include any kind of branching or fold, the cellobiose dimer are linked with the disordered zone [86]. When cellulose microfibrils are chemically transformed into CNCs rather than physically, energy consumption is reduced and shorter, rod-like nanocrystals with increased crystallinity are created. Mechanically refined wood cellulose samples exhibited a lower crystalline proportion (0.05-0.55) than rod-like wood CNC (0.6) created through acid hydrolysis [87]. Strong acid hydrolysis is often used to eliminate the amorphous domains that are evenly distributed throughout the microfibrils. Strong acids may easily hydrolyze the low-order amorphous portions while leaving the crystalline areas alone. In 1951, Ranby [88], published the first report on the properties of cellulose in the colloidal state with sulfuric acid solution. Ranby [88] used a moderate temperature acid solution to achieve acid-catalyzed cellulose fiber fragmentation. The cellulose exposure for a limited time enhances the separation of cellulose fibrils from the compact structure, leading to the separation of lignocellulose in the acidic solution. The lignocellulose's separation from the cellulose structure results in the formation of cellulose nanofibrils. The needle-like geometry of the produced cellulose fibrils can be confirmed by using a transmission electron microscope and electron diffraction studies [89]. The nanocellulose or cellulose nanocrystals (CNCs) is another form of crystalline cellulose separated from the cellulose fibrils. A number of methods are reported for the synthesis of CNCs from the fibrils of cellulose. The chemical and mechanical methods that are exploited for the breakdown of polysaccharide starch, can similarly be utilized for cellulose. However, the morphology and inherent structural characteristics of CNCs will differ for different synthesis technique applications [90].

The acid hydrolysis is commonly exploited for synthesis of nanocellulose from cellulosic materials. Both crystalline (ordered) and amorphous (disordered) region coexist in cellulose chains; the former are easily destroyed by acid, while the latter are left as residue [71,91]. Sulfuric acid is used in the majority of acid hydrolysis [92,93]. Because the hydroxyl group is esterified by sulfate ions, nanocrystalline cellulose is not only highly isolated but also diffused as a persistent colloid system [94,95]. The key factors of the properties of the resultant nanocellulose are reaction time, temperature, and acid concentration [90,91]. The biggest disadvantage of acid hydrolysis is the acid wastewater created during the washing process to neutralize the pH value of the nanocellulose solution. The normal cleaning approach is to add cold water and then centrifuge it until the pH is neutral [96]. Another alternative for washing the generated materials is to use an alkaline, such as sodium hydroxide, to neutralize the pH value [97].

Maiti et al. [98] exploited acid hydrolysis with 47% sulfuric acid to separate nanocellulose from three types of biomass. After the reaction was completed, the acid was removed by centrifugation and washing with deionized water, followed by the addition of 0.5 N sodium hydroxide to neutralize the suspension and another wash with distilled water. With the use of a catalyst, such as the 2,2,6,6-tetramethylpiperidine-1-oxyl radical (TEMPO), and a primary oxidant, such as hypochlorite, the hydroxyl group of cellulose may be oxidized to carboxylates [99]. As a consequence, the resultant nanofibrillated cellulose has a carboxylic acid surface and is 3-4 nm in diameter and a few microns in length [100]. The TEMPO-mediated oxidation is achieved in high-pH water by first dissolving TEMPO and NaBr and then commencing the oxidation with the addition of NaClO. Furthermore, you may use an alternative TEMPO/NaClO/$NaClO_2$ oxidation system for this process under neutral or moderate acid conditions [100]. Because of the high aspect ratio and uniform width (3-4 nm) of TEMPO-oxidized cellulose nanofibers, transparent and flexible displays, gas-barrier films for packaging, and nanofiber filling for composite materials [101,102] are all achievable.

Fan et al. [103] proposed the mechanism of enzymatic hydrolysis of cellulose. The authors found that the rate of enzymatic hydrolysis will be largely dependent on the crystalline compactness of the cellulose structure rather than the surface area available for the enzymatic activity. The higher the resistance offered, the more compact the structure [103]. Enzymatic hydrolysis is a biological treatment approach that uses enzymes to break down or change cellulose fibers [104]. Most enzyme-based biological therapies need just a modest environment, albeit the treatment itself takes a long time to complete [104,105]. Enzymatic

hydrolysis is often used in conjunction with other treatments to alleviate this issue. Moniruzzaman et al. [105] explored the process of enzymatic hydrolysis using laccase and discovered that pretreatment with an ionic liquid to enhance the available surface area was successful in extracting cellulose fibers from wood chips. It was discovered that the nanocellulose generated had more crystallinity and thermal stability than natural wood fibers. The most frequent mechanical procedures are ball milling, ultrasonication, and high-pressure homogenization. Every high pressure homogenization (HPH) procedure includes driving a cellulose slurry through a fast-moving, highly compressed tube [104]. Impact and shear forces in fluid break cellulose microfibrils into nanometer-sized fragments. According to Li et al. [106], several researchers have succeeded in separating nanocellulose from sugarcane bagasse using high pressure homogenization. The generated nanocellulose was 10-20 nm in size and crystallinity was lower than that of the original cellulose. High pressure homogenization was used to separate nanocellulose from cotton cellulose; the resultant nanocellulose had a diameter of roughly 20 nm and displayed worse thermal stability and crystallinity than raw cotton cellulose. Crystallinity was diminished due to the breakdown of cellulose's intermolecular and intramolecular hydrogen bonding during the high pressure homogenization process. Ultrasound hydrodynamic forces are employed to defibrillate cellulose fiber during the ultrasonication process. When liquid molecules absorb ultrasonic energy, mechanical oscillatory power is produced, resulting in the formation, expansion, and implosion of tiny gas bubbles [107]. Tang et al. [108] employed ultrasonication for 5 hours at 70 ^{o}C to remove nanocellulose from pure wood pulp filter paper, yielding a product with an 85.38% yield and a nanocellulose width of 10-100 nm.

Table 2.2 Types of Cellulose nanoparticles and their properties

S. No.	Type of nanocellulose	Typical sources	Average size
1	Cellulose nanocrystal (CNC)	Wood, cotton, hemp, flax, wheat straw, rice straw, mulberry bark, ramie, MCC, Avicel, tunicin, algae, bacteria, etc.	Diameter: 5–70 nm Length: 100–250 nm (from plant); 100 nm–several micrometers (from cellulose of tunicates, algae, bacteria)
2	Cellulose Nanofibrillated (CNF)	Wood, sugar beet, potato tuber, hemp, flax, etc.	Diameter: 5–60 nm Length: several micrometers

The combined physicochemical approach may also provide an improved solution for CNC synthesis. In the present research, cellulosic material was converted into nanoscale cellulose in both batch and continuous approaches. The conventional acid hydrolysis with ultrasound

irradiation in batch approach was employed for the size reduction operation and achieved the CNF. However, in the second approach, the synthesis of CNCs, the continuous hydrodynamic cavitation method was used in conjunction with a mildly acidic cellulose suspension. The CNC was produced after both approaches were studied for variation in the morphology and physical characteristics and reported. The time and cost effectiveness of the process are the major concerns for the synthesis of CNC. In the present research work, conventional acid hydrolysis was intensified with cavitation assistance for the synthesis of CNC. The hybrid approach to CNC production is advantageous in terms of both cost effectiveness and reduced time consumption. The yield of the process was also found to be higher than that of individual techniques applied for the same.

2.3 Need for the modification of conventional acid hydrolysis approach for the synthesis of Starch and cellulose nanoparticles.

Lower yield and higher time consumption for the particle size reduction are the two major limitations of the acid hydrolysis process. The rate of hydrolysis is determined by the molecular composition and the resistance provided for acid interactions. The penetration of acidic molecules in the complex structure and further interaction with hydroxyl bonds or glucose based bonds are again dependent on the mass transfer rate of acidic molecules and their mass transfer flux from bulk solution to the inside of granules. All these issues are present with conventional acid hydrolysis. The studies report the modification of acid hydrolysis with enzymatic pretreatment that reduces the hydrolysis time to 50 h. though the process induces an additional stage of enzymatic hydrolysis [52]. The limitation of the process is that the quantity of the enzymatic hydrolysis is restricted. As a result, the modification in conventional acid hydrolysis was concentrated with a more intense approach.

The degradation of the starch or cellulose granules in the acidic medium is basically due to the interaction of glucoside-bonded glucose monomers of polysaccharides with the acid molecules. The amorphous region interacts intensively as compared with the crystalline region and gets dissociated in the solution. The removal of the amorphous region from the granules leads to an increase in the crystalline nature of the residual structure of the granule. The same technique was intensified with the cavitation assistance and intensified to produce the higher yield of nanoparticles. The conventional acid hydrolysis process is time bound, and also the conversion is uncontrolled and is not uniform in size. The mechanical approach in combination with the chemical degradation could results in the intensified process development for the synthesis of starch and cellulose nanoparticles in economical sustainable approach.

Acid hydrolysis has been used for a long time to change starch and its characteristics. Hydrolysis of potato starch, at room temperature for 30 days in a 15 % H_2SO_4 solution, yielded an acid-resistant fraction with a low molecular weight, as described by Li et al. [109]. The two stage acid hydrolysis of polysaccharide granules was reported in literature [72,110] completed in fast step followed by slower hydrolysis. The first stage is where the randomly packed amylose and amylopectin monomers interact with the acid in the amorphous region. Lower stability is observed in glucose molecules where the first carbon is inked with the fourth carbon molecules via α (1,4) glucoside linkage to form the ring structure. The dissociation of acid in the suspension develops the radicals, which are highly interactive. The radicals penetrated very easily in the amorphous region due to the presence of space between randomly arranged amylose and amylopectin molecules. The glucoside linkage is susceptible to the interaction with the radicals generated by acid molecules and gets dissociated in the suspension.[98,111]. The overall hydrolysis rate will be dependent on the penetration rate of acid inside the polysaccharide granules. The ultrasound or cavitation assistance will provide the shock waves in the suspension. The shear stress developed due to these shock waves is high enough to produce cracks on the surface of starch granules or cellulose fibrils. Thus, the rate of mass transfer of acid along with the acid penetration into the interior of the granules enhances the hydrolysis rate. The higher the exposure to the cavitation condition, the higher the hydrolysis rate that can be found. As a result of the shear stress developed during the cavitation, the crystalline region of the granules also gets disturbed, which allows for rapid and higher quantities of acid penetration inside the granules [112].

2.4 Need for the nanocomposite films for the packaging application and role of bionanoparticles

There is significant interest in the development of bio-based polymers and new process technologies that may minimize reliance on fossil fuels and transition to a sustainable materials foundation. The invention of bio-nanocomposites has opened the way for novel, high-performance, lightweight green nanocomposite materials to replace non-biodegradable petroleum-based plastic packaging. Polylactic acid (PLA), polycaprolactone (PCL), poly-(butylene succinate) (PBS), and polyhydroxybutyrate (PHB) have all been thoroughly investigated as possible bio-nanocomposites for packaging applications (PHB) [113,114]. Among the various possible nanoscale fillers, layered silicate nanoclays such as montmorillonite and kaolinite stand out. Food packaging development prioritizes high barrier characteristics against the passage of oxygen, carbon dioxide, flavor compounds, and water

vapor. Antimicrobial properties, oxygen scavenging ability, enzyme immobilization, and indication of the degree of exposure to potentially harmful factors such as low temperatures or oxygen levels are just a few examples of how several nanostructures can be useful in providing active and/or smart properties to food packaging systems. The complete dispersion of nanoparticles and the increase of clay compatibility with polymers remain unanswered problems [115,116].

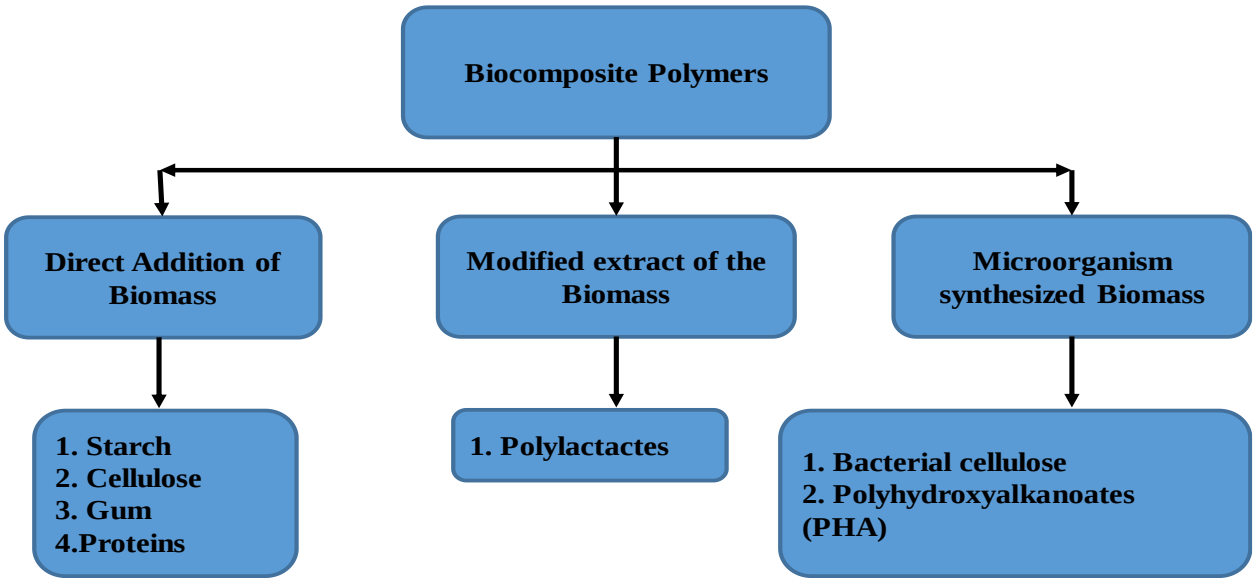

Figure 2.6 Classification of bio-composite polymers

The figure 2.6 illustrate the basic classification of the biocomposite polymers. The fundamental function of food packaging is to protect the food contained inside from potentially dangerous components such as spoilage bacteria, chemical pollutants, oxygen, moisture, light, external force, and so on while it is being kept, transported, and eaten. Obtaining a suitable shelf life and maintaining food quality and safety are dependent on packaging materials that provide physical protection and provide appropriate physicochemical conditions for goods. When creating a food packaging, it must be airtight, limit moisture gain or loss, and keep out germs and gases that might affect the flavor or fragrance of the food [117,118]. Food packaging nowadays acts as more than simply a container; it also offers critical barrier protection and performs a range of other essential duties. Food packaging varies substantially from containers used to store electronics, home furniture, and other items due to safety considerations and a much shorter shelf life. Because the objectives and demands of packed items vary, fundamental packaging materials such as paper and paperboard, plastic, glass, metal, and combinations of materials with varied chemical natures and physical structures are used. However, there has

been continuous research and development of new kinds of packaging materials to improve their effectiveness in preserving food quality while also making them simpler to process and use [119,120].

Plastics generated from petroleum have been among the most often used of the four basic packaging materials since the mid-twentieth century. This is owing mostly to its cheap cost, mobility, simplicity of manufacture, great aesthetic quality, and remarkable physico-chemical properties. More than 40% of all plastics are used for packaging, with over half of them utilized for food storage containers and containers. Once their useful life was up, the packaging materials should biodegrade in a reasonable length of time without causing environmental problems. Because synthetic plastic packaging materials are not easily degraded in the environment after use, their extensive use in the packaging of many types of food has raised serious environmental concerns. There is a lot of concern about the environmental impact of throwaway plastic packaging, particularly considering the shortage of adequate disposal solutions [121,122]. A growing number of people are looking for environmentally friendly alternatives to synthetic plastic packaging materials, such as biodegradable packaging materials derived from renewable sources (biopolymers) for use in short-term packaging and disposable applications such as disposable cutlery, disposable plates, cups, and utensils. Excellent mechanical and barrier properties, as well as biodegradability at the end of their life cycle, are distinguishing features of biodegradable packaging materials derived from renewable biological resources, also known as biopolymers [114].

Biopolymers have been researched as a packaging material as an environmentally acceptable alternative to typical plastics, which do not degrade and are not renewable. Biopolymer packaging materials have the potential to improve food quality and extend shelf life by functioning as gas and solute barriers in addition to conventional kinds of packaging. Furthermore, because of their flexibility as transporters, antioxidants, antifungal agents, antimicrobials, pigments, and other nutrients are readily included into biopolymer packaging materials [123]. Before bio based primary packaging materials may be employed in a commercial environment, a number of difficulties must be solved. Among the difficulties that must be addressed are the possibility of microbial growth and the release of toxic substances in packaged meals. In reality, the comparably poor mechanical and high hydrophilic properties with limited processibility of such biopolymer-based packaging materials pose a considerable hurdle to their commercial utilization [124,125].

Protein and carbohydrate packing films have good mechanical properties and are efficient oxygen barriers at low to moderate relative humidity levels, but since they are hydrophilic, they are poor water vapor barriers. Despite multiple studies showing a significant improvement in film characteristics, the physical, thermal, and mechanical qualities of biopolymer-based packaging films are still insufficient, posing hurdles in industrial applications. Bio-nanocomposites with better barrier, tensile, and thermal properties have recently been identified as a promising approach for improving the properties of these biopolymer-based packaging materials [120]. Bio-nanocomposites include particles (nanoparticles) with at least one dimension in the nanometer range that are embedded in a biopolymer matrix (1–100 nm). Because of their high aspect ratio and surface area, nanoparticles are a potential new class of materials known as bio- nanocomposites. As a result, studies have been done to develop bio-nanocomposites for food packaging films with improved mechanical, barrier, rheological, and thermal properties [126].

2.4.1 Polyurethane polymer based material for sustainable packaging film in combination with SNPs and CNCs.

The polyurethanes are widely recognized as one of the most adaptable materials currently available. Based on how their structures affect their properties, polyurethanes (PUs) are a group of flexible materials that can be used in many ways. Due to their unique mechanical, physical, biological, and chemical properties, PUs have been reported in the literature [127,128]. This is because they can be made to fit the needs of a wide range of applications. Changes to the manufacturing process or the raw materials used to make PU-based materials, as well as the use of sophisticated characterization strategies, can help improve their properties and performance. PUs that are good for different kinds of specialized uses can be made by changing the raw materials and manufacturing process in the right way. The goal of this study is to learn more about the chemistry, classification, and synthesis of PUs [129]. The specific application such as PU coatings were resistant to mustard gas and corrosion. In view of their sustainability towards a comfortable adaptation with the blended substance for the present research work, the nanocomposite films (of SNPs or CNC and PU) were synthesized. Nanocomposite thin films of SNP or CNC-based polyurethane were investigated and tested for packaging applications. The mechanical and thermal resistance of film, along with its barrier properties for water vapor, oxygen, and bacterial cells, have been studied and reported in the present work.

2.5 Nanoadsorbents and its applications for waste water treatment

The advancement in the nanotechnology during last few decade will offered new opportunities for making processes more efficient and provide greener techniques for the final conversion. The easiness in the separation of nanoscale products increases its possibility to exposure for number of application such as in field of heath, electrochemistry, food, biology and material science. The commercial application of silver nanoparticles for various applications such as optical applications such as light harvesting applications [130], in electronically conductive adhesives [131], and biomedical imaging and photo thermal therapy as silver nanoparticles possess the unique plasmonic and easy surface chemistry for a variety of functionalization with silver [132,133]. The effluent treatment with the nanotechnology applications is emerging for significant zero liquid discharge ideology achievement. Table 2.2 summarizing the reported literature on the biomass nanoparticles used for the separation of various metal ions form the waste.

Table 2. 3 Reported biosorption materials for the removal of heavy metals.

S. no	Biomass material	Metal	Biosorption capacity (mg g^{-1})	pH	Reaction time (h)	Adsorbent concentration (g L^{-1})	Ref
1	Orange peels	Pb	1.22	4.5-6	1	1.67	[134]
2	Oryza sativa	Cd	20.70	6	0.166	16	[135]
3	Olive pomace	Cu	10 ± 0.1	5	–	10	[135]
4	Rice husk ash	Se	2.007	2–8	∼100	1–10	[136]
5	Rice husk ash	Zn	9.588	2–8	∼1	1–10	[136]
6	Corn stover	Cr	84 ± 10	3	24	10	[137]
7	Soybean hulls	Cr	58 ± 2	3	24	10	[137]

Due to the increasing industrialization, a wide range of pollutants, some of which are very bad for human health, are being dumped into wastewater. Heavy metal ions, such as Pb^{2+}, Cd^{2+}, Zn^{2+}, Ni^{2+}, and Hg^{2+}, are very dangerous and non-biodegradable, and may cause major health problems in both animals and people. Heavy metal ions may be found in wastewater from a variety of industries. Chemical, battery, metallurgy, leather tanning, and mining companies are among those in this category. Direct discharge of wastewater containing heavy metal ions into natural water endangers aquatic life and may enrich the wastewater via precipitation and adsorption, presenting a risk to human health through the food chain. As a result, decontaminating wastewater by eliminating harmful metal ions is becoming more important [138].

Conventional procedures for removing heavy metal ions include chemical precipitation, reverse osmosis, electrochemical treatment methods, ion exchange, membrane filtration, coagulation, extraction, irradiation, and adsorption. Because of its low cost-effectiveness, high efficiency, and ease of operation for removing trace amounts of heavy metal ions, adsorption technology is regarded as the most promising approach for removing heavy metal ions from effluents. Metal ion adsorption research has concentrated on a broad range of materials, including activated carbons, clay minerals, chelating chemicals, and chitosan/natural zeolites [139–141]. Although traditional sorbents are excellent in removing heavy metal ions from wastewater, their low sorption capacities and efficiencies severely limit their utilization. Nanomaterials are a novel sorbent for extracting heavy metal ions from wastewater, outperforming traditional sorbents. Nanomaterials are those with particle sizes ranging from 1 nm to 100 nm. Nanomaterials, which exhibit distinct properties based on their size and shape, have been the topic of extensive research for more than a decade [142]. As nanoscience and nanotechnology have matured in recent years, they have shown incredible potential for resolving environmental challenges [143,144]. Nanostructure adsorbents have shown to be significantly more effective and fast in water treatment than their more traditional competitors. Nanomaterials that are used as sorbents to remove heavy metal ions from wastewater must meet the following criteria: The nanosorbents themselves must be safe first and foremost. Second, even though the concentrations of contaminants were low, the sorbents had great sorption capacities and selectivities. There was an easy way to get rid of the dirt that had stuck to the surface of the micro adsorbent. Fourth, the sorbents could be used over and over again forever. There has been an increase in interest in the development of resilient and effective wastewater treatment technology. Chemical precipitation, membrane processes, coagulation, extraction, advanced oxidation, photo-catalysis, and adsorption have all been used for this purpose [145].

Among these strategies, adsorption has shown to be particularly effective in removing organic pollutant from wastewater. Adsorption is a fundamental surface phenomena in which contaminants are selectively removed from an aqueous solution by adsorbing the solute (adsorbate) to a solid surface (adsorbent). Adsorption offers reduced costs, a simpler design, and a better effectiveness in eliminating minute quantities of harmful contaminants when compared to other alternative techniques. Despite the fact that considerable natural and synthesized materials like zeolites [146], metal-organic-frameworks (MOFs) [147], biomaterials [145], natural/modified clays [148], flyash [149], activated carbons [150], and

nanomaterials [151] have been studied as adsorbents for a long period, development of new efficient, low cost, and recyclable adsorbents retaining high adsorption capacities remains a key area of the advancements for adsorption technology.

Nanomaterials with a large surface area and nanosized holes are now playing an important role in the development of novel adsorbents for wastewater treatment [152–154]. They are essentially any substance that can be manufactured with particle sizes of 100 nm or smaller in at least one dimension. Tunable materials often have unique features (surface area, pore size volume, and structure, for example) at the nanoscale that vary from their bulk-sized attributes [150]. As a result, these appealing features, together with strong reactivity and sorption capacity, are projected to give good separation performance for water/wastewater treatment, allowing the use of unusual water sources. During the acid hydrolysis with H_2SO_4 significant sulpate group attached on the surface of starch nanoparticles. These functional group gives negative charge to the generated SNPs, which helps them to maintain the stability in the suspension. The surface charged nanoparticles produced during the ultrasound-assisted acid hydrolysis process are exploited for the adsorption of copper ions from synthetic aqueous solutions. To the extent of our knowledge, very few studies have been reported on the utilization of SNPs as nanoadsorbents. The studies have been focused on the efficiency of Cu removal from synthetic wastewater. The results of the lab scale can be implemented on the industrial scale through iterative optimization of the approach.

2.6 Gaps identification based on the state of art review

The conventional acid hydrolysis process required a higher acid concentration, which made the process more difficult to operate. The corrosion and its by products are the major concern of the conventional acid hydrolysis process. The hydrolysis rate of biomass (starch and cellulose) was substantially slower owing to the cell wall resistance to acid penetration. As a consequence, the process yield was much lower. The slower acid hydrolysis rate in the traditional technique will not cause a substantial variation in crystallinity of the biomass nanoparticles (starch and cellulose). The typical acid hydrolysis technique has a poor yield of around 16 %. For the production of starch and cellulose nanoparticles, high pressure homogenizers, enzymatic degradation, 2,2,6,6-Tetra Methyl-1-Piperidine Oxoammonium (TEMPO) oxidation, and precipitation techniques are all energy and chemical demanding approaches.

The narrower particle size distribution, and higher crystallinity of nanoparticles where essentially required for the effective applications of bionanoparticles. The existing methods are failed to provide the narrower particle size distribution with the nanoscale particle size. The higher chemical consumption and energy demanding reported processes are not much economical for the production of stable nanosized biomass (starch and cellulose) particles. There is need for the greener approach for the production of bionanoparticles in the larger scale for its commercial applications. The optimized technique with lower energy and chemical consumption need to explore.

Synthesis of starch and cellulose nanoparticles using ultrasound is a promising approach due to its efficiency and environmental friendliness. However, there are still gaps in knowledge and understanding that need to be addressed to optimize this synthesis method. Ultrasound parameters such as amplitude, frequency, and treatment time play a crucial role in the synthesis of nanoparticles. However, there is a lack of understanding regarding the effects of these parameters on the size, morphology, and yield of the nanoparticles. Optimization of these parameters is necessary to achieve better synthesis efficiency and reproducibility. Although ultrasound has been used to synthesize starch and cellulose nanoparticles in the laboratory, the scale-up and commercialization of this process remain a challenge. There is a need for more efficient and cost-effective methods for large-scale production of nanoparticles that can meet the demand for various applications.

The nanocomposite film based on the biomass nanoparticles (starch and cellulose) shows higher strength and needs to be explored more for its efficacies. The uniform distribution of nanoparticles in the polymer suspension is a major obstacle to large-scale production with current nanocomposite film production processes. This study looked into the uniform distribution and optimal thickness of nanocomposite films for mechanical and thermal strengths, as well as oxygen, water vapour, and bacterial cell transmission barriers.

The following gaps are identified and become a motivation for the research work presented here

- There is a need to identify an effective approach for producing nanoscale particles of starch or cellulose. Current methods are time and chemical consuming processes.
- Scale-up and commercialization of bionanoparticles (starch and cellulose) synthesis
- The current packaging materials are synthetic and require replacement with biocompatible materials.

- There is a need for a cost-effective method to remove heavy metal ions from wastewater due to their potential damage.

2.7 Problem statement and motivation

Waste from petroleum-based goods is a big problem globally, and it is growing more relevant in all nations. The proposed approach is to employ green, biomass-based renewable goods or sources for commercial purposes. These renewable biomasses have tremendous potential to supply solutions such as excellent sources of energy, chemicals, essential oils, and additives. Packaging applications, which are now based on petroleum-based polymers, produce a large amount of pollutants. The fundamental criterion for these packing films is that they have high mechanical and thermal robustness as well as minimal water vapour and bacterial penetration. The addition of nanofillers to the polymer matrix improves all of these qualities. Many biodegradable components have been described for the manufacture of edible films and coatings, including rice starch [155], fish skin [156], meat [157], and others. The mechanical strength of the described film and coatings is sufficient to compete with currently available packaging materials. As a result, different biomaterials must be used to substitute nanofillers in the biocompatible polymer solution.

These nanocomposite films of the next generation may be manufactured using biomaterial nanoparticles to increase the mechanical and thermal resistance of the basic polymer matrix. The solution will not completely remove the polymer-based packaging sheets or coating, but it may be used to remove some of them. As a result, the starch and cellulose biomaterials were chosen for future study in the creation of polymer-based nanocomposite films. Chemical-based adsorbents considerably aggravated the issue of solid waste disposal. The pollutant transforms into a new form that is more difficult to deal with using typical full-cycle disposal approaches. Bio-nanoparticles may be investigated as adsorbents for heavy metal ion extraction from wastewater. The utilization of starch and cellulose nanoparticles as adsorbents is investigated in this study. Various technologies, including nanoemulsion, suspension polymerization, acid hydrolysis, and ionic liquid hydrolysis, were used to convert copious starch and cellulose polysaccharides at the nanoscale. According to reports, the effective yield of present methods is less than 20%.

Starch and cellulose nanoparticles have several uses in areas such as food, cosmetics, and medicines. To commercialize bio-nanoparticles, an effective, efficient, and low-cost green technique to synthesis of these biomass nanoparticles is required. The bio-nanoparticles' industrial uses were hampered by the intricacy of their production method. The PI method to

bio-mass nanoparticle synthesis might give a solution for a robust and continuous, economically feasible process. These nanoscale biomaterials have a wide range of uses, including drug delivery surfaces, nanofillers, adsorbents, and many more. To improve mechanical and thermal resistance, petroleum-based synthetic monomers were utilized as nanofillers in the polymer matrix. These nanocomposite thin films are also resistant to microorganisms and have a greater water vapour barrier. It is envisaged that bio-based nanocomposite films would accomplish a similar result by replacing the petroleum-based synthetic filler with bio nanoparticles (cellulose and starch nanoparticles). These nanocomposite films may be useful in packaging applications.

Problem statement: Create a more effective and environmentally friendly process for generating starch and cellulose nanoparticles, then use these biomass-based nanoparticles to create nanocomposite thin films for packaging applications and nanoadsorbent.

2.7.1 Novelty of the proposed work

The shortcomings of native starch, such as poor tolerance to a broad range of processing conditions and poor functional properties, can be overcome through physical, chemical or enzyme modification, and starch has been made a useful polymer as a result of this property. Different physicochemical and biological properties have been observed in starch nanoparticles when compared to native starch, with higher solubility, reaction surface, absorptive capacity, and biological penetration rate. Starch is commonly chemically modified by oxidation. Oxidized starch is commonly produced by reacting a specified amount of oxidizing agent with starch under controlled temperature and pH. The oxidation process is time consuming and energy demanding process along with lower yield. The second most common modification of starch was with the acid hydrolysis. The conventional acid hydrolysis was intensified using ultrasound assistance. The cavities generated during the process was helpful for the achieving higher mass transfer rate of acid towards the biomass (starch and cellulose granules). The shear force generated during bubble collapse provides develops the shock waves in the fluid due to which the film resistance surrounding to the biomass get overcome by the acid molecules. The higher mass transfer of acid molecules on the surface of biomass increases the hydrolysis rate. This phenomenon will reduces the overall conversion time of biomass from micron size to the nanoscale. Some of notable novelty of the process are listed as,

- The crystallinity of the produced starch and cellulose nanocrystals could be improved. The increased thermal and mechanical resistance is attributed to the higher crystallinity of bionanoparticles.
- The Surface activity of the bionanoparticles could be improve with the acidic functional group interaction during hydrolysis.
- The cavitation effect can increase the mass transfer rate of acid which intensify the acid hydrolysis of the bionanoparticles (starch and cellulose).
- The narrower particle size distribution of synthesized bionanoparticles can be produce at the optimum conditions of the hydrolysis process.
- The sustainable bionanocomposite of polymers can be effective solution for the virgin petroleum based polymers packaging systems.

2.7.2 Limitation of the process

The use of ultrasonic sonication (US) equipment for the synthesis of cavities in the acoustic cavitation technique was the process' main weakness. The US system has its own limitations, such as limited volume treatment and a greater energy demand to run a large volume, which prevented it from being used commercially. The reproducibility of the synthesis process is a significant challenge in ultrasound assisted acid hydrolysis synthesis. Variations in the ultrasound parameters, reaction conditions, and starch/cellulose source can lead to significant differences in the properties of the synthesized nanoparticles, making it difficult to reproduce the synthesis process consistently. The following are some restrictions on US assistance:

- The scale-up of the production of bionanoparticles
- Larger energy required in during acoustic cavitation approach.
- Optimization of hydrodynamic cavitation approach as well as acoustic cavitation.

References:

[1] H.N. Englyst, S.M. Kingman, J.H. Cummings, Classification and measurement of nutritionally important starch fractions., Eur. J. Clin. Nutr. 46 Suppl 2 (1992) S33-50.

[2] G.Y. Wiederschain, Polysaccharides. Structural diversity and functional versatility, in: Biochem., 2007: pp. 675–675. https://doi.org/10.1134/s0006297907060120.

[3] D.D. LeCorre, E. Vahanian, A. Dufresne, J. Bras, D. Le Corre-bordes, A. Dufresne, Enzymatic Pretreatment for Preparing Starch Nanocrystals, Biomacromolecules. 13 (2012) 132–137. https://doi.org/10.1021/bm201333k.

[4] E. Bertoft, K. Piyachomkwan, P. Chatakanonda, K. Sriroth, Internal unit chain composition in amylopectins, Carbohydr. Polym. 74 (2008) 527–543.

[5] N. Lin, J. Huang, A. Dufresne, Preparation, properties and applications of polysaccharide nanocrystals in advanced functional nanomaterials: A review, Nanoscale. 4 (2012) 3274–3294. https://doi.org/10.1039/c2nr30260h.

[6] B. Duan, P. Sun, X. Wang, C. Yang, Preparation and properties of starch nanocrystals/carboxymethyl chitosan nanocomposite films, Starch - Starke. 63 (2011) 528–535. https://doi.org/10.1002/star.201000136.

[7] E. Bertoft, Understanding starch structure: Recent progress, Agronomy. 7 (2017). https://doi.org/10.3390/agronomy7030056.

[8] A. Imberty, H. Chanzy, S. Perez, A. Buleon, V. Tran, New three-dimensional structure for A-type starch, Macromolecules. 20 (1987) 2634–2636. https://doi.org/10.1021/ma00176a054.

[9] A. Imberty, S. Perez, A revisit to the three-dimensional structure of B-type starch, Biopolymers. 27 (1988) 1205–1221. https://doi.org/10.1002/bip.360270803.

[10] R.N. Waduge, D.N. Kalinga, E. Bertoft, K. Seetharaman, Molecular Structure and Organization of Starch Granules from Developing Wheat Endosperm, Cereal Chem. 91 (2014) 578–586. https://doi.org/10.1094/CCHEM-02-14-0020-R.

[11] S. Wang, L. Copeland, Effect of Acid Hydrolysis on Starch Structure and Functionality : A Review, Crit. Rev. Food Sci. Nutr. 55 (2015) 1081–1097. https://doi.org/10.1080/10408398.2012.684551.

[12] M.A. El-Sheikh, New technique in starch nanoparticles synthesis, Carbohydr. Polym. 176 (2017) 214–219. https://doi.org/10.1016/j.carbpol.2017.08.033.

[13] S. Kumari, B.S. Yadav, R.B. Yadav, Synthesis and modification approaches for starch nanoparticles for their emerging food industrial applications: A review, Food Res. Int. 128 (2020) 108765. https://doi.org/10.1016/j.foodres.2019.108765.

[14] P.J. Jenkins, A.M. Donald, The Effect of Acid Hydrolyis on Native Starch Granule Structure, Starch Starke. 49 (1997) 262–267. https://doi.org/10.1002/star.19970490703.

[15] A. David Chena, S. Evzen, U. Pavel, M. Eva, Starch nanoparticles – two ways of their preparation, Czech J. Food Sci. 36 (2018) 133–138. https://doi.org/10.17221/371/2017-CJFS.

[16] L. Jayakody, R. Hoover, The effect of lintnerization on cereal starch granules, Food Res. Int. 35 (2002) 665–680. https://doi.org/10.1016/S0963-9969(01)00204-6.

[17] H.Y. Kim, S.S. Park, S.T. Lim, Preparation, characterization and utilization of starch nanoparticles, Colloids Surfaces B Biointerfaces. 126 (2015) 607–620. https://doi.org /10.1016/j.colsurfb.2014.11.011.

[18] H. Angellier, L. Choisnard, S. Molina-Boisseau, P. Ozil, A. Dufresne, Optimization of the preparation of aqueous suspensions of waxy maize starch nanocrystals using a response surface methodology., Biomacromolecules. 5 (2004) 1545–1551. https://doi. org/10.1021/ bm049914u.

[19] D. LeCorre, J. Bras, A. Dufresne, Influence of native starch's properties on starch nanocrystals thermal properties, Carbohydr. Polym. 87 (2012) 658–666. https://doi.org /10. 1016/j.carbpol.2011.08.042.

[20] D.D. LeCorre, J. Bras, A. Dufresne, Influence of botanic origin and amylose content on the morphology of starch nanocrystals, J. Nanoparticle Res. 13 (2011) 7193–7208. https://doi.org/10.1007/s11051-011-0634-2.

[21] H. Angellier, S. Molina-Boisseau, P. Dole, A. Dufresne, Thermoplastic Starch−Waxy Maize Starch Nanocrystals Nanocomposites, Biomacromolecules. 7 (2006) 531–539. https://doi.org/10.1021/bm050797s.

[22] de la Concha, Brenda B. Sanchez, Edith Agama-Acevedo, Maria C. Nuñez-Santiago, Luis A. Bello-Perez, Hugo S. Garcia, and Jose Alvarez-Ramirez. Acid hydrolysis of waxy starches with different granule size for nanocrystal production, Journal of Cereal Science 79 (2018): 193-200. https://doi.org/10.1016/j.jcs.2017.10.018.

[23] H.-Y. Kim, J.H. Lee, J.-Y. Kim, W.-J. Lim, S.-T. Lim, Characterization of nanoparticles prepared by acid hydrolysis of various starches, Starch - Starke. 64 (2012) 367–373. https://doi.org/10.1002/star.201100105.

[24] E.Y. Park, M.J. Kim, M. Cho, J.H. Lee, J.Y. Kim, Production of starch nanoparticles using normal maize starch via heat-moisture treatment under mildly acidic conditions and homogenization, Carbohydr. Polym. 151 (2016) 274–282. https://doi.org/10.1016/j.carbpol.2016.05.056.

[25] S. Selvaraju, K. Archana, S. Ramu, N. Sivarajasekar, P.B.S. Naveen, Synthesis and characterization of starch nanoparticles from cassava Peel, J. Bioresour. Bioprod. 3 (2018). https://doi.org/10.21967/jbb.v3i4.179.

[26] X. Li, C. Qiu, N. Ji, C. Sun, L. Xiong, Q. Sun, Mechanical, barrier and morphological properties of starch nanocrystals-reinforced pea starch films, Carbohydr. Polym. 121 (2015) 155–162. https://doi.org/10.1016/j.carbpol.2014.12.040.

[27] J.-L.L. Putaux, S. Molina-Boisseau, T. Momaur, A. Dufresne, Platelet Nanocrystals Resulting from the Disruption of Waxy Maize Starch Granules by Acid Hydrolysis, Biomacromolecules. 4 (2003) 1198–1202. https://doi.org/10.1021/bm0340422.

[28] M.J. Jivan, M. Yarmand, A. Madadlou, Encapsulation of date palm pit extract via particulation of starch nanocrystals in a microemulsion, Int. J. Food Sci. \& Technol. 49 (2014) 920–923. https://doi.org/10.1111/ijfs.12359.

[29] A.D. Betancur, G.L. Chel, Acid Hydrolysis and Characterization of Canavalia ensiformis Starch, J. Agric. Food Chem. 45 (1997) 4237–4241. https://doi.org/10.1021/jf970388q.

[30] N. Lin, J. Yu, P.R. Chang, J. Li, J. Huang, Poly(butylene succinate)-based biocomposites filled with polysaccharide nanocrystals: Structure and properties, Polym. Compos. 32 (2011) 472–482. https://doi.org/10.1002/pc.21066.

[31] Y. Qin, C. Liu, S. Jiang, L. Xiong, Q. Sun, Characterization of starch nanoparticles prepared by nanoprecipitation: Influence of amylose content and starch type, Ind. Crops Prod. 87 (2016) 182–190. https://doi.org/10.1016/j.indcrop.2016.04.038.

[32] H. Dong, Q. Zhang, J. Gao, L. Chen, T. Vasanthan, Comparison of morphology and rheology of starch nanoparticles prepared from pulse and cereal starches by rapid antisolvent nanoprecipitation, Food Hydrocoll. 119 (2021) 106828. https://doi.org/10.1016/j.foodhyd.2021.106828.

[33] A. Hebeish, M.H. El-Rafie, M.A. EL-Sheikh, M.E. El-Naggar, Ultra-Fine Characteristics of Starch Nanoparticles Prepared Using Native Starch With and Without Surfactant, J. Inorg. Organomet. Polym. Mater. 24 (2014) 515–524. https://doi.org/10.1007/s10904-013-0004-x.

[34] Y. Tan, K. Xu, C. Liu, Y. Li, C. Lu, P. Wang, Fabrication of starch-based nanospheres to stabilize pickering emulsion, Carbohydr. Polym. 88 (2012) 1358–1363. https://doi.org/10.1016/j.carbpol.2012.02.018.

[35] S. Juna, S. Hayden, M. Damm, C.O. Kappe, A. Huber, Nanoprecipitation of native pea starches treated in alkaline media at various temperatures employing a dedicated microwave reactor, Starch Starke. 66 (2014) 124–131. https://doi.org/10.1002/star.201300066.

[36] S. Juna, S. Hayden, M. Damm, C.O. Kappe, A. Huber, Microwave mediated preparation of nanoparticles from wx corn starch employing nanoprecipitation, Starch - Stärke. 66 (2014) 316–325. https://doi.org/10.1002/star.201300067.

[37] S.F. Chin, S.C. Pang, S.H. Tay, Size controlled synthesis of starch nanoparticles by a simple nanoprecipitation method, Carbohydr. Polym. 86 (2011) 1817–1819. https://doi.org/10.1016/j.carbpol.2011.07.012.

[38] S.F. Chin, A. Azman, S.C. Pang, Size Controlled Synthesis of Starch Nanoparticles by a Microemulsion Method, J. Nanomater. 2014 (2014). https://doi.org/10.1155/2014/763736.

[39] J. Wu, Y. Huang, R. Yao, S. Deng, F. Li, X. Bian, Preparation and Characterization of Starch Nanoparticles from Potato Starch by Combined Solid-State Acid-Catalyzed Hydrolysis and Nanoprecipitation, Starch - Stärke. 71 (2019) 1900095. https://doi.org/10.1002/star.201900095.

[40] S. Shabana, R. Prasansha, I. Kalinina, I. Potoroko, U. Bagale, S.H. Shirish, Ultrasound assisted acid hydrolyzed structure modification and loading of antioxidants on potato starch nanoparticles, Ultrason. Sonochem. 51 (2019) 444–450. https://doi.org/10.1016/j.ultsonch.2018.07.023.

[41] T.J. Mason, Power ultrasound in food processing—The way forward, in: M.J.W. Povey, T.J. Mason (Eds.), Ultrasound Food Process., Blackie Academic and Professional, London, n.d.: pp. 105–126.

[42] R. Czechowska-biskup, B. Rokita, S. Lotfy, Degradation of chitosan and starch by 360-kHz ultrasound, Carbohydr. Polym. 60 (2005) 175–184. https://doi.org/10.1016/j.carbpol.2004.12.001.

[43] S. Bel Haaj, A. Magnin, C. Petrier, S. Boufi, Starch nanoparticles formation via high power ultrasonication, Carbohydr. Polym. 92 (2013) 1625–1632. https://doi.org/10.1016/j.carbpol.2012.11.022.

[44] A. Garcia-gurrola, S. Rincon, A.A. Escobar-Puentes, A. Zepeda, J.F. Perez-Robles, F. Martinez-Bustos, J.F. Perez-robles, F. Martinez-Bustos, Synthesis and succinylation of starch nanoparticles by means of a single step using sonochemical energy, Ultrason. Sonochem. 56 (2019) 458–465. https://doi.org/10.1016/j.ultsonch.2019.04.035.

[45] P. Liu, F. Xie, M. Li, X. Liu, L. Yu, P.J. Halley, L. Chen, Phase transitions of maize starches with different amylose contents in glycerol–water systems, Carbohydr. Polym. 85 (2011) 180–187. https://doi.org/10.1016/j.carbpol.2011.02.006.

[46] S. Boufi, S. Bel Haaj, A. Magnin, F. Pignon, M. Imperor-Clerc, G. Mortha, Ultrasonic assisted production of starch nanoparticles: Structural characterization and mechanism of disintegration, Ultrason. Sonochem. 41 (2018) 327–336. https://doi.org/10.1016/j.ultsonch.2017.09.033.

[47] A.F.K. Minakawa, P.C.S. Faria-Tischer, S. Mali, Simple ultrasound method to obtain starch micro- and nanoparticles from cassava, corn and yam starches, Food Chem. 283 (2019) 11–18. https://doi.org/10.1016/j.foodchem.2019.01.015.

[48] M. Ahmad, A. Gani, I. Hassan, Q. Huang, H. Shabbir, Production and characterization of starch nanoparticles by mild alkali hydrolysis and ultra-sonication process, Sci. Rep. 10 (2020) 3533. https://doi.org/10.1038/s41598-020-60380-0.

[49] A.R. Jambrak, Z. Herceg, D. Subaric, J. Babic, M. Brncic, S.R. Brncic, T. Bosiljkov, D. Cvek, B. Tripalo, J. Gelo, Ultrasound effect on physical properties of corn starch, Carbohydr. Polym. 79 (2010) 91–100. https://doi.org/10.1016/j.carbpol.2009.07.051.

[50] N.K. Rastogi, Opportunities and Challenges in Application of Ultrasound in Food Processing, Crit. Rev. Food Sci. Nutr. 51 (2011) 705–722. https://doi.org/10.1080/10408391003770583.

[51] Y. Ding, J. Kan, Characterization of nanoscale retrograded starch prepared by a sonochemical method, Starch - Stärke. 68 (2016) 264–273. https://doi.org/10.1002/star.201500313.

[52] D. Le Corre-bordes, A. Dufresne, Enzymatic Pretreatment for Preparing Starch, Biochem. 13 (2017) 132–137. https://doi.org/10.1021/bm201333k.

[53] J.-Y. Kim, D.-J. Park, S.-T. Lim, Fragmentation of Waxy Rice Starch Granules by Enzymatic Hydrolysis, Cereal Chem. 85 (2008) 182–187. https://doi.org/10.1094/CCHEM-85-2-0182.

[54] D. Liu, Q. Wu, H. Chen, P.R. Chang, Transitional properties of starch colloid with particle size reduction from micro- to nanometer, J. Colloid Interface Sci. 339 (2009)

117–124. https://doi.org/10.1016/j.jcis.2009.07.035.

[55] A.M. Shi, D. Li, L.J. Wang, B.Z. Li, B. Adhikari, Preparation of starch-based nanoparticles through high-pressure homogenization and miniemulsion cross-linking: Influence of various process parameters on particle size and stability, Carbohydr. Polym. 83 (2011) 1604–1610. https://doi.org/10.1016/j.carbpol.2010.10.011.

[56] M.S. Hale, J.G. Mitchell, Motion of Submicrometer Particles Dominated by Brownian Motion near Cell and Microfabricated Surfaces, Nano Lett. 1 (2001) 617–623. https://doi.org/10.1021/nl015575o.

[57] L. Martin-Banderas, M. Flores-Mosquera, P. Riesco-Chueca, A. Rodriguez-Gil, A. Cebolla, S. Chavez, A.M. Ganan-Calvo, Flow Focusing: a versatile technology to produce size-controlled and specific-morphology microparticles., Small. 1 (2005) 688–692. https://doi.org/10.1002/smll.200500087.

[58] R.F. Tester, J. Karkalas, X. Qi, Starch—composition, fine structure and architecture, J. Cereal Sci. 39 (2004) 151–165. https://doi.org/10.1016/j.jcs.2003.12.001.

[59] Y. Ding, J. Kan, Optimization and characterization of high pressure homogenization produced chemically modified starch nanoparticles, J. Food Sci. Technol. 54 (2017) 4501–4509. https://doi.org/10.1007/s13197-017-2934-8.

[60] A. Akhavan, E. Ataeevarjovi, The effect of gamma irradiation and surfactants on the size distribution of nanoparticles based on soluble starch, Radiat. Phys. Chem. 81 (2012) 913–914. https://doi.org/10.1016/j.radphyschem.2012.03.004.

[61] S. Singh, N. Singh, R. Ezekiel, A. Kaur, Effects of gamma-irradiation on the morphological, structural, thermal and rheological properties of potato starches, Carbohydr. Polym. 83 (2011) 1521–1528. https://doi.org/10.1016/j.carbpol.2010.09.06

[62] J. Bao, Z. Ao, J. Jane, Characterization of Physical Properties of Flour and Starch Obtained from Gamma-Irradiated White Rice, Starch - Starke. 57 (2005) 480–487. https://doi.org/10.1002/star.200500422.

[63] M. Lamanna, N.J. Morales, N.L. García, S. Goyanes, Development and characterization of starch nanoparticles by gamma radiation: Potential application as starch matrix filler, Carbohydr. Polym. 97 (2013) 90–97. https://doi.org/10.1016/j.carbpol.2013.04.081.

[64] D. Binh, Pham Thi Thu Hong, Nguyen Ngoc Duy, Nguyen Thanh Duoc, Nguyen Nguyet Dieu, A study on size effect of carboxymethyl starch nanogel crosslinked by electron beam radiation, Radiat. Phys. Chem. 81 (2012) 906–912. https://doi.org/10.1016/j.radphyschem.2011.12.016.

[65] L.S. Lai, J.L. Kokini, Physicochemical Changes and Rheological Properties of Starch during Extrusion (A Review), Biotechnol. Prog. 7 (1991) 251–266. https://doi.org/10.1021/bp00009a009.

[66] D. Le Corre, J. Bras, A. Dufresne, Starch nanoparticles: A review, Biomacromolecules. 11 (2010) 1139–1153. https://doi.org/10.1021/bm901428y.

[67] E. Garcia-Armenta, L.A. Picos-Corrales, G.F. Gutierrez-Lopez, R. Gutierrez-Dorado, J.X.K. Perales-Sanchez, S. Garcia-Pinilla, F. Reynoso-Garcia, J.M. Martinez-Audelo, M.A. Armenta-Manjarrez, Preparation of surfactant-free emulsions using amaranth starch modified by reactive extrusion, Colloids Surfaces A Physicochem. Eng. Asp. 608 (2021) 125550. https://doi.org/10.1016/j.colsurfa.2020.125550.

[68] D. Song, Y.S. Thio, Y. Deng, Starch nanoparticle formation via reactive extrusion and related mechanism study, Carbohydr. Polym. 85 (2011) 208–214. https://doi.org/10.1016/j.carbpol.2011.02.016.

[69] H.-Y. Kim, S.S. Park, S.-T. Lim, Preparation, characterization and utilization of starch nanoparticles, Colloids Surfaces B Biointerfaces. 126 (2015) 607–620. https://doi.org/10.1016/j.colsurfb.2014.11.011.

[70] A. Dufresne, J.-Y. Cavaille, W. Helbert, New Nanocomposite Materials: Micro crystalline Starch Reinforced Thermoplastic, Macromolecules. 29 (1996) 7624–7626. https://doi.or g/10.1021/ma9602738.

[71] R.J. Moon, A. Martini, J. Nairn, J. Simonsen, J. Youngblood, Cellulose nanomaterials review: Structure, properties and nanocomposites, 2011. https://doi.org/10.1039/c0cs00108b.

[72] K. Fleming, D.G. Gray, S. Matthews, Cellulose Crystallites, Chem. – A Eur. J. 7 (2001) 1831–1836. https://doi.org/10.1002/1521-3765(20010504)7:9

[73] J. George, S.N. Sabapathi, Siddaramaiah, Water Soluble Polymer-Based Nanocomposites Containing Cellulose Nanocrystals, in: V.K. Thakur, M.K. Thakur (Eds.), Eco-Friendly Polym. Nanocomposites Process. Prop., Springer India, New Delhi, 2015: pp. 259–293. https://doi.org/10.1007/978-81-322-2470-9_9.

[74] S.J. Eichhorn, C.A. Baillie, N. Zafeiropoulos, L.Y. Mwaikambo, M.P. Ansell, A. Dufresne, K.M. Entwistle, P.J. Herrera-Franco, G.C. Escamilla, L. Groom, M. Hughes, C. Hill, T.G. Rials, P.M. Wild, Review: Current international research into cellulosic fibres and composites, J. Mater. Sci. 36 (2001) 2107–2131. https://doi.org/10.1023/A:1017512029696.

[75] A. Mihranyan, Cellulose from cladophorales green algae: From environmental problem to high-tech composite materials, J. Appl. Polym. Sci. 119 (2011) 2449–2460. https://doi.org/10.1002/app.32959.

[76] J. Sugiyama, R. Vuong, H. Chanzy, Electron diffraction study on the two crystalline phases occurring in native cellulose from an algal cell wall, Macromolecules. 24 (1991) 4168–4175. https://doi.org/10.1021/ma00014a033.

[77] S. Masaoka, T. Ohe, N. Sakota, Production of cellulose from glucose by Acetobacter xylinum, J. Ferment. Bioeng. 75 (1993) 18–22. https://doi.org/10.1016/0922-338X(93)90171-4.

[78] J. George, K. V Ramana, S.N. Sabapathy, A.S. Bawa, Physico-Mechanical Properties of Chemically Treated Bacterial (Acetobacter xylinum) Cellulose Membrane, World J. Microbiol. Biotechnol. 21 (2005) 1323–1327. https://doi.org/10.1007/s11274-005-3574-0.

[79] J. George, K.V. Ramana, S.N. Sabapathy, J.H. Jagannath, A.S. Bawa, Characterization of chemically treated bacterial (Acetobacter xylinum) biopolymer: some thermo-mechanical properties., Int. J. Biol. Macromol. 37 (2005) 189–194. https://doi.org/10.1016/j.ijbiomac.2005.10.007.

[80] D.N. Thompson, M.A. Hamilton, Production of Bacterial Cellulose from Alternate Feedstocks, in: B.H. Davison, J. McMillan, M. Finkelstein (Eds.), Twenty-Second Symp. Biotechnol. Fuels Chem., Humana Press, Totowa, NJ, 2001: pp. 503–513. https://doi.org/10.1007/978-1-4612-0217-2_43.

[81] Y. Zhao, J. Li, Excellent chemical and material cellulose from tunicates: diversity in cellulose production yield and chemical and morphological structures from different tunicate species, Cellulose. 21 (2014) 3427–3441. https://doi.org/10.1007/s10570-014-0348-6.

[82] H. V Lee, S.B.A. Hamid, S.K. Zain, Conversion of Lignocellulosic Biomass to Nanocellulose: Structure and Chemical Process, Sci. World J. 2014 (2014) 631013. https://doi.org/10.1155/2014/631013.

[83] L. Brinchi, F. Cotana, E. Fortunati, J.M. Kenny, Production of nanocrystalline cellulose from lignocellulosic biomass: Technology and applications, Carbohydr. Polym. 94 (2013) 154–169. https://doi.org/10.1016/j.carbpol.2013.01.033.

[84] R.H. Newman, J.A. Hemmingson, Carbon-13 NMR distinction between categories of molecular order and disorder in cellulose, Cellulose. 2 (1995) 95–110. https://doi.

org/10.1007/BF00816383.

[85] R.M.A. Domingues, M.E. Gomes, R.L. Reis, The Potential of Cellulose Nanocrystals in Tissue Engineering Strategies, Biomacromolecules. 15 (2014) 2327–2346. https://doi.org/10.1021/bm500524s.

[86] M.M. de Souza Lima, R. Borsali, Rodlike Cellulose Microcrystals: Structure, Properties, and Applications, Macromol. Rapid Commun. 25 (2004) 771–787. https://doi.org/10.1002/marc.200300268.

[87] I.A. Sacui, R.C. Nieuwendaal, D.J. Burnett, S.J. Stranick, M. Jorfi, C. Weder, E.J. Foster, R.T. Olsson, J.W. Gilman, Comparison of the Properties of Cellulose Nanocrystals and Cellulose Nanofibrils Isolated from Bacteria, Tunicate, and Wood Processed Using Acid, Enzymatic, Mechanical, and Oxidative Methods, ACS Appl. Mater. Interfaces. 6 (2014) 6127–6138. https://doi.org/10.1021/am500359f.

[88] B.G. Ranby, Fibrous macromolecular systems. Cellulose and muscle. The colloidal properties of cellulose micelles, Discuss. Faraday Soc. 11 (1951) 158–164. https://doi.org/10.1039/DF9511100158.

[89] S.M. Mukherjee, J. Sikorski, H.J. Woods, Electron-Microscopy of Degraded Cellulose Fibres, J. Text. Inst. Trans. 43 (1952) T196–T201. https://doi.org/10.1080/19447025108659661.

[90] B.L. Peng, N. Dhar, H.L. Liu, K.C. Tam, Chemistry and applications of nanocrystalline cellulose and its derivatives: A nanotechnology perspective, Can. J. Chem. Eng. 89 (2011) 1191–1206. https://doi.org/10.1002/cjce.20554.

[91] G. Siqueira, J. Bras, A. Dufresne, Cellulosic bionanocomposites: A review of preparation, properties and applications, Polymers (Basel). 2 (2010) 728–765. https://doi.org/10.3390/polym2040728.

[92] D. Bondeson, A. Mathew, K. Oksman, Optimization of the isolation of nanocrystals from microcrystalline celluloseby acid hydrolysis, Cellulose. 13 (2006) 171–180. https://doi.org/10.1007/s10570-006-9061-4.

[93] X.M. Dong, J.-F. Revol, D.G. Gray, Effect of microcrystallite preparation conditions on the formation of colloid crystals of cellulose, Cellulose. 5 (1998) 19–32. https://doi.org/10.1023/A:1009260511939.

[94] K. Das, D. Ray, N.R. Bandyopadhyay, T. Ghosh, A.K. Mohanty, M. Misra, A study of the mechanical, thermal and morphological properties of microcrystalline cellulose particles prepared from cotton slivers using different acid concentrations, Cellulose. 16

(2009) 783–793. https://doi.org/10.1007/s10570-009-9280-6.

[95] P. Lu, Y.-L. Hsieh, Preparation and properties of cellulose nanocrystals: Rods, spheres, and network, Carbohydr. Polym. 82 (2010) 329–336. https://doi.org/10.1016/ j.carbpol. 2010.04.073.

[96] N. Johar, I. Ahmad, A. Dufresne, Extraction, preparation and characterization of cellulose fibres and nanocrystals from rice husk, Ind. Crops Prod. 37 (2012) 93–99. https://doi.org/ 10.1016/j.indcrop.2011.12.016.

[97] N. Wang, E. Ding, R. Cheng, Thermal degradation behaviors of spherical cellulose nanocrystals with sulfate groups, Polymer (Guildf). 48 (2007) 3486–3493. https://doi.org/10.1016/j.polymer.2007.03.062.

[98] S. Maiti, J. Jayaramudu, K. Das, S.M. Reddy, R. Sadiku, S.S. Ray, D. Liu, Preparation and characterization of nano-cellulose with new shape from different precursor, Carbohydr. Polym. 98 (2013) 562–567. https://doi.org/10.1016/j.carbpol.2013.06.029.

[99] A. Isogai, Wood nanocelluloses: fundamentals and applications as new bio-based nanomaterials, J. Wood Sci. 59 (2013) 449–459. https://doi.org/10.1007/s10086-013-1365-z.

[100] H. Fukuzumi, T. Saito, T. Iwata, Y. Kumamoto, A. Isogai, Transparent and High Gas Barrier Films of Cellulose Nanofibers Prepared by TEMPO-Mediated Oxidation, Biomacromolecules. 10 (2009) 162–165. https://doi.org/10.1021/bm801065u.

[101] S. Liu, Z.-X. Low, Z. Xie, H. Wang, TEMPO-Oxidized Cellulose Nanofibers: A Renewable Nanomaterial for Environmental and Energy Applications, Adv. Mater. Technol. 6 (2021) 2001180. https://doi.org/10.1002/admt.202001180.

[102] A. Serra, I. González, H. Oliver-Ortega, Q. Tarrès, M. Delgado-Aguilar, P. Mutjé, Reducing the amount of catalyst in TEMPO-oxidized cellulose nanofibers: Effect on properties and cost, Polymers (Basel). 9 (2017). https://doi.org/10.3390/polym9110557.

[103] L.T. Fan, Y.-H. Lee, D.H. Beardmore, Mechanism of the enzymatic hydrolysis of cellulose: Effects of major structural features of cellulose on enzymatic hydrolysis, Biotechnol. Bioeng. 22 (1980) 177–199. https://doi.org/10.1002/bit.260220113.

[104] H.P.S.S. Abdul Khalil, Y. Davoudpour, M.N. Islam, A. Mustapha, K. Sudesh, R. Dungani, M. Jawaid, Production and modification of nanofibrillated cellulose using various mechanical processes: A review, Carbohydr. Polym. 99 (2014) 649–665. https://doi.org/10.1016/j.carbpol.2013.08.069.

[105] M. Moniruzzaman, T. Ono, Separation and characterization of cellulose fibers from

cypress wood treated with ionic liquid prior to laccase treatment, Bioresour. Technol. 127 (2013) 132–137. https://doi.org/10.1016/j.biortech.2012.09.113.

[106] J. Li, X. Wei, Q. Wang, J. Chen, G. Chang, L. Kong, J. Su, Y. Liu, Homogeneous isolation of nanocellulose from sugarcane bagasse by high pressure homogenization, Carbohydr. Polym. 90 (2012) 1609–1613. https://doi.org/10.1016/j.carbpol.2012.07.03

[107] P.B. Filson, B.E. Dawson-Andoh, Sono-chemical preparation of cellulose nanocrystals from lignocellulose derived materials, Bioresour. Technol. 100 (2009) 2259–2264. https://doi.org/10.1016/j.biortech.2008.09.062.

[108] L. Tang, B. Huang, Q. Lu, S. Wang, W. Ou, W. Lin, X. Chen, Ultrasonication-assisted manufacture of cellulose nanocrystals esterified with acetic acid, Bioresour. Technol. 127 (2013) 100–105. https://doi.org/10.1016/j.biortech.2012.09.133.

[109] W. Li, H. Corke, T. Beta, Kinetics of hydrolysis and changes in amylose content during preparation of microcrystalline starch from high-amylose maize starches, Carbohydr. Polym. v. 69 (2007) 398-405–2007 v.69 no.2. https://doi.org/10.1016/j.carbpol.2006. 12.022.

[110] M.I. Khalil, A. Hashem, A. Hebeish, Preparation and Characterization of Starch Acetate, Starch - Stärke. 47 (1995) 394–398. https://doi.org/10.1002/star.19950471005.

[111] F. Hu, S. Fu, J. Huang, D.P. Anderson, P.R. Chang, Structure and Properties of Polysaccharide Nanocrystals, 2015. https://doi.org/10.1002/9783527689378.ch2.

[112] V.S. Hakke, U.D. Bagale, S. Boufi, G.U.B. Babu, S.H. Sonawane, Ultrasound Assisted Synthesis of Starch Nanocrystals and It's Applications with Polyurethane for Packaging Film, J. Renew. Mater. 08 (2020) 239–250. https://doi.org/10.32604/jrm.2020.08449.

[113] H. Nguyen, W. Zatar, H. Mutsuyoshi, Mechanical properties of hybrid polymer composite, 2017. https://doi.org/10.1016/B978-0-08-100787-7.00004-4.

[114] J.W. Rhim, P.K.W. Ng, Natural biopolymer-based nanocomposite films for packaging applications, Crit. Rev. Food Sci. Nutr. 47 (2007) 411–433. https://doi.org/10.1080/104 08390600846366.

[115] B. Schumann, M. Schmid, Packaging concepts for fresh and processed meat – Recent progresses, Innov. Food Sci. Emerg. Technol. 47 (2018) 88–100. https://doi.org/10. 1016/j.ifset.2018.02.005.

[116] S.M. Emadian, T.T. Onay, B. Demirel, Biodegradation of bioplastics in natural environments, Waste Manag. 59 (2017) 526–536. https://doi.org/10.1016/j.wasman. 2016.10.006.

[117] S. Tunc, O. Duman, Preparation and characterization of biodegradable methyl cellulose/montmorillonite nanocomposite films, Appl. Clay Sci. 48 (2010) 414–424. https://doi.org/10.1016/j.clay.2010.01.016.

[118] P. Bordes, E. Pollet, L. Averous, Nano-biocomposites: Biodegradable polyester/nano clay systems, Prog. Polym. Sci. 34 (2009) 125–155. https://doi.org/10.1016/j.progpolymsci.2008.10.002.

[119] M. Dick, T.M.H. Costa, A. Gomaa, M. Subirade, A.D.O. Rios, S.H. Flôres, Edible film production from chia seed mucilage: Effect of glycerol concentration on its physicochemical and mechanical properties, Carbohydr. Polym. 130 (2015) 198–205. https://doi.org/10.1016/j.carbpol.2015.05.040.

[120] R. Sharma, S.M. Jafari, S. Sharma, Antimicrobial bio-nanocomposites and their potential applications in food packaging, Food Control. 112 (2020) 107086. https://doi.org/10.1016/j.foodcont.2020.107086.

[121] J.-W.W. Rhim, H.-M.M. Park, C.-S.S. Ha, Bio-nanocomposites for food packaging applications, Prog. Polym. Sci. 38 (2013) 1629–1652. https://doi.org/10.1016/j.progpolymsci.2013.05.008.

[122] J. Rhim, H. Park, C. Ha, Progress in Polymer Science Bio-nanocomposites for food packaging applications, Prog. Polym. 38 (2013) 1629–1652. https://doi.org/10.1016/j.progpolymsci.2013.05.008.

[123] Q. Zhang, M. Song, Y. Xu, W. Wang, Z. Wang, L. Zhang, Bio-based polyesters: Recent progress and future prospects, Prog. Polym. Sci. 120 (2021) 101430. https://doi.org/10.1016/j.progpolymsci.2021.101430.

[124] R.A. Ilyas, S.M. Sapuan, R. Ibrahim, H. Abral, M.R. Ishak, E.S. Zainudin, A. Atiqah, M.S.N. Atikah, E. Syafri, M. Asrofi, R. Jumaidin, Thermal, Biodegradability and Water Barrier Properties of Bio-Nanocomposites Based on Plasticised Sugar Palm Starch and Nanofibrillated Celluloses from Sugar Palm Fibres, J. Biobased Mater. Bioenergy. 14 (2019) 234–248. https://doi.org/10.1166/jbmb.2020.1951.

[125] H.M.C. Azeredo, M.F. Rosa, L.H.C. Mattoso, Nanocellulose in bio-based food packaging applications, Ind. Crops Prod. 97 (2017) 664–671. https://doi.org/10.1016/j.indcrop.2016.03.013.

[126] F. Wu, M. Misra, A.K. Mohanty, Challenges and new opportunities on barrier performance of biodegradable polymers for sustainable packaging, Prog. Polym. Sci. 117 (2021). https://doi.org/10.1016/j.progpolymsci.2021.101395.

[127] X. Zhou, Y. Li, C. Fang, S. Li, Y. Cheng, W. Lei, X. Meng, Recent Advances in Synthesis of Waterborne Polyurethane and Their Application in Water-based Ink: A Review, J. Mater. Sci. Technol. 31 (2015) 708–722. https://doi.org/10.1016/j.jmst.2015.03.002.

[128] M.F. Sonnenschein, Polyurethanes Science, Technology, Markets and Trends, 1st ed., John Wiley & Sons, Inc., Hoboken, New Jersey, New Jersey, 2015. http://www.wiley.com/go/permissions.

[129] J. Chen, Q. Wang, M. Luan, J. Mo, Y. Yan, X. Li, Polydopamine as reinforcement in the coating of nano-silver on polyurethane surface: Performance and mechanisms, Prog. Org. Coatings. 137 (2019). https://doi.org/10.1016/j.porgcoat.2019.105288.

[130] O.M. Bakr, V. Amendola, C.M. Aikens, W. Wenseleers, R. Li, L. Dal Negro, G.C. Schatz, F. Stellacci, Silver nanoparticles with broad multiband linear optical absorption., Angew. Chem. Int. Ed. Engl. 48 (2009) 5921–5926. https://doi.org/10.1002/anie.200900298.

[131] M. Umadevi, A. Jegatha Christy, Optical, structural and morphological properties of silver nanoparticles and its influence on the photocatalytic activity of TiO2, Spectrochim. Acta Part A Mol. Biomol. Spectrosc. 111 (2013) 80–85. https://doi.org/10.1016/j.saa.2013.03.062.

[132] Y. Oh, D. Suh, Y. Kim, E. Lee, J.S. Mok, J. Choi, S. Baik, Silver-plated carbon nanotubes for silver/conducting polymer composites., Nanotechnology. 19 (2008) 495602. https://doi.org/10.1088/0957-4484/19/49/495602.

[133] I. Sur, D. Cam, M. Kahraman, A. Baysal, M. Culha, Interaction of multi-functional silver nanoparticles with living cells., Nanotechnology. 21 (2010) 175104. https://doi.org/10.1088/0957-4484/21/17/175104.

[134] Z. Xuan, Y. Tang, X. Li, Y. Liu, F. Luo, Study on the equilibrium, kinetics and isotherm of biosorption of lead ions onto pretreated chemically modified orange peel, Biochem. Eng. J. 31 (2006) 160–164. https://doi.org/10.1016/j.bej.2006.07.001.

[135] F. Pagnanelli, S. Mainelli, S. De Angelis, L. Toro, Biosorption of protons and heavy metals onto olive pomace: Modelling of competition effects, Water Res. 39 (2005) 1639–1651. https://doi.org/10.1016/j.watres.2005.01.019.

[136] A.G. El-Said, N.A. Badawy, A.Y. Abdel-Aal, S.E. Garamon, Optimization parameters for adsorption and desorption of Zn(II) and Se(IV) using rice husk ash: kinetics and equilibrium, Ionics (Kiel). 17 (2011) 263–270. https://doi.org/10.1007/s11581-010-

0505-3.

[137] L.H. Wartelle, W.E. Marshall, Chromate ion adsorption by agricultural by-products modified with dimethyloldihydroxyethylene urea and choline chloride, Water Res. 39 (2005) 2869–2876. https://doi.org/10.1016/j.watres.2005.05.001.

[138] J. Lee, S. Mahendra, P.J.J. Alvarez, Nanomaterials in the Construction Industry: A Review of Their Applications and Environmental Health and Safety Considerations, ACS Nano. 4 (2010) 3580–3590. https://doi.org/10.1021/nn100866w.

[139] Ferda Gonen, Adsorption study on orange peel: Removal of Ni(II) ions from aqueous solution, African J. Biotechnol. 11 (2012) 1250–1258. https://doi.org/10.5897/ajb11.1753.

[140] O.E. Abdel Salam, N.A. Reiad, M.M. ElShafei, A study of the removal characteristics of heavy metals from wastewater by low-cost adsorbents, J. Adv. Res. 2 (2011) 297–303. https://doi.org/10.1016/j.jare.2011.01.008.

[141] X. Wang, Y. Guo, L. Yang, M. Han, J. Zhao, X. Cheng, Nanomaterials as Sorbents to Remove Heavy Metal Ions in Wastewater Treatment, J. Environ. Anal. Toxicol. 02 (2012). https://doi.org/10.4172/2161-0525.1000154.

[142] C. Gao, W. Zhang, H. Li, L. Lang, Z. Xu, Controllable Fabrication of Mesoporous MgO with Various Morphologies and Their Absorption Performance for Toxic Pollutants in Water, Cryst. Growth Des. 8 (2008) 3785–3790. https://doi.org/10.1021/cg8004147.

[143] Y.Y. Wang, Y.X. Liu, H.H. Lu, R.Q. Yang, S.M. Yang, Competitive adsorption of Pb(II), Cu(II), and Zn(II) ions onto hydroxyapatite-biochar nanocomposite in aqueous solutions, J. Solid State Chem. 261 (2018) 53–61. https://doi.org/10.1016/j.jssc.2018.02.010.

[144] S. De Gisi, G. Lofrano, M. Grassi, M. Notarnicola, Characteristics and adsorption capacities of low-cost sorbents for wastewater treatment: A review, Sustain. Mater. Technol. 9 (2016) 10–40. https://doi.org/10.1016/j.susmat.2016.06.002.

[145] N.B. Singh, G. Nagpal, S. Agrawal, Rachna, Water purification by using Adsorbents: A Review, Environ. Technol. Innov. v.11 (2018) 187-240–2018 v.11. https://doi.org/10.1016/j.eti.2018.05.006.

[146] N. Jiang, R. Shang, S.G.J. Heijman, L.C. Rietveld, High-silica zeolites for adsorption of organic micro-pollutants in water treatment: A review, Water Res. 144 (2018) 145–161. https://doi.org/10.1016/j.watres.2018.07.017.

[147] V.-H. Nguyen, S.M. Smith, K. Wantala, P. Kajitvichyanukul, Photocatalytic

remediation of persistent organic pollutants (POPs): A review, Arab. J. Chem. 13 (2020) 8309–8337. https://doi.org/10.1016/j.arabjc.2020.04.028.

[148] T. Ngulube, J.R. Gumbo, V. Masindi, A. Maity, An update on synthetic dyes adsorption onto clay based minerals: A state-of-art review, J. Environ. Manage. 191 (2017) 35–57. https://doi.org/10.1016/j.jenvman.2016.12.031.

[149] F. Mushtaq, M. Zahid, I.A. Bhatti, S. Nasir, T. Hussain, Possible applications of coal fly ash in wastewater treatment., J. Environ. Manage. 240 (2019) 27–46. https://doi.org/10. 1016/j.jenvman.2019.03.054.

[150] Suhas, V.K. Gupta, P.J.M. Carrott, R. Singh, M. Chaudhary, S. Kushwaha, Cellulose: A review as natural, modified and activated carbon adsorbent, Bioresour. Technol. 216 (2016) 1066–1076. https://doi.org/10.1016/j.biortech.2016.05.106.

[151] Y. Zhang, B. Wu, H. Xu, H. Liu, M. Wang, Y. He, B. Pan, Nanomaterials-enabled water and wastewater treatment, NanoImpact. 3–4 (2016) 22–39. https://doi.org/10.1016/j. impact.2016.09. 004.

[152] P.K. Gautam, A. Singh, K. Misra, A.K. Sahoo, S.K. Samanta, Synthesis and applications of biogenic nanomaterials in drinking and wastewater treatment., J. Environ. Manage. 231 (2019) 734–748. https://doi.org/10.1016/j.jenvman.2018.10.104.

[153] Y. Wu, H. Pang, Y. Liu, X. Wang, S. Yu, D. Fu, J. Chen, X. Wang, Environmental remediation of heavy metal ions by novel-nanomaterials: A review., Environ. Pollut. 246 (2019) 608–620. https://doi.org/10.1016/j.envpol.2018.12.076.

[154] H. Sadegh, G.A.M. Ali, V.K. Gupta, A.S.H. Makhlouf, R. Shahryari-ghoshekandi, M.N. Nadagouda, M. Sillanpaa, E. Megiel, The role of nanomaterials as effective adsorbents and their applications in wastewater treatment, J. Nanostructure Chem. 7 (2017) 1–14. https://doi.org/10. 1007/s40097-017-0219-4.

[155] A. Cano, A. Jimenez, M. Chafer, C. Gonzalez, A. Chiralt, Effect of amylose : amylopectin ratio and rice bran addition on starch films properties, Carbohydr. Polym. 111 (2014) 543–555. https://doi.org/10.1016/j.carbpol.2014.04.075.

[156] joaquin G.-E. carol L.-D.P.H.R. catala; Rafael Gavara, Advances in antioxidant active food packaging, Trends Food Sci. Technol. 35 (2013) 42–51. https://doi.org/10.1016/ j.tifs.2013.10.00 8.

[157] S. Galus, J. Kadzinska, Food applications of emulsion-based edible films and coatings, Trends Food Sci. Technol. 45 (2015) 273–283. https://doi.org/10.1016/j.tifs.2015.07. 011.

Chapter 3. Synthesis of starch nanoparticles (SNPs) with intensified acid hydrolysis process.

3.1 Introduction

Starch is a naturally occurring biopolymer that plays an important part in human diet. Good sources include root vegetables and cereal grains such as rice, corn, wheat, barley, maize, tapioca, potato, and others. Starch is made up of two molecules: amylose, which has a straight chain, and amylopectin, which has a branched chain. Combining these two starch components results in granules ranging in size from 1 to 100 m. Starch has been used for thickening, gelling, and stabilizing functions in a wide variety of culinary and non-food goods. Another use for starch is drug and bioactive delivery systems. The natural form, on the other hand, has substantial flaws. It has low solubility, retrogradability, digestibility, and functional properties. As a result, various different physical, chemical, and enzymatic strategies have been developed to mitigate these disadvantages or give new benefits. Because of their exceptional quality and many possible applications, starch nanoparticles are gaining prominence. Many sectors have looked at them as potentially helpful biomaterials for novel uses, including the food, cosmetics, and pharmaceutical industries, as well as the composites business. Hydrolysis using acid, enzymes, or a combination of the two, regeneration, and mechanical treatments like as extrusion, irradiation, ultrasound, or precipitation with a co solvent are all feasible methods for producing starch nanoparticles. The limitation on the present SNP synthesis approaches are they are time consuming, required huge amount of solvent, and generates the environmental affecting pollutants has major concern. The nanoparticles manufactured from starch or a starch derivative are always beneficial, keeping in this view there is need for the simple, sustainable and low-cost manufacturing procedures [1].

Liu et al. [2] recently reported the structural variation in the SNCs synthesized from waxy maize starch (WMS) and waxy potato starch (WPS). The acid hydrolysis method was used for the synthesis of SNCs from native starch. The hydrolysis mechanism reported different for two starches through the same concentration of acid suspension. As the source of the starch molecular weights is different, potato starch shows a higher rate of hydrolysis than that of maize starch. The higher the hydrolysis rate, the lower the resistance offered by the outer lamellar structures or the higher the concentration of amylose present in the granules. The existence of an exo-corrosion pattern in the potato starch was prominent, whereas an endo-corrosion pattern was observed in the maize starch. The morphology of both synthesized

nanocrystals is reported to be parallelepiped for maize starch and round for potato starch. This indicates that the acid interaction with the starch granules is different and will depend on the amylose and amylopectin content of the native starch. The debranching of amylose and amylopectin in the presence of acid significantly produces lower carbon products such as glucose and sucrose. The process of hydrolysis will dependent on the resistance offered by these amylose and amylopectin interactions in the lamellar structure of natives starch molecules. Depending on the precursor material used, synthetic nanoparticles (SNPs) can be produced in one of two ways: either by building up atoms or molecules in a controlled manner in the form of small primary cores, as in a bottom-up process, or by breaking down larger, bulkier materials or microparticles to produce smaller ones, as in a top-down process [3]. Recently by altering the ratio of amylose to amylopectin present in maize starches, Gutierrez et al. [4] synthesize SNPs of controllable size using nanoprecipitation and microemulsion techniques. Nanoprecipitation made SNPs with sizes between 59 and 118 nm. These sizes got bigger when a surfactant was added to the watery medium. With the microemulsion method, it is easier to make particles with diameters between 35 and 147 nm. The type of maize used determined the size and shape of the particles that were made. Moran et al. [5] synthesized starch nanoparticles with the controlled size using microemulsion based approach. The W/O microemulsion was synthesized with the various organic solvent, and stable composition was used for the precipitation of starch slurry. The synthesized starch nanoparticles are found to be spherical in shape with the average size of nanoparticles is ranging between 30-40 nm. Moran et al. [5] proposed that, by controlling the ratio of water and organic solvent as well as reagent concentration in the microemulsion, the controlled size of starch nanoparticles could be synthesized with the microemulsion.

In the another approach Ahmad et al. [1] synthesized the starch nanoparticles from the unutilized sources such as horse chestnut, water chestnut and lotus stem. Ahmad et al. [1] proposed the mild alkali hydrolysis in combination with the ultrasound irradiation. The starch was suspended in the NaoH solution of known concentration followed by the 30 minutes of ultrasound irradiation produces the starch suspension. The synthesized slurry was co-precipitate with the addition of ethanol. The synthesized SNPs where confirmed by the analysis. The SNPs synthesized with mild alkali hydrolysis with ultrasound irradiation shows enhancement in the thermal stability, and antioxidant properties [1].

Chang et al.[6] synthesized the starch nanoparticles with different sizes through the precipitation approach. The etherification of potato starch results in the cationic starch

nanoparticles in the proposed method. The enzymatic modification of native starch granules to produce SNPs are environmental friendly processes. Tao et al [7] reported the production of SNPs with hybrid combination of enzymatic hydrolysis followed by recrystallization.

In the similar context, Zhau et al. [8] demonstrate the synthesis of starch nanoparticles with the combined effects of acid hydrolysis and ultrasound irradiation. The hydrochloric acid was used for the hydrolysis of starch. The synthetic SNP has a yield 27 % with particles sized 200-250 nm. A wide particle size distribution was observed, as well as increased thermal resistance.

The existing physical and chemical conversion methods for the synthesis of starch nanoparticles have lower yields as well as being more energy- and time-demanding. Thus, the accelerated process required for the synthesis of SNPs in order to benefit from their commercial nanoscale applications. In the same context, ultrasound assistance during the conventional acid hydrolysis was primarily focused on achieving the aim of synthesising starch nanoparticles. Experimentation with intensification of acid hydrolysis of native starch using ultrasonic cavitation assistance is mentioned in Chapter 3. The experimental process and separation of starch nanoparticles (SNP) are documented, and SNP production is confirmed using several analytical methods. The amylose content of the starch is responsible for its behavior in chemical and physical conversion. The long, straight chain of glucose units in compact and structured placement represents the crystalline phase of the starch. The amylose and amylopectin composition of starch has an effect on the acid activity of the starch granule [9]. The acid hydrolysis reaction mechanism follows two major stages. The relatively fast initial rate is thought to correspond to the hydrolysis of the amorphous parts within starch granules, whereas the slow process is attributed to the concomitant hydrolysis of the crystalline part. Amorphous regions within starch granules are thought to be more accessible to acid attack due to the loose packing of starch chains compared to the crystalline regions. In the crystalline zone of the starch granule, it was found that the structured arrangement of amylose and amylopectin was dominant, whereas in the amorphous phase was constituted with the random orientation of these two components [10]. The higher proportion of glucopyranose rings in amylose shows a slower conversion rate after acid interaction, due to which the rate of acid hydrolysis reduces significantly. Thus, the higher the amylose content in the starch granule, the higher will be the resistance to the acid hydrolysis observed in starch [11]. The aim of the present section was to achieve the intensification acid hydrolysis of starch granules to produce the starch nanoparticles. All of the experiments in this report were conducted using commercially

available starch granules with an amylose proportion of 27.5 (±1.2) %. The initial moisture content of the starch powder was less than 15 % and the pH is in the range of 4.0–7.0.

3.2 Experimental procedure

3.2.1 Materials

The maize corn starch and laboratory-grade sulphuric acid were purchased from Alfa Aesar and Merck, respectively. Two stage centrifugation was used for the separation of hydrolysed starch from the suspension. In all the preparations, deionized (D. I.) water was used. The schematic representation of the experimentations was depicted in figure 3.1 below.

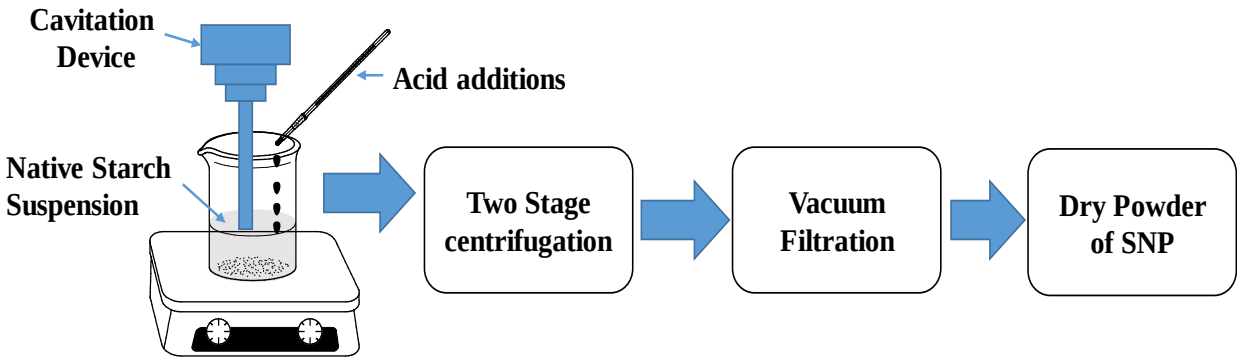

Figure 3.1 Schematic representation of SNP synthesis through ultrasound assisted acid hydrolysis process.

3.2.2. Experiment

The experiments are divided into two sections. The figure 3.2 illustrate the overall block diagram of the process. In the first section, conventional acid hydrolysis is conducted with (3 M) sulphuric acid. The conventional acid hydrolysis process was carried out for 48 h. The 1.67 g of maize corn starch was well mixed with the 3 M H_2SO_4 solution. The magnetic stirrer was employed to achieve the well mixed condition. After 48 hours, the acidic solution was neutralized with a sodium hydroxide solution. After complete neutralization (pH close to 7), the starch granules were centrifuged from the solution and vacuum dried at 40 ^oC for 6 hours in a vacuum dryer [12].

In the second section, ultrasonic assisted acid hydrolysis was carried out for the synthesis of SNP as follows; 1.67 g of starch was mixed in deionized water (55 mL) and sonicated for 20 min using a 20 kHz probe sonicator (Dakshin ultrasonicator, Mumbai, India) of tip size 20 mm at the power input of 220 Watts (3 sec on and 1 sec off, pulse mode). In the presence of ultrasonic irradiation, 0.5 M (50 mL) sulphuric acid was added dropwise to the above starch-

water solution for the next 20 min. In order to achieve maximum acid hydrolysis, sonication was continued for another 30 min at 30 °C. 0.25 M (100 mL) of NaOH solution was used to neutralize the unreacted acid, and the dropwise addition proceeded until a pH of 7 was achieved at room temperature. A two-stage centrifugation (Eppendorf® Centrifuge, 5430R, Germany) was used to separate the produced SNPs from the suspension. In the first stage the centrifugation was run at 1000 rpm for 5 min., in this stage the microcrystalline starch get agitates at the bottom of the centrifugal tubes. The clear suspension of SNPs was separated from submicron sized starch. The clear suspension from centrifugal tubes further treated with centrifugation at the speed of 9000 rpm for 5 min.

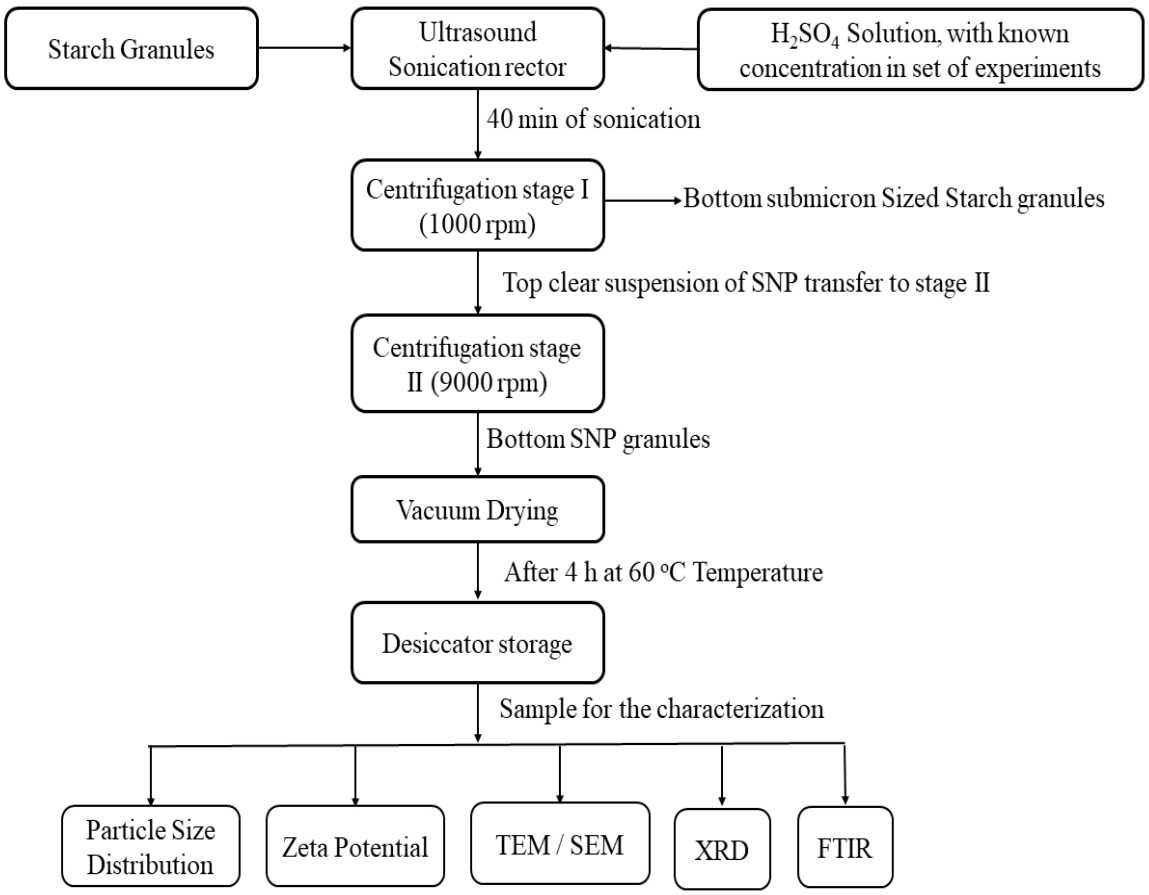

Figure 3.2 Block diagram of the SNP synthesis process

In this second stage of centrifugation SNPs get separate out at the bottom of tubes and solution get separated. The slurry residual from the centrifuge was further washed with 600 mL of deionized water in order to remove impurities like traces of acid and base. The vacuum dryer is used to dry the thick slurry to get the powder form of SNP. The dried powder of SNP are stored in the desiccator to avoid the contamination of moisture. The SNP synthesize in both the

sections were compared to understand the effect of ultrasound assistance to the acid hydrolysis process. The PI of acid hydrolysis process was carried out to achieve the SNP in 40 min. However, the conventional process required 48 h for the total conversion [12].

The yield of SNP synthesized was calculated on the basis of the weight of separated nano granules of starch after drying. In the first stage of centrifugation (1000 rpm, 5 min). The coarser submicron sized starch granules are observed to settle down at the bottom, and nanoparticles are still remain in the supernatant. In the second stage of centrifugation, the supernatant from the first stage is centrifuged for 5 min at 9500 rpm. At this high speed, the nanoparticles from suspension gets settled down at the bottom of the centrifuge tube, which were then dried and the weight was noted. The yield of the SNP synthesis calculated based on nanoparticles separated in the second stage. The overall mass balance of starch particles was taken as basis for the calculation of net mass of SNPs.

3.3 Characterization of starch nanoparticles

3.3.1 Particle Size Analysis and Zeta Potential Measurement

The particle size and zeta potential measurements of SNP were performed at 25 °C using a Malvern nanosizer (Nano ZS, Zen 3600) using the dynamic light scattering (DLS) method. SNP was added to deionized water and homogenized by bath sonication until an obscuration of less than 10 % was recorded. The refractometer was used to measure the exact value of refractive index for the starch suspension. The value of the refractive index is 1.33, which is almost similar to the deionized water used in the experimentation with the zeta sizer. The particle size distribution for the SNPs was reported using the DLS principle. The stability of SNPs in suspension was assessed by using the zeta potential of the SNPs in solution [13].

3.3.2 Morphology of the starch nanoparticle

The morphological characteristics of the SNPs were revealed using transmission electron microscopy (TEM) and scanning electron microscopy (SEM). For TEM imaging (TEM instrument, PHILIPS, CM 200), it was run at 200 kV and 2.4 A° resolution. The TEM micrographs of the fabricated SNPs were utilized to study the surface morphology. The sample for TEM analysis was prepared by spreading a drop of the SNPs suspension (0.2 % w/v) on a glow discharged carbon coated grid. To conduct the SEM analysis of SNPs, SEM (TESCAN-Vega 3 LMU model microscope, Fuveau, France) operating at an accelerating voltage of 20 kV was used [14].

3.3.3 Thermogravimetric Analysis (TGA) of SNP

TGA analysis was done with TGA-6/DTG of NETZSCH STA 2500 (precision of temperature measurement ± 2 °C, microbalance sensitivity < 5 μg). The percentage weight loss of the sample was recorded continuously as function of temperature, under dynamic conditions, in the range of 30-600 °C. The experiments were carried out at atmospheric pressure, under a nitrogen atmosphere, with a flow rate of 60 mL/min, at a linear heating rate of 10 °C/min. The small mass of sample material i.e., 20 mg was filled in the crucible whereas the reference crucible was kept empty in case of native starch as well as SNP. The experiment was carried out in triplicate to check the reproducibility of results [15].

3.3.4 X-ray Diffraction (XRD) Analysis

Bruker D8 advanced X-ray diffractometer was used to collect the XRD spectra of the SNP. Copper Kα (Cu Kα) radiations were used to produce the X-ray with the wavelength of 0.154 nm and were recorded on the 2θ scale, ranging from 5° to 50° with the step size of 0.018 in 2θ [16].

3.3.5 Fourier Transform Infrared Spectroscopy (FTIR) of SNPs

The FTIR spectra (Shimadzu-8400 FTIR instrument, Japan) were obtained using the KBr pellet method. KBr was mixed with SNPs, and the mixture was converted into a pellet for the analysis. The spectral resolution was 4/cm, whereas the scanning range was 4000-400 cm^{-1} to record the FTIR spectrum [16].

3.4 Process parameter optimization for reduce particle size and process variable affecting starch nanoparticle synthesis.

The kinetics of acid hydrolysis suggest that the rate of diffusion of acid molecules during the hydrolysis of starch will have a significant effect on the overall hydrolysis of starch granules. The ultrasound assistance during the hydrolysis induces the additional driving force of the mass transfer of acid molecules towards the surface of the starch granules. At the molecular level, each H_2SO_4 molecule of acid gets dissociated in the water, and in two stages, it releases two hydrogen ions (H^+) and (SO_4^{2-}) ions in the water. As it is a strong acid, each molecule reacts with the starch granules. The hydrogen ions react with the glucose monomer chain of α-1, 4-d-glucopyranose and the product is dissolved in the suspension. The sulphonic group ($-OSO_3\ -$) attached to the surface of the starch granule. The greater the number of hydrogen ions, the faster the hydrolysis. However, at the higher concentration of hydrogen ions, the resistance offered by the compact crystalline zone of starch granules will be the same, as a result of which

the hydrolysis rate will be slower. Thus, it is necessary to optimize the concentration of acid during hydrolysis.

The ultrasound irradiation of the suspension creates the cavities inside the suspension. During the cavity collision, the local hot spot generation was developed, as discussed previously. The amount of energy required to develop the cavities inside the suspension increases as the irradiation time increases, and the corresponding effective operation cost of the process changes. Thus, in order to make the system economically viable, the two major process parameters must be optimized. The process parameter during the experimentations was optimized after the successful achievement of SNPs. The operational parameters such as acid concentration required for the hydrolysis and time of Ultrasound (US) exposure by the starch suspension.

3.4.1 Acid concentration optimization

The H_2SO_4 acid concentration was optimized by varying its values during the hydrolysis of starch. The number of experimentations was conducted to obtain the optimum value of acid concentration. Initially, the acid solutions (sulphuric acid, 50 mL) of different concentrations (0.5 M, 1 M, 2 M, and 3 M) were prepared using deionized water. The 1.67 g of native starch particles was dispersed in the deionized water by using sonication for the 5 min. The suspension of starch in deionized water further exposed to the ultrasound irradiation with simultaneous dropwise addition of acidic solution. The separate experiment was conducted for the individual acid concentration. The overall ultrasound irradiation during the hydrolysis process was restricted to 405 min for each experimentation. For this process, a probe sonicator (20 kHz, probe tip diameter 20 mm, 120 W, pulse mode 3 sec on and 1 sec off, Dakshin ultrasonicator, Mumbai, India) was employed. The overall power dissipation to the suspension of starch granules and water was 202 W for 100 mL suspension with 40 % power setting (power density = 0.808 W cm^{-3}). The temperature of the system was maintained below 15 ^{o}C, by immersing the whole vessel in a thermostat bath. The solution after sonication was stirred continuously for 10 min, followed by neutralization with NaOH (0.25 M) to maintain the pH at 7. The acid hydrolyzed starch solution was then centrifuged (using Eppendorf® Centrifuge, 5430R, Germany) in two-stages. At first, centrifugation at 1000 rpm for 5 min separated microscale starch particles from the suspension. The coarser micron-sized starch granules are observed to be settled down at the bottom, and nanoparticles will remain in the supernatant. The obtained sub-micron starch particles were dried and stored separately. In the second stage, the supernatant from the first stage is centrifuged for 5 min at 9500 rpm. At this high speed, the

nanoparticles from suspension settled down at the bottom of the centrifuge tube, which then dried and, washed several times by deionized water to obtain the acid and base free SNPs. The precipitate of SNPs where dried by using vacuum drier at 40 ^{o}C for 6 h., and the weight was noted. The overall mass balance for native starch granule induced in the hydrolysis process with two major outputs as submicron and nanoscale starch granules was consider during the calculation of net yield of SNPs during the overall intensified acid hydrolysis process. The SNPs synthesised with the mentioned acid concentration was separate out by following same process and stored in the desiccator to avoid the moisture and bacterial contamination.

For comparison, the synthesis of SNPs was also carried out by the conventional method of acid hydrolysis. For this, acid hydrolysis of native starch was carried out using 3 M sulphuric acid and agitation (300 rpm) through magnetic stirring for 48 h. After 2 days of acid hydrolysis, the starch slurry was separate from the acid solution by two stage centrifugation (Eppendorf® Centrifuge, 5430R, Germany) approach. The second stage outcome of centrifugation was wasted with base and deionized water before vacuum dried. The slurry of SNPs were then vacuum dried and stored using a desiccator to avoid the contamination of water and bacteria. The yield of SNPs was calculated by considering the overall mass balance of starch.

3.4.2 Optimization of ultrasound irradiation time.

After the optimization of the acid concentration during the hydrolysis process of starch. The value of the acid concentration of 0.5 M was found optimized for the higher yield of SNPs during intensified approach. During the irradiation time optimization the experiments was conducted with fixing the acid concentration 0.5 M. The similar process was followed for the synthesis of SNPs with only variation in the ultrasound irradiation exposure to the suspension during dropwise addition of acid. The variation of the exposure time was conducted from 10 min to 80 min. The individual experiment was conducted for the synthesis of SNPs for each irradiation time and separated SNPs where analysed for the particle size measurement using Malvern nanosizer (Nano ZS, Zen 3600).

3.5 Result and discussion:

The size reduction during the acid hydrolysis was attributed to its interactions with the acidic surroundings. α-(1→4)-glycosidic linkage in amylose and branched α-(1→4) and α-(1→6)-glycosidic bonds in amylopectin were significant during the hydrolysis. The hydroxyl radicals in the acidic suspension interact with both of these linkages in the starch granules. The hydrolysis of amylose and amylopectin results in the generation of lower-carbon compounds

such as glucose (straight chain) and fructose. As a result, the greater the extent of hydrolysis in starch granules, the more completely the structure is destroyed into the basic forms of glucose and fructose. The amylose present in the starch granules was observed to be in an unbranched chain of about 22–30 monomers. Due to the unavailability of branches, the possibility of the amylose associating with other components in the structure is lower. Amylopectin, on the other hand, is a branched polymeric chain with α-(1→6)-glycosidic linkages that contribute to a few layers of the starch structure's compact structure. The helical structure of starch has specific layers according to its layer-by-layer arrangement. The intermolecular interaction between amylose and amylopectin was low in the amorphous region of the starch. However, the intermolecular linkages between amylose and amylopectin induce the higher compactness in the region. The hydroxyl ions' interaction with these two components as well as the branched chains of amylopectin induces the compact arrangements in the crystalline zone [17].

The amorphous region and crystalline region of starch are different from each other because of the randomness in the orientations of amylose and amylopectin polymeric chains in the zone. The regular and compact arrangement of branched amylopectin with a very small concentration of amylose was seen in the crystalline region of starch. On the other hand, the higher concentration of amylose will not develop a compact structure due to the unavailability of branches in the polymeric structure of amylose, which generates randomness in the orientation of both components in the amorphous region of starch. During the acid hydrolysis, the amorphous region of starch is more susceptible to the acid interaction, and due to its loosely packed structure, the penetration of acid molecules in this region was higher, which resulted in a higher extent of hydrolysis. However, in the crystalline region, the compactness of the structure will offer higher resistance to the acid's penetration. Thus, the hydrolysis rate in the crystalline region was lower, which is attributed to the higher concentration of amylopectin. The helix structure of starch offers alternative layers of crystalline and amorphous regions. Thus, in the conventional acid hydrolysis approach, the overall hydrolysis rate was observed to be lower, as well as the yield of lower-sized starch granules, which is limited by the higher extent of hydrolysis and the resistance offered by the crystalline region.

The intensification of the acid hydrolysis process was achieved with the ultrasound assistance. The cavitation developed during the ultrasound irradiation are developed, nurtured, and collapsed in the suspension. The ultrasound irradiation to the starch granule dispersed suspension induces the cavitation effects at higher frequency. When the cavities collapse the hot zone are developed at which temperature reach to 1500 K and pressure about 100 bar. These

collapse of the cavities develops the shock waves in the suspension. These shock waves generates the physical impact on the surface of starch granule as well as on the liquid surrounding. The physical impact on the surface of starch granules can develops the cracks or physical destruction of the starch granules [18]. The impact on the suspension surrounding the starch granules will have a significant effect on the mass transfer coefficient of acid molecules in the suspension. The mass transfer coefficient of acid molecules was found to increase, and this induces the higher acidic molecules on the surface of starch granules. The penetration of acid molecules will be higher due to the cracks or partial destruction of granules. This higher penetration rate of acid granules increases the hydrolysis rate. The intermediate layers inside the starch granules are exposed to the acidic media easily, resulting in a decrease in the overall resistance offered by the starch granules as well as a high rate of acid molecule penetration in the starch granules due to the physical impact of collapses. Both of these activities increase during cavitation-assisted acid hydrolysis. At the nanoscale, the produced starch granules are significantly smaller. The morphology and particle size of synthesized starch granules are confirmed by the following analytical methods:

3.5.1 Particle Size Distribution using DLS

The particle size of synthesized SNP was ensured with DLS. Avery dilute aqueous suspension of dried SNP was sonicated by using bath sonicator for 5 min as mentioned in the standard procedure for the sample preparation. Figure 3.3 shows the mono-modal nature of recorded scattered light from DLS. The hydrodynamic radius for the starch particles was centred about 500 nm synthesized with conventional acid hydrolysis process. The overall time required for the conversion is 48 h for 3 M concentrated H_2SO_4. However, in the synthesis of SNP by intensified acid hydrolysis approach the particle size distribution was centred to 300 nm, along with very less time as compared to the conventional hydrolysis method. To avoid the effect of acid concentration on the crystallinity of synthesized SNP, optimization of acid concentration is essential. The stability for the average particle size distribution of SNPs synthesized with individual approach was mentioned in table 3.1. The particle size of synthesized SNPs cannot be confirmed with the DLS alone as it gives overall hydrodynamic sphere radius rather than exact radius for the particle. Further analysis for the confirmation of SEM for synthesized SNPs was conducted for the confirmation of the results by zeta sizer.

The stability of the SNPs synthesized by conventional acid hydrolysis was observed higher extent as the surface charges developed during the hydrolysis was above ±25 mV. The zeta potential for the particles is actually a measurement of the surface charges associated with the

crystalline structure of particle. The agglomeration between the nanoparticles is induce because of Van der Waals forces. In the suspension when the Van der Waals forces of attraction was higher than nanoparticles becomes unstable and agglomeration process starts in the suspension. Thus, it can be conclude that Higher the value of surface charges in the suspension, more will be the repulsive interaction exist between the particles and nanoparticles in the suspension are more stable [19,20].

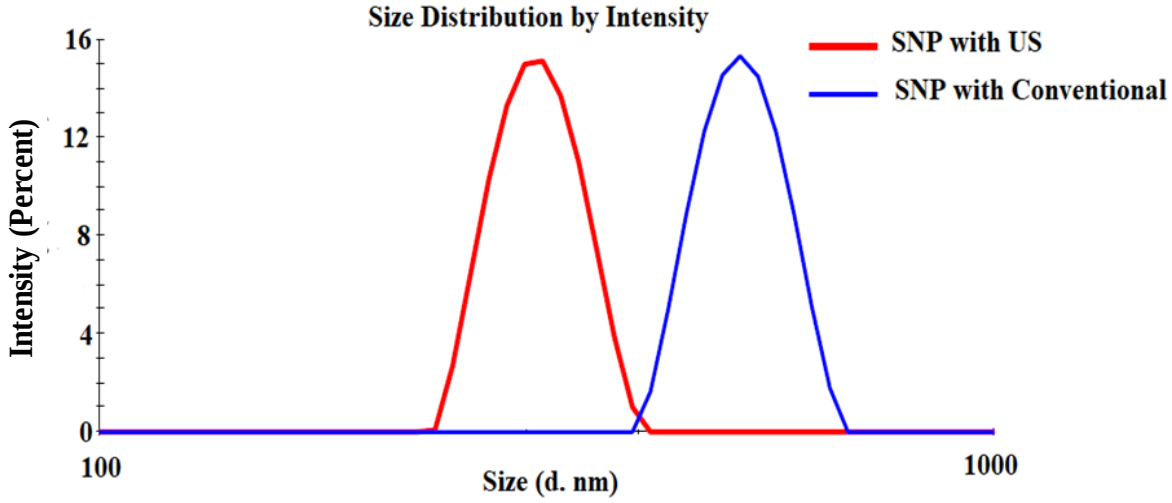

Figure 3.3 Particle size distribution (PSD) for the SNP synthesized with ultrasound (US) assisted and conventional acid hydrolysis process.

Table 3.1 Particle size specification of SNPs synthesized with different methods

SNPs with different approach	Acid hydrolysis with Ultrasound assistance	Conventional Acid hydrolysis
Average Particle size	297 nm ± 12.52	501 nm ± 32.20
Zeta Potential	-21.09 mV	-29.31 mV

The yield of SNP was found to be 42 % by mass balance method. The combined effect reduces the time interval as well as more efficiently increases the yield. Amini et al. [13] have reported that the starch particles may not be fully hydrolysed. They reported that a lower concentration of acid would give rise to the nanoscale particle size of starch; the yield is more at a higher temperature and with more sonication time. The acid hydrolysis yield of starch granules at higher temperature was observed to be equivalent to the present yield [14].

3.5.2 Zeta Potential

The Surface charge on the SNP synthesized by conventional and ultrasound assisted hydrolysis methods was found and reported in Table. 3.1. It was found that, the zeta potential of SNP synthesized by conventional method has lower value than that of SNP synthesized by ultrasound assisted acid hydrolysis method. A lower value of zeta potential indicates unstable suspension. Negative value of both SNP indicates the presence of sulphate group ($-OSO_3-$) on the surface of SNP. It has also been reported that the presence of sulphate group ($-OSO_3-$) on the surface of SNP was responsible for negative zeta potential value [21]. SNP synthesized by hydrolysis has much higher stability as compared to other methods of synthesis such as TEMPO oxidation [3,22] or ultrasound [18] because of the presence of negative charge, presence of electrostatic repulsion between similarly charged SNP did not allow them to agglomerate. Zeta potential of SNP was found to be enhanced with ultrasound assistance.

3.5.3 Morphology Study of Starch Nanoparticles

Figure 3.4 represents the microscopic image of synthesized SNPs with two different approach. Figure 3.4 (a) depicted the transmission electron microscopy (TEM) for the synthesized SNPs through intensified acid hydrolysis approach. The particle size of synthesized SNPs are below 10 nm was confirmed with the TEM image. The average particle size where analysed with the ImageJ image processing software for the better understanding of average size measurement of particles. The predicted average particle size was 9 nm with average of 269 particles analysed by the software. From Figure 3.4 (a), it is observed that, SNP with oval shape morphology and size in the range of 10-50 nm was obtained, which is in harmony with DLS measurement. Kim et al. [23] reported the different methods for the synthesis of SNP including the three- stage effective hydrolysis. They also mentioned that acid hydrolysis is a slow process with the starch as it has a semi-crystalline structure. The speed of acid hydrolysis depends upon the packaging structure of crystalline regime of starch and total crystallinity of starch. Boufi et al. [21] and Shabana et al. [14] reported different shapes of SNP such as round edge, polygon and irregular platelets this is due to the extent of hydrolysis completed with starch granules. The synthesis of SNP with combined effect of sonication and acid hydrolysis was confirmed with the SEM image. The second part of figure 3.4 (b) SEM image for the SNP through conventional acid hydrolysis approach after 48 h of process. The average particle size was observed from the image was ranging from 200-300 nm. Because the hydrolysis rate is dynamic and the resistance offered by the starch granules increases with time, the process takes a long time to completion. The rate of hydrolysis is not constant during acid hydrolysis using the

standard technique because the amorphous phase slows down the reaction with time. However, the crystalline portion of the SNP gives more resistance to the acid interaction.

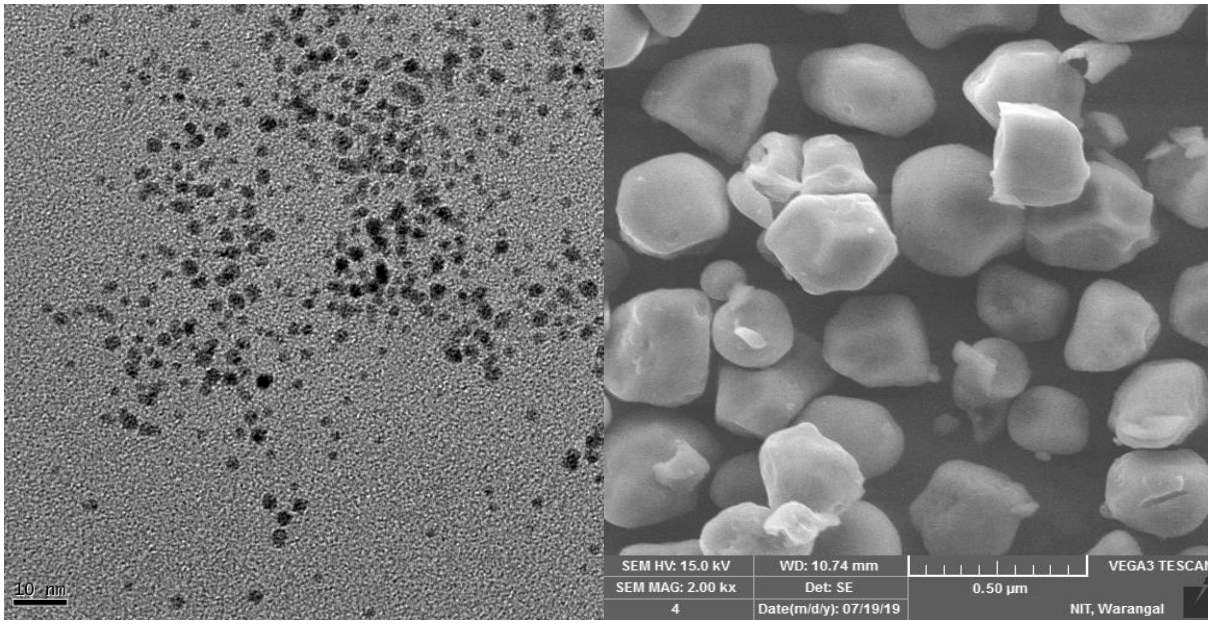

a) TEM of SNPs with intensified approach b) SEM of SNP with Conventional approach

Figure 3.4 Morphology of synthesized SNP through a) Ultrasound assisted intensified, b) Conventional acid hydrolysis approach.

3.5.4 XRD analysis for synthesized SNPs

The crystallinity comparison of SNP synthesized by conventional hydrolysis and ultrasound assisted hydrolysis was observed from the XRD pattern of SNP in Figure 3.5, which the highest peak exists at 2θ value of 17.90°, and its full width at half maximum intensity of the peak is 0.5668, for the X-ray wavelength of 0.1540 nm. The Debye-Scherer formula provides the average crystallite size of 14.83 nm, which is analogous to SEM analysis. The crystallinity is an important characteristic of the nanostructure. Polysaccharide starch is made up of glucose. The amylose and amylopectin are major parts of starch due to which it is identified as natural polymer. Amorphous regions of starch granules are attributed to the presence of amylose and amylopectin in random interactions, whereas branched amylopectin are interact with the amylose with recuing ends to generate the compact structure known as crystalline region of the starch. From figure 3.4 it was confirmed that, the randomness of the starch shape size was observed with the ultrasound-assisted acid hydrolysis process. The shear stress developed due to the high frequency of sonication develops a crack on the surface of starch granules, which will allow penetration of acid inside the starch granule. This allows for higher interaction of amylose and amylopectin with acid, which induces a rise in the acid hydrolysis rate. However,

with conventional acid hydrolysis, due to the lower rate of hydrolysis, the shape and size of the starch granules are nearly uniform.

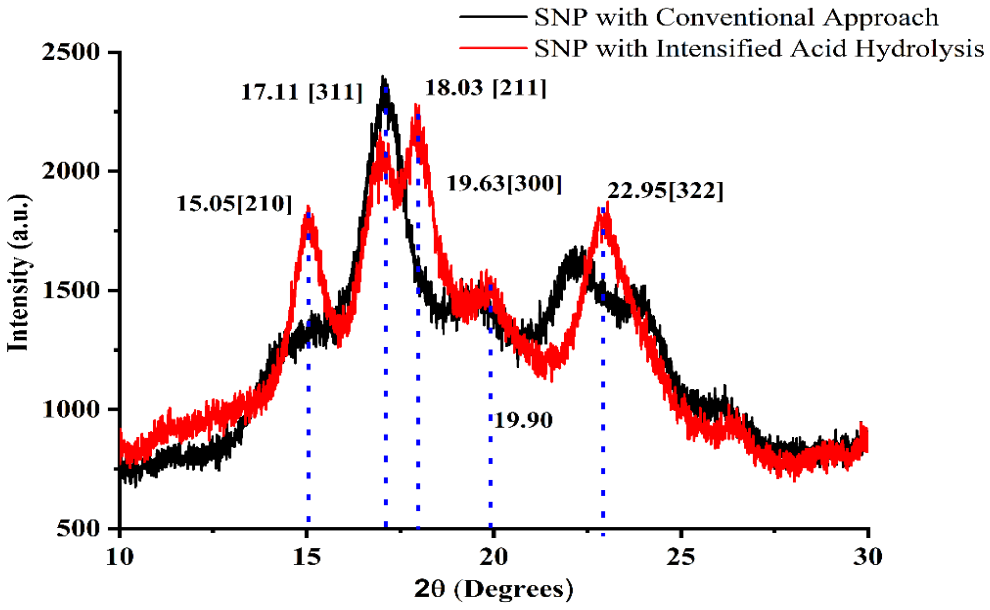

Figure 3.5 XRD analysis of the SNP Synthesis two individual approaches as US assisted intensified and conventional acid hydrolysis process.

Table 3.2 XRD spectrum peak specifications and crystalline plane values [13,18,21]

Peak no	Angle value (2θ)	hkl value For the SNP	Crystallinity %	d Å
1	15.05	2 1 0	41.27	5.403
2	17.11	3 1 1	53.19	5.181
3	18.02	2 1 1	-	4.922
4	19.63	3 3 0	-	3.125
5	22.95	3 2 2	17.45	3.037

The mass transfer rate of acid molecules under ultrasound assistance was higher due to shock waves developed during the cavitation. The figure shows that almost similar effects of hydrolysis were found in both approaches. The single peak with the wider angle was discovered using conventional acid hydrolysis at 17.11º. The two peaks observed with the US-assisted approach are at 17.11° and 18.02°, indicating a significant change in the granule's overall crystallinity. A similar mechanism was reported by Baufi et al. [24].

The comparative analysis of XRD diffraction pattern can be observed in the figure 3.5. The conventional acid hydrolysis of starch granules for 48 h of operation was observed to be more

crystalline with single prominent peak. The area under the diffraction curves are observed to be have higher values as compared to the diffraction of SNPs through intensified acid hydrolysis. IT clearly indicates the slight amorphous nature of SNPs synthesized by the conventional acid hydrolysis approach. The reason behind could be slower and constant interaction of acid for longer time duration. The acid molecules associated with the inner layers of starch granules interact slowly to break the glycosidic linkage and generated hydrolysed product are not completely removed from the starch structure. As, the process is slower the intermediate attachment of hydroxyl linkages could be at the higher end due to which the hydrolysed product of amylose and amylopectin required time to losses the exact place from cluster. The hydrolysed starch through conventional process shows single prominent peak. On the other hand, cavitation assistance induces the turbulence with each cycle of pulse mode. The higher impacts of shock waves are becomes the driving force for the displacement of hydrolysed intermediate hydrolysis products of amylose and amylopectin both. Thus, the clear crystalline structure was observed from the results of XRD diffraction shown in figure 3.5

The combined effect of ultrasound irradiation and acid hydrolysis eliminates the amorphous region of native starch to some extent. Figure 3.5 shows comparison of SNP synthesized by two different approaches. Figure 3.5 shows the comparison of native SNP synthesized with conventional acid hydrolysis as well as by ultrasound assisted acid hydrolysis. The increase in the crystallinity index of SNP synthesized by ultrasound assisted acid hydrolysis was observed to be 21.6 % as compared to SNP synthesized by conventional acid hydrolysis. The area under the sharp peaks observed for the SNP synthesized by ultrasound assisted acid hydrolysis was higher than the area under the sharp peaks for the SNP synthesized by conventional acid hydrolysis. This rise in the area under the sharp peaks indicates significant increase in the crystallinity of SNP synthesized by ultrasound assisted acid hydrolysis. The rise in crystallinity by 46 % was observed due to ultrasound assistance during acid hydrolysis of native starch.

The XRD pattern reported by Amini et al. [13] shows lower crystallinity effect as compared to the presented method for the synthesis of SNP. They prepared the SNP with an acid concentration of 4.5 M that is very high in comparison with the present work of acid concentration of 0.5 M. This indicates that there is a significant effect of sonication on the crystallinity of SNP. Many researchers have reported that the higher time of sonication and temperature may lead to a decrease in crystallinity of SNP [25,26]. On the contrary, to this, we did not notice any decrease in crystallinity, presumable due to the contribution of ultrasound in

reducing the time for the hydrolysis process. In addition to this, the rise in crystallinity of SNP synthesized with acid hydrolysis was successfully reported [27,28].

3.5.5 Thermal Properties of synthesized SNPs with different approach.

The thermal resistance of the synthesized SNPs was analysed by using Thermogravimetric analysis (TGA). The difference in the overall mass or loss of mass of sample on the inert heating of the sample of SNPs produced by both conventional and hybrid methodologies is shown in Figure 3.6. The SNP produced by both methods, first showed a weight loss around 120 °C due to the evaporation of moisture content in the sample, where water bonds with starch get broken. In the second stage, both SNP experienced a sudden weight loss of around 250 °C at different mass loss rates. The observation from the results obtained can be used to conclude that in the conventional acid hydrolysis of starch, the crystalline region of SNP shows gradual thermal degradation in three stages. While the SNPs were created using ultrasound-assisted acid hydrolysis, there were two stages of thermal degradation observed. In the first phase, all but about 8 % of the initial weight of starch granules decreased, which is attributed to the unbounded moisture associated with the SNP granules. The SNP synthesized with the conventional hydrolysis method has a sharp drop due to the presence of a higher amorphous portion, while in other SNPs the weight loss increases gradually. As a result of the ultrasound assistance during acid hydrolysis, the extent of starch hydrolysis and crystallinity of SNP increase. The results are in resemblance with as reported by [29–31].

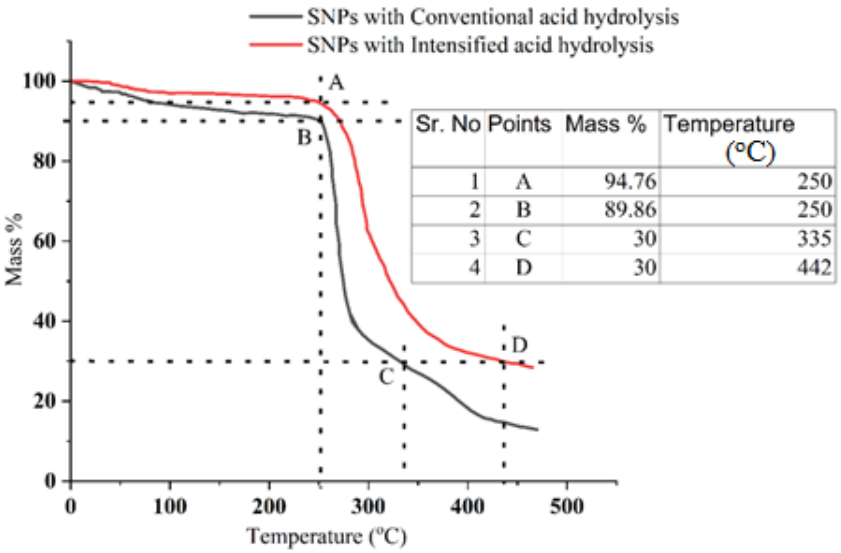

Sr. No	Points	Mass %	Temperature (°C)
1	A	94.76	250
2	B	89.86	250
3	C	30	335
4	D	30	442

Figure 3.6 TGA analysis for SNP synthesized by both methods

At 250 ^{o}C, the second mass change occurs. Both SNPs synthesized had a similar temperature for the second stage. However, the mass percent in both SNPs differs, with the SNPs synthesized via ultrasound-assisted acid hydrolysis exhibiting a second stage of major mass loss of 5 % and the SNPs synthesized via conventional acid hydrolysis exhibiting a mass loss of 12 %. The mass loss in the SNPs through the intensified approach was lower than the mass loss in the SNPs through the conventional acid hydrolysis approach. The lower mass loss could be attributed to the higher crystallinity of synthesized SNPs. The SNPs synthesized through acid hydrolysis show amorphous behaviour. When burned in an inert and controlled environment, these amorphous SNP granules exhibit a faster thermal degradation rate. In the third stage of mass loss, as depicted in figure 3.6, at around 30 % mass, it will be observed at 335 ^{o}C in conventional acid hydrolysis, whereas it was observed around 440 ^{o}C in intensified acid hydrolysis. The higher temperature indicates the higher resistance offered by the SNPs synthesized with the current proposed methods.

3.5.6 FTIR analysis of SNPs

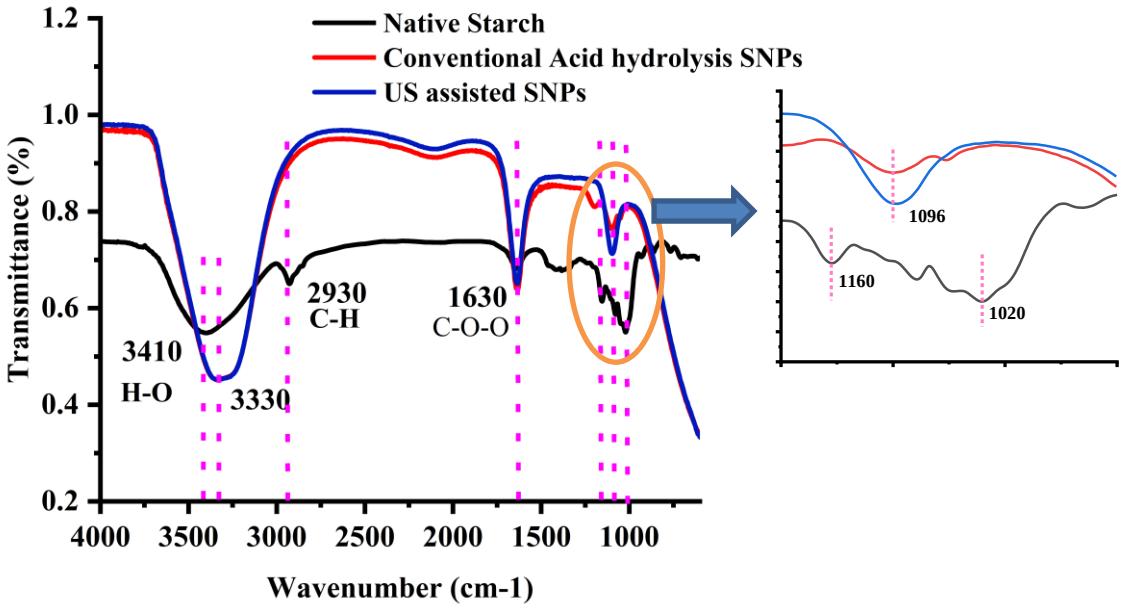

Figure 3.7 FTIR spectra of native starch, SNPs synthesized through conventional and ultrasound assisted acid hydrolysis process.

The FTIR spectrum shown in figure 3.7 indicates the surface functional group associated with the native starch as well as SNPs synthesized with two different approaches. The native starch had a significant peak of hydroxyl group stretching at 3410 cm^{-1}, but the SNP synthesized with

conventional and intensified acid hydrolysis processes had a slight shift in the stretching of similar groups at 3330 cm^{-1}.

Table 3.3 FTIR spectra list of chemical functional group with wavenumber

Sr. No.	Wavenumber (cm^{-1})	Functional group
1	3410, 3330	O-H bond stretching, hydroxyl function group presence.
2	2930	C-H bond stretching
3	1630	C-O-O bond vibrational stretching, Characteristics of glucosidic linkages
4	1160, 1020	C-O bond stretching.
5	1096	Modified asymmetric vibration stretching of C-O bond.

The conventional and intensified acid hydrolysis approaches have a similar effect on the hydroxyl functional group. The C-H bond is the second significant bond found in the structure. The hydroxyl ions from the acid molecules will directly interact with the C-H bond in the acid hydrolysis reaction. The C-H bond specifically affects the hydrolysis process. The residual water molecules associated with the starch granule show their specific peak at 1630 cm^{-1}. The C-O bond vibrations associated with the glucose anhydrous units were observed in the native starch at 1020 cm^{-1} and 1160 cm^{-1}, which meaningfully disappear in the SNPs synthesized and appear at 1096 cm^{-1}. The vibrational energy variations in the ultrasound assisted approach were found to be much more dominant as compared with the conventional acid hydrolysis approach. The figure 3.6 shows that the vibrational energy window of the SNP synthesized with intensified acid hydrolysis was much higher than that of the native starch as well as the SNP synthesized with a conventional acid hydrolysis approach. This rise in the intensity attributed due to the cross-linkages developed during the hydrolysis in the SNPs [18,26,32].

3.5.7. Effect of acid concentration on the SNPs synthesized through intensified acid hydrolysis approach.

3.5.7.1 Particle size distribution and stability of SNPs in suspension

The SNPs obtained from the ultrasound-assisted hydrolysis method were evaluated for their particle size distribution and stability using the dynamic light scattering (DLS) measurements. The comparative particle size distribution is shown in Figure 3.8. The ultrasound-assisted hydrolysis process found to be more efficient as compared to the conventional hydrolysis [14,18].

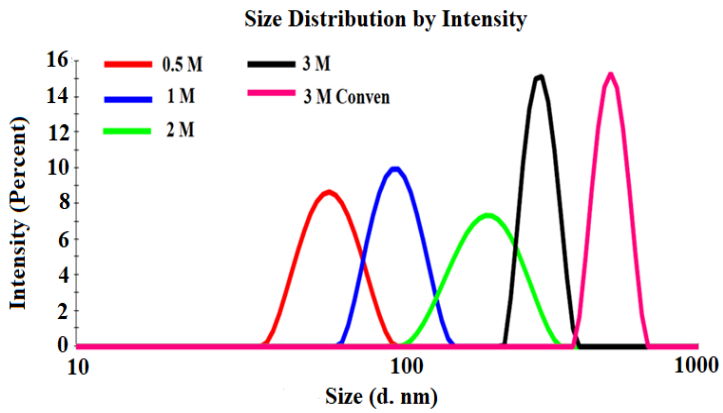

Acid concentration used during hydrolysis M	Particle Size (PSD) nm
0.5	63
1	102
2	207
3	323
3 (Conventional Approach)	629

Figure 3.8 PSD starch nanoparticles with different acid concentration

The size of native starch particles was reduced when subjected to sonication. In the conventional method, the particle size was observed in the range of 500-600 nm, after 48 h of hydrolysis. In contrast, in the case of ultrasound treated starch hydrolysis, the particle sizes were below 200 nm, and notably, it was applied for 40 minutes only. A reduction in the time of SNPs synthesis arises from cavitation effects. The cavities generated in the starch suspension during ultrasound irradiation are collapse with high impact, producing higher local temperatures and pressures [33]. These cavities collapse randomly in the solution. When they collapse near or on the surface of starch particles, the high impact physically damages the surfaces of starch, increasing acid diffusion inside the starch particles. The hydrolysis rate is found to increase owing to higher acid diffusion in the starch particles, reducing the hydrolysis time in the synthesis of SNPs. The only drawback with sonication is the rise in local temperature during the collapse of cavities, inducing the gelatinization of starch. Thus, a control on temperature is necessary during operation to avoid the gelatinization effect in the starch particles. Figure 3.8 shows the effect of acid concentration on the particle size distribution. As the acid concentration increases, the particle size of SNPs also increases. This rise in particle size with acid concentration is due to the agglomeration of SNPs after the hydrolysis [12]. The collapse of cavities in the solution enhances the temperature and pressure suddenly for a fraction of time. This collapse in solution induces the dissociation of water and acid in the form of free radicals. This instantaneous rise in temperature and pressure due to the collapse of cavities generates high energy, which is higher than the bond dissociation energy of water and sulphuric acid, leading to the generation of free hydroxyl ($\cdot$OH) radicals from water and sulphonic group (-SO_2-OH) [24].

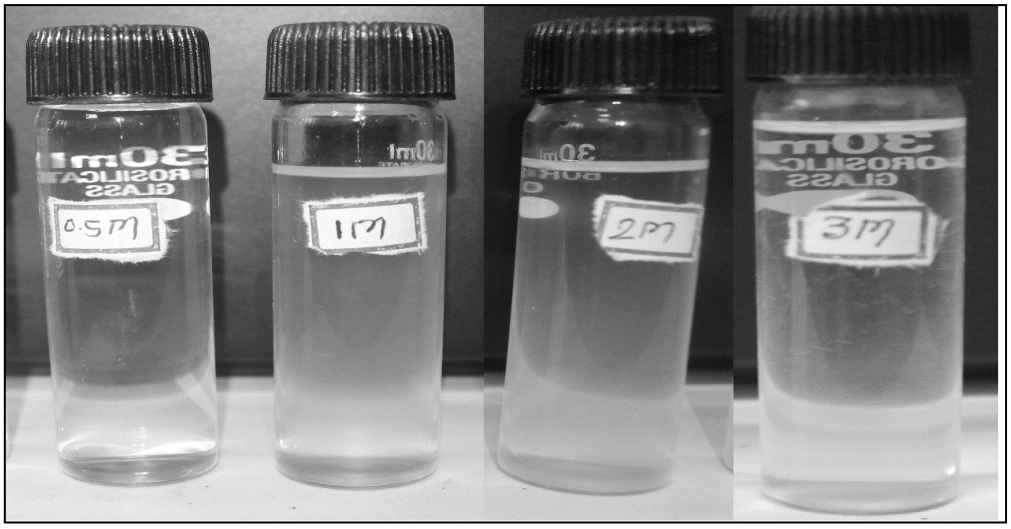

Figure 3.9 Suspension of SNPs after intensified acid hydrolysis.

These radicals are reactive, and their presence on the surface of SNPs was confirmed by infrared spectrometry and the enhanced zeta potential of particles. These charged sulphonic groups are responsible for the repulsive force between SNPs when they are lower in number. The esterification of the surface hydroxyl groups of SNPs with sulfuric acid is another side reaction that continues to the generation of sulphate groups on SNPs, as reported in the preparation of starch nanocrystals [34]. As the concentration of sulphuric acid increases, the radicals of the sulphonic group also increase, leading to an increase in the agglomeration of synthesized SNPs during the process. From Figure 3.9, it has been observed that as the acid concentration lowers, the suspension becomes clear and transparent.

The acid interaction with starch particles plays an important role during its simultaneous exposure to sonication. The cavities generated during sonication create a high impact that breaks the structure of starch, allowing the penetration of acid in the inner cores of starch. The amorphous portion of starch (amylopectin) reacts with acid and breaks its branches, reducing the complexity of starch structure [10,35]. Hence, the reduction in the size of starch particle is due to the effects of both acid interaction as well as sonication. The ultrasound application causes acid interaction more effective with the amorphous part of the starch. Simultaneously it also generates free radicals in the suspension which interact with the surface of starch, as confirmed from the peaks of the functional groups of FTIR [18,36,37]. As compared to the traditional technique, SNPs have been proven to be more stable in the ultrasound-assisted hydrolysis process. The size of SNPs is in the range of 50-70 nm with the average particle size (PSD) of 63 nm. Table 3.4 shows the variations in the stability of each SNPs in the suspension. The sonication assists not only in the physical destruction of starch particles but also in

reducing the agglomeration rate of SNPs. Moreover, ultrasound does not have any effect on the crystallinity of SNPs.

Table 3.4 PSD and zeta potential of SNPs.

SNPs synthesized approach	H_2SO_4 concentration (M)	Average size (nm)	Average zeta potential (mV)	Time of hydrolysis (h)
SNP with ultrasound assisted acid hydrolysis	0.5	63	-28.6	0.67 (40 min.)
	1	102.6	-19.8	
	2	207.1	-12.5	
	3	323.4	-8.5	
SNP with conventional acid hydrolysis	3	629.3	-24.4	48

The yield of the synthesized SNPs demonstrates a decreasing trend as the acid concentration increases. The yield (based on dry mass) includes the losses during the process. The maximum yield of 42 % was obtained using an acid concentration of 0.5 M, higher to the earlier reported by Amini et al. [13], where an acid concentration of 3 M was employed. However, the conventional acid hydrolysis shows a yield 16 %, depending on the hydrolysis time and origin of starch with same acid concentration and hydrolysis time.

Acid interaction with starch particles can be divided into three stages. In the first mild stage acid interacts with the outer surface of starch particles. In the second intermediate stage, where the outer surface of the starch slightly distracts, and diffusion of acid to the inner part of the starch could be observed. The acid diffusion to the inner parts of starch granule enhances the hydrolysis rate as the amorphous phase of starch is exposed to acid. The linear chain of the amorphous amylose breaks down faster than that of the crystalline breached structure of amylopectin. In the third stage of hydrolysis, acid interacts with the amylopectin of starch. The destruction of amylopectin induces the gelatinization effect in the starch suspension. Thus, acid interaction with starch particles plays a vital role in the production of starch nanoparticles.

The time of acid interaction with starch particles may have an impact on the particle size reduction of the synthesized SNPs. Subjecting the suspension to high-frequency ultrasound irradiation for 40 min generates $HO^{\bullet}$ radicals and $^{-}OH\text{-}SO_2$ functional group interacts with the surface of SNPs. These radicals and charged ions contribute to the potential for the dispersed SNPs in solution. The minimal potential shows more stability, and all the synthesized SNPs exhibited good stability in the water suspension as observed from their zeta potential values, which is similar to the already reported observations [3,38].

3.5.7.2 Morphologies of the SNPs synthesized with different acid concentration

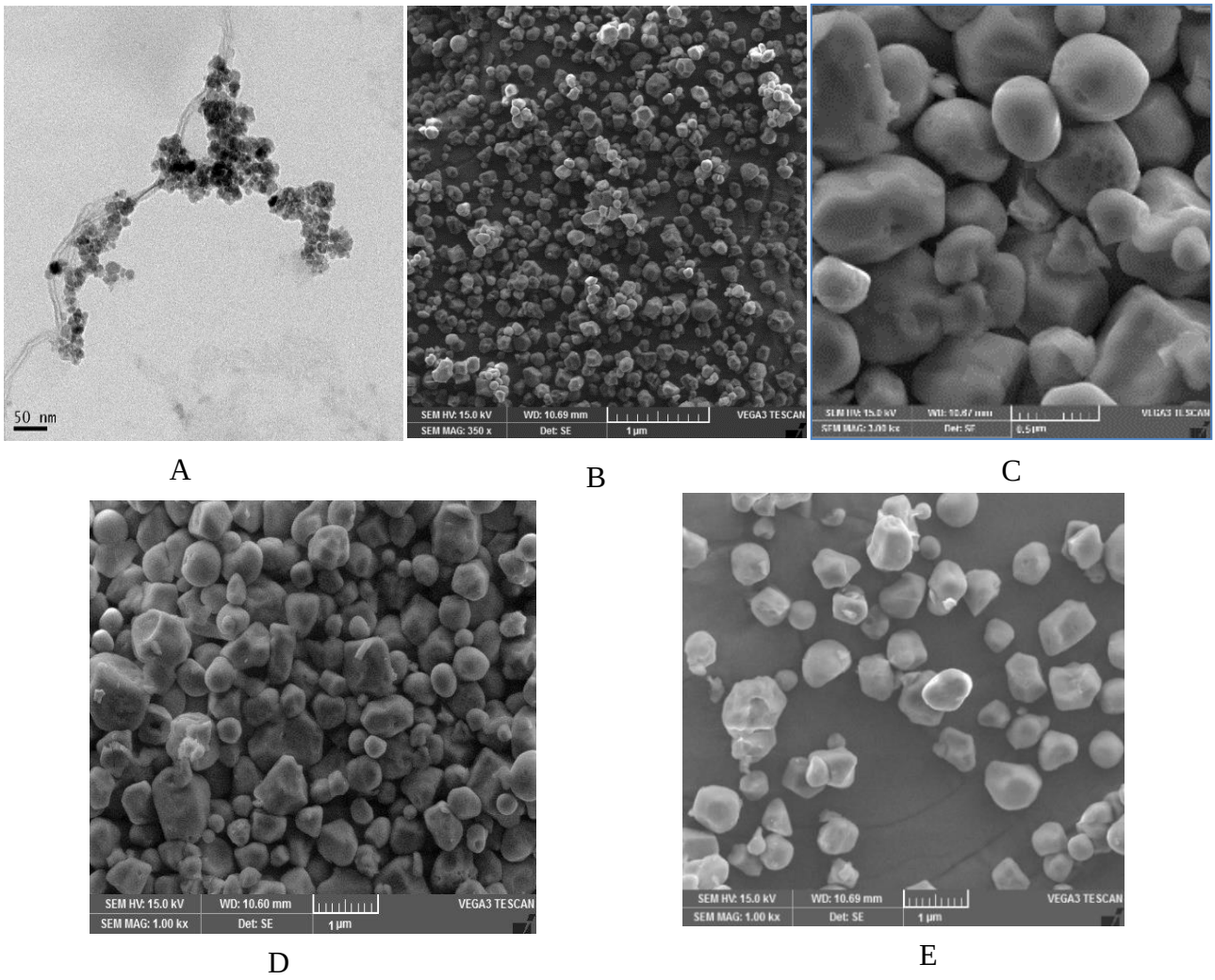

Figure 3.10 (A) TEM of SNPs with 0.5 M H_2SO_4 (B) SEM of SNPs with 1 M H_2SO_4 (C) SEM of SNPs with 2 M H_2SO_4 (D) SEM of SNPs with 3 M H_2SO_4 (E) SEM of SNPs with 3 M H_2SO_4 by the conventional method.

At lower acid concentration, more water molecules dissociate to give $HO^{\bullet}$ radicals, due to which the potential of SNPs with low acid concentration was observed in the range of -21 mV to +21 mV, indicating a more stable structure in the suspension. The effects were observed to reduce as the concentration of acid increases. Zeta potential of SNPs indicates the negative charge on the surface, making them valuable carrier of anions in medical applications. The colloidal phase of all the synthesized SNPs exhibit a narrow size distribution as the polydispersity index of all the suspension is below 0.7. A suspension of colloidal nanoparticles below a polydispersity index of 0.7 with narrow size distribution and better colloidal stability has been reported [39].

TEM and SEM micrographs are shown in Figure 3.10, which reveal the morphologies of the SNPs using different acid concentrations and ultrasound cavitation. The nanosized SNPs were noted through TEM (Figure 3.10A). Figure 3.10 confirms that the SNPs are generally spherical, oval, and irregular in shape, and uniform size distribution is not achieved with this method. A similar morphology of SNPs was already reported [21]. The spherical particles of SNPs with the short-chain arrangement are visible in TEM (Figure 3.10 A) and are in the range of 40-60 nm. This is the smallest range of SNPs found at a lower concentration of acid. The SNPs at higher acid concentration is in the range of 100 to 250 nm, which were found with an increase in the acid concentration. These SNPs were also observed under SEM (Figure 3.10 B, C, D, E). The aggregate in the solution shows a larger size of SNPs. The larger size aggregates of SNPs are found at 3 M acid concentration. The morphological studies of SNPs with SEM and TEM confirm the irregular size distribution associated with this synthesis process. The size of SNPs with 1 M acid concentration varies from the lowest (below 100 nm) and to a maximum (above 200 nm). The randomness in the shape of the starch nanoparticles is due to the impact of cavities during ultrasound propagation as well as acid interaction. Figure 3.10 displays the oval, and spherical shape of SNPs, similar to the earlier reports [13,14,21].

3.5.7.3 X-ray diffraction (XRD) analysis of SNPs

The synthesized SNPs with different acid concentrations possess different crystalline structures. The effect of acid concentration on the crystallinity of SNPs was studied by using XRD diffraction. Figure 3.11 (a, b and c) shows the comparison of the XRD spectrum for the SNPs synthesized using different concentrations of acid. A semi-crystalline nature of SNPs could be noted from this spectrum. The crystallinity of synthesized SNPs was affected by the acid concentration. The XRD spectrum shows a relatively high crystallinity of SNPs with the usage of ultrasound during acid hydrolysis. Ultrasound cavitation leads to the physical damage of native starch particles due to the high impact of cavities. This cavitation effect induces a rise in the rate of hydrolysis. The reduction in the amorphous phase of the native starch particles increases the crystallinity in the synthesized SNPs. The table 3.5 gives an overview of the H-K-L values of the crystalline structure of SNPs with different acid concentrations. The peak intensity and its height for the SNPs synthesized with different acid concentrations show significantly different hkl values. This observation clearly indicates the different acid interactions with the starch granules. The hydroxyl group associated with the different acid concentrations is different, and overall its interaction with the complex covalent bonds of starch was observed to be significantly different.

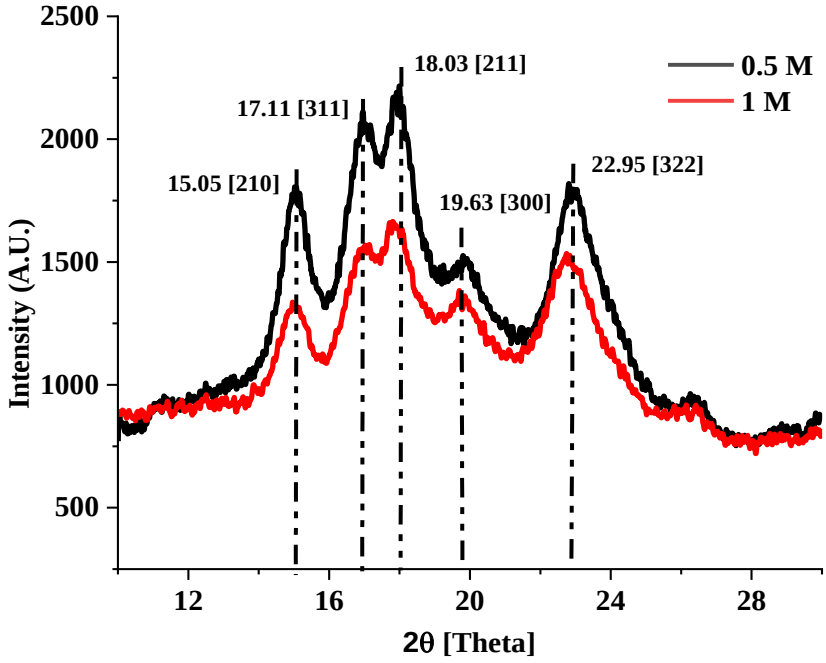

(a) XRD spectra of SNPs synthesized by H_2SO_4 with 0.5 M and 1 M concentrations

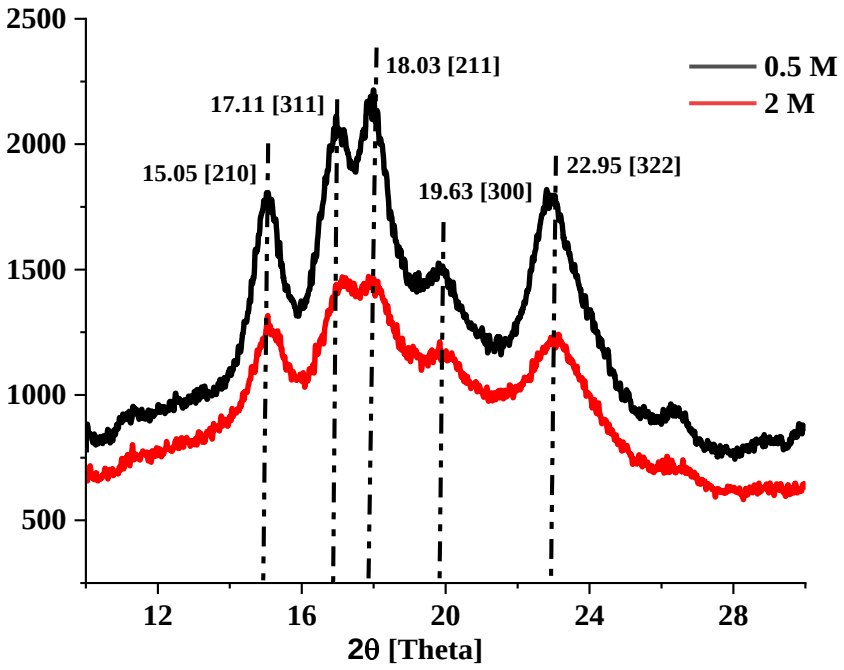

(b) XRD spectra of SNPs synthesized by H_2SO_4 with 0.5 M and 2 M concentrations

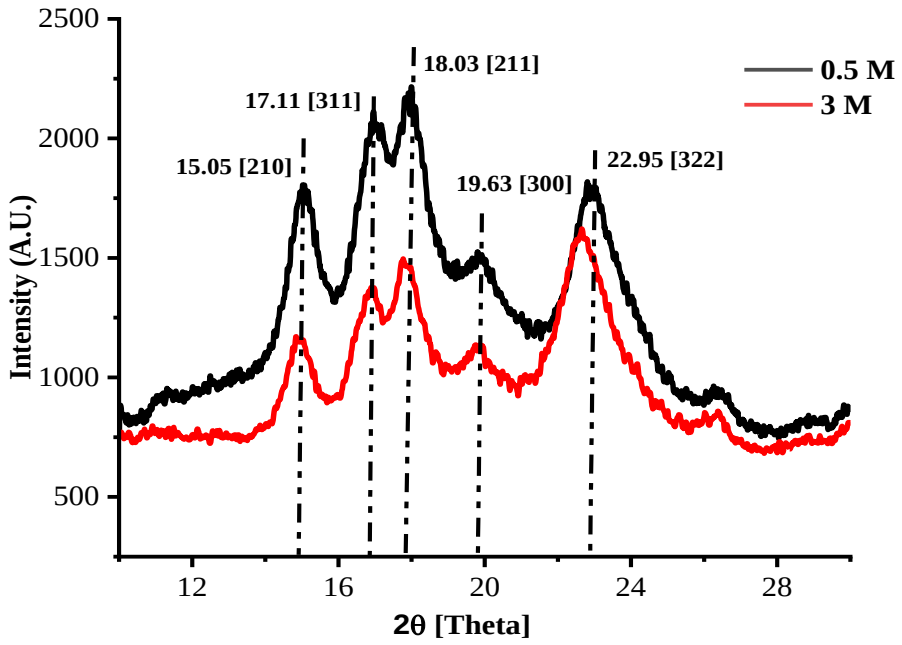

(c) XRD spectra of SNPs synthesized by H_2SO_4 with 0.5 M and 3 M concentrations

Figure 3.11 X-ray diffraction spectra of SNPs synthesized by different concentration of H_2SO_4.

The characteristic A-type diffraction patterns are seen at 15.220°, 17.046°, 17.973°, 19.874°, and 26.400°. These significant peaks show variations with a change in the acid concentration. The critical A-type and V-type spectra of SNPs are unaffected by varying the acid concentration. The crystallinity of SNPs was observed to be higher with the lowest concentration of acid, which could be due to the dominant effect of sonication. It is found in figure 3.11 (a, b, and c) the area under the bi-nodal peaks for the lower acid concentration increases with the peak intensity. The narrower peak distribution is attributed to the extent of the amorphous region's separation from the starch granule. The higher concentration of acid interaction with the starch granules with ultrasound assisted acid hydrolysis shows more amorphous nature rather than the crystalline nature as the XRD diffraction peaks shows wider distribution. This could be because of the Ostwald ripening phenomenon amongst generated nanoparticles at the higher acid concentration. The slight shift at higher concentration in figure 3.11 (c) at peak 22.95 could be because of the random association of SNPs during agglomeration process. The hydrolysis time required for the conventional method was 48 h, whereas, for the ultrasound-assisted acid hydrolysis, it is only 40 min.

Table 3.5 SNPs synthesized with different acid concentration

Acid concentration	Angle value (θ)	h k l value For the SNP	d (Å)	Crystallinity index
0.5 M	9.015	2 1 1	4.922	0.57
1 M	9.015	1 1 0	5.718	0.50
2 M	9.015	1 1 1	5.191	0.48
3 M	9.015	2 2 0	5.321	0.43

The variation in the d-spacing between the crystalline planes indicates the hydrolysis interaction variation. At the lower acid concertation lower d spacing shows the compactness in the crystalline phase of SNPs whereas, at higher concentration the d spacing rise could be due regeneration of crystalline phase during ripening process. The crystallinity index (C_I) of the individual SNPs was calculated, as described earlier. The crystallinity index between 17^o and 18^o for the SNPs was calculated and recorded as 0.57, 0.50, 048, 0.43, and 0.41 with an increase in the acid concentration. As reported, the crystallinity is a quantitative indicator of the crystallinity of particles. It has been found that the crystallinity of SNPs decreases as the acid concentration increases. The combined effect of sonication and free radicals for the hydrolysis of branched amylopectin affects the destruction of the branched structure, reducing the crystallinity of resultant SNPs. As the acid concentration increases the combined effect and hence the resultant crystallinity of SNPs also reduces. The relative crystallinity of SNPs reduces by 20 % as the acid concentration varies from 0.5 M to 1 M. whereas, with a change in the acid concentration from 1 M to 2 M the relative crystallinity reduces only by 10 %. The crystallinity of SNPs is more than native starch by 30 %, as reported earlier [40,41]. The intensity variation amongst the all samples significantly observed, the peak intensity observed to be higher in the case of SNPs with the 0.5 M acid concentration as well as with the 3 M acid hydrolysis in conventional mode. The effect of 48 h of hydrolysis could be seen meaningfully with in the 40 minutes of intensified acid hydrolysis approach. It indicates the hydrolysis extent was higher as compared with the conventional acid hydrolysis.

3.5.7.4 Fourier Transform Infrared Spectroscopy (FTIR) of SNPs

As shown in Figure 3.12, FTIR was recorded to understand the percentage of light transmitted by the SNPs. This transmittance is used to identify the associated functional groups. The significant peak at 1650 cm^{-1} is due to the vibrational bond energy of the hydroxyl group. This peak associated with all SNPs confirms that the hydroxyl functional group is associated with SNPs. The S=O bond vibrations are seen at 1196 cm^{-1}, a characteristics peak confirming the presence of sulphonic group associated with SNPs [42].

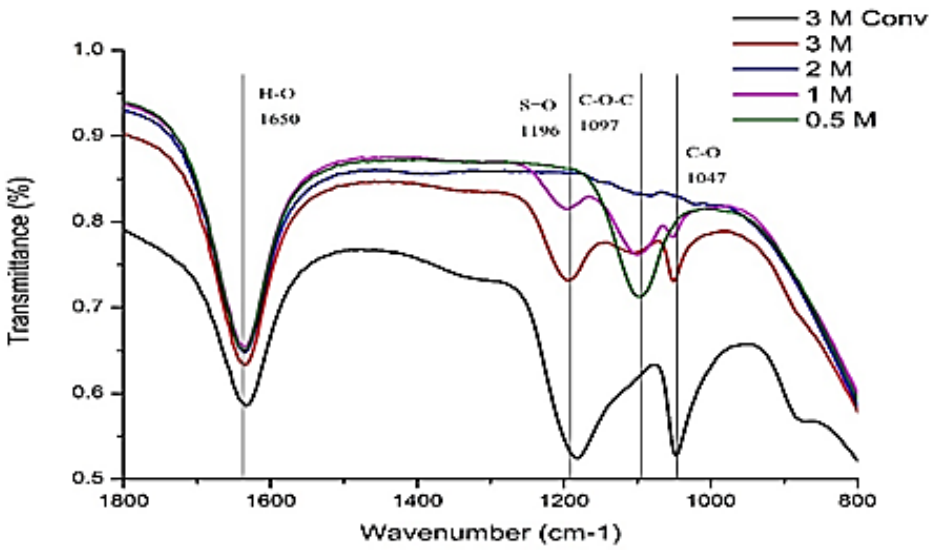

Figure 3.12 Fourier Transform Infrared spectra (FT-IR) of SNP synthesized using H_2SO_4 of different concentrations.

Table 3.6 Specification of Chemical Functional group associated with the SNPs

S	Wavenumber (cm-1)	Chemical bond
1	1650	H-O bond stretching from active sites of starch
2	1196	S-O bond stretching
3	1097	C-O-C bond stretching
4	1047	C-O vibrational energy

The sulphonic functional group is not significantly found at lower acid concentration. The presence of these functional groups also supports the results obtained from zeta potential measurements. The peak at 1097 cm^{-1} endorses the stretching of C-O bond associated with the structure of SNPs. The significant presence of sulphonic functional group associated with SNPs at higher acid concentration is responsible for the higher potential charges on the SNPs. This potential charge induces the agglomeration of nanoparticles, and hence the size of SNPs slightly increases. The hydrolysis rate during the conventional approach was significantly slow, as can be seen from the slight intensity difference for the glucosidic linkages associated with the starch granules. Figure 3.12 shows the significant presence of glycosidic linkages at wavenumber 1097 cm^{-1}. The shock waves developed during the cavitation have a significant physical impact. The acid interaction with the amylose and amylopectin was observed to be higher, due to which the glycosidic linkages were dismissed in the synthesized SNPs.

3.5.8 Effect of ultrasound irradiation exposure time during acid hydrolysis of starch.

The intensification of acid hydrolysis was achieved with cavitation assistance. Cavitation in suspension occurs in both batch and continuous modes. In the batch operations, the ultrasound irradiation was achieved by using the sonication device. As the exposure to ultrasound irradiation varies, the structural size of the synthesized starch nanoparticles also shows significant variations. The results of the study of variation in the ultrasound irradiation time conclude that, as the exposure time increases for the suspension, the overall synthesized particle size reduces at the cost of higher energy consumption.

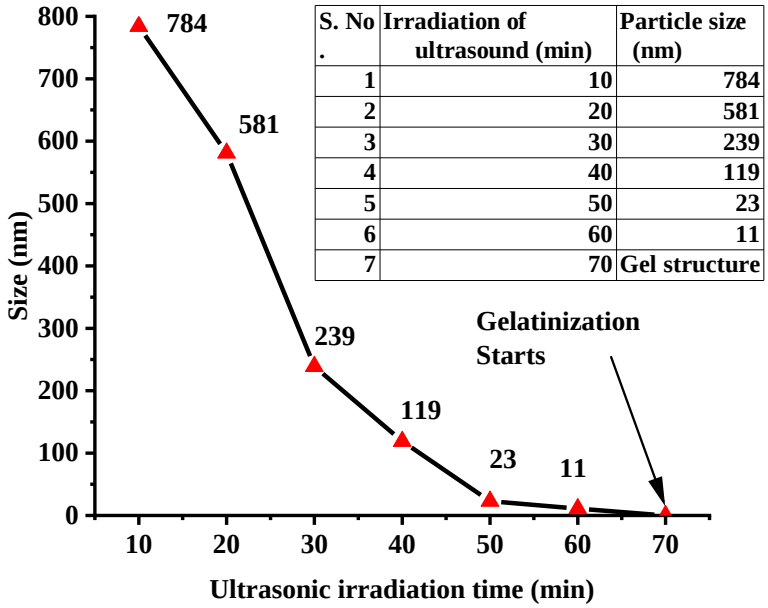

S. No.	Irradiation of ultrasound (min)	Particle size (nm)
1	10	784
2	20	581
3	30	239
4	40	119
5	50	23
6	60	11
7	70	Gel structure

Figure 3.13 Effect of ultrasound irradiation time on the hydrolysis of starch

The starch (corn starch) structure shows complete breaks in the basic structure, and gelatinization occurs at an exposure time of 70 minutes during the acid hydrolysis with an acid concentration of 0.5 M. Figure 3.13 depicts the particle size of starch granules during different ultrasound irradiation exposure times in an intensified acid hydrolysis approach. The mass transfer rate of acid molecules increases due to shock waves developed during the cavitation. These mechanical shock waves also develop the shear in the suspension, which is much stronger for very tiny moments of cavity collapse. These shears develop the cracks in the starch granule, which make way for the impingement of acid inside the starch granule. The hydrolysis rate increases due to the physical destruction of starch granules. The physical destruction of starch granules, or the formation of cracks on their surfaces, is responsible for the randomness in the shape and geometry of the SNPs formed during the intensified acid hydrolysis approach.

Overall, an oval shape was observed, as opposed to the plate-like structure observed in the conventional acid hydrolysis approach.

3.6 Process economics evaluations

The acoustic cavitation assistance to the conventional acid hydrolysis generates the intensification in the process in terms of improved efficiency (yield 42%), and conversion time reduction on the cost of additional energy for the cavitation. The energy required during the cavitation was calculated.

3.6.1 Overall Energy estimate for conversion of starch to nanoparticles.

The equipment specification of probe ultrasonic cavitator used was, power of horn: 200 W, amplitude used during experiments 70 %, operating frequency: 20 kHz, sonication time: 40 min, processing volume: 100 mL.

Running time of sonicator, during which power required = 3 sec., on and 1 sec., off, pulse mode of operation was used, thus in one cycle =4 sec

Cycles in Minutes = 60/4 = 15 cycles

Over all energy demanding seconds in a minutes = 60 – 15 = 45 sec

Average starch particle size before intensified acid hydrolysis treatment: 1000 nm.

Particle size obtained after 40 min sonication: 63 nm

Electrical energy required to run the cavitator for 40 min:

= [electrical power input to the device, J/s x [Utilized power, %] x [Running time of the equipment]

= 200 J/s × 0.7 × [40 min × 45 s] = 252 kJ

Processing volume: 100 mL = 100×10^{-6} m^3

The energy supplied per unit volume of the suspension = Electrical energy supplied/processing volume

= 252 kJ / 100×10^{-6} m^3

= 2.52×10^6 kJ/m^3

Overall particle size variation achieved = Initial size of starch granules – size obtained after intensified acid hydrolysis.

= 1000 – 63 = 937 nm

Total energy consumed per unit of particle size reduction was calculated as = Energy consumed for overall operation / particle size variation achieved

= 2.52×10^6 kJ/m^3 / 937 nm

$= 2.689 \times 10^3$ kJ/(m^3.nm)

The energy required to convert the overall size reduction from 1 µm to 63 nm was 2.689 X 10^3 kJ. However, the observed yield of the SNPs during intensified acid hydrolysis was 42% at minimal acid concentration of 0.5 M.

Thus, overall energy consumed by the process = Energy consumed during the conversion / Yield of the process

$= 2.689 \times 10^3$ kJ / 0.42

$= 6.40 \times 10^3$ kJ

The transducer efficiency and the other equipment performance energy losses associated with the ultrasound sonication was considered as 20 % of overall energy consumed during the operation gives actual energy consumed by the process.

Actual energy consumed by the overall process = $6.40 \times 10^3 / 0.2 = 32 \times 10^3$ kJ

The commercial energy unit prices in India, considered to be 10 Rs/KWh, and 1KWh is approximately 3.6×10^3 kJ.

Thus the energy cost required to convert the per kg of starch granules of average size 1 micron to the nanosize below 100 nm is about

Energy cost per g of starch = [Total energy required / energy per unit cost] x [Cost of energy per unit.]

Energy cost per unit kg of starch = [32×10^3 kJ / 3.6×10^3 kJ] x [10 ₹] = 88.89 ₹ = 1.08 $.

Thus the additional cost of 88.89 ₹ (1.08 $) per unit kg of starch for the overall conversion to nanoscale.

3.6.2 Intensified acid hydrolysis of starch process economics

The conventional acid hydrolysis approach to starch nanoparticle synthesis was intensified with the additional cavitation effect implemented during the actual hydrolysis of starch. The acid mass transfer rate increased due to the cavitation effects of the higher hydrolysis extent. This phenomenon requires additional energy to complete the process and achieve the desired results. The amount of 88.89 Rs (1.08 $.) per kg of starch was additionally required due to the addition of cavitation effect in the conventional acid hydrolysis approach of nanoparticle synthesis. The significant reduction in the process operation time form 48 h to 40 minutes was the major outcome form the intensification of the process. The cost estimation presented here are on the basis of initial sample where the native starch particle size was average about 1 µm. There must be significant effect of initial size initial of native starch granules on the overall energy

requirement for the conversion. The proposed cost only consider the additional energy aspect of the intensified acid hydrolysis approach.

The effectiveness of the present process in comparison with the reported SNP synthesis approaches such as conventional acid hydrolysis, enzymatic conversion, milling, and only sonication approach was discussed in the table 3.7. The overall consideration of advantage and limitation of each process, the present approach gives higher yield on the cost of higher production rate as well as time for the conversion.

Table 3.7 Comparison of the SNP synthesis approaches with the present study

Methods	Highlights	Advantages	Limitation	Ref
Sulphuric acid Hydrolysis	3 M H_2SO_4 concentration 5 days 15.7 % yield for 15 % starch concentration 40 ^oC Operating temperature	No degradation of the granule crystalline areas. Uniform size distribution	Time requirement Higher acid concertation For the downstream operation higher concentration of Base required for the neutralization Chemical residues can be harmful for human health	[10]
Hydrochloric acid Hydrolysis	4.5 M HCl concentration required 5 days Lower yield of 13% for the 15 % starch concertation	Higher stable SNP where synthesized with higher zeta potential. Colloidal dispersion improvement was observed	Time required for the conversion was higher. Higher concentrated acidic and basic solution required Lower yield	[8]
Milling	Greener approach Direct mechanical destruction	affect the physicochemical characteristics of starch	Forming more amorphous nanoparticles. Sharp reduction in nanoparticle crystallinity	[39]

			with increasing milling time.	
Enzymatic hydrolysis	Greener approach, Enzymatic hydrolysis was achieved	Relative crystallinity 55%. Process yield above 85%.	Time and enzyme concentrations may alter the ratio of amorphous and crystalline zones. Production of slower. Limitation on the production rate.	[19]
Sonication	Greener approach Ultrasound irradiation applied to the starch suspension	No chemical required Lower downstream operation Easier Yield 23%	Scale up difficulties 120 minutes continuous irradiation required large amount of energy.	[18]
Present studies	Combination of sonication and acid hydrolysis (hybrid process) Ultrasound irradiation during the acid hydrolysis	Relative crystallinity was 83% yield 42% for 15% Starch concentration	Scale up difficulty Efficient for only pilot scale HC could be used for the higher production in when applied in parallel operations.	-

3.7 Conclusions

The SNPs synthesized through the ultrasound-assisted acid hydrolysis process is a robust method for the synthesis of SNP. The proposed methods require a very short time of about 40 min for the SNPs synthesis, which is much less than the 48 h in the conventional acid hydrolysis process. The crystallinity of the SNP produced with the intensified acid hydrolysis approach is found to be higher at about 86 %, which is nearly twice that of the conventional acid hydrolysis process. The SNPs shows higher thermal resistance than that of native starch; however, both the SNPs synthesized through acid hydrolysis have a significantly similar thermal operating

window. When comparing two SNPs synthesized using different methods, the thermal window of working for SNPs synthesized via acid hydrolysis is lower than that of the conventional acid hydrolysis method. This effect is attributed to intermediate compounds, and the amount of amorphous region was found to be greater in the SNPs synthesized through the conventional acid hydrolysis process. The duration of ultrasound irradiation has a significant impact on the size of the synthesized particle of SNP. As the exposure time increases and the particle size of SNP decreases, the threshold for the process will be the gelatinization condition attained by the starch suspension. The starch structure became disorganized under gelatinization conditions, resulting in a gel-like, thick viscous suspension. The experimental results showed that 70 minutes of exposure time would attain the gelatinization condition for the corn starch.

In the intensified approach to acid hydrolysis of starch, acid concentration plays an important role. From the results, it was observed that an enhancement in the hydrolysis rate of starch particles due to cavitation effects had been found. The highest yield of 42 % was noted at 0.5 M H_2SO_4 within 40 min of sonication time. It is also found that the crystallinity of the synthesized SNPs reduces as the acid concentration increases. The relative crystallinity reduces by 10 % as the acid concentration increases from 0.5 M to 1 M. However, it reduces to 18 % and 23 % when acid concentration changes to 2 M and 3 M, respectively. The conventional acid hydrolysis has the highest interaction of an acid with starch particles, even though the relative crystallinity of SNPs using a 0.5 M acid concentration is 20 %, which is more than the crystallinity obtained through the conventional method. At the lowest acid concentration of 0.5M, SNPs in the size range of 10–20 nm were noted. Also, the size of SNPs slightly increased as the acid concentration increased. The critical peaks of the XRD spectra confirm the synthesis of SNPs. The decreasing pattern of the crystallinity index of SNPs between 17^o and 18^o, as shown in the XRD spectrum, confirms that the crystallinity of SNPs decreases as the acid concentration increases. The overall additional cost required to achieve the intensified effect in the acid hydrolysis for the conversion of micron scale starch granule to starch nanoparticles below 100 nm was 88.89 ₹ (1.08 $.) per g of native starch.

References

[1] M. Ahmad, A. Gani, I. Hassan, Q. Huang, H. Shabbir, Production and characterization of starch nanoparticles by mild alkali hydrolysis and ultra-sonication process, Sci. Rep. 10 (2020) 3533. https://doi.org/10.1038/s41598-020-60380-0.

[2] C. Liu, K. Li, X. Li, M. Zhang, J. Li, Formation and structural evolution of starch nanocrystals from waxy maize starch and waxy potato starch, Int. J. Biol. Macromol. 180 (2021) 625–632. https://doi.org/10.1016/j.ijbiomac.2021.03.115.

[3] H.-Y. Kim, S.S. Park, S.-T. Lim, Preparation, characterization and utilization of starch nanoparticles, Colloids Surfaces B Biointerfaces. 126 (2015) 607–620. https://doi.org/10.1016/j.colsurfb.2014.11.011.

[4] G. Gutierrez, D. Moran, A. Marefati, J. Purhagen, M. Rayner, M. Matos, Synthesis of controlled size starch nanoparticles (SNPs), Carbohydr. Polym. 250 (2020) 116938. https://doi.org/10.1016/j.carbpol.2020.116938.

[5] D. Moran, G. Gutierrez, R. Mendoza, M. Rayner, C. Blanco-Lopez, M. Matos, Synthesis of controlled-size starch nanoparticles and superparamagnetic starch nanocomposites by microemulsion method, Carbohydr. Polym. 299 (2023) 120223. https://doi.org/10.1016/j.carbpol.2022.120223.

[6] Y. Chang, Z. Hu, P. Wang, J. Zhou, Synthesis, characterization, and flocculation performance of cationic starch nanoparticles, Carbohydr. Polym. 269 (2021) 118337. https://doi.org/10.1016/j.carbpol.2021.118337.

[7] X. Tao, L. Zhan, Y. Huang, P. Li, B. Liu, P. Chen, Preparation, characterization and evaluation of capsaicin-loaded indica rice starch nanoparticles, Food Chem. 386 (2022) 132692. https://doi.org/10.1016/j.foodchem.2022.132692.

[8] L. Zhou, X. He, N. Ji, L. Dai, Y. Li, J. Yang, L. Xiong, Q. Sun, Preparation and characterization of waxy maize starch nanoparticles via hydrochloric acid vapor hydrolysis combined with ultrasonication treatment, Ultrason. Sonochem. 80 (2021). https://doi.org/10.1016/j.ultsonch.2021.105836.

[9] V. Singh, S.Z. Ali, Properties of starches modified by different acids, Int. J. Food Prop. 11 (2008) 495–507. https://doi.org/10.1080/10942910802083774.

[10] H.-Y. Kim, J.H. Lee, J.-Y. Kim, W.-J. Lim, S.-T. Lim, Characterization of nanoparticles prepared by acid hydrolysis of various starches, Starch - Starke. 64 (2012) 367–373. https://doi.org/10.1002/star.201100105.

[11] H. Angellier, S. Molina-Boisseau, A. Dufresne, Waxy maize starch nanocrystals as filler

in natural rubber, in: Macromol. Symp., 2006: pp. 132–136. https://doi.org/10.1002/masy.200690009.

[12] V.S. Hakke, U.D. Bagale, S. Boufi, G.U.B. Babu, S.H. Sonawane, Ultrasound Assisted Synthesis of Starch Nanocrystals and It's Applications with Polyurethane for Packaging Film, J. Renew. Mater. 08 (2020) 239–250. https://doi.org/10.32604/jrm.2020.08449.

[13] A. Mohammad Amini, S.M.A. Razavi, A fast and efficient approach to prepare starch nanocrystals from normal corn starch, Food Hydrocoll. 57 (2016) 132–138. https://doi.org/10.1016/j.foodhyd.2016.01.022.

[14] S. Shabana, R. Prasansha, I. Kalinina, I. Potoroko, U. Bagale, S.H. Shirish, Ultrasound assisted acid hydrolyzed structure modification and loading of antioxidants on potato starch nanoparticles, Ultrason. Sonochem. 51 (2019) 444–450. https://doi.org/10.1016/j.ultsonch.2018.07.023.

[15] J. Saeng-on, D. Aht-Ong, Production of starch nanocrystals from agricultural materials using mild acid hydrolysis method: Optimization and characterization, Polym. from Renew. Resour. 8 (2017) 91–116. https://doi.org/10.1177/204124791700800302.

[16] Q. Sun, G. Li, L. Dai, N. Ji, L. Xiong, Green preparation and characterisation of waxy maize starch nanoparticles through enzymolysis and recrystallisation, Food Chem. 162 (2014) 223–228. https://doi.org/10.1016/j.foodchem.2014.04.068.

[17] A.A. Escobar-Puentes, A. García-Gurrola, S. Rincón, A. Zepeda, F. Martínez-Bustos, Effect of amylose/amylopectin content and succinylation on properties of corn starch nanoparticles as encapsulants of anthocyanins, Carbohydr. Polym. 250 (2020). https://doi.org/10.1016/j.carbpol.2020.116972.

[18] S. Bel Haaj, A. Magnin, C. Petrier, S. Boufi, Starch nanoparticles formation via high power ultrasonication, Carbohydr. Polym. 92 (2013) 1625–1632. https://doi.org/10.1016/j.carbpol.2012.11.022.

[19] Y. Hao, Y. Chen, Q. Li, Q. Gao, Preparation of starch nanocrystals through enzymatic pretreatment from waxy potato starch, Carbohydr. Polym. 184 (2018) 171–177. https://doi.org/10.1016/j.carbpol.2017.12.042.

[20] R. Chang, N. Ji, M. Li, L. Qiu, C. Sun, X. Bian, H. Qiu, L. Xiong, Q. Sun, Green preparation and characterization of starch nanoparticles using a vacuum cold plasma process combined with ultrasonication treatment, Ultrason. Sonochem. 58 (2019) 104660. https://doi.org/10.1016/j.ultsonch.2019.104660.

[21] S. Boufi, S. Bel Haaj, A. Magnin, F. Pignon, M. Impéror-Clerc, G. Mortha, Ultrasonic

assisted production of starch nanoparticles: Structural characterization and mechanism of disintegration, Ultrason. Sonochem. 41 (2018) 327–336. https://doi.org/10.1016/j.ultsonch.2017.09.033.

[22] D. Le Corre, J. Bras, A. Dufresne, Starch nanoparticles: A review, Biomacromolecules. 11 (2010) 1139–1153. https://doi.org/10.1021/bm901428y.

[23] H.Y. Kim, D.J. Park, J.Y. Kim, S.T. Lim, Preparation of crystalline starch nanoparticles using cold acid hydrolysis and ultrasonication, Carbohydr. Polym. 98 (2013) 295–301. https://doi.org/10.1016/j.carbpol.2013.05.085.

[24] S. Boufi, H. Kaddami, A. Dufresne, Mechanical performance and transparency of nanocellulose reinforced polymer nanocomposites, Macromol. Mater. Eng. 299 (2014) 560–568. https://doi.org/10.1002/mame.201300232.

[25] B. Momenpoor, F. Danafar, F. Bakhtiari, Size Controlled Preparation of Starch Nanoparticles from Wheat Through Precipitation at Low Temperature, J. Nano Res. 56 (2019) 131–141. https://doi.org/10.4028/www.scientific.net/JNanoR.56.131.

[26] C. Liu, M. Li, N. Ji, J. Liu, L. Xiong, Q. Sun, Morphology and Characteristics of Starch Nanoparticles Self-Assembled via a Rapid Ultrasonication Method for Peppermint Oil Encapsulation, J. Agric. Food Chem. 65 (2017) 8363–8373. https://doi.org/10.1021/acs.jafc.7b02938.

[27] C. Metzger, S. Sanahuja, L. Behrends, S. Sängerlaub, M. Lindner, H. Briesen, Efficiently extracted cellulose nanocrystals and starch nanoparticles and techno-functional properties of films made thereof, Coatings. 8 (2018) 1–19. https://doi.org/10.3390/coatings8040142.

[28] M. Lamanna, N.J. Morales, N.L. García, S. Goyanes, Development and characterization of starch nanoparticles by gamma radiation: Potential application as starch matrix filler, Carbohydr. Polym. 97 (2013) 90–97. https://doi.org/10.1016/j.carbpol.2013.04.081.

[29] F. Fathi, A. Dadkhah, H. Namazi, Characterisation and surface chemical modification of starch nanoparticles with lactid through ring opening polymerisation, Int. J. Nanoparticles. 7 (2014) 37–48. https://doi.org/10.1504/IJNP.2014.062012.

[30] J. Castaño, R. Bouza, S. Rodríguez-Llamazares, C. Carrasco, R.V.B. Vinicius, Processing and characterization of starch-based materials from pehuen seeds (Araucaria araucana (Mol) K. Koch), Carbohydr. Polym. 88 (2012) 299–307. https://doi.org/10.1016/j.carbpol.2011.12.008.

[31] C.A. Kumar Varma, S.G. Panpalia, K.J. Kumar, Physicochemical and release kinetics

of natural and retrograded starch of Indian palmyrah shoots, Int. J. Biol. Macromol. 66 (2014) 33–39. https://doi.org/10.1016/j.ijbiomac.2014.02.018.

[32] G. Zhou, Z. Luo, X. Fu, Preparation and characterization of starch nanoparticles in ionic liquid-in-oil microemulsions system, Ind. Crops Prod. 52 (2014) 105–110. https://doi.org/10.1016/j.indcrop.2013.10.019.

[33] Y. Liu, J. Yu, L. Copeland, S. Wang, S. Wang, Gelatinization behavior of starch: Reflecting beyond the endotherm measured by differential scanning calorimetry, Food Chem. 284 (2019) 53–59. https://doi.org/10.1016/j.foodchem.2019.01.095.

[34] J.-L.L. Putaux, S. Molina-Boisseau, T. Momaur, A. Dufresne, Platelet Nanocrystals Resulting from the Disruption of Waxy Maize Starch Granules by Acid Hydrolysis, Biomacromolecules. 4 (2003) 1198–1202. https://doi.org/10.1021/bm0340422.

[35] B.B. Sanchez de la Concha, E. Agama-Acevedo, M.C. Nunez-Santiago, L.A. Bello-Perez, H.S. Garcia, J. Alvarez-Ramirez, Acid hydrolysis of waxy starches with different granule size for nanocrystal production, J. Cereal Sci. 79 (2018) 193–200. https://doi.org/10.1016/j.jcs.2017.10.018.

[36] Y. Jin, N. Hengl, S. Baup, F. Pignon, N. Gondrexon, M. Sztucki, A. Romdhane, A. Guillet, M. Aurousseau, Ultrasonic assisted cross-flow ultrafiltration of starch and cellulose nanocrystals suspensions: Characterization at multi-scales, Carbohydr. Polym. 124 (2015) 66–76. https://doi.org/10.1016/j.carbpol.2015.01.073.

[37] A.F.K. Minakawa, P.C.S. Faria-Tischer, S. Mali, Simple ultrasound method to obtain starch micro- and nanoparticles from cassava, corn and yam starches, Food Chem. 283 (2019) 11–18. https://doi.org/10.1016/j.foodchem.2019.01.015.

[38] S. Wang, L. Copeland, Effect of Acid Hydrolysis on Starch Structure and Functionality : A Review, Crit. Rev. Food Sci. Nutr. 55 (2015) 1081–1097. https://doi.org/10.1080/10408398.2012.684551.

[39] C.M. Patel, M. Chakraborty, Z.V.P. Murthy, Fast and scalable preparation of starch nanoparticles by stirred media milling, Adv. Powder Technol. 27 (2016) 1287–1294. https://doi.org/10.1016/j.apt.2016.04.021.

[40] H.Y. Kim, J.A. Han, D.K. Kweon, J.D. Park, S.T. Lim, Effect of ultrasonic treatments on nanoparticle preparation of acid-hydrolyzed waxy maize starch, Carbohydr. Polym. 93 (2013) 582–588. https://doi.org/10.1016/j.carbpol.2012.12.050.

[41] D. Le Corre, H. Angellier-Coussy, Preparation and application of starch nanoparticles for nanocomposites: A review, React. Funct. Polym. 85 (2014) 97–120.

https://doi.org/10.1016/j.reactfunctpolym.2014.09.020.

[42] H. Zhang, Y. Tian, Y. Bai, X. Xu, Z. Jin, Structure and properties of maize starch processed with a combination of α-amylase and pullulanase, Int. J. Biol. Macromol. 52 (2013) 38–44. https://doi.org/10.1016/j.ijbiomac.2012.09.030.

Chapter 4. Synthesis of Cellulose nanofibers / nanocrystals (CNF/CNC) with intensified acid hydrolysis process.

4.1 Introduction

The cellulose has great potential to meet the ever-increasing need for eco-friendly, biocompatible materials because to its wide availability, rapid renewal, and low environmental impact. The microstructure of cellulose commercially used in the form of cotton was used since decades in textile industry. The micron and nanoscale cellulose are shows significant aspect ratio which makes them used for many purposes. The nanoscale particles of cellulose was classified in to two major forms as cellulose nanofibers (CNF) and nanocrystals (CNC). The Physical, mechanical, and/or chemical techniques may be used to produce purified cellulose fibers from lignocellulosic sources [1]. We're interested in producing as much pure cellulose as possible, which is a hierarchically structured material with both highly crystalline domains (ordered cellulose chains stabilized by inter and intramolecular hydrogen bonding) and amorphous domains (where the cellulose chains are not hydrogen-bonded to one another) (disordered cellulose chains). When pure cellulose fibers are chemically or physically destroyed, nanosized cellulose, also known as nanocelluloses (NC), cellulose nanocrystals (CNC), or cellulose nanowhiskers (CNC), is created, and it has a variety of desirable properties. These characteristics include a high aspect ratio (10-100), a large specific surface area (250-500 m^2/g), a low density (1.6 g/cm^3), and a high crystallinity (up to 99 %) [2]. High shear homogenization, ball milling, and grinding are just a few of the latest mechanical treatments that have shown efficient in producing nanoscale or micrometer cellulose particles with a high aspect ratio [3]. Evidence shows that a high shear homogenization approach, with a reported average aspect ratio of 52, might be utilized to separate cellulose whiskers from microcrystalline cellulose.

4.1.2 Introduction to Cellulose Nanofibers

The cellulose nanofibers (CNF) are widely synthesized from the wooden source. The cellulose nanoparticles from the wooden source was in the form of fibers. The length of the nanoscale structure was minimum greater than diameter in 100 to 150 fold. In general findings the CNF was reported with the dimensions as about 3 nm in diameter and micron scale in the length [4]. The cellulose nanofibers shows the crystalline and amorphous section as like the starch. The only difference is presence of bi-molecular monomer in the cellulose nanofibers. Because CNF has specific optical, mechanical, and barrier capabilities, it was added to polymer matrices to

improve their mechanical, thermal, and permeability properties. Cotton, kenaf, banana, oil palm, bamboo, wheat, rice, and bagasse are just a handful of the numerous cellulose-rich plants that may be used to make nanofibres. The source is chosen based on the availability of the fibre in the region of application, the chemical components required for the application, and the venture's economic viability [5].

In cellulose nanofibers, there exist crystalline and amorphous domains with diameters of roughly 20 nm and lengths of many micrometers and possesses a high aspect ratio. CNF is primarily produced using a mechanical pressure process that breaks down wood pulp into smaller bits. However, commercial production of CNF is disadvantageous because to the significant energy consumption required by the several runs through the homogenizers [6]. As a consequence, novel energy-efficient chemical and enzymatic hydrolysis procedures before or after homogenization have emerged. In an acid hydrolysis procedure, sulphuric acid is often used to disrupt the glycosidic linkages between the cellulose chains. Because the development of sulphate groups on CNF prevented the particles from aggregating, this approach produced stable colloidal suspensions [7]. However, the large time requirement for the conversion during acid hydrolysis as well as the quantity limitation on enzyme production make the process more difficult to implement on a commercial scale. The additional problem of corrosion during acid hydrolysis also needs a solution [8]. Enzymatic hydrolysis has lately witnessed exponential development as a green alternative to acid hydrolysis due to its capacity to be done in an aqueous media without the use of any toxic chemicals. Enzymatic hydrolysis produces CNF with a higher aspect ratio than acid hydrolysis, which increases the functioning of nanocomposites. Furthermore, enzymatic hydrolysis gave CNF with a significant number of hydroxyl and carboxyl groups, which may be further functionalized using traditional organic chemistry and, on the other hand, promote CNF dispersion into hydrophobic polymers and resins through hydrogen bond formation. Xylanase and cellulase were extensively used as free biocatalysts in the enzymatic hydrolysis of cellulose to create CNF. Cellulase, in particular, is a complex of endoglucanases, exoglucanases, and β-glycosidases that work together to hydrolyze the 1, 4, β-glucosidic bonds in cellulose. However, due to the difficulty in isolating the enzyme from the reaction mixture after use, free-form cellulose can only be used once. Furthermore, the enzyme's catalytic activity must be quenched at the end of the process by boiling to prevent the complete hydrolysis of cellulose to sugars [9].

Yassin et al. [10] demonstrate the separation of cellulose nanofibers (CNF) using cellulose immobilized on inexpensive and simple-to-form polymeric gel disks. These disks are

composed of a carrageenan gel substrate and a hyperbranched polyamidoamine that covalently links to cellulose through a glutaraldehyde spacer. The immobilized cellulose gel disks are easy to separate and reuse, and after six cycles they maintain around 85 % of their initial activity. Effectively digesting cellulose strands, immobilized cellulose produced nanofibers with a diameter of 15-35 nm and a length of several micrometers. Figure 4.1 depicts typical techniques for converting cellulose into CNF. Domini et al. [11] used a sustainable technique to extract CNF from millet husk, which is often regarded as agricultural waste. To eliminate non-cellulosic substances, pre-treatments such as mercerization, steam explosion, and chlorine-free peroxide bleaching were used. CNFs is extracted from bleached millet husk pulp by homogenization followed by acid hydrolysis (5 % oxalic acid). The diameter (10-12 nm) and crystallinity index (58.5 %) of isolated CNFs are typical of type-I cellulose.

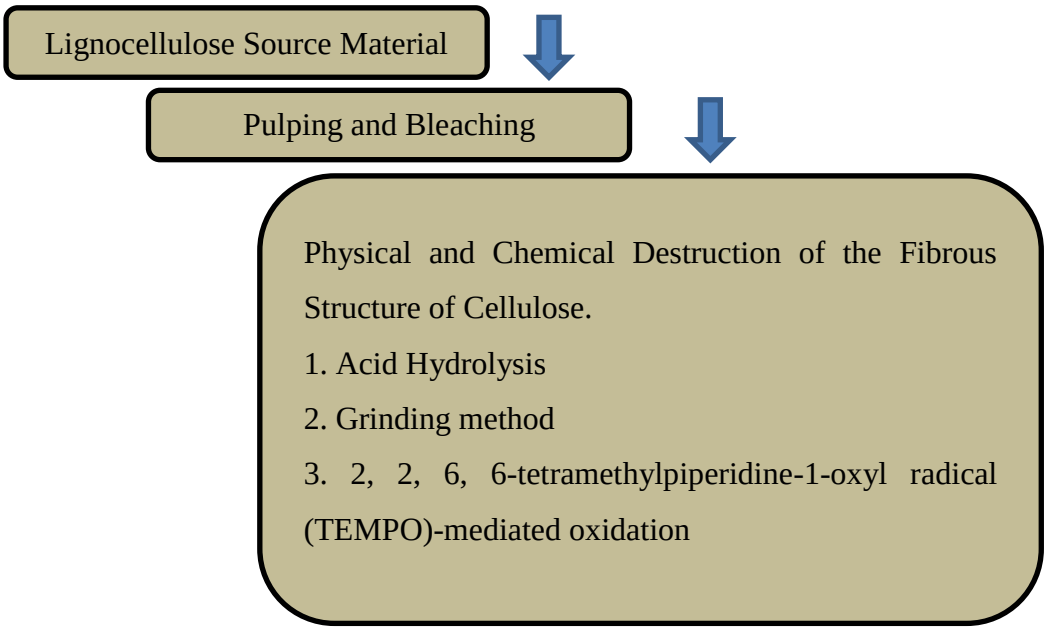

Figure 4.1 Conventional methods for the synthesis of cellulose nanofibers from source cellulose.

Many fields of study have taken note of recent developments in the synthesis of highly crystalline cellulose-based nanoscale biomaterials, specifically cellulose nanocrystals, including bioresource engineering, materials science and engineering, biological and biomedical engineering, and bio-nanotechnology (CNCs). Natural lignocellulosic fibers include pectin, waxes, proteins, lipids, ash, pigments, and extractive compounds in addition to cellulose, hemicelluloses, and lignin, making them one of the most abundant renewable raw materials on the planet [12]. The composition and qualities of lignocellulosic fibers are affected

by the origin, type of fibre, plant species, and growing circumstances of the parent plant. Cotton, flax, hemp, jute, kenaf, sisal, ramie, curaua, pineapple, bamboo, coir, and a variety of other lignocellulosic fibers may be extracted, treated, and functionalized before use in textiles and polymer composites. Significant effort has also been expended in the conversion of lignocellulosic fibers into high-value materials and polymers such as cellulose, lignin, and hemicellulose. Because lignocellulosic fibers have a sophisticated hierarchical structure in which the constituents are connected with each other, fractionating the original fibers into value-added products is difficult [13]. Mechanically degrading the original cellulose macrofibers into nanofibers typically requires many passes through the disintegration equipment, resulting in substantial energy consumption that must be overcome for CNF commercialization to be viable. Two disadvantages that prohibit CNFs from being widely used are their slow dewatering rate in papermaking and the poor compatibility of hydrophilic reinforcers with hydrophobic polymers in polymer composites. The most practical solution is to chemically alter CNFs to reduce the amount of hydrophilic hydroxyl groups.

4.1.3 Introduction to cellulose nanocrystals.

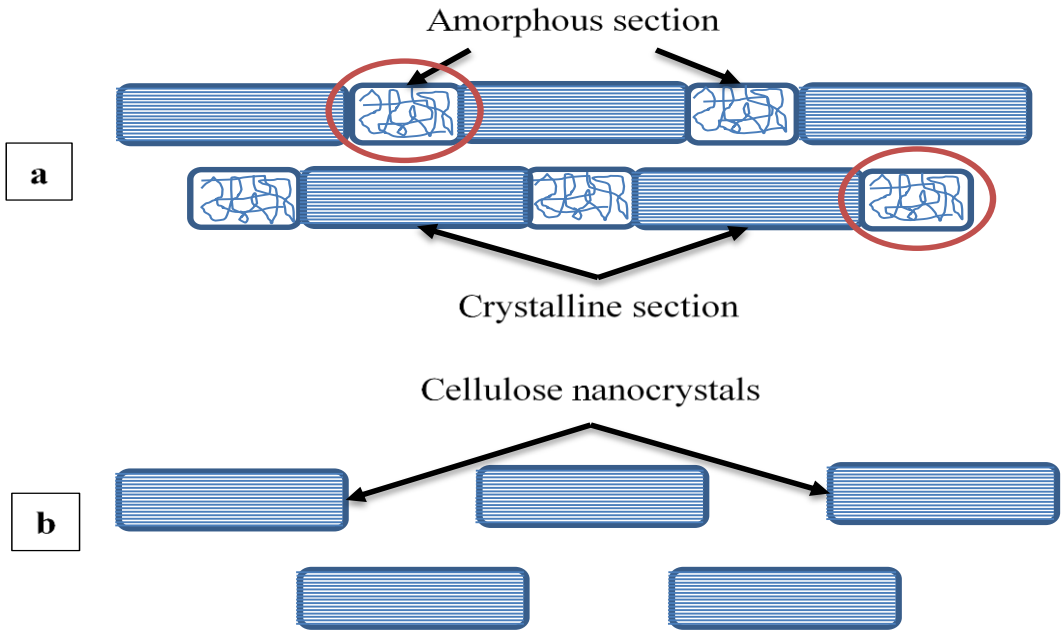

Figure 4.2 a) Schematic representation of orientation of crystalline and amorphous sections of cellulose fibers b) crystalline segments as cellulose nanocrystals after the mechanical/ chemical treatment.

Cellulose nanocrystals (CNC) has a longer rod-like structure and much less flexibility than CNF due to its greater crystallinity. The nanocrystalline particles are formed when amorphous

domains are separated and local crystalline connections between nanofibrils are broken by hydrolysis with extremely concentrated acids. Because the formation of sulphate ester groups results in a negative particle charge, when CNCs are generated using sulphuric acid, the phase stability of the nanocrystalline particles improves. The industrialized approach for CNC synthesis is shown in figure 4.2. By treating cellulose with a highly concentrated acid, nanocrystalline cellulose particles may be formed by shattering amorphous domains during hydrolysis (6-8 M). The end products of full hydrolysis of the amorphous fraction of the cellulose granules are sucrose and glucose, both of which are soluble in the solvent and so may be separated from the cellulose fibers. When cellulose fibers are split, an amorphous region of the cellulose is released, leaving behind small, segmented crystalline sections.

Ogunjobi et al [14] used the siam weed for the synthesis of cellulose nanocrystals. The series of operations such as dewaxing, bleaching, alkali followed by the final acid hydrolysis was employed on the siam weed to extract the CNCs. They reported the 66 % of crystallinity of synthesized CNCs after the complete preparation. Bandera et al. [15] reported that cellulose whiskers obtained by hand had the same reinforcing capacity as whiskers acquired commercially. Due to its ability to form sulphate-modified surface areas, high crystallinity, and great colloidal stability in water, sulphuric acid hydrolysis is the most dependable approach for creating CNC in terms of chemical processing. The hydrolysis parameters (time, temperature, agitation, and acid concentration), as well as the starting cellulose supply, all influence the shape, surface charge density (sulphur content), and properties of acid hydrolyzed-CNC. Onkarappa et al. [16] exploited the natural rubber resource Hevea brasiliensis, for the extraction of cellulose. They reported on the comparative study of conversion of cellulose to cellulose nanocrystals by three different approaches. The acid hydrolysis, ultrasound assistance process, and (2,2,6,6-Tetramethylpiperidin-1-yl)oxyl (TEMPO) oxidation process were used for the synthesis of CNCs. The CNCs synthesized by TEMPO oxidation approach show higher thermal resistance and a larger aspect ratio.

Acid hydrolysis has proven to be the most widely used method for debranching cellulose during natural fibre synthesis. The acid concentration during cellulose breakdown must be optimized since it impacts the pace at which the cellulose's strong hydroxyl glucosidic bonds are broken. However, it is also critical to prevent obtaining complete cellulose hydrolysis, since this would result in the creation of smaller carbon molecules like glucose and below. It has been discovered that a sulphuric acid concentration of 50 wt % is ideal. CNCs, like starch, have a

distinct form after hydrolysis that might be linked to the substance's genesis. Because of the density and concentration of its elements, cellulose's structure gives it resistance to acid contact. The CNCs have been synthesized using organic acids such as ascorbic acid and oxalic acid, as well as powerful inorganic acid systems such as sulphuric acid (H_2SO_4) and hydrochloric acid (HCl). Because the concentrated acid employed is so harmful, toxic, and corrosive, the acid hydrolysis process has severe environmental and equipment corrosion issues. As a result, some scientists have combined H_2O_2 and H_2SO_4 to drastically decrease the acid level to less than 10% by weight. Using Lewis acid as a co-catalyst, the concentration of H_2SO_4 used in the synthesis of CNC was recently lowered from 2 M to 1 M. A heterogeneous solid acid was used alone in the hydrolysis process to produce spherical nanocellulose, which offers various advantages over liquid acids in terms of sustainability, reaction activity, recoverability, and reusability.

Tian et al. [17] reported the synthesis of the CNCs from the potato through the green analytical method. The synthesized nanocellulose is reported to have a granular size of 23.44 nm. During the sulphuric acid hydrolysis approach, the acid interaction with the amorphous region will be higher due to the random arrangement of the monomers, which results in the separation of the amorphous region from the cellulose structure. The resistance offered by the crystalline region is much higher than that of the amorphous region, thus the crystalline region will remain, as in CNCs, due to the source cellulose's structural stability [18]. The sulphate-half ester functional group is associated on the surface of CNCs during acid hydrolysis, specifically with H_2SO_4, due to the intensive effect of higher acid concentration. The surface charged CNCs show substantial stability in the aqueous solution. The hazardous condition that can arise with the use of strong acids in the synthesis process of CNCs, is the major concern as the process operation becomes unsafe. The harsh equipment corrosion, the requirement of huge amounts of water, energy, and the environmental pollution concerns make the process not economically viable as the yield of the process is low. Thus, a substantial, environment friendly, and economical process was required for the replacement for the conventional use of strong acid [19].

The synthesis of cellulose nanostructures in the form of fibers and crystals was discussed in this section. The intensified approach is used in the synthesis process. For the synthesis of cellulose nanofibers (CNF), conventional acid hydrolysis was enhanced with ultrasound assistance. Cellulosic raw cotton is directly utilized for the synthesis of nanofibers [18]. However, the microcrystalline cellulose (MCC) with an initial average size of 8–12 µm was

exploited for the synthesis of cellulose nanocrystals (CNC). The cavitation induces the acidic suspension of MCC with the help of hydrodynamic cavitation. CNC production was in a continuous mode of operation. The confirmation of the synthesized CNF/CNC is achieved with various analytic methods.

4.2 Experimental procedure for the synthesis of cellulose nanoparticles (CNF/CNC)

The two different approaches for the development of cavitation was utilized for the synthesis of individual CNF and CNC. The cavitation developed under the irradiation of high frequency ultrasound (29 kHz) exploited for the development of cavities in the cotton fibers in acidic solution. However, in the second approach hydrodynamic cavitation was used in which the cavitating device (orifice plate) develops the required pressure difference and cavities are generated in the solution. The raw material used for the synthesis of CNF and CNC are different in the study. The raw cotton used as cellulose source with the average PSD about 1000 nm whereas, the microcrystalline cellulose (MCC) was exploited for the synthesis of CNC with intensified acid hydrolysis process.

4.2.1 Materials

The untreated native cellulose fibres were purchased from the local market of the Warangal India. The laboratory-grade sulphuric acid, NaOH were purchased from Merck Pvt Ltd. Two stage centrifugation was used for the separation of hydrolysed starch from the suspension. In all the preparations, deionized (D. I.) water was used.

4.2.2 Synthesis of cellulose nanofibers through ultrasound assisted acid hydrolysis process.

In the experiment, cotton was used as cellulosic raw material for the synthesis of cellulose nanofibers (CNF). The cotton fibers are prewashed with alternate (1N) NaOH solutions and (1M) H_2SO_4 solutions for 10 minutes each for three cycles. The pre-washing with an alternate base and acid solution was for the removal of impurities associated with the surface of cotton fibers. After three cycles of acid-base washing, the cotton is washed with deionized water until the cotton suspension has a pH of 7. These pre-washed cotton fibers were then vacuum dried for 4 hours at 50 ^{o}C. The weight difference before and after the vacuum drying operation was noted for the calculation of surface bound moisture removal. The mass balance of cotton fibers across the vacuum dryer aids in determining the percentage moisture removal from the initial cotton. The sample of cotton is considered for the intensified acid hydrolysis process only when 98 % of the surface-bound moisture has been removed in the vacuum dryer [20]. Based on the

fact that cellulose has a basic hydrocarbon composition fairly identical to that of starch granules, we decided on an acid concentration of 0.5 M to begin off the intensified acid hydrolysis.

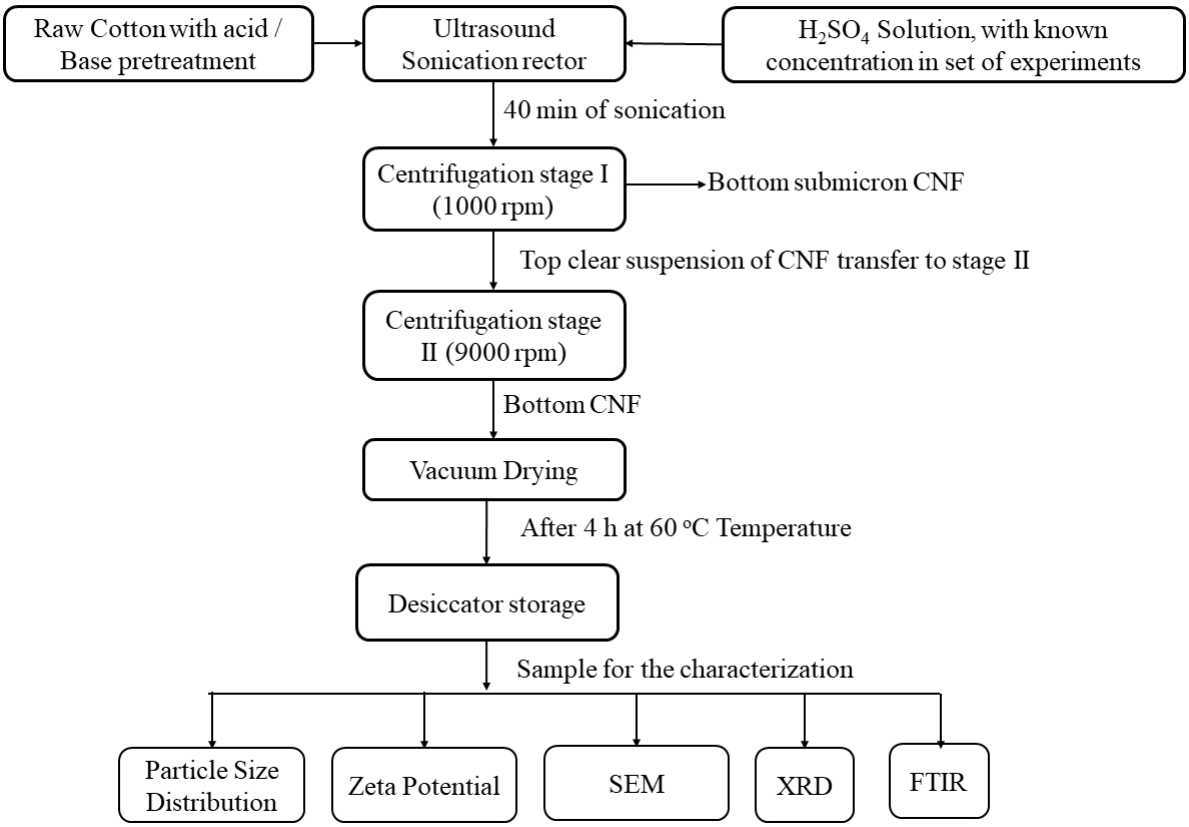

Figure 4.3 Block diagram for the CNF synthesis from cotton fibers

Figure 4.3 illustrates the block diagram for the synthesis process of CNFs from raw cotton. The pre-washed cotton fibers with the weight of 1 g were dispersed in the 100 mL of deionized water with the help of mechanical agitation. The cotton fibres dispersion was sonicated with the help of horn (20 mm diameter) probe sonicator used in glass beaker surround with cooling water (Dakshin Mumbai India 20 kHz,120 W) at 225 V and 0.9 A in pulse mode (3 s on and 2 s off). The flask containing the cotton fibre suspension was subjected to adding a 50-mL solution of 0.5 M H_2SO_4 dropwise during ultrasound irradiation. The temperature was kept steady during the whole process (4 ^oC). The ultrasonic irradiation at 20 kHz was used during the acid hydrolysis of cotton fibres. A 20 mm diameter horn was used in direct contact with 100 ml suspension. Ultrasound was used for the acid hydrolysis of the cotton fibres using H_2SO_4 (0.25 mol L^{-1}). The overall power dissipation to the suspension of starch granules and water was 202 W for 100 mL suspension (power density = 2.02 W cm^{-3}). The ultrasound

irradiation was continued for 40 minutes, after which the suspension in the flask was neutralized by adding 1 N NaOH solution to it until the solution had a pH of 7. The neutralized suspension of cotton was introduced in the centrifugation process.

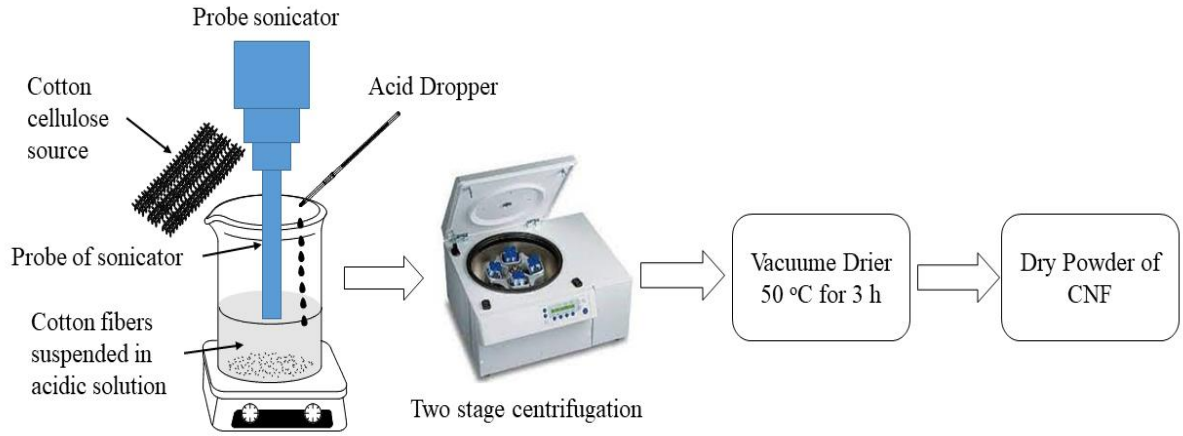

Figure 4.4 Plan for the experimental procedure for the synthesis of cellulose nanofibers.

Two-stage centrifugation was employed for the separation of sub-micron and nanoscale cellulosic masses separately. The first stage of centrifugation was operated at 1000 rpm for 10 minutes, whereas the supernatant from the first stage was again tried in the centrifugation chamber at 9500 rpm for 10 minutes. The thick slurry separated from the centrifugation tube was dried for 4 h at 50 ^{o}C to remove moisture. The dried powder of cellulose nanofibers (CNF) was then stored in the desiccator to avoid moisture and bacterial contamination. Figure 4.4 illustrates the plan of experiments for the synthesis process of CNFs from raw cotton. The overall mass balance was used for the calculation of yield of the process.

4.3 Characterization of cellulose nanofibers (CNF)

4.3.1 Particle size distribution and Zeta Potential of synthesized cellulose nanofibres.

The particle size and zeta potential measurements of CNF were performed at 25 °C using a Malvern nanosizer (Nano ZS, Zen 3600) using the dynamic light scattering (DLS) method. The Measurement range of equipment was 0.3 nm to 150 μm with accuracy of +/- 10 % typical, classical 90° Dynamic Light Scattering (DLS) was exploited.

4.3.2 Surface morphology of cellulose nanofibers (CNF)

The morphological characteristics of the CNFs were revealed using Scanning electron microscopy (SEM). To conduct the SEM analysis of Cotton fibres and CNFs, SEM (TESCAN-

Vega 3 LMU model microscope, Fuveau, France) operating at an accelerating voltage of 30 kV was used.

4.3.3 XRD analysis of Cellulose nanofibers

Bruker D8 advanced X-ray diffractometer was used to collect the XRD spectra of the Cotton fibres and CNFs. Copper Kα (Cu Kα) radiations were used to produce the X-ray with the wavelength of 0.154 nm and were recorded on the 2θ scale, ranging from 5° to 50° with the step size of 0.018 in 2θ

4.4 Acid hydrolysis mechanism of cellulose from cotton to achieve the CNF

The figure 4.5 depicted the experimental procedure and mechanism of intensified acid hydrolysis of cotton fibres due to cavitation assistance. The cavitation developed due to the high frequency sound waves are has three phase life cycle. As the sound waves transferred from the solution, due to the compression and rarefaction repetitive propagation pattern of sound waves the liquid media exposed to the pressure drop. The compression cycle developed sudden compression of liquid molecules (high pressure zone) where as in rarefaction region the liquid media expressions sudden expansion (lower pressure zone). These alternative pressure variation zones at high frequency of sound waves, when lower than the vapour pressure of liquid medium (water) the vapour cavities are developed.

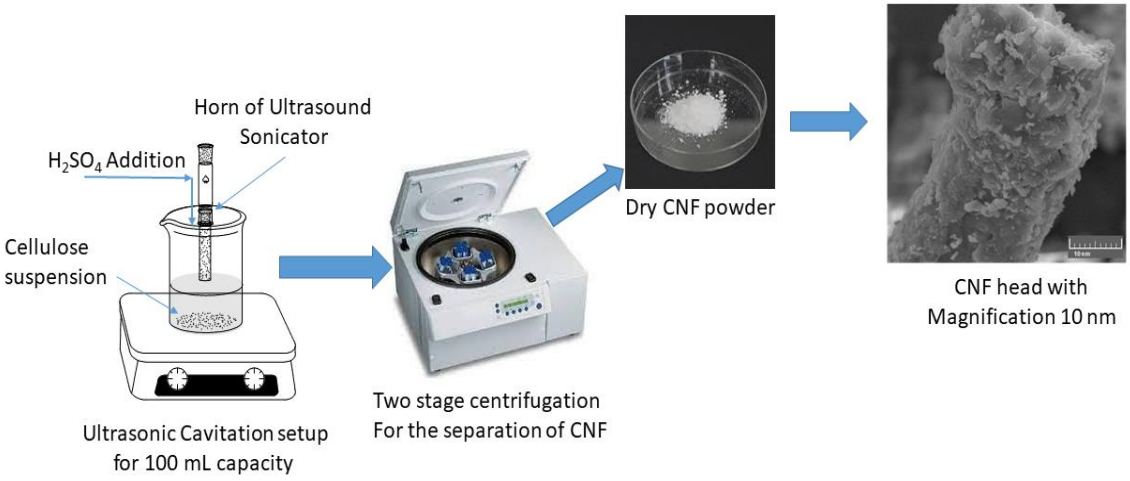

a) Experimental strategy for the synthesis of CNF

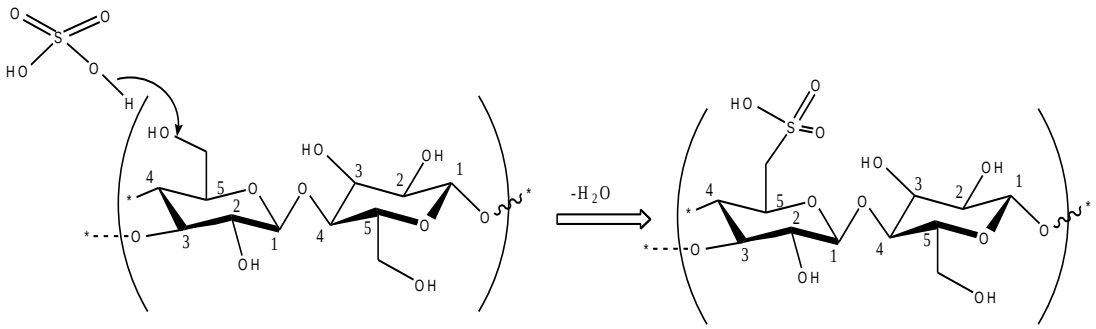

b) Attachment of sulphate groups on the cellulose basic monomer during acid hydrolysis.

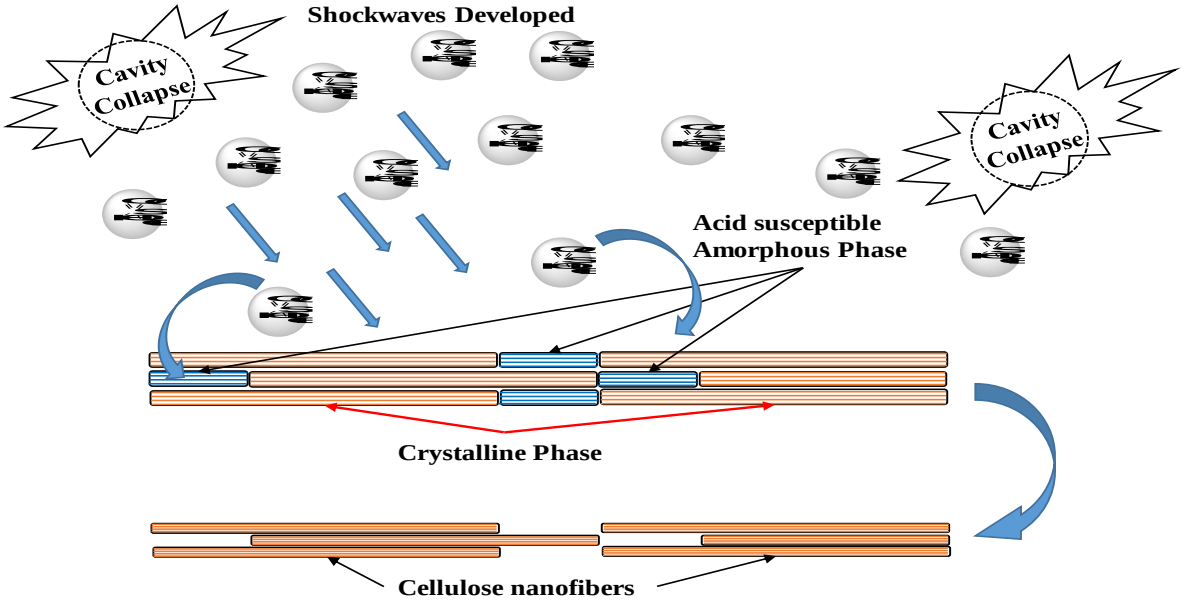

c) Mechanism of cavitation assisted acid hydrolysis approach for the synthesis of CNF from the cotton fibers.

Figure 4.5 Experimental procedure and mechanism of intensive acid hydrolysis due to cavitation assistance.

The vapour phase production were continued till the regional pressure below the vapour pressure of liquid medium. With the virtue of system cycle, when the pressure starts to recover in the second half of rarefaction cycle the cavities or bubbles of vapour exposed with rising pressure environment. The pressure on the bubble gets increases till the starting zone of compression cycle. At these point due to higher external pressure the bubbles starts to collapse with higher intensity. These higher intense collapses of bubble develops the hot zone as mentioned previously [21]. The intense collapse of the cavities induces the higher diffusion of acid molecules on the surface of native cellulose fibrils. The shock waves developed due to the collapse of the cavity at the hot zone are responsible for the physical native cellulose fibrils which provides additional expose of the amorphous phase to the acid molecules. The increases

hydrolysis extent of native cellulose fibrils results in the lower size segments of stable crystalline sections as shown in the Figure 4.5 (c) [22,23].

The conventional acid hydrolysis of cotton fibers required the higher concentration of acid as the cellulose shows compact outer protective layers on its surface of cell. The higher concentration of acid can only able to interact and destruct the outer layer of the cellulosic material. This makes process hazardous and unsafe for the operation. At the higher concentration of acid the corrosion is another problem to be deal with. The 6-8 M H_2SO_4 was commonly used for the synthesis of CNF with the conventional approach. The mechanical agitation in the conventional acid hydrolysis has significant role for the effective interaction of acid with the cotton fibre surfaces. However, the cavitation assistance will be develop higher temperature, pressure (shear) and the shock waves all these are responsible for the enhancement of acid interaction with the amorphous sections of cotton fibres. Thus the acid concentration was not necessary to be higher end. In the present approach we used the acid concentration of 0.5 M for the minimum size of CNC, based on acid concentration optimization during the experiments.

The mass of pellet from the centrifugal tubes was noted in each stage of centrifugation. Following complete water evaporation, the separated nanoscale mass of cellulose was determined. The separation techniques used for the separation of nanofibril structure are significant in the calculation of the exact yield of the process. As the three hydroxyl groups are present in the structure of cellulose polymer granules. The acid hydrolysis generates the two major products in the suspension: micro- and nanocellulose structures. The mechanical impact developed during the collapse of cavities at a higher pressure difference develops the sub-nanodendrons on the surface of CNF, as can be observed in the FESEM image. These dendrons are responsible for the interlocking of nanostructures with each other as well as adjacent microcellulose structures. Centrifugation provides the centrifugal forces required for the separation of such potential interlocking in CNFs. Overall, 39 % of the maximum yield was achievable with an acid concentration of 0.5 M.

4.5 Results and discussion on the synthesis of cellulose nanofibers.

The synthesis of CNF was reported to be achieved with the various methods such as steam explosion treatment [24], high pressure homogenization [25], ultrasonic technique [26], acid-/ alkaline-hydrolysis [27] and enzyme-assisted hydrolysis [28], also the combined processes [29]. These methods can be used to produce different types of CNC [30]. Among these techniques, acid hydrolysis has been widely employed for CNF synthesis because to its low

operating temperatures and strong suspension stability [31]. However, a number of limitations still need to be reconsidered, such as potential degradation of cellulose, time-consuming production process, and low yield. To overcome these drawbacks, some new methods have been developed, such as purely physical method of high-intensity ultrasonication [32], and ultrasonic-assisted chemical method [33]. Ultrasound energy may be delivered to cellulose chains through cavitation, a process that includes the development, expansion, and collapse of cavities in a liquid. As a result, mechanical shearing forces often degrade the linkages that binds cellulose microfibrils together. This facilitates the breakdown of cellulose fibers into nanofibers. The existence of two phases within the cellulose demonstrates the occurrence of different hydrolysis speeds during rapid acid hydrolysis. The cavitation created during ultrasonic irradiation causes increased turbulence, shock waves, and high pressure impact. These considerations explain why the acid in the suspension travels faster. Cavitation increases the force of acid molecules striking the amorphous zone. Cellulose hydrolysis is principally responsible for the breakdown of amorphous areas and local inter-fibrillar linkages. When cellulose samples are ultrasonically treated, fibrils ranging in size from 20 nm to several microns form. The separation strategy is an important step in extracting the CNF from the suspension. The major advantage of the ultrasound assisted acid hydrolysis is that due to shearing action and improved diffusion of acid inside the native cotton there is reduction in particle size of the CNFs. Which is not observed in the conventional acid hydrolysis process.

4.5.1 Particle size distribution and zeta potential of cellulose nanofibers

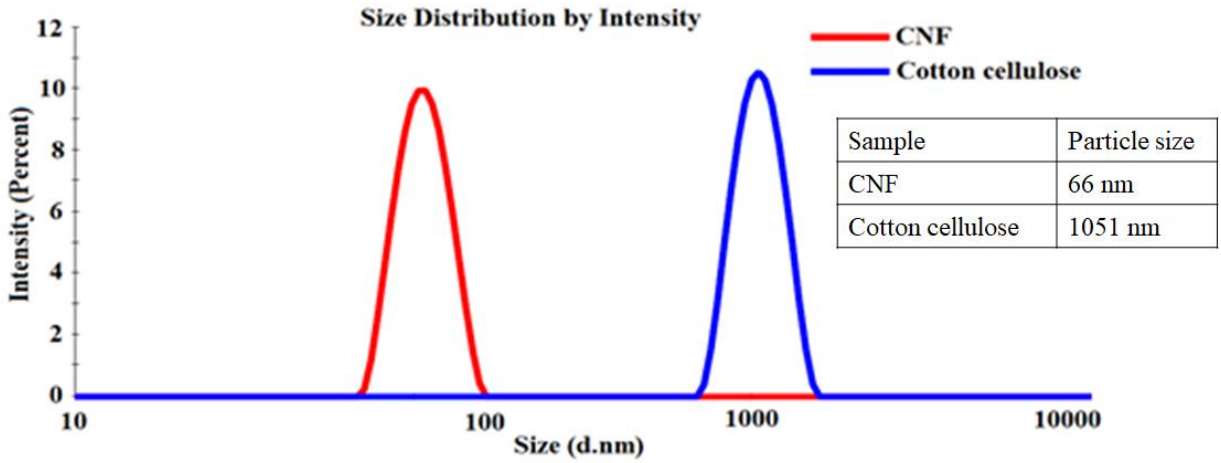

Figure 4.6 Particle size analysis by Malvern nanosizer for the cotton fibres after pre-wash and synthesized CNF during intensified acid hydrolysis.

The Malvern nanosizer was used for the analysis of the hydrodynamic diameter (thickness) of the fibril portion of cotton, which is not hydrolyzed during the acid interaction. Figure 4.6 depicts a particle size analysis of CNF and cotton, and the zeta potential of synthesized CNF in water suspension. The overall particle size distribution of cotton fibers after the ultrasound-assisted acid hydrolysis was observed to be centered on 70 nm (> 100 nm), which clearly indicates the synthesis of nanoscale cotton fibers after the hydrolysis process. The valid point in the claimed results is that we cannot predict which dimension of non-hydrolyzed cotton fibre is at the nanoscale which is similar to CNF reported by El Achaby et al.[34]. The scattered light recorded in the instrument contains no information about the type of particle that causes light deflection. Thus, the present results need to be validated for dimensional analysis with FESEM to understand the morphology of the synthesized fibers.

Table 4.1 Zeta potential analysis of CNF

Sample	Zeta potential	Electrophoretic mobility
CNF	-2.7 mV	-0.000005 cm^2/Vs

The confirmation of one of its dimensions being at the nanoscale could be concluded from the particle size analysis of CNF. The zeta potential value of synthesized CNF was observed a higher (-0.7 mV) extent of stability at the pH value of suspension is 3. The surface charges on CNF are attributed to the H_2SO_4 acid used for the hydrolysis. The unreacted sulfonic functional group is attached to the hydroxyl functional group of glucose. This chemical interaction between two functional groups is not very strong due to the compact structure of the glucose ring in the cellulose [35]. Also, the two glucose rings are connected to each other in the monomer of cellulose in a twisted orientation, which generates the stable intermolecular forces. The hydroxyl functional group at the reducing end of the glucose-based polymer cellulose could only be part of functional group interactions [36,37]. The particle size and zeta potential of synthesized CNF was shows similarity with Farooq et al. [38] they reported the PDS of synthesized CNF ranging from 90-120 nm along with stable zeta potential value of +/- 5.8 with the 3 M H_2SO_4 acid.

4.5.2 Morphological Analysis of the CNF.

The SEM and FESEM were utilized for the analysis of CNF. The first, untreated cotton sample was used to gain a morphological understanding of the cotton structure. The cotton fibers show an overall diameter centered at 1-2 µm. However, the CNF synthesized after the ultrasound

assisted acid hydrolysis shows a fibre diameter of around 10–20 nm with an overall length of not more than 80 nm. Figure 4.7 depicts the observations from scanning electron microscopy (cotton fibers) and field emission scanning electron microscopy (CNF). The cotton fibers in the suspension show a higher tendency for agglomeration and form the thick slurry. The cavitation develops shock waves and a high value of shear stress in the suspension, due to which the physical destruction of cotton fibers could be possible. The collapse of the cavities are random and generates the high pressure (1-100 bar) and temperature about 1500 K. These intensive energy zone when directly exposed to the cotton fibres the possibility of physical destruction is much higher as similarly explain by Boufi et al. [39] for the synthesis of starch nanocrystals. As a result, the acid penetration rate in the cellulose fibers significantly increases [40]. The amorphous region of cotton fibres gets in contact with the acid molecules, and the hydrolysis extent will be greater. The un-hydrolysed cellulose consists of a higher proportion of the crystalline region of cotton, due to which the crystalline nature of CNF is much higher than the initial cotton used for the experiments. Cotton fibre fragmentation is attributed to the physical impact of cavitation shear as shown in Figure 4.7 (b).

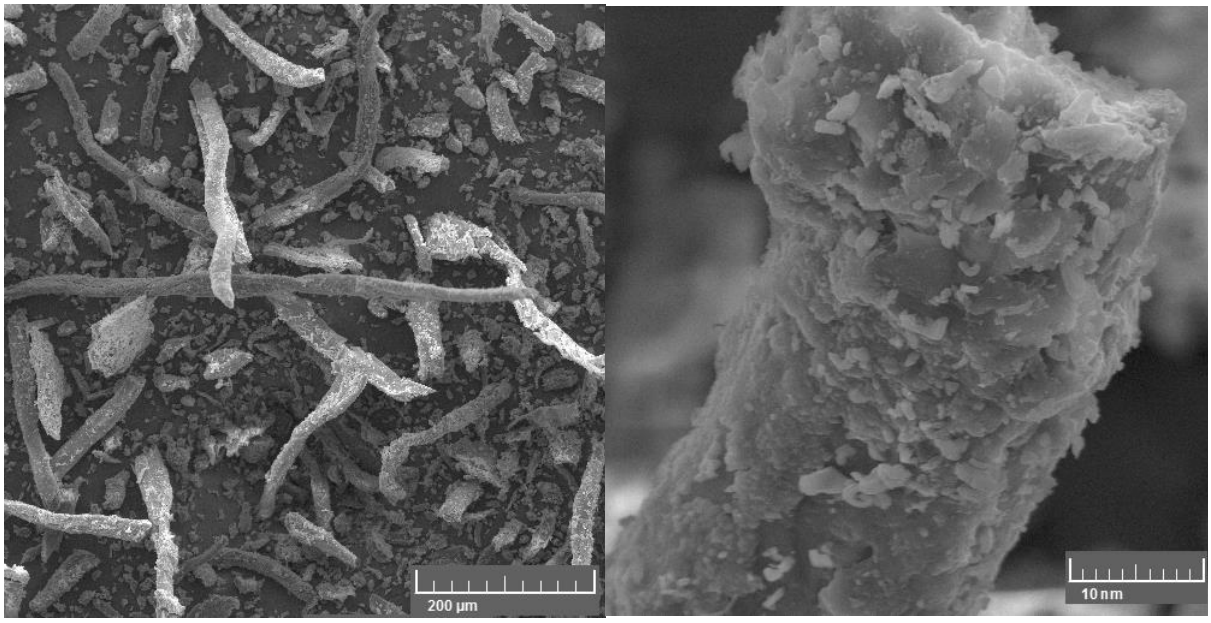

a) Cotton fibres after the acid- base wash b) Cellulose nanofibers

Figure 4.7 The morphology of cotton fibres before and after the intensified acid hydrolysis treatment, a) the cotton fibres after the acid –base pre-wash b) is synthesized fibre of CNF after the treatment.

Because of randomness in the collapse of cavities and cotton fibre potions, the CNF length is not uniform. The shear and impact forces generated during the cavities collapse in the

suspension defibrillate the fibers of the cotton. The combined effects of acid hydrolysis and cavitation induced shear are responsible for the size reduction of cotton fibres. The aspect ratio which is ration of length to the width of CNF was found to be higher after the 40 minutes of US irradiation. The aspect ratio of CNFs synthesized by present method was found to be higher than the CNFs synthesized by Paakko et al. [41]. They proposed the CNFs synthesis with enzymatic hydrolysis of wood source cellulosic material. The similar defibrillate was also observed in the high pressure homogenizer explore by Ferrer et al. [42] The morphology of the CNF in Figure 4.7 (b) shows minor cracks, which commonly form during shock wave exposure. Acid interaction with the cotton fibers will be uniform in all dimensions as cotton fibers are dispersed in the acidic solution. Thus, the cracks in the fibre during the acid hydrolysis could only develop when the fibers allowed the penetration of acid molecules inside their structure.

Another possibility of developing cracks on the surface of cellulose fibril structure is due to the shear force caused during the collapse of cavities. The pressure drop of more than 100 bar will be developed for very small instant of time results in the shear force. These shear forces are responsible for the physical force impact on the surface of cellulose fibers. The physical impact was much strong which results in the formation of cracks or physical damage or segments of cellulose fibrils. The random destruction in the cellulose fibrils structure increases acid penetration to the inner layer of the fibre, this will enhance the exposure of inner layers of cellulose to the acid environment as results of which significant rise in the acid hydrolysis rate. Due to the shock waves generated during the cavitation the mass transfer rate of acid molecules was much higher as a result of which, the acid penetration rate inside the fibers increases, the amorphous region's interaction with the acid will develop the cracks on the CNF surface. Cavitation causes a higher acid hydrolysis rate in both approaches, which is responsible for the direct or indirect particle size reduction of cotton fibers [43,44].

4.5.3 Crystalline structure analysis of CNF with X-ray diffraction (XRD) spectrometry.

The acid interaction of glucose in the cotton fibres is hydrolysis which is a typical approach for deconstructing cellulose complex structure and retrieving its component monosaccharides. The polymerization and crystallinity indices of cotton cellulose are both rather high. Because of this, cotton cellulose is more resistant to acid hydrolysis than other celluloses. Obtaining solid hydrolyzates of soluble sugar oligomers is advantageous after cellulose hydrolysis. The resulting hydrolyzates have a high glucose concentration. The major picks in the Figure 4.8 was observed at 2θ value of 12.35^{o} (101), 20.24^{o} (110), 21.98^{o} (100) and 35.52^{o} (211) are with

their respective plane. The acid hydrolysis of cotton fibres shows reduction in the amorphous region of the cotton, giving rise in the crystallinity of the synthesized CNF. The Debye–Scherrer equation was used for the calculation of crystalline size by using maximum diffraction peak

$$\text{Crystalline Size (D)} = \frac{k\lambda}{\beta \cos\theta} \qquad \text{(Eq 4.1)}$$

Where K is known as the Scherer's constant (K=0.94), λ is the X-ray wavelength (1.54178Å), β is full width at half maximum (FWHM) of the diffraction peak, and θ is the angle of diffraction. The table 4.2 gives the comparative analysis for the CNF and cotton fibers in details.

Table 4.2 Comparative analysis for the CNF and Cotton cellulose

Sample	Highest peak	HKL	Crystalline size (D) by Debye–Scherrer equation	Size by FESEM
CNF	20.24	1 1 0	113 nm	37 nm
Cotton Cellulose	20.24	1 1 0	1784 nm	2000 nm

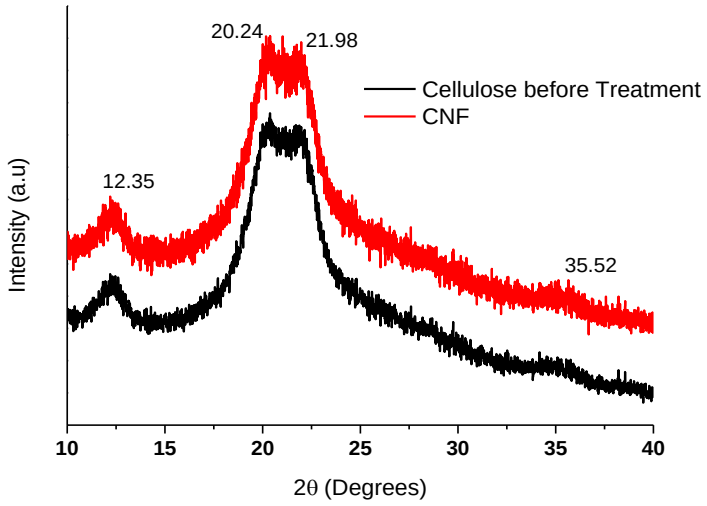

Significant peak	HKL values
12.35º	101
20.24º	110
21.98º	100
35.52º	211

Figure 4.8 XRD spectrum of the Cotton fibres and CNF.

The repeating O-H-O-H bonds form a zigzag pattern between cellulose micro fibril chains in the crystalline lattice. The separation between consecutive layer chains is about 0.450 nm, while the separation between adjacent O1 bonds along the long axis of the molecule is around 0.240 nm. O_3 and O_5 of the following glucosidic residue are separated by 0.331 nm due to intramolecular hydrogen bonding. All these hydroxyl and oxygen linkages interact with the

acid molecules during the hydrolysis reaction. The peak intensity as well the sharpness of peak increases, whereas the peaks becomes narrower in case of CNF spectrum. The amorphous region when the glucosidic based monomer are randomly packed with each other shows lower resistance for the penetration and destruction of oxygen based linkages. This interaction generally produces sugar from the glucose structure and get dissolved in the solution. Since, the compact structure of glucosidic monomers in the crystalline region offers higher resistance for the acid penetration due to which the crystalline structure remains as it is after short exposure of acid suspension. The reduced amorphous region from the cotton induces the rise in the crystalline value of synthesized CNF.

4.5.4 Fourier transform infrared spectroscopy (FTIR) spectra analysis of CNF

Figure 4.9 illustrates the FTIR spectra of hydrolyzed cotton before and after intensified acid hydrolysis using Fourier transform infrared spectroscopy. The cotton cellulose has its unique characteristics of a peak around 3350 cm^{-1} for the –OH linkage stretching and for the $–CH_2$ linkage it is in the region of 2890 cm^{-1}. Both the peak are significantly found in cotton fibres as well in CNF spectrum. The peak at 1550 cm^{-1} is due to the attachment of additional functional groups -OH, such as a sulfonic functional group from acid, to the hydrolyse the cotton fibers during the treatment. The bending vibrations of -CH are characterized by a peak at 1380 cm^{-1}. The peak at the 1372 cm^{-1} is attributed for $-CH_2$ bending, whereas for -CH bending it is at 1333 cm^{-1} and for $-CH_2$ bending it is at 1317 cm^{-1}. C-O-C-O-C bond stretching in cellulose is shown by peaks at 1063, 1058, 1112, 1030, and 896 cm^{-1}.

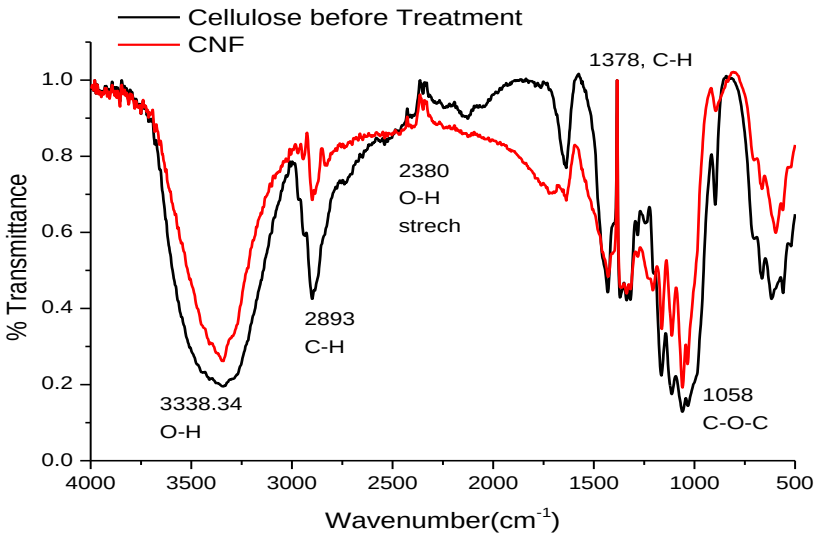

Peak (cm^{-1})	Chemical Functional groups
3300-3600	Vibration linkages between O-H from water
2893	C-H bond stretching
2380	Hydroxyl bond stretching O-H
1378	Attributed to C-H bond stretching
1100, 1096, 1058	All are attributed to the vibrational stretching of C-O-C linkages.

Figure 4.9 Fourier transform infrared spectroscopy spectrum of the Cotton and CNF.

The interamolecular hydrogen linkages between C-H and O-H has major influence on the FTIR spectrum. The acid interaction during hydrolysis of cotton fibres affect on the hydrogen bonds. The hydroxyl functional group from sulfonic functional group develops additional attractive and repulsive forces in the crystalline structure of remaining CNF. The peak shifted towards the higher wavelength which is attributed additional hydroxyl bond interaction developed in the CNF during acid hydrolysis [45].

4.6 Synthesis of cellulose nanocrystals (CNC) through the continuous hydrodynamic cavitation assisted acid hydrolysis process.

Microcrystalline cellulose (MCC) was used for the synthesis of cellulose nanocrystals (CNC). During these experiments, the cavitation induction approach in the MCC suspended acidic solution is different. Instead of ultrasound irradiation, cavities are developed by using the hydrodynamic cavitation approach. The major advantage of the hydrodynamic cavitation approach is that the process is continuous, and acid recovery even at lower concentrations could be possible with minimal losses. The greener approach can handle large quantities of MCC for the production of CNC with effectively higher yields and within optimal time requirements.

4.6.1 Materials

The microcrystalline cellulose (MCC) purchased from Sigma-Aldrich Chemicals Private Limited, Bangalore, India. The white powder of MCC has pH in the range of 5-7.5 for 100 g/L aqueous solution, as mentioned on the MSDS of MCC. The MCC was as it is used for the all set of experimentations without any pre-wash as like cotton cellulose. The deionised water was used for preparation of all the solution required in the experiments.

4.6.2. Experimental procedure for synthesis of CNC.

The intensive cavitation effect was created using hydrodynamic cavitation during the acid hydrolysis of microcrystalline cellulose (MCC). The 0.25 M sulphuric acid solution (5 L) was prepared using deionized water and placed in the storage tank of the hydrodynamic cavitation

setup. The 50 g of MCC were added to the storage tank and well mixed with the mechanical agitation. In the cavitation processes, an effective pressure difference of about 7 bars across the orifice plate was required. The plunger pump, coupled with the motor of 1.5 H.P. power output, was exploited for the circulation of MCC-acidic suspension through the setup. The treated fluid was again collected in the storage tank. The suspension of MCC recycled through cavitation was set up for 15 minutes of operation. The treated suspension taken out was neutralized with the 0.5 N NaOH solution till it had a pH of 7. CNC was separated from MCC suspension using a two-stage centrifugation method. In the first stage, sub-micron-sized cellulose and un-hydrolyzed MCC were separated, whereas in the second stage, CNC slurry was extracted from the centrifugation operation. The vacuum drying process was employed at 50 ^{o}C temperature for 6 h to get dry white powder of the CNC. The dry powder of CNC was stored in the desiccator to avoid moisture and bacterial contamination. Figure 4.10 shows the overall block diagram for the synthesis process of CNC.

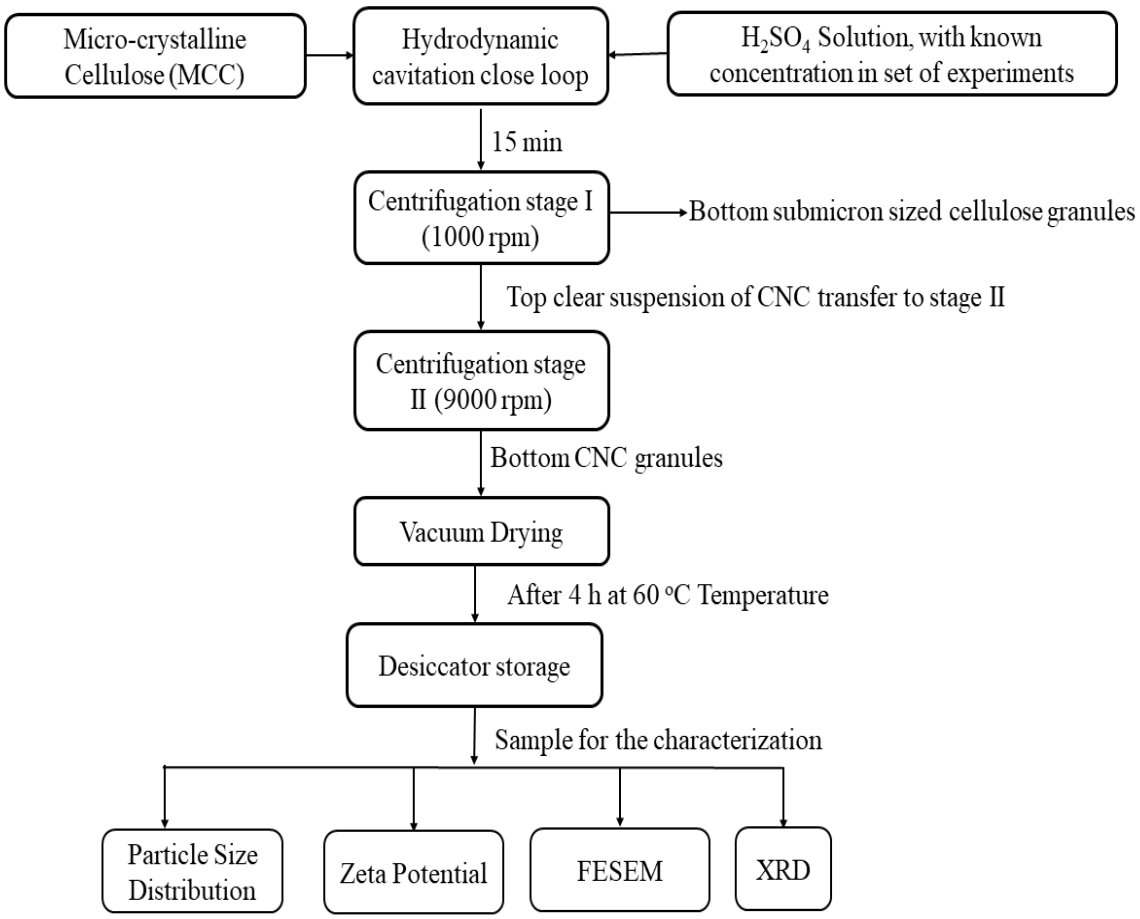

Figure 4.10 Block diagram for the CNC synthesis from MCC

4.6.3 Mechanism of the hydrodynamic cavitation acid hydrolysis of MCC.

At the higher speed of circulation, the suspension experiences the sudden contraction of the flow area at the orifice plate. The pressure of the suspension before and after the orifice plate was measured using the pressure gauges. The sudden contraction of the flow area induces higher pressure across the orifice; this high pressure crosses the vapour pressure of water, and the water molecules start to change phase from the liquid phase to the vapour phase. The vapour was initially generated, and later, as the pressure increased, the quantity of vapour-phase water molecules increased; this is called the nucleation of cavities or bubbles. The three stages of cavities in hydrodynamic cavitation are nucleation, nurture, and collapse. As the flow reclaims the flow area, the pressure drop in the fluid is restored i.e. $\Delta P \rightarrow 0$. In this condition, the hydraulic pressure on the external surface of the bubble increases by a significantly large amount. Simultaneously, the vapor phase of water molecules starts to condense. The hydraulic pressure at the bubble's boundary creates momentum in the imaginary boundary between the vapour phase and the liquid phase towards the bubble's centre, while the vapour phase water molecules begin to condensate, i.e., they begin to travel towards the imaginary phase boundary. The two oppositely developed bodies develop kinetic momentum when they collide, which produces a large amount of energy in terms of heat as well as pressure (shear). For a very short period of time, the energy released in the form of heat raises the local temperature of the collapsed point of bubble from 1000 K to 5000 K and the pressure to 100 to 500 bars. The collapse of the cavities in the fluid generates a hot zone, which generates H^+ and ^-OH radicals from the splitting of water molecules. These radicals are highly active compounds, which provide additional driving force for the hydrolysis.

The process of MCC acid hydrolysis in the cavitation was more or less similar to that developed using high-frequency ultrasound irradiation. At the hot zone during the collapse of the bubble, shock waves are generated due to the conversion of a huge amount of kinetic energy into heat and pressure. This conversion was completed in a very short period of time, roughly within 10^6 of a second. As a result, the molecules that undergo the phase change from vapor to liquid generate a large number of shock waves (shear). When shock waves strike MCC surfaces near the hot region, the outer layer of cellulose cells is broken or fragmented. This fragmentation can be observed in the form of dendrons or cracks on the surface of the CNC morphology. The fragmentation point allows acid molecules to enter the cellulose compact structure, resulting in an increase in hydrolysis extent and rate in the MCC. Another theory says that the shock waves that develop when the cavities collapse induce a higher rate of acid molecular mass transfer in

the suspension. When the mass transfer rate of acid molecules in the suspension goes up, the rate at which cellulose particles are broken down by water goes up. Hydrolysis preferentially hydrolyzes disordered amorphous domains and local inter fibrillar contacts of cellulose, while stable crystallites remain intact and may be separated as cellulose nanocrystals particles.

We were able to calculate the yield of the CNC created by the current technique by using the total mass balance of the MCC. The initial mass of the MCC was recorded at the commencement of the experiment. The acidic solvent containing the cellulose nanoparticles was neutralized after the operation was completed by adding NaOH solution until the suspension reached pH 7. The cellulose nanoparticles were separated from the remainder of the fluid using two rounds of centrifugation. The first stage spins at 1000 revolutions per minute to separate micron and submicron cellulose nanoparticles, while the second stage spins at 9500 revolutions per minute for 10 minutes to eliminate any leftover supernatant. It is possible to obtain faster dispersion of nanocellulosic crystals. Separated cellulose nanocrystals (CNC) slurries (pellets) are dried in a nitrogen-purged vacuum drier. Based on the measured dry powder weight, the following calculation was used to calculate CNC yield:

$$Yield = \frac{W_2}{(W_0 - W_1)}\ x\ 100 \qquad \text{(Eq. 4.2)}$$

Where W_o is the initial mass (weight) of the MCC used for the experiment, W_1 is the weight of slurry (pellet) in the first stage of centrifugation, and W_2 is the weight of slurry (pellet) in the second stage of centrifugation.

4.6.3.1 Optimization of process parameters: acid concentration, and inlet pressure during hydrodynamic cavitation.

The SS material was used with the motor power of 1.5 H.P. was employed for the maximum capacity of 7 lit acidic suspension of MCC. The line size used to build the experimental set up was used as nominal bore 2 inch (DN 50 mm), Outside Diameter 60.3 mm, Schedule 10, wall thickness 2.8 mm and internal diameter of 54.7 mm. The cavitation effect was achieved through the sudden contraction of flow using an orifice plate. For the present study, an orifice plate with a hole at the centre of the plate and a 2 mm diameter was employed. The orifice opening to inner diameter of the pipe was 1:25 was constant throughout the experiments. The operation took an average of 15 minutes.

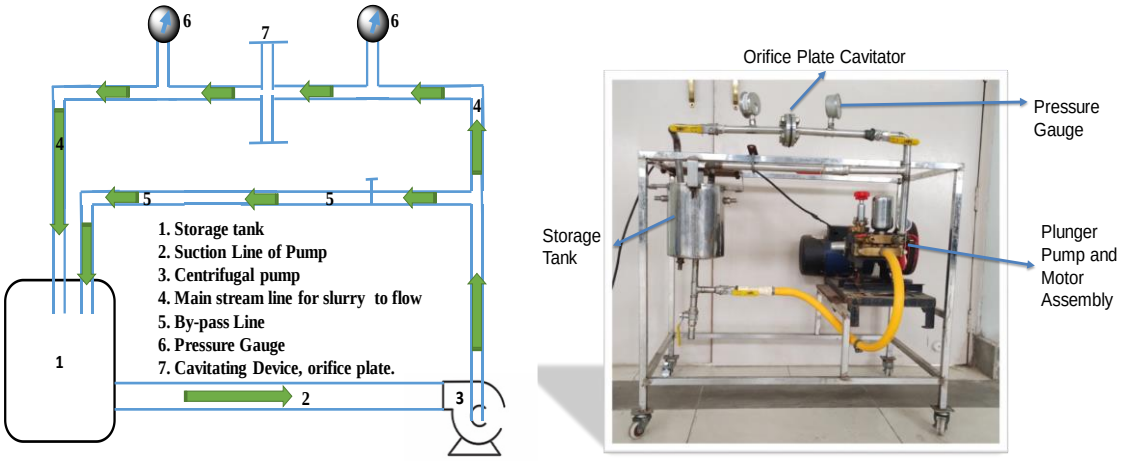

a b

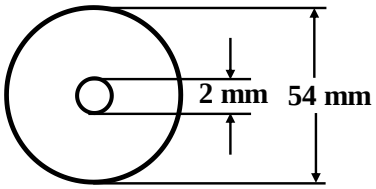

c

Figure 4.11 a) Schematic diagram for the hydrodynamic cavitation assisted acid hydrolysis of cellulose granules, and b) hydrodynamic cavitation setup image for the synthesis of CNC through the intensified acid hydrolysis process. c) Schematic diagram of orifice cavitation device.

The cavitation condition after the orifice plate is significantly affected by the inlet pressure. The variation in the inlet pressure of fluid entering the orifice was achieved with the bypass line operation valve. The inlet pressure for the present study varied from 5 kg/cm^2 to 10 kg/cm^2, with an increment of 1 kg/cm^2 with each individual experiment. CNC's corresponding particle size was recorded. During the experiments, the acid concentration was varied from 0.25 to 1.75 with increments of 0.25 (M). The individual experiments were carried out for the understanding of effects of parameter variation. The Figure 4.11 illustrate the hydrodynamic cavitation setup for the synthesis of CNC from MCC. The cavitator used in the present setup was orifice plate as mentioned with the 1 mm orifice opening at the centre of the plate.

4.7 Characterization of cellulose nanocrystals (CNC).

4.7.1 Particle Size distribution

The particle size and zeta potential measurements of CNC were performed at 25 °C using a Malvern nanosizer (Nano ZS, Zen 3600) using the dynamic light scattering (DLS) method. SNP was added to deionized water and homogenized by bath sonication until an obscuration

of less than 10 % was recorded. The refractometer was used to measure the exact value of refractive index for the starch suspension. The value of the refractive index is 1.33, which is almost similar to the deionized water used in the experimentation with the zeta sizer. The particle size distribution for the SNPs was reported using the DLS principle.

4.7.2 Field emission scanning electron microscope (FESEM) analysis for synthesized CNC.

To investigate the morphology of synthesized CNC, a field-emission scanning electron microscope (FE-SEM; Gemini 500; M/s Carl Zeiss) was utilized. The samples were preserved using silica gel and kept at 25 degrees Celsius. The CNC samples were then dried completely before being mounted on bronze rods and coated with gold plasma. The samples were seen using a 20 kV accelerating voltage.

4.7.3 X-ray powder diffraction (XRD) analysis for synthesized CNC.

The preconditioning of MCC and CNC samples with different acid concentrations were achieved in a desiccator at 35 % relative humidity for 3 days. The preconditioning is necessary to maintain the moisture content in the sample before XRD analysis. The Bruker D8 advanced diffractometer using copper Kα (Cu Kα) radiation (λ =0.154 nm) was used. The intensity was recorded in the range of 10^{o}- 30^{o} (2θ) with a step size of 0.018 and measuring for 2 sec per point. The XRD spectra were also utilized to estimate and quantify the extent of the relative crystallinity of the synthesized CNCs.

4.8 Result and discussion on the analysis of CNC

The microcrystalline cellulose (MCC) shows the significant resistance for the acid solution impingement due to lower concentration of amorphous section as compared with the native cellulose source. The continuous process of cavitation was employed for the intensification of acid hydrolysis. After the neutralization of suspension, the CNC was separated with the help of centrifugation operation. The dry powder of white colour CNC was produced after the vacuum drying of CNC slurry from the centrifugation operation. The synthesis of CNC was confirmed with the PSD, XRD, and FESEM.

4.8.1 Particle size distribution (PSD) of cellulose nanocrystals.

The particle size of CNC separated from the slurry was analysed with the Malvern nanosizer (Nano ZS, Zen 3600). The Figure 4.12 gives the recorded observations from the Malvern nanosizer (Nano ZS, Zen 3600) instrument. From the Figure 4.12, the size of CNC produced was centered at around 60-70 nm crystal size. The produced size of CNC were also validated

with the morphological analysis using FESEM imaging process. The sharp peak and narrower scattering of the PSD indicates the uniform size distribution in the synthesized CNC.

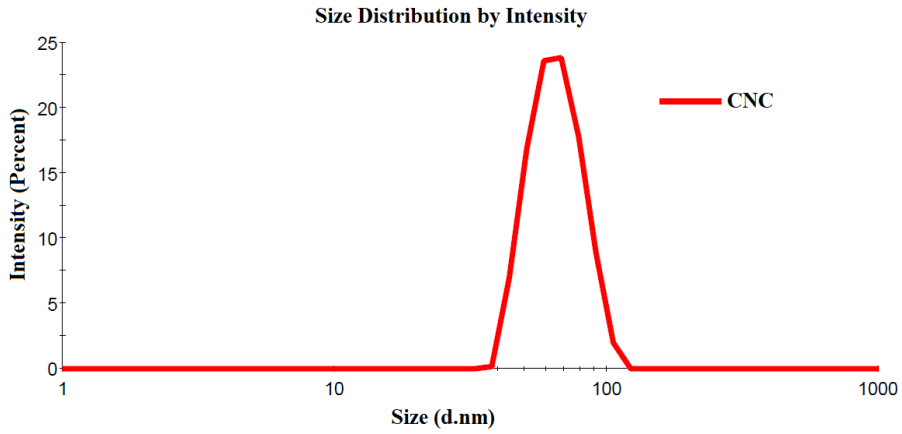

Sample	Size (d. nm)	St. Dev (d. nm)
CNC	66	12.55

Figure 4.12 Particle size distribution of CNC synthesized during intensified acid hydrolysis.

4.8.2 Morphology of synthesized CNC granule.

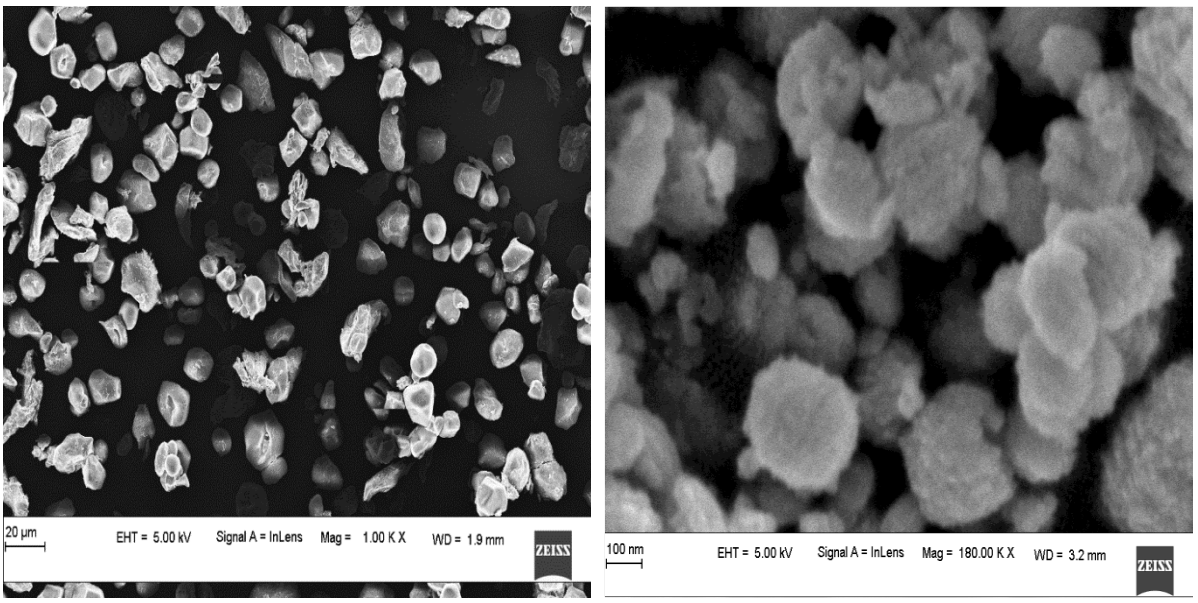

a) FESEM image for the MCC b) FESEM image for the CNC synthesized

Figure 4.13 FESEM images of a) microcrystalline cellulose (MCC) and b) synthesized cellulose nanocrystals (CNC).

Figure 4.13 shows the morphological difference between the MCC and produced CNC using same instrument. The FESEM shows the morphological difference between the cellulose before and after treatment. Figure 4.13 (a) with the magnification 20 µm indicates the MCC crystalline size before the intensified acid hydrolysis process was around 7-10 µm which is much higher than that of produced size of CNC. The produced CNC are shows uniform particle size which is average 70 nm. The particle size analysis by zeta sizer also confirms the same. The overall particle size distribution in the Figure 4.13 (b) can be observed uniform which is attributed to the hydrodynamic cavitation effect. In the process of particle size reduction of cellulose the polydispersity of the cellulose structure in the form of amorphous and crystalline region gets reduces and which is results in uniform distribution of the particle size in the produced CNC. The shear stress developed during the cavitation process along with the fluid flowing friction are responsible for the increasing acid hydrolysis rate of MCC.

4.8.3 XRD spectrum of synthesized CNC.

The compactness of the structure of the cellulose and its nano forms are analysed using x-ray diffraction spectrum is depicted in the Figure 4.14. The presence of CNC characteristic peaks demonstrated that CNCs were effectively synthesized from MCC using continuous hydrodynamic cavitation assisted acid hydrolysis approach [15]. In the Figure 4.14, the comparative analysis of CNC synthesized with different acid concentration is also included. The XRD spectrum of shows significant peaks at 14.65 º, 16.74º, 22.58º, and 28.92º attributed to the structural planes (100), (110), (200), and (004) respectively for the cellulosic structure. During the acid hydrolysis reduction of glucosidic monomers in bi-molar monomer of cellulose was occurred and converted in the sugar. The rise in the crystallinity was observed during the hydrolysis of MCC attributed to the reduction in the amorphous region of cellulose. The overall operation of hydrodynamic cavitation was run for the 15 min, which significantly helpful for the desired particle size from micronscale to nanoscale. The intensity rise was significantly found with hydrolysed MCC (CNC) as compared with non-hydrolysed MCC. The acid concentration shows a drastic effect on the crystallinity of synthesized CNC. With increasing acid concentrations, the specific peaks at 14.65º and 28.92 º vanish.

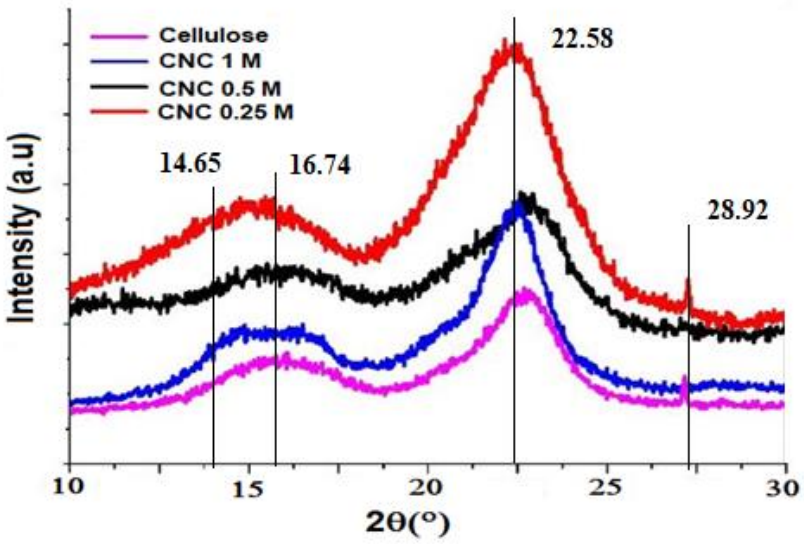

Peak	hkl values
14.65	1 0 0
16.74	1 1 0
22.58	2 0 0
28.92	0 0 4

Figure 4.14 XRD diffraction of CNC with different acid concentration.

This indicates the particles get a higher extent of hydrolysis, during the process at higher acid concentrations. During the separation process, the CNCs with higher acid concentrations agglomerate. The agglomerated CNC shows higher amorphous regions, and the results observed in Figure 4.12 support the same [46,47]. The peak height and width at the lower acid concentration (0.25 M) are much lower as compared with the higher acid concentrations of 0.5 and 1 M. The fact that the peak width at 22.58^{o} is wider for 1 M acid concentration indicates that there is a predominant amorphous region during agglomeration, resulting in final separated CNCs.

The large and diffuse XRD pattern of MCC revealed that the bulk of the material was amorphous. Some peaks faded when the acid concentration was increased from 30 to 50 % due to the complete separation of the cotton's amorphous component [3]. Ultrasound and acid hydrolysis worked together to accelerate the oxidation of cellulose and disintegrate its amorphous structure. The XRD patterns clearly show the amorphous-to-crystalline transition caused by the combination of ultrasonic and acid treatment [48]. On the molecular level, ultrasound created shear, which opened up the cellulose's glycosidic bonds to the acid [49]. The crystallite size of CNCs was determined using Scherrer's formula [50].

$$D = \frac{K\lambda}{\beta \cos\theta} \qquad \text{(Eq. 4.3)}$$

where, D is crystallite size, K is Braggs constant, β is Full width at half maximum, θ is Bragg angle, and λ is X-ray wavelength. The d-spacing of the crystals was 3.93 Å, as determined by

the (200) peak. The table 4.3 gives the overview on the calculated value of crystalline size by Scherrer's formula and PSD of synthesized CNC, at the highest peak of 22.58^{o},(200)

Table 4.3 Comparative analysis of CNC size synthesized with different acid concentration.

Sample	Highest peak	H k l	Crystalline size (D) by Debye–Scherrer equation	Size by PSD
0.25 M CNC	22.58	2 0 0	113 nm	63 nm
0.5 M CNC	22.58	2 0 0	178 nm	117 nm
1 M CNC	22.58	2 0 0	206 nm	160 nm
MCC	22.58	2 0 0	983 nm	1007 nm

As, the acid concentration increases the peak 22.58^{o} spreading increases in the spectrum significantly indicates that the crystallinity of the CNC generated at lower acid concentration is higher than that of CNC with higher concentration. The similar trend results were reported by the Th. I. Shaheen and Hossam E. Emam [23]. The cavitation assistance during the acid hydrolysis significantly alters the hydrolysis rate due to intense localized hot zone and shear force. The glyosidic linkages in the cellulose are exposed with the acid and water interaction which results in the formation of crystalline sediments as CNC. The extent of hydrolysis at lower acid concentration can be at lower end with lower native charge value. At higher acid concentration the extent of hydrolysis is much higher and initially synthesized CNC could be of lower size even below 10 nm. However, the generated charge on the CNC could be higher as extent of hydrolysis is more, more number of sulphate and hydroxyl function groups are associated with the surface of CNC. Thus, accordingly Ostwald phenomenon the CNC particles get closure and linkages are formed between the nanophase cellulose. These linkages are in the virtue of higher charge thus, the resultant CNC shows higher amorphous extent rather than compact crystalline structure. This could be a reason for the lower crystallinity of the synthesized CNC in the intensified acid hydrolysis. Following that, we spent some time comparing our CNCs to the existing literature, marveling at how much clearer ours were [51]. The crystallinity of the CNCs synthesized from MCC is 81.23 %, which is greater than the 72.22 % observed in previous work [52].

4.8.4 Effect of acid concentration variation on the particle size of synthesized CNC

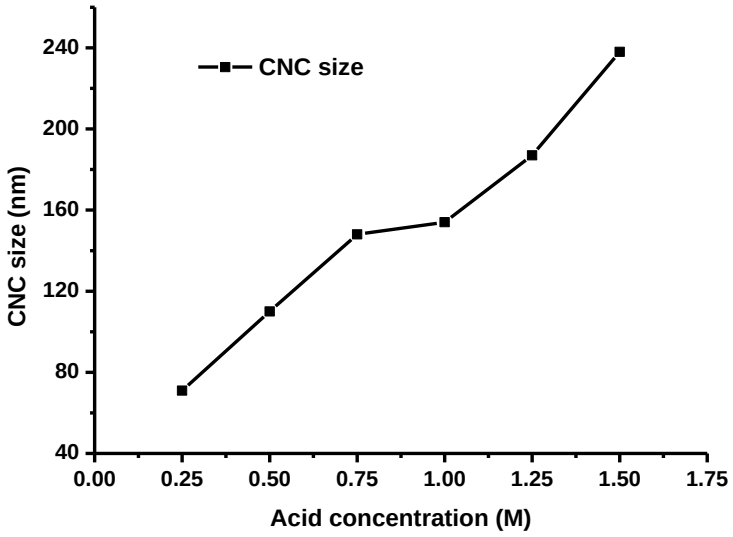

Figure 4.15 Effect of acid concentration on the particle size of CNC synthesized during hydrodynamic cavitation assisted acid hydrolysis.

The acid concentration significantly effects on the synthesized particle size of CNC. The higher acid concentration associated hydrodynamic cavitation, induces the higher concentration of radicals available for the hydrolysis of cellulose. The Two major theories are responsible for the higher particle size of CNC or lower hydrolysis rate of MCC. One of the theory suggest that as the concentration of acid molecules increases in the water, the density of the mixture significantly higher. These higher density liquids has higher value of vapour pressure thus the window between the stable pressure of the liquid and the vapour pressure of liquid medium is reduces. This reduced window of pressure difference reduces the intensity of cavities collapses. Due to which the diffusion rate and impingement rate of acid molecule inside the MCC structure is lower. This will reduces the overall hydrolysis rate effects in higher particle size of CNC produced. However at lower acid concentration density difference is insignificant [53,54]. The second theory, suggest that the CNC produced at the higher acid concentration possess higher surface charges which induces the higher rate of agglomeration of produced CNC particles. Thus the effective particle size of CNC at their acid concentration is higher as compared with the lower acid concentration. The experimental observations from Figure 4.15 revels that, at the lower acid concertation particle size synthesized CNC shows in lower extent whereas the acid concertation increase the particle size shows increasing pattern [55,56].

4.8.5 Effect of Inlet pressure during hydrodynamic cavitation process on the particle size of the synthesized CNCs

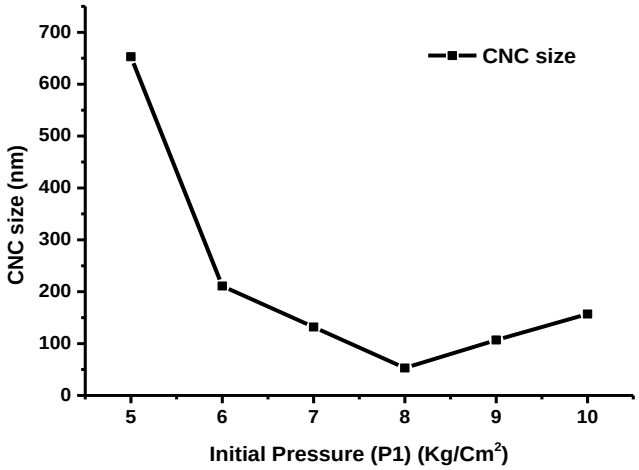

Figure 4.16 Effect of initial pressure before orifice in the hydrodynamic cavitation on the particle size of CNC synthesized during acid hydrolysis.

The inlet pressure has significant effects on the particle size of the CNC synthesized during the hydrodynamic cavitation based acid hydrolysis. In the process of the hydrodynamic cavitation inlet pressure of has directly effects on the cavitation number. When the liquid pass through the orifice the kinetic energy of the liquid increases dramatically within the fraction of time on the cost of pressure. The downstream of the orifice experiences significant turbulent flow pattern. The liquid jet was observed with the formation of vena-contractra could also call as throat of the design [57]. In the downstream of the orifice the pressure starts to regenerate after the vena-contractra rapidly. The moment when the pressure goes down below vapour pressure of the liquid medium, the bubbles are developed. The nucleation, nurture and collapse all three life cycle phases of the bubble takes very short time when system regain its pressure from lower value to the average value [58]. The cavities when collapse develops the hot zone, and produces the chance for higher inception rate of acid molecules inside the compact structure of MCC. The diffusion rate of acid inside the MCC structure increases the rate of hydrolysis significantly as compared with the conventional acid hydrolysis. The cavities are developed till the system recover its original pressure p_o which is depends on the initial pressure value before the orifice entrance. Thus, the significant inlet pressure p_1 value of were studied for its effect on the particle size [59].

The most fundamental non-dimensional parameter, which is since then utilized for evaluating the potential for cavitation, the cavitation number (σ)

$$\sigma = \frac{p_0 - p_v}{\rho v^2/_2} \quad \text{(Eq. 4.4)}$$

p_0 is fully recovered downstream pressure, where as p_v is the vapour pressure of the liquid medium. The υ is the critical velocity at the vena-contractra (Throat) of the jet. The cavitation number could also be increase with the presence of dissolved gasses as well as impurities in the liquid media. For every flow, cavitating or not, can be attributed by a cavitation number, its value again depends on the geometry, fluid, fluid temperature and the velocity of the flow. The conditions at which cavitation first appears can also be

$$\sigma_i = -C_{p,min} \quad \text{(Eq. 4.5)}$$

Where index i stands for "incipient" and σi for incipient cavitation number. $C_{p,min}$ is minimum cavitation number required for the effective cavitation impact to develop the hot zone in the flowing fluid. Lowering the value of cavitation number results in the appearance of cavitation or the increase of extent of already present cavitation [60].

Figure 4.16 depicted the observation of variation of inlet pressure on the particle size of CNC. It was been observed that the particle size of CNC significantly decreases as the inlet pressure of the system increases until it reach to threshold of 8 kg/cm^2 after which the particle size of CNC get increases. The fall in the particle size of CNC was attributed to enhanced acid hydrolysis rate due to shear developed during the cavitation. However, after the threshold inlet pressure, the shock waves develops the lower particle size again but it could be possible that the produced CNC at lower size are unstable in the acid-water mixture and present pH value. The rise in the particle size attributed to Ostwald ripening phenomenon [61]. The instability of CNC at higher pressure, possibly creates the agglomeration in the synthesized lower sized CNC, which produces the larger size CNC in the final observations. Thus, the optimum condition for the inlet pressure of the system could be consider for threshold value of 8 kg/cm^2.

4.9 Economical aspect of the intensified acid hydrolysis approach for the synthesis of CNF and CNC.

4.9.1 Energy economics of hydrodynamic cavitation approach for the CNC synthesis.

Energy requirements to achieve the size reduction in the cellulose. The CNF synthesized using the ultrasound assisted aid hydrolysis process, however the CNC are produced with the hydrodynamic cavitation assisted acid hydrolysis process. The comparative analysis of both the methods was discussed below.

Power required for the hydrodynamic cavitation

Motor consuming power per sec = 1.5 H.P. X 0.746 = 1.119 KW

The motor was working for the 15 min = 1.119 KJ/S x 60 sec x 15 min = 1007 KJ

Processing volume = 5 lit = 5 x 10^{-3} m^3

Energy density = Amount of energy per unit volume = 1007 kJ/ 5 x 10^{-3} m^3 = 201.4 x 10^3 kJ/m^3

Energy required per unit size reduction

Average size for MCC = 1000 nm

Average size for synthesized CNC = 70 nm

Average size reduction = 1000 - 70 = 930 nm

Total energy utilized = Energy density /change in particle size = 201.4 x 10^3 (kJ/m^3) / 930 nm

= 216.55913 kJ/ m^3.nm.

The overall yield we achieved with the 58 %, by considering the commercial available energy The commercial energy unit prices in India, considered to be 10 Rs/KWh, and 1KWh is approximately 3.6 x 103 kJ.

Thus the energy cost required to convert the per g of MCC granules of average size 1 micron to the nanosize below100 nm is about

Energy cost per g of MCC = [Total energy required / energy per unit cost] x [Cost of energy per unit.]

Energy cost per unit g of MCC = [216.55913kJ / 3.6 x 10^3 kJ] x [10 Rs] = 0.60155 Rs. (0.0073 $)

Thus the additional cost of 0.60155 ₹ (0.0073 $) per unit gram of MCC for the overall conversion to CNC was observed.

4.9.2 Energy efficiency analysis of acoustic cavitation approach for the intensification of acid hydrolysis for the synthesis of CNF from cotton.

The acoustic cavitation assistance to the conventional acid hydrolysis generates the intensification in the process in terms of improved efficiency (yield 39 %), and conversion time reduction on the cost of additional energy for the cavitation. The energy required during the cavitation was calculated.

The equipment specification of probe ultrasonic cavitator used was, power of horn: 200 W, amplitude used during experiments 70 %, operating frequency: 20 kHz, sonication time: 40 min, processing volume: 100 mL.

Running time of sonicator, during which power required = 3 sec., on and 1 sec., off, pulse mode of operation was used, thus in one cycle =4 sec

Cycles in Minutes = 60/4 = 15 cycles

Over all energy demanding seconds in a minutes = 60 – 15 = 45 sec

Average cotton particle size before intensified acid hydrolysis treatment: 1000 nm.

Particle size obtained after 40 min sonication: 87 nm.

Electrical energy required to run the cavitator for 40 min:

= [electrical power input to the device, J/s x [Utilized power, %] x [Running time of the equipment]

= 200 J/s × 0.7 × [40 min × 45 s] = 252 kJ

Processing volume: 100 mL = 100×10^{-6} m^3

The energy supplied per unit volume of the suspension = Electrical energy supplied/processing volume

= 252 kJ / 100×10^{-6} m^3

= 2.52×10^6 kJ/m^3

Overall particle size variation achieved = Initial size of cotton fibril – size obtained after intensified acid hydrolysis for CNF.

= 1000 – 87 = 913 nm

Total energy consumed per unit of particle size reduction was calculated as = Energy consumed for overall operation / particle size variation achieved

= 2.52×10^6 kJ/m^3 / 913 nm

= 2.760×10^3 $kJ/(m^3.nm)$

The energy required to convert the overall size reduction from 1 µm to 87 nm was 2.760 X 10^3 kJ. However, the observed yield of the SNPs during intensified acid hydrolysis was 39 % at minimal acid concentration of 0.5 M.

The commercial energy unit prices in India, considered to be 10 Rs/KWh, and 1KWh is approximately 3.6 x 10^3 kJ.

Thus the energy cost required to convert per g of cotton fibers of average size 1 micron to the nanosize below 100 nm is.

Energy cost per g of cotton fibers = [Total energy required / energy per unit cost] x [Cost of energy per unit.]

Energy cost per unit g of starch = [2.760 x 10^3 kJ / 3.6 x 10^3 kJ] x [10 Rs] = 7.667 ₹, (0.093 $)

Thus the additional cost of 7.667 ₹, (0.093 $) per g of cotton for the overall conversion to CNC.

4.9.3 Economics aspect of the two different approach to achieve the nanoscale cellulose structure.

The energy requirement for the generation of cavitation with the help of high frequency sound waves (acoustic) was much higher than that hydrodynamic cavitation approach. Thus the

overall cost required to process the granule of cellulose to produce the nanocellulose in hydrodynamic cavitation assisted acid hydrolysis is significantly low. The process is close looped and able to handle the higher quantity of the MCC for the production of CNC. The only bottleneck, in the said process is corrosion occurred during the flow of acid in the experimental setup.

Among the different sustainable materials, cellulose is considered more important and has a simpler chemical structure, making it easily accessible on our planet. Cellulose can be processed into more diverse structures than other materials. However, despite the significant advantages of CNCs, their energy consumption and production costs have limited their widespread applications in comparison to other materials. The acid hydrolysis is more commonly used than other methods, where a given concentration of desired acid is mixed with deionized water and the purified starting material. Different resources have been subjected to assays using various acids such as sulfuric acid, hydrobromic acid, hydrochloric acid, phosphoric acid, maleic acid, and hydrogen peroxide to extract CNCs. Sulfuric and hydrochloric acids are more commonly used than other acids for the acid hydrolysis of cellulose. The particle size, morphology, crystallinity, thermal stability, and mechanical properties of CNCs are significantly influenced by the temperature and time of hydrolysis procedure, nature, and concentration of acid, and fiber-to-acid ratio. Mechanical methods have been investigated more extensively than other methods for the production of nanoscale cellulose particles, either as part of the fabricating process employing combinations of acid hydrolytic, oxidative, and enzymatic treatment, or directly. These methods, namely microfluidization, ultrasonication, high pressure homogenization or ball milling, are compared to each other. Compared to other approaches, the oxidation method using TEMPO oxidation shows some significant disadvantages, including the use of toxic TEMPO reagents (which can cause environmental problems), longer oxidation time, and restricted oxidation at C6 primary hydroxyl groups in CNCs. Enzymatic routes for the synthesis of CNCs have been found to be more promising in terms of yields, selectivity, and operating conditions when compared to chemical processes. Nonetheless, this technique is comparatively hindered by both economical (i.e., higher cost of cellulose enzyme) and technical (long processing period as a rate limiting step of cellulose degradation) constraints. The rate of enzymatic hydrolysis has been found to be slower compared to other processes, and is affected by numerous factors including structural features resulting from pre-treatment and enzyme mechanism. Table 4.4 compares some of the

reported methods for the synthesis of CNC and presents the advantages and limitations of each approach.

Table 4. 4 Reported methods for the synthesis of CNC comparison with the present study

Synthesis approach	Description	Advantages	Limitations	Ref
Acid hydrolysis	Hydrogen ions of acids react with glycosidic bonds between the monosaccharide units	Thermally stable Mechanically strong CNC 36 h for the conversion Crystallinity 85%	Higher acid concentration required Time consuming Difficulties in the operations	[7]
Enzymatic pre-treated acid hydrolysis	Ezymatic pre-treated cotton fibers goes through acid hydrolysis	Mechanically strong and thermal stable CNC Overall conversion consist of 1 h of enzymatic treatment and 1 h of acid hydrolysis	More amorphous nature of CNC Overall all crystallinity about 65%	[23]
Oxalic acid dihydrate	Acid hydrolysis	No solvent Required Simple procedure The solvent used for washing can be recycled Less time-consuming methods Environmental friendly techniques	Results in CNCs of low crystallinity index Poor dispersibility	[13]
High pressure homogenization	Mechanical	NO crystallinity variations	Demanding high levels of pressure or kinetic energy	[9]
Sonication	Mechanical impact of cavity collapses used	No chemical requirement NO crystallinity variations	Randomness in the morphology of the synthesized CNC	[26]

	for the size reduction	ultrasonication at power of 1500 W	Higher energy requirement	
Enzymatic hydrolysis	Fermentation	Amorphous form of stable CNC synthesized Time required for the conversion 36 H	Downstream process are required Limited in the production rate Higher time required for the conversion	[10]
Present study	Acid hydrolysis assisted of cavitation by HC	Close loop system Overall crystallinity 86% Yield 48% Time required for the conversion 40 minutes	Quantity of mass to be operated are limited Large scale application was difficult in current situation.	

4.10 Conclusions

The robust method of ultrasound-assisted acid hydrolysis produces the CNF from the cotton cellulose. The green approach produces the nano-febrile structure of cellulose with a scale of 10–20 nm length and about 5-8 nm diameter. The stability of CNF in the water was observed at a fixed pH value and found to be stable. The thermal resistance of synthesized CNF is much better than that of cotton cellulose, and it also shows the higher crystallinity of synthesised CNFs. The significant higher yield of 39 % was observed with the acoustic cavitation approach for the intensification of acid hydrolysis during the synthesis of CNF was observed.

Microcrystalline cellulose (MCC) was exploited in the continuous cavitation approach for the synthesis of cellulose nanocrystals (CNCs). The average particle size of synthesized CNC were in the range of 60-70 nm. The crystallinity of synthesized CNCs improves significantly after acid hydrolysis. The cavitation achieved in continuous operations contributes significantly to the enhancement of acid molecule mass transfer as well as the rate of acid molecule impingement inside the MCC granules. The synthesized spherical-shaped CNCs are stable. The yield of the process is 58 %, which is effectively higher than the yield of conventional acid

hydrolysis. The process is robust, and optimized conditions such as 0.25 M acid concentration and 8 bar inlet pressure suggest a higher yield of CNC from the acid suspension of MCC at an orifice opening of 1 mm at the centre of the plate. The effect of orifice opening numbers and their orientation on the orifice plate could be investigated in future work.

References

[1] A. Rangan, M. V Manchiganti, R.M. Thilaividankan, S.G. Kestur, R. Menon, Novel method for the preparation of lignin-rich nanoparticles from lignocellulosic fibers, Ind. Crops Prod. 103 (2017) 152–160. https://doi.org/10.1016/j.indcrop.2017.03.037.

[2] D. Trache, M.H. Hussin, C.T. Hui Chuin, S. Sabar, M.R.N. Fazita, O.F.A. Taiwo, T.M. Hassan, M.K.M. Haafiz, Microcrystalline cellulose: Isolation, characterization and bio-composites application—A review, Int. J. Biol. Macromol. 93 (2016) 789–804. https://doi.org/10.1016/j.ijbiomac.2016.09.056.

[3] L. Di Giorgio, L. Martin, P.R. Salgado, A.N. Mauri, Synthesis and conservation of cellulose nanocrystals, Carbohydr. Polym. 238 (2020) 116187. https://doi.org/10.1016 /j.carbpol. 2020.116187.

[4] S. Chkirida, N. Zari, R. Bouhfid, A. el kacem Qaiss, Insight into the bionanocomposite applications on wastewater decontamination: Review, J. Water Process Eng. 43 (2021) 102198. https://doi.org/10.1016/j.jwpe.2021.102198.

[5] H. Yuan, J. Peng, T. Ren, Q. Luo, Y. Luo, N. Zhang, Y. Huang, X. Guo, Y. Wu, Novel fluorescent lignin-based hydrogel with cellulose nanofibers and carbon dots for highly efficient adsorption and detection of Cr(VI), Sci. Total Environ. 760 (2021) 143395. https://doi.org/10.1016/j.scitotenv.2020.143395.

[6] A. Kafy, H.C. Kim, L. Zhai, J.W. Kim, L. Van Hai, T.J. Kang, J. Kim, Cellulose long fibers fabricated from cellulose nanofibers and its strong and tough characteristics, Sci. Rep. 7 (2017) 1–8. https://doi.org/10.1038/s41598-017-17713-3.

[7] K. V Neenu, C.D. Midhun Dominic, P.M.S. Begum, J. Parameswaranpillai, B.P.

Kanoth, D.A. David, S.M. Sajadi, P. Dhanyasree, T.G. Ajithkumar, M. Badawi, Effect of oxalic acid and sulphuric acid hydrolysis on the preparation and properties of pineapple pomace derived cellulose nanofibers and nanopapers, Int. J. Biol. Macromol. 209 (2022) 1745–1759. https://doi.org/10.1016/j.ijbiomac.2022.04.138.

[8] K. Li, C.M. Clarkson, L. Wang, Y. Liu, M. Lamm, Z. Pang, Y. Zhou, J. Qian, M. Tajvidi, D.J. Gardner, H. Tekinalp, L. Hu, T. Li, A.J. Ragauskas, J.P. Youngblood, S. Ozcan, Alignment of Cellulose Nanofibers: Harnessing Nanoscale Properties to Macroscale Benefits, ACS Nano. 15 (2021) 3646–3673. https://doi.org/10.1021/acsnano.0c07613.

[9] M. Moniruzzaman, T. Ono, Separation and characterization of cellulose fibers from cypress wood treated with ionic liquid prior to laccase treatment, Bioresour. Technol. 127 (2013) 132–137. https://doi.org/10.1016/j.biortech.2012.09.113.

[10] M.A. Yassin, A.A.M. Gad, A.F. Ghanem, M.H. Abdel Rehim, Green synthesis of cellulose nanofibers using immobilized cellulase, Carbohydr. Polym. 205 (2019) 255–260. https://doi.org/10.1016/j.carbpol.2018.10.040.

[11] C.D. Midhun Dominic, V. Raj, K. V Neenu, P.M.S. Begum, K. Formela, M.R. Saeb, D.D. Prabhu, P. Poornima Vijayan, T.G. Ajithkumar, J. Parameswaranpillai, Chlorine-free extraction and structural characterization of cellulose nanofibers from waste husk of millet (Pennisetum glaucum), Int. J. Biol. Macromol. 206 (2022) 92–104. https://doi.org/10. 1016/j.ijbiomac.2022.02.078.

[12] D. Trache, M.H. Hussin, M.K.M. Haafiz, V.K. Thakur, Recent progress in cellulose nanocrystals: sources and production, Nanoscale. 9 (2017) 1763–1786. https://doi.org/10. 1039/C6NR09494E.

[13] A. Pandey, Pharmaceutical and biomedical applications of cellulose nanofibers: a review, Environ. Chem. Lett. 19 (2021) 2043–2055. https://doi.org/10.1007/s10311-021-01182-2.

[14] J.K. Ogunjobi, A.I. Adewale, S.A. Adeyemi, Cellulose nanocrystals from Siam weed: Synthesis and physicochemical characterization, Heliyon. 9 (2023) e13104. https://doi.org /10.1016/j.heliyon.2023.e13104.

[15] D. Bandera, J. Sapkota, S. Josset, C. Weder, P. Tingaut, X. Gao, E.J. Foster, T. Zimmermann, Influence of mechanical treatments on the properties of cellulose nanofibers isolated from microcrystalline cellulose, React. Funct. Polym. 85 (2014) 134–141. https://doi.org/10.1016/j.reactfunctpolym.2014.09.009.

[16] H.S. Onkarappa, G.K. Prakash, G.H. Pujar, C.R. Rajith Kumar, M.S. Latha, V.S.

Betageri, Hevea brasiliensis mediated synthesis of nanocellulose: Effect of preparation methods on morphology and properties, Int. J. Biol. Macromol. 160 (2020) 1021–1028. https://doi.org/10.1016/j.ijbiomac.2020.05.188.

[17] W. Tian, X. Gao, J. Zhang, J. Yu, J. Zhang, Cellulose nanosphere: Preparation and applications of the novel nanocellulose, Carbohydr. Polym. 277 (2022) 118863. https://doi.org/10.1016/j.carbpol.2021.118863.

[18] R.M.A. Domingues, M.E. Gomes, R.L. Reis, The Potential of Cellulose Nanocrystals in Tissue Engineering Strategies, Biomacromolecules. 15 (2014) 2327–2346. https://doi.org/10.1021/bm500524s.

[19] M.A. Torlopov, E. V Udoratina, I.S. Martakov, P.A. Sitnikov, Cellulose nanocrystals prepared in $H_3PW_{12}O_{40}$-acetic acid system, Cellulose. 24 (2017) 2153–2162. https://doi.org/10.1007/s10570-017-1256-3.

[20] V.S. Hakke, V.K. Landge, S.H. Sonawane, G. Uday Bhaskar Babu, M. Ashokkumar, E. M. M. Flores, The physical, mechanical, thermal and barrier properties of starch nanoparticle (SNP)/polyurethane (PU) nanocomposite films synthesised by an ultrasound-assisted process, Ultrason. Sonochem. 88 (2022) 106069. https://doi.org/10.1016/j.ultsonch.2022. 106069.

[21] P.R. Gogate, Application of cavitational reactors for water disinfection: Current status and path forward, J. Environ. Manage. 85 (2007) 801–815. https://doi.org/10.1016/j.jenvman. 2007.07.001.

[22] Q. Xiang, J.S. Kim, Y.Y. Lee, A Comprehensive Kinetic Model for Dilute-Acid Hydrolysis of Cellulose, in: B.H. Davison, J.W. Lee, M. Finkelstein, J.D. McMillan (Eds.), Biotechnol. Fuels Chem. Twenty-Fourth Symp., Humana Press, Totowa, NJ, 2003: pp. 337–352. https://doi.org/10.1007/978-1-4612-0057-4_27.

[23] T.I. Shaheen, H.E. Emam, Sono-chemical synthesis of cellulose nanocrystals from wood sawdust using Acid hydrolysis, Int. J. Biol. Macromol. 107 (2018) 1599–1606. https://doi.org/10.1016/j.ijbiomac.2017.10.028.

[24] B. Deepa, E. Abraham, B.M. Cherian, A. Bismarck, J.J. Blaker, L.A. Pothan, A.L. Leao, S.F. de Souza, M. Kottaisamy, Structure, morphology and thermal characteristics of banana nano fibers obtained by steam explosion, Bioresour. Technol. 102 (2011) 1988–1997. https://doi.org/10.1016/j.biortech.2010.09.030.

[25] H.P.S.S. Abdul Khalil, Y. Davoudpour, M.N. Islam, A. Mustapha, K. Sudesh, R. Dungani, M. Jawaid, Production and modification of nanofibrillated cellulose using

various mechanical processes: A review, Carbohydr. Polym. 99 (2014) 649–665. https://doi. org/10.1016/j.carbpol.2013.08.069.

[26] W. Li, J. Yue, S. Liu, Preparation of nanocrystalline cellulose via ultrasound and its reinforcement capability for poly(vinyl alcohol) composites, Ultrason. Sonochem. 19 (2012) 479–485. https://doi.org/10.1016/j.ultsonch.2011.11.007.

[27] N. Johar, I. Ahmad, A. Dufresne, Extraction, preparation and characterization of cellulose fibres and nanocrystals from rice husk, Ind. Crops Prod. 37 (2012) 93–99. https://doi.org/10.1016/j.indcrop.2011.12.016.

[28] A. Gaquere-Parker, T. Taylor, R. Hutson, A. Rizzo, A. Folds, S. Crittenden, N. Zahoor, B. Hussein, A. Arruda, Low frequency ultrasonic-assisted hydrolysis of starch in the presence of α-amylase, Ultrason. Sonochem. 41 (2018) 404–409. https://doi.org/10. 1016/j.ultsonch. 2017.10.007.

[29] H. Lu, Y. Gui, L. Zheng, X. Liu, Morphological, crystalline, thermal and physicochemical properties of cellulose nanocrystals obtained from sweet potato residue, Food Res. Int. 50 (2013) 121–128. https://doi.org/10.1016/j.foodres.2012.10.01

[30] M. Henriksson, G. Henriksson, L.A. Berglund, T. Lindström, An environmentally friendly method for enzyme-assisted preparation of microfibrillated cellulose (MFC) nanofibers, Eur. Polym. J. 43 (2007) 3434–3441. https://doi.org/10.1016/j.eurpolymj. 2007.05.038.

[31] S. Fujisawa, E. Togawa, S. Kimura, Large specific surface area and rigid network of nanocellulose govern the thermal stability of polymers: Mechanisms of enhanced thermomechanical properties for nanocellulose/PMMA nanocomposite, Mater. Today Commun. 16 (2018) 105–110. https://doi.org/10.1016/j.mtcomm.2018.05.002.

[32] Y. Jin, N. Hengl, S. Baup, F. Pignon, N. Gondrexon, M. Sztucki, A. Romdhane, A. Guillet, M. Aurousseau, Ultrasonic assisted cross-flow ultrafiltration of starch and cellulose nanocrystals suspensions: Characterization at multi-scales, Carbohydr. Polym. 124 (2015) 66–76. https://doi.org/10.1016/j.carbpol.2015.01.073.

[33] W. Chen, H. Yu, Y. Liu, P. Chen, M. Zhang, Y. Hai, Individualization of cellulose nanofibers from wood using high-intensity ultrasonication combined with chemical pretreatments, Carbohydr. Polym. 83 (2011) 1804–1811. https://doi.org/10.1016/j.carb pol.2010.10.040.

[34] M. El Achaby, N. El Miri, H. Hannache, S. Gmouh, H. Ben youcef, A. Aboulkas, Production of cellulose nanocrystals from vine shoots and their use for the development

of nanocomposite materials, Int. J. Biol. Macromol. 117 (2018) 592–600. https://doi.org /10.1016/j.ijbiomac.2018.05.201.

[35] D. Trache, A.F. Tarchoun, M. Derradji, T.S. Hamidon, N. Masruchin, N. Brosse, M.H. Hussin, Nanocellulose: From Fundamentals to Advanced Applications, 2020. https://doi.org /10.3389/fchem.2020.00392.

[36] K. Stana-Kleinschek, S. Strnad, V. Ribitsch, Surface characterization and adsorption abilities of cellulose fibers, Polym. Eng. & Sci. 39 (1999) 1412–1424. https://doi.org/10. 1002/pen.11532.

[37] A. Batool, S. Valiyaveettil, Surface functionalized cellulose fibers – A renewable adsorbent for removal of plastic nanoparticles from water, J. Hazard. Mater. 413 (2021) 125301. https://doi.org/10.1016/j.jhazmat.2021.125301.

[38] A. Farooq, M.K. Patoary, M. Zhang, H. Mussana, M. Li, M.A. Naeem, M. Mushtaq, A. Farooq, L. Liu, Cellulose from sources to nanocellulose and an overview of synthesis and properties of nanocellulose/zinc oxide nanocomposite materials, Int. J. Biol. Macromol. 154 (2020) 1050–1073. https://doi.org/10.1016/j.ijbiomac.2020.03.163.

[39] S. Boufi, S. Bel Haaj, A. Magnin, F. Pignon, M. Impéror-Clerc, G. Mortha, Ultrasonic assisted production of starch nanoparticles: Structural characterization and mechanism of disintegration, Ultrason. Sonochem. 41 (2018) 327–336. https://doi.org/10.1016/j. ultsonch.2017.09.033.

[40] R. Sharma, S.M. Jafari, S. Sharma, Antimicrobial bio-nanocomposites and their potential applications in food packaging, Food Control. 112 (2020) 107086. https://doi. org/10.1016/j.foodcont.2020.107086.

[41] M. Paakko, M. Ankerfors, H. Kosonen, A. Nykanen, S. Ahola, M. Osterberg, J. Ruokolainen, J. Laine, P.T. Larsson, O. Ikkala, T. Lindström, Enzymatic Hydrolysis Combined with Mechanical Shearing and High-Pressure Homogenization for Nanoscale Cellulose Fibrils and Strong Gels, Biomacromolecules. 8 (2007) 1934–1941. https://doi. org/10.1021/bm061215p.

[42] A. Ferrer, I. Filpponen, A. Rodriguez, J. Laine, O.J. Rojas, Valorization of residual Empty Palm Fruit Bunch Fibers (EPFBF) by microfluidization: production of nanofibrillated cellulose and EPFBF nanopaper., Bioresour. Technol. 125 (2012) 249–255. https://doi.org /10.1016/j.biortech.2012.08.108.

[43] T.B. Rouf, J.L. Kokini, Natural biopolymer-based nanocomposite films for packaging applications, Bionanocomposites Packag. Appl. (2017) 149–177. https://doi.org/10.

1007/978-3-319-67319-6_8.

[44] E. Trovatti, H. Tang, A. Hajian, Q. Meng, A. Gandini, L.A. Berglund, Q. Zhou, Enhancing strength and toughness of cellulose nanofibril network structures with an adhesive peptide, Carbohydr. Polym. 181 (2018) 256–263. https://doi.org/10.1016/j.carbpol.2017.10.073.

[45] S. Bano, Y.S. Negi, Studies on cellulose nanocrystals isolated from groundnut shells, Carbohydr. Polym. 157 (2017) 1041–1049. https://doi.org/10.1016/j.carbpol.2016.10.069.

[46] Y. Yoo, J.P. Youngblood, Green One-Pot Synthesis of Surface Hydrophobized Cellulose Nanocrystals in Aqueous Medium, ACS Sustain. Chem. Eng. 4 (2016) 3927–3938. https://doi.org/10.1021/acssuschemeng.6b00781.

[47] S. Liu, Z.-X. Low, Z. Xie, H. Wang, TEMPO-Oxidized Cellulose Nanofibers: A Renewable Nanomaterial for Environmental and Energy Applications, Adv. Mater. Technol. 6 (2021) 2001180. https://doi.org/10.1002/admt.202001180.

[48] Y. Wang, N. Li, S. Duan, Y. Zhang, Y. Wang, B. Zhang, S. Ren, L. Zhang, Cellulose nanocrystal-based enhancement of ultrasound microbubbles for increased tolerance of mechanical index values, Cellulose. 29 (2022) 9531–9547. https://doi.org/10.1007/s10570-022-04870-6.

[49] R. Rohaizu, W.D. Wanrosli, Sono-assisted TEMPO oxidation of oil palm lignocellulosic biomass for isolation of nanocrystalline cellulose, Ultrason. Sonochem. 34 (2017) 631–639. https://doi.org/10.1016/j.ultsonch.2016.06.040.

[50] Y. Lee, H. Zhang, H.-Y. Yu, K.C. Tam, Electroconductive cellulose nanocrystals — Synthesis, properties and applications: A review, Carbohydr. Polym. 289 (2022) 119419. https://doi.org/10.1016/j.carbpol.2022.119419.

[51] Y. Liu, H. Wang, G. Yu, Q. Yu, B. Li, X. Mu, A novel approach for the preparation of nanocrystalline cellulose by using phosphotungstic acid, Carbohydr. Polym. 110 (2014) 415–422. https://doi.org/10.1016/j.carbpol.2014.04.040.

[52] I.K. (Al-K. Ibrahim, S.M. Hussin, Y.M. Al-Obaidi, Extraction of cellulose nano crystalline from cotton by ultrasonic and its morphological and structural characterization, Int. J. Mater. Chem. Phys. 1 (2015) 99–109.

[53] N. El Miri, K. Abdelouahdi, M. Zahouily, A. Fihri, A. Barakat, A. Solhy, M. El Achaby, Bio-nanocomposite films based on cellulose nanocrystals filled polyvinyl alcohol/chitosan polymer blend, J. Appl. Polym. Sci. 132 (2015) 1–13. https://doi.

org/10.1002/app.42004.

[54] V.S. Hakke, U.D. Bagale, S. Boufi, G.U.B. Babu, S.H. Sonawane, Ultrasound Assisted Synthesis of Starch Nanocrystals and It's Applications with Polyurethane for Packaging Film, J. Renew. Mater. 08 (2020) 239–250. https://doi.org/10.32604/jrm.2020.08449.

[55] S. Shrestha, B. Wang, P. Dutta, Nanoparticle processing: Understanding and controlling aggregation, Adv. Colloid Interface Sci. 279 (2020) 102162. https://doi.org/10.1016/j.cis.2020.102162.

[56] S. Cabanas-Polo, K.S. Suslick, A.J. Sanchez-Herencia, Effect of reaction conditions on size and morphology of ultrasonically prepared $Ni(OH)_2$ powders, in: Ultrason. Sonochem., Elsevier B.V., 2011: pp. 901–906. https://doi.org/10.1016/j.ultsonch.2010.11.017.

[57] S.S. Low, M. Yew, C.N. Lim, W.S. Chai, L.E. Low, S. Manickam, B.T. Tey, P.L. Show, Sonoproduction of nanobiomaterials – A critical review, Ultrason. Sonochem. 82 (2022) 105887. https://doi.org/10.1016/j.ultsonch.2021.105887.

[58] S. Raut-Jadhav, M.P. Badve, D. V. Pinjari, D.R. Saini, S.H. Sonawane, A.B. Pandit, Treatment of the pesticide industry effluent using hydrodynamic cavitation and its combination with process intensifying additives (H_2O_2 and ozone), Chem. Eng. J. 295 (2016) 326–335. https://doi.org/10.1016/j.cej.2016.03.019.

[59] S.R. Shirsath, A.P. Patil, R. Patil, J.B. Naik, P.R. Gogate, S.H. Sonawane, Removal of Brilliant Green from wastewater using conventional and ultrasonically prepared poly(acrylic acid) hydrogel loaded with kaolin clay: A comparative study, Ultrason. Sonochem. 20 (2013) 914–923. https://doi.org/10.1016/j.ultsonch.2012.11.010.

[60] J. Carpenter, M. Badve, S. Rajoriya, S. George, V.K. Saharan, A.B. Pandit, Hydrodynamic cavitation: An emerging technology for the intensification of various chemical and physical processes in a chemical process industry, Rev. Chem. Eng. 33 (2017) 433–468. https://doi. org/10.1515/revce-2016-0032.

[61] V.S. Hakke, S. Sonawane, S. Anandan, S. Sonawane, M. Ashokkumar, Process intensification approach using microreactors for synthesizing nanomaterials—a critical review, Nanomaterials. 11 (2021) 1–21. https://doi.org/10.3390/nano11010098.

Chapter 5. Investigation of Physio-Thermo-Mechanical Properties for the SNP – PU nanocomposite films.

5.1 Introduction

The petroleum-based polymers are widely used for various applications. Polymers are used extensively in the packaging industry, specifically for food. Single-use plastics, which are generally derived from petroleum and are not biodegradable, have largely supplanted more sustainable packaging solutions, resulting in environmental deterioration. As a result, the use of renewable resources has gained traction. Paper-based items are now the most easily available ecological alternative to plastic packaging, but they plainly cannot compete with plastic's flexibility. Paper goods are inferior to other materials in numerous situations due to their limited water resistance, durability, and suppleness. Paper products are a feasible solution for both protective and interior packing. Food packaging films must be sturdy, transparent, moisture-resistant, and create a powerful barrier against moisture and gas since they come into contact with moisture-rich foods that are often sealed under inert gas circumstances. Classic petroleum-based non-biodegradable polymers have been extensively employed in the packaging industry because of their excellent processibility, low cost, unique mechanical and barrier properties, and broad application during the previous decade. However, as a side consequence, it caused a lot of pollution. As a result, there has recently been a surge of interest in developing biodegradable materials to replace their non-biodegradable counterparts. As a consequence, we must investigate other choices, such as bio-based polymers, to meet the diverse needs of our economic activities.

In the recent reported literature Pluta-Kubica et al. [1] demonstrate the synthesis of furcellaran nanocomposite film with silver nanoparticles for the packaging application of food material with in situ polymerization approach. The film improved the microbiological quality of cheeses during storage. The Sharaby et al. [2] prepared the pectin-based films reinforced with crystalline nanocellulose (CNC) and zinc oxide nanoparticles by solvent-casting method. The film shows the enhanced UV-blocking, thermal, and antibacterial properties of active films against well-known foodborne pathogens. Optimal active films exhibited higher mechanical, water vapor barrier properties compared to pristine pectin films. Starch and its derivatives have gained considerable attention because of their abundance in nature and wide potential for various applications in food industries, polymer nanocomposite coatings, and films [3]. The structural modification of starch granules has been reported with the ultrasound (US) assistance

[4,5]. The cohesion forces were induced in the liquid to produce disruption in the liquid during the cavitation phenomenon. Ultrasonic irradiation creates cavities that collapse resulting in localized high pressures and temperatures, leading to the formation of radicals. Furthermore, the generation of shock waves during bubble collapse significantly improves mass transfer and emulsification processes, two critical factors that influence reaction rates and improve reactant de-agglomeration. Javaid et al. [6] nanocomposite of modified polyurethane through the isophorone diisocyanates (IPDI) was reaction with hydroxyl terminated polybutadiene (HTPB) and waxy corn starch through step growth polymerization reaction between NCO−terminated prepolymer and chain extenders. The role of starch in the nanocomposite was used as extenders. The green chemistry approach for the synthesis of biomass-based nanoparticles using US can bring some advantages as compared to larger reactors as it can be eco-friendly, non-thermal technology [7,8]. The high intensity irradiation of US may cause the destruction of microcapsules in the solution. Inui et al. [9] studied the phenomenon of destruction of microcapsules of starch under US irradiation. The shear stress induced due to the collapse of bubbles in solution is one of the reasons for the physical destruction of structure of starch [9]. Haaj et al. [10] found that at high intensity US irradiation (24 kHz, horn tip diameter 13 mm, 170 W) physically damage the crystalline structure of starch. They also reported the higher yield for the synthesis of SNP as compared to the conventional acid hydrolysis method. Zhou et al. [11] reported acid vapour hydrolysis assisted with US irradiation (20–25 kHz) for the synthesis of elliptical shaped SNP. However, they also found that gelatinization temperature and overall crystallinity of synthesized SNP were lower than the native starch granules. A uniform distribution of nanoparticles can be easily achieved by ultrasonic irradiation. Shear force is one of the main parameters affecting the nanoparticles' distribution in the polymer suspension and is induced due to the shock waves developed during the collision of cavities in the suspension. Girard et al. [12] reported the effect of sonication on the dispersion of cellulose nanocrystals. They found that upon increasing the energy level, cellulose nanocrystals are dispersed in the water, which was confirmed by the rheological studies. Ultrasound assistance provides enough energy to the suspension to break the agglomerates. However, the multiple particle interactions and the higher local concentration of nanoparticles can overcome the dispersion energy induced by the US. Sumitomo et al. [13] conducted a comparison study for the synthesis of nanoparticle suspension through the mechanical stirring and US irradiation. They discovered that US is much more effective than mechanical agitation in achieving a

suspension of nanoparticles. The viscosity and average size of the aggregates in suspension decreased as the irradiation time increased. [14].

Starch is hydrophilic in nature, it also shows poor water vapour, oxygen and bacterial passage barrier properties. For the application of starch-based polymer films for wider applications, it is necessary to overcome these limitations. The synthesis of starch-based polymeric films using various plasticizers has been reported in the literature [15]. The addition of plasticizers such as glycerol [16,17], formamide [18], urea, sucrose, and sorbitol [19] effectively enhances the mechanical properties of polymer film such as tensile strength, modulus of elasticity, break-even point. These modified starch-based nanocomposite polymer films are sensitive to moisture and heat, due to the hydrophilicity of the starch granules [9]. The blending of proteins with starch brings hydrophobicity in the starch-based polymer films as well as increases the tensile strength of the polymer film [20]. SNPs can be used as nanofillers in the continuous matrix of other natural or synthetic polymers for the production of packaging films [3,21]. The reinforcement of SNPs not only improves the mechanical and physical properties but also the biodegradability of the host polymer matrix. An effective reduction in water vapour and oxygen permeability of rubber latex was successfully demonstrated through blending of SNPs with natural rubber latex by Angellier et al. [22]. Concha et al. [23] found a 50 % increase in the relative crystallinity of granules due to a reduction of starch granule size. This rise in the crystallinity of starch granule in SNPs provides strength and increases the rigidity of the host polymer [24].

Polyurethane (PU) is the most popular polymer used in various products and applications owing to its low cost and low toxicity. However, poor wear and tear resistance, optical properties, and lower hardness are the drawbacks of PU based films. The modification of PU-based films has been studied and demonstrated by various blending materials, such as vegetable oil [25], coumarin derivatives [26], nano-silver [27], cellulose nanocrystals [28], etc. This results in an improvement of the mechanical, physical, and chemical properties of the PU films. Zhang et al. [29] used thermoplastic PU and blended it with the lactic acid to achieve greater interfacial compatibility with PU. They found enrichment in the mechanical properties of the PU-based polylactic acid film. In another study, Zhang et al. [30] reported the improvement of the mechanical and optical properties of PU-based films by the addition of monocrystalline cellulose. They found that the variation in hardness is only 1.5 %, but the properties like abrasion resistance of PU based films with monocrystalline cellulose were enhanced by 60 %, a good achievement for coating application. Another successful attempt reported by Lu et al.

[31] was the blending of glycerol plasticized starch granules with PU. The reported PU film presented enhanced surface area, hydrophobicity, and water resistance. However, the toughness of the film was not affected. Yazdi et al. [32] modified the PU matrix with the addition of multi-walled carbon nanotubes. The authors reported enhancements in the modulus of elasticity and tensile strength of the PU film modified with multi-walled carbon nanotubes. The commercially available water-born PU has a wide range of applications, starting from polymer barrier coating for food, decorative, protective coatings, and PU foam. The PU polymer structure is adaptive and easily accommodates or is compatible with the filler material in the suspension. Though starch is abundantly found, its synthesis and applications are not well explored. The abundantly available starch can be converted to the nanoscale using intensified ultrasound-assisted acid hydrolysis. Further, the PU used is a water based resin, which can be used for coatings. The nanocomposite form the PU are being renewable, having specific strength and modulus, non-toxicity, and ease of handling could be the suitable base polymer solution for the synthesis of nanocomposite films. The widely available biomass starch shows improved properties at the nanoscale, such as higher mechanical and thermal resistance. The SNPs' granules show higher crystallinity with respect to the original native starch. Such intriguing properties of SNPs can be used to create nanocomposite films with improved mechanical and thermal performance. The water vapour permeability, oxygen permeability, and bacterial cell permeability of these nanocomposite films were analysed for their utilization in packaging industries.

In this section, the synthesized SNPs were used as nanofillers in the polyurethane polymer matrix. Polyurethane (PU), as discussed in Chapter 2, is the base product of a reaction between alcohol (-OH) and isocyanate (NCO) in the form of a urethane group, which is the monomer for the PU. This is the most commonly used polymer for various applications due to its rigidity, flexibility, and adaptive polymer structure. It contains many additional groups such as ethers, esters, and some aromatic compounds. The SNP produced by the intensified acid hydrolysis method was used as a nanofiller in the PU polymer matrix to investigate its effect on the thermal, mechanical, and water vapour barrier properties of the coating or thin film. Experiments were carried out on various compositions of SNP loading for all of these thin film properties. The synthesized thin films could be used for packaging applications.

5.2 Preparation of SNP-PU nanocomposite thin films.

The dispersion of 205 mg of SNP in deionised water (50 mL, 200 mL glass beaker) was achieved with the 5 min US irradiation in pulse mode (3 s on and 2 s off). The pulse mode was

utilized to control the temperature of the suspension. SNP dispersion in deionized water may aid in their interaction and dispersion in PU solution. It also helps to adjust the viscosity of the SNP in the PU solution composite before application of the substrate during evaporation and the casting method of film preparation. The dispersion of SNP in the solution of PU was accomplished via 20 kHz sonication (5 minutes) at a temperature of 20 ^{o}C. The well-dispersed SNP-PU nanocomposite suspension is used for the next process of thin sheet preparation through solvent evaporation and casting methodology [33].

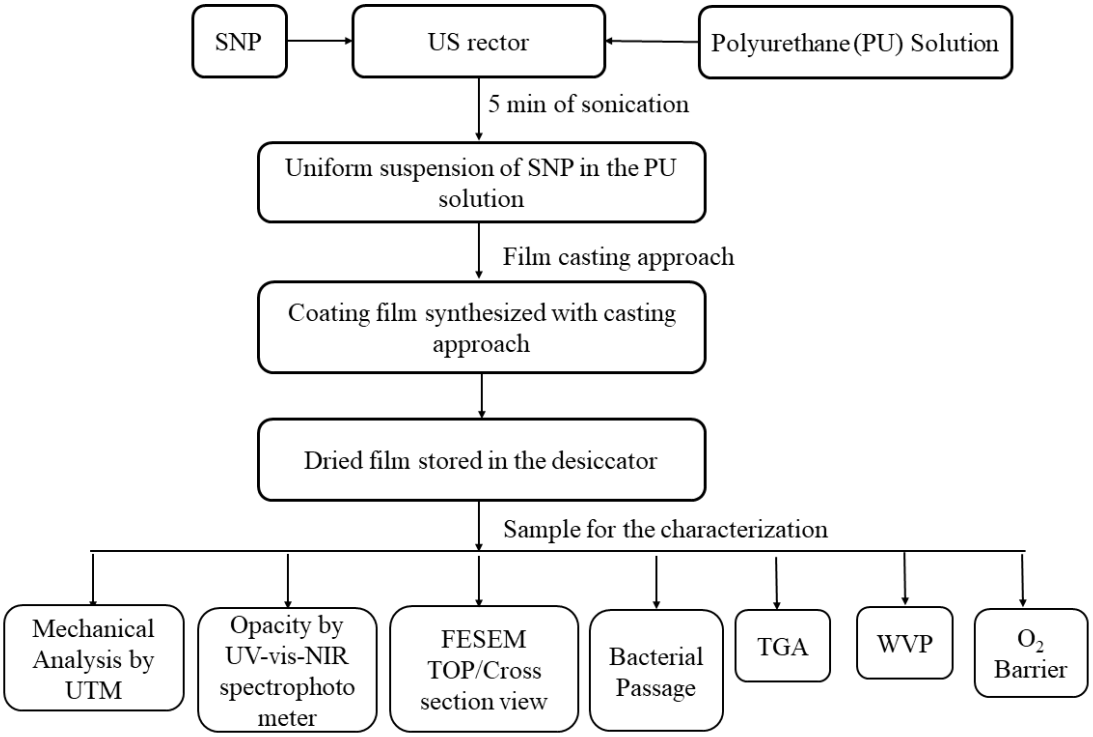

Figure 5.1 Block diagram for the synthesis of SNP-PU nanocomposite coating film.

5.2.1 SNP based PU nanocomposite thin film synthesis approach.

The uniformly blended mixture of SNP and PU was exploited for the synthesis of films through the casting technique. The 200 µm thickness of the nanocomposite sheets of well dispersed SNPs in PU solution was achieved using stainless steel (SS) film applicator 9031 (Samriddhi International Inc, Mumbai India). The produced nanocomposite thin sheets were then dried with the help of vacuum oven (VT 6025, Thermo Fisher Scientific India Pvt. Ltd.). Films of PU with SNP of 5, 10, 20, and 30 % (wt) were synthesized and examined for variations properties such as mechanical property, transmission resistance to bacteria, and water vapor permeability (WVP) at different temperatures. The 5 % (wt) SNP is blended with the PU

solution with the help of ultrasonic irradiation. This suspension is used to synthesize the nanocomposite film denoted as SP1. The different amounts of SNP in the PU solution are 10 % (SP2), 20 % (SP3), and 30 % (SP3). These were made and stored in the desiccator to keep them away from getting wet and contaminated by bacteria. The film applicator was used for the synthesis of uniform-thickness PU films. The thickness of the film was verified by the digital thickness measurement device from the coating thickness gauge PCE-CT 80 (PCE Instruments UK). The random checks at different points confirm that the film's thickness is the same everywhere.

5.3 Characterization of SNP-PU nanocomposite thin films.

5.3.1 Morphological study of nanocomposite starch PU films

Field emission scanning electron microscope (FESEM) (FEI Quanta 200F integrated with Oxford-EDS system IE 250 X Max 80, Netherlands) 50X to approx. 200,000X, 2 kV to 30 kV, was used to examine the morphology of films. FESEM cross-sectional views of the film verified a consistent distribution of SNPs. The 1 cm X 1 cm size of the sample specimen was used for the analysis. In order to better understand how the SNPs are dispersed throughout the PU polymer matrix, two sets of images were taken of these nanocomposites: one from the sample's top surface, and another from a cross-section across its thickness. The crosssectional image represents how the particles are distributed along the thickness and a macroscopic view of the composite substrate interface.

5.3.2 Thermophysical property analysis of thin films

Thermogravimetric analysis (TGA) was used to estimate the glass transition temperatures of the films and the perfect thermal resistance. The TGA studies were performed on the Perkin-Elmer instrument (TGA 8000, USA) under a nitrogen environment to demonstrate the thermo-physical behaviour of nanocomposite film. An automated Mettler balance was used to weigh 6 samples of the thin films with a weight of about 5 mg was introduced in the pans. TA fast press was used to seal the pan after it was put on a spacer insert. The reference was an empty pan with a cover that was sealed to provide a sufficient heat capacity. The film was tested three times and TGA was carried out at a heating rate of 5 ^{o}C min^{-1} from 25 to 350 ^{o}C with nitrogen gas flowing at a rate of 60 mL min^{-1}. The enthalpy change (H) was calculated using the weight of the film and represented as J g^{-1} of dry matter.

5.3.3 Mechanical property analysis of nanocomposite SNP-PU films

The mechanical characteristics of the film were determined using the Universal Testing Machine (UTM) T 150 tensile tester (KLA, India). The mechanical properties were performed using UTM machine as per the ASTM D 882 [34] standard test methods. The specimen (100 mm length x 3 mm thickness x 20 mm breadth) was taken in a tensile machine to determine the elongation (% E), and the tensile strength (TS) for the film with the constant crosshead speed of 5 mm/min.

$$\%\ \text{elongation}\ (\%\ \text{E}) = \frac{(L_f - L_i)}{L_i}\ \text{X}\ 100 \qquad \text{(Eq. 5.1)}$$

L_f is the final length of sample while L_i is the initial length of sample.

5.3.4 UV-visible spectrophotometry for the light transmittance and opacity

UV-vis-NIR spectrophotometer (Cary 5000, Agilent technologies, USA) was used to observe the UV-Vis response of the nanocomposite film. The transmission (%T) was noted for different samples considering virgin PU film as the baseline. The individual component transmittance at 600 nm wavelength was noted. Lambert-Beer's equation was used to convert transmittance observation in absorbance. The opacity of films was calculated by,

$$Opacity = \frac{abs_{600}}{X} \qquad \text{(Eq. 5.2)}$$

where X is the thickness of thin-film in mm [35,36].

5.3.5 Determination of bacterial passage through synthesized nanocomposite starch PU films

To understand whether the films allowed the passage of bacteria, the following experiment was performed. Six sterilized conical flasks were taken and 20 ml sterilized Luria-Bertani broth media was added to each of them. The mouth of the conical flasks was tightly sealed using the films and exposed to the environment for 24 h. One flask was left unsealed to act as a control. After exposure for 24 h, the conical flasks were incubated at 37 ºC for 24 h at 180 rpm. Following this, the absorbance of the culture was measured at 600 nm using a spectrometer (UV-1800 model, Shimadzu Analytical Pvt. Ltd., India). The cultures were then diluted and spread plated on Luria-Bertani agar plates. These plates were maintained at 37 ºC for 12 h and the bacterial count in each agar plate was determined. The total bacterial count in each conical flask was calculated after considering the dilution factor. All experiments were performed in triplicate and the standard error of the mean was calculated [36,37].

5.3.6 Determination of water vapor permeability of nanocomposite film

WVP tests were conducted using ASTM (1996) [26] method E96 with some modifications. Each film sample was sealed over a circular opening of a cylindrical vessel of an opening diameter of 6 cm. The cylindrical vessel was filled with water. The desiccator temperature was monitored by a water-heated thermostat (28 ^{o}C, 35 ^{o}C, and 40 ^{o}C) and a temperature measuring indicator was placed inside the desiccator to monitor the temperature. To maintain the relative humidity (RH) across the film, anhydrous calcium chloride (75 % RH) was placed in the desiccator. The effect of temperature on the water vapour transmission from inside vessel to outside through the film was observed. The weight difference of vessel and cross-sectional area of film were used to calculate the water vapours permission rate (WVPR). After the attainment of steady-state (about 32 h), the WVP (g/Pa.s.m) was calculated as per equation 5.3.

$$WVP = [WVPR/S\ (R_1 - R_2)]\ d \qquad \text{(Eq. 5.3)}$$

Where S is the saturation vapor pressure of water (Pa) at the test temperature, R_1 is the RH in the desiccator, R_2 is the RH in the permeation cell and d is the film thickness (m).

5.3.7 Oxygen barrier performance of the composite film

To measure the oxygen permeability of thin films, samples of thin films were examined using the ASTM 3985 standard test [38]. By inserting the test sample in one of the chambers, permeation cells were employed to create a barrier between two compartments. Both chambers were entirely decommissioned. Following that, one compartment was filled with nitrogen, while the other was filled with oxygen. Because of the barrier, oxygen may seep into the nitrogen carrier gas and be transported to the colorimetric detector, causing an electrical current to flow. The signal's strength was related to the quantity of oxygen flowing into the detector.

5.4. Result and discussion

It was observed that, in the ultrasonically treated starch granules, the reduction in the particle size as well as a narrower particle size distribution (PSD) were observed in a very short time as compared to other particle size reduction methods. However, the morphology of the produced SNPs was also altered from a plate-like structure to an oval shape under ultrasonic irradiation. The dispersion of SNP in the PU polymer solution was achieved with the ultrasound assistance. The temperature of the blend was maintained below 20 ^{o}C. The cavitation develops the sufficient turbulence and shear force on the both phases to achieve the dispersion of SNP nanofillers in the polymer solution. The films synthesized by the casting method shown smooth

surface. It has been seen that intense sharing due to ultrasound helps in the dispersion of nanofillers SNP in PU polymer matrix. This uniform dispersion of nanofiller due to sonication significantly improves the mechanical and electrical properties of polymer nanocomposite, which are always better than conventional methods.

Due to the lower concentration of SNP in the PU suspension, the sulpate and hydroxyl functional group linkages with the isocyanides are prominent, whereas the agglomeration of SNP in the PU suspension was absent. Moreover, up to a certain limitation on the SNP concentration, no agglomeration was observed in the prepared nanocomposite films. The hydroxyl functional groups present on the surface of SNPs develop a strong interaction with the extender of PU polymer. The PU monomer consists of isocyanide and polyol linked with each other, due to which the PU monomer has six significant active sites for hydrogen bond linkages. The hydroxyl functional group forms strong ionic bond connections with the PU polymeric chain. The crystalline structure of SNP will act like individual nuclei surrounded by the PU solution. At lower concentrations of SNP, the formation of these nuclei adds strength to the PU structure. The morphology of the synthesized SNP-PU nanocomposite thin films are analysed with FESEM and reported in Figure 5.2. The polypeptide base was used for the casting of nanocomposite thin films. The thickness of thin film restricted by the use of film coater device. The 200 micron film was synthesized with the uniform film thickness. FESEM images in Figure 5.2 show the cross-sectional view of nanocomposite films.

5.4.1 Morphological studies of starch PU nanocomposite films.

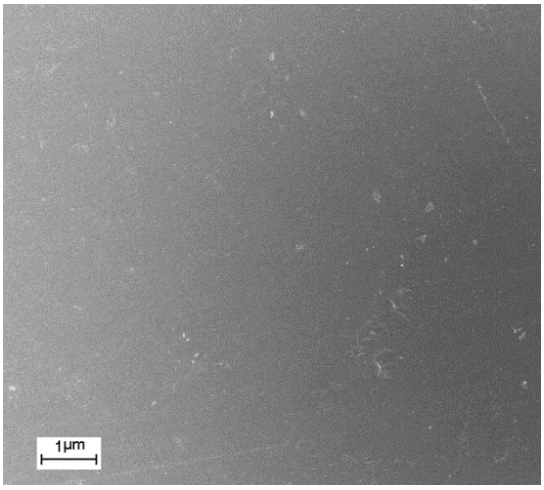

a) SP 1 (5 % SNP)

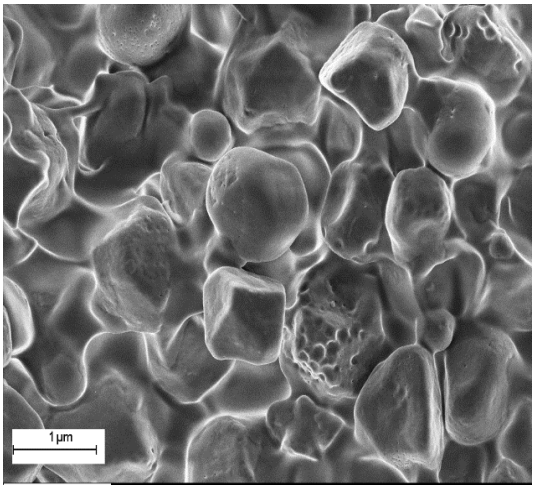

e) SP 1 (5 % SNP)

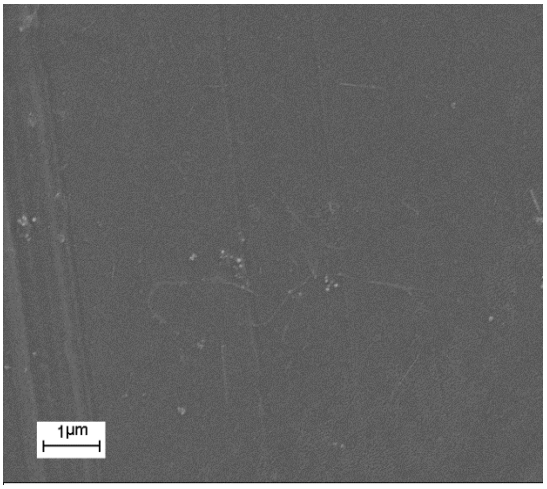

b) SP 2 (10 % SNP)

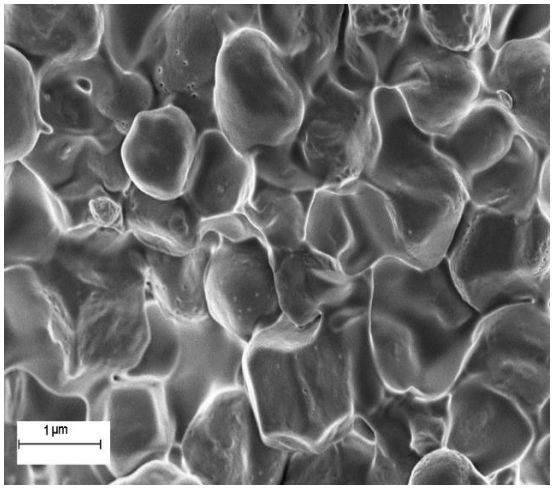

f) SP 2 (10 % SNP)

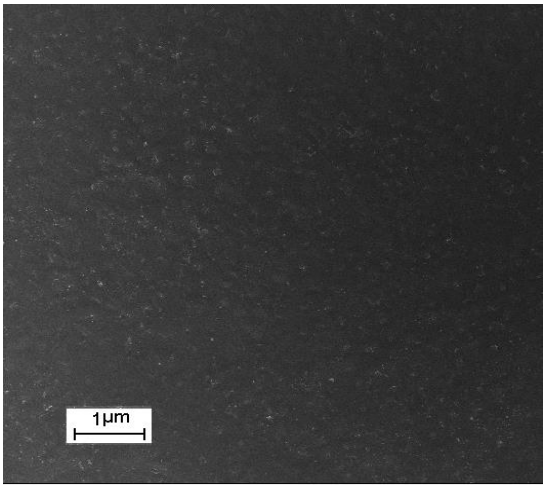

c) SP 3 (20 % SNP)

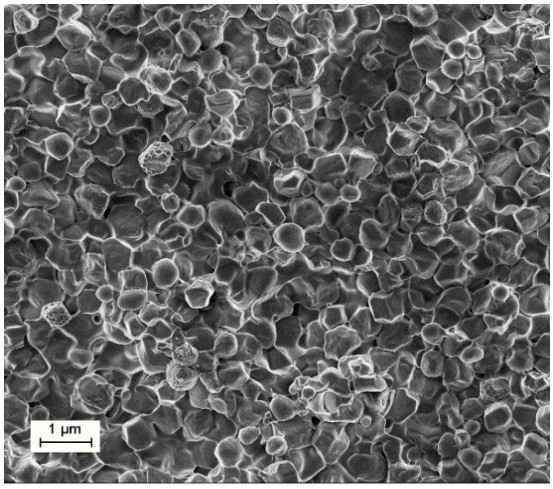

g) SP 3 (20 % SNP)

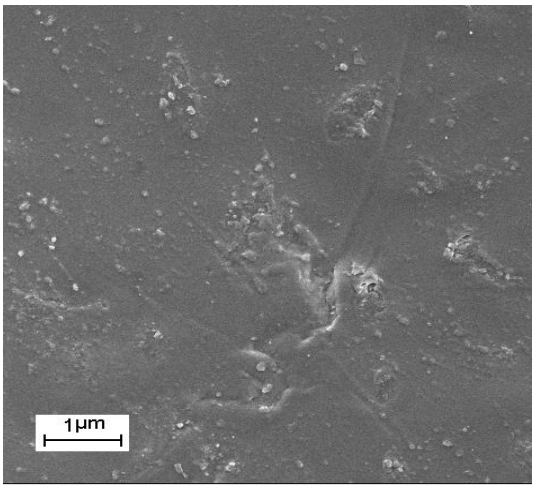

d) SP4 (30 % SNP)

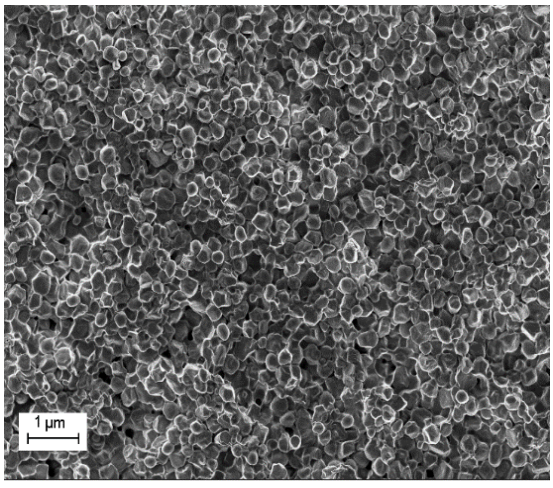

h) SP4 30 % SNP

Figure 5.2 FESEM images of films a) SP1, b) SP2, c) SP3, and d) SP4 are the surface microstructure views, and e) SP1, f) SP2, g) SP3, and h) SP4 are the cross-sectional view of film.

The ultrasound-assisted uniform distribution of the SNPs in the film can be clearly observed in the cross-sectional view of the FESEM images. The FESEM in Figure 5.2 (a, b, c, and d) shows a top view of the film. When the SNP nanofiller dispersed in the PU matrix using ultrasonic irradiation, there will be a significant structural modification in the PU polymer complex. The FESEM in Figure 5.2 (e, f, g, and h) shows cross section view of the films for the understanding of the dispersion of SNPs along the thickness of the nanocomposite film. The images are taken for top view and cross section in of the PU starch nanocomposite film. It is clearly shows from the cross section of sample that with increase in the loading of starch nanoparticles from (5 to 30 wt %, all right hand side Figure 5.2) in PU matrix, this is clearly shows that using ultrasound irradiation, more number of entanglement of starch nanoparticles occurs in PU due to enhanced shearing effect.

The addition of nanoparticles induces the additional molecular bonding and interaction in the PU polymer complex. These additional molecular interactions develop the higher mechanical and thermal properties in the nanocomposite films. The increase in number of SNP per unit volume of polymer not only induces additional strength but also additional water and bacterial barrier to the PU matrix. Thus, the mechanical agitation is ineffective to achieve better dispersion over ultrasound assisted technique for starch nanoparticles loading into PU. The hydroxyl and sulphate functional group on the surface of SNP develops the linkages with the polyethers or ester-based polyols from the PU polymer solution. These linkages are barely strong which provides the additional and stable support to the flexible PU structure. The new linkages with in the SNP centered PU dominated in the nanocomposite film due to which significant reduction in the flexibility of the native PU polymer matrix was observed. Several factors affect the homogeneity of the nanocomposite film [39]. Flocculation, coagulation, and agglomeration should be prevented during the homogenization of the SNP with the polymer matrix [40]. During the preparation of composites above 30 % SNP additions, these phenomena are very common, thus the synthesized films show lumps of SNP, and uneven distribution across the film surface. The uneven distribution of SNP is a major issue due to which the strength, barrier properties, and thermal properties of nanocomposite can be affected [41].

5.4.2 Thermal-physical properties of the SNP-PU thin film

Differential scanning calorimetry (DSC), and thermogravimetric analysis (TGA), have been used to evaluate thermal properties of SNP in PU polymer solution. Better heat resistance is achieved by using a thermosetting polymer in conjunction with SNPs as a nanofiller in the PU polymer. The SNP addition in PU results in a wide thermogram from 64 ^{o}C to 93 ^{o}C. There

had been no consistent mixing of the components. Table 5.1 shows effective T_g and Tm for the thin films of individual nanocomposite films.

Table 5.1 DSC analysis of SNP-PU nanocomposites film.

	Film composition	T_g (^oC)	T_m (^oC)	-ΔH (J g^{-1})
PU	100 % PU	33.6	64.7	3.34
SP1	5 % SNP + 95 % PU	38.1	73.2	8.51
SP2	10 % SNP + 90 % PU	42.3	80.9	11.29
SP3	20 % SNP + 80 % PU	47.8	87.6	14.89
SP4	30 % SNP + 70 % PU	51.2	93.3	17.33

The significant difference in the T_g was observed for the nanocomposite film as the SNP concentration increased. The second order transition temperature T_g and melting point temperature T_m rise by a few degrees, which significantly increases the processibility. At the 30 % SNP addition, the (T_m-T_g) increases to 42 ^{o}C, but for PU film it was observed to have 31 ^{o}C only. This increasing temperature (T_g) from 33.6 ^{o}C to 47.8 ^{o}C will help to enhance the coating application temperature. The significant shift in the T_g of the nanocomposite was attributed to the additional crystallinity provided by the SNPs.

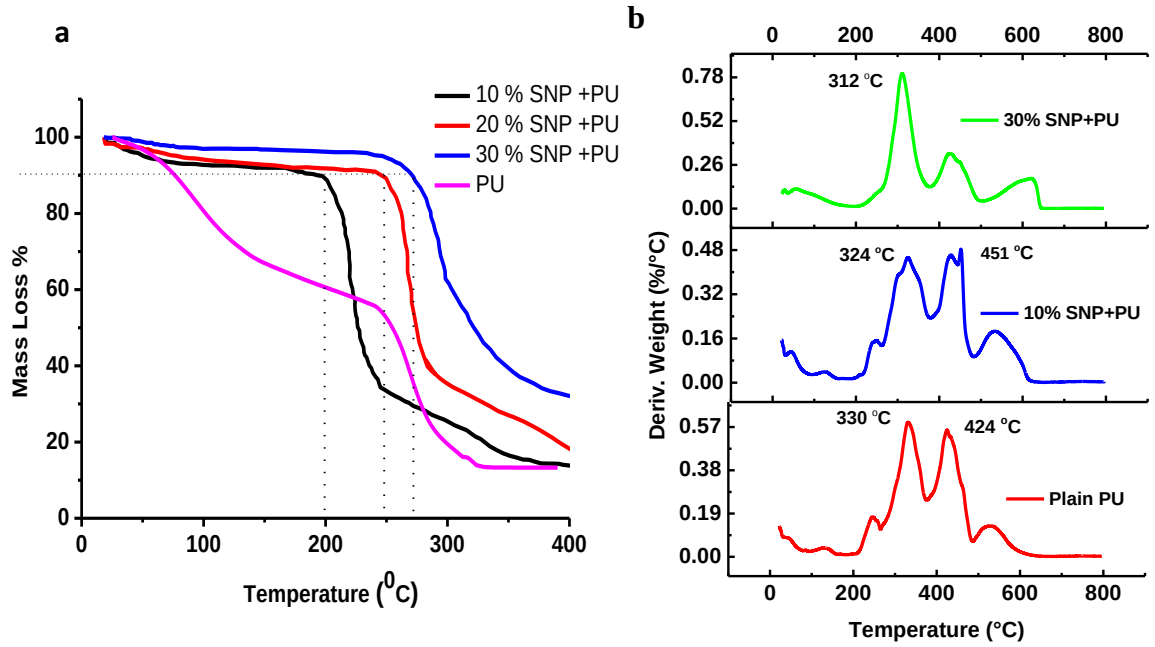

Figure 5.3 Thermal degradation of the nanocomposite films with different composition of SNP and PU a) TGA and b) DTG

The crystallinity of the nanocomposite film increases with the SNP concentration in nanocomposite films. The thermal decomposition of composite film was studied using a first

derivative plot of weight % with respect to temperature. Figure 5.3 illustrates the decomposition nature of different nanocomposite films against temperature. The rise in the -ΔH corresponds to the additional SNP mass in the polyurethane solution. The crystalline structure of the synthesized SNP blend with the PU solution develops the homogeneous suspension. The interaction between the surface activated SNP granules and the PU solution is the prominent reason behind the rise in the -ΔH observed during the DSC of nanocomposite film. The hydrogen linkages in the SNPs and PU solution requires additional energy for the disengagement which results in higher energy difference with the addition of SNP. There is rise in the -ΔH occurs, when starch nanoparticles are added into the PU composite. The phenomena responsible for it is the local nucleation and crystallinity. The SNP concentration rise in the PU solution develops the hydrogen primary linkages as well as secondary linkages in terms of sulphates functional group. All these are responsible for the need of additional energy during the thermal decomposition of nanocomposite. With more addition of the starch nanoparticles there will significant improvement occurs in the crystallization process i.e. the more number of polymeric changes are surrounded near the starch nanoparticles [42].

Figure 5.2 shows that as the concentration of SNP in the PU solution increases, the compactness of the film increases significantly. The melting energy will be higher as the compactness of the film increases [46, 47]. The presence of SNP requires a significant amount of enthalpy, Table 5.1 illustrates that, as with a 5 % addition of SNP, the enthalpy rise is about 5 J g-1. However, adding more SNP to PU solution results in significantly lower enthalpy additions, which are around 3 J/g for each 10 % SNP increase. The additional energy at an initial 5 % SNP can be attributed to higher PU-SNP interaction. At lower concentrations of SNP, higher polymeric interaction requires more energy. At higher concentrations, SNP granules become closer together and surface interaction increases. This leads to a lowering of the energy requirement per g of SNP granule. Table 5.1 shows that increasing the concentration of SNP in PU solution from zero to 5 % increases the change in enthalpy per gm of nanocomposite film by 5 J. Furthermore, for a similar 10 % rise in SNP concentration, the enthalpy change is 8 J /g [43].

Thermogravimetric analysis (TGA) and differential thermal analysis (DTA) of the thermoset composite thin sheets are shown in Figure 5.3. TGA was carried out to understand the thermal stability and weight loss when increasing from room temperature to 800 °C at a rate of 10 °C/min. Initial weight loss was 10 % for the pure PU thin sheet, which was observed to be below 100 °C due to the loss of volatile components present in the solution and moisture. A major weight loss of 40 % occurred when the sample was heated from 200 to 300 °C. Both of

the losses were due to the presence of low molecular weight components and amorphous components present in the PU. However, the addition of SNP to the PU solution shows higher resistance to thermal degradation. The reason behind it could be the strong linkages between the sulphate and hydroxyl functional group in associated with the free end of polyurethane during the blending of SNP to PU. The polyethers or ester-based polyols where active in the PU polymer solution generates the strong linkages between the hydroxyl and sulphate functional group on the surface of starch nanoparticles. These linkages are much stronger and rigid in nature. Thus, the nanocomposite thin films shows higher rigidity in comparison with native polyurethane films. These increase in the rigidity with the SNP additions results in the delayed in the second stage mass degradation in the nanocomposite films. The energy required for the second stage degradation was more due to additional energy required for the breaking of hydroxyl and sulphate functional group from SNP bonded with the polyethers or ester-based polyols from the PU suspension. Also, from the TGA analysis, it was confirmed that the degradation rate of nanocomposite film get decreases as the SNP composition increases in the nanocomposite thin films. The results show that the first weight loss of 10 % in the SNP added thin composite sheets occurred at a temperature of 200 to 300 °C, which is much more than basic PU thin films. In this first stage of mass loss was observed due to the amount of moisture present in thin sheet. As reported by Liu et al. [44] starch shows the first degradation at about 100 ^{o}C, whereas second stage of degradation was observed around 350 ^{o}C. The SNP dispersed using US in the PU solution shows additional energy requirement for the degradation of complex with respect to virgin PU.

As the weight percent of SNP in the PU solution increases, the resistance to thermal degradation also increases. The degradation window for the PU film was observed in between 100 to 300 ^{o}C. However, the SNP added nanocomposite shows higher degradation window which is starts from 200 ^{o}C to more than 400 ^{o}C. It could be possible that, addition of SNP in the polymer matrix develops an ionic bond with the PU components. These electrostatic bonds develop heat resistance in the nanocomposite thin sheets. The degradation rate of thin sheets decreases as the quantity of SNP added more. The uniform mixing of the SNP in the PU matrix substantially increases the thermal resistance of the film up to certain limitations. The Multistage decomposition DTG curves also favour the same conclusion as the TGA output of thermal analysis.

5.4.3 Mechanical properties analysis.

The uniform mixing is the key feature to getting the film's effective physical, mechanical, and thermal strengths. These films show the various structural changes that occur when they are exposed to external force. The uniform distribution of the SNPs for each composition helps to strengthen the film through the cross-section. The distribution of force applied on the PU film was divided into the starch granules which provides additional strength to the PU polymer structure. Figure 5.4 shows the mechanical strength characteristics of the nanocomposite films. Figure 5.4 (a) gives the variation of tensile stress of the nanocomposite, whereas Figure 5.4 (b) gives a clear idea of the flexural stress of nanocomposites. The crystalline structure of SNPs acts as an individual nucleus surrounded by the polymer solution. Hydrogen bonds formed between the polymer solution and the surface of the SNP contribute to making the flexible structure of the PU polymer stronger.

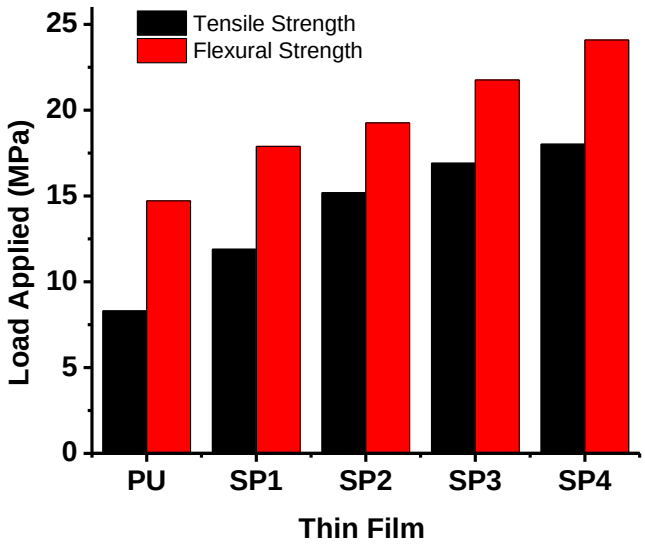

Figure 5.4 Mechanical characteristics of nanocomposite films: a) tensile strength (MPa) and b) flexural strength (MPa).

It was found that as the concentration of nanofiller increases the tensile stress resistance and flexural stress resistance of nanocomposite films rise. The increase in tensile stress indicates a significant improvement in the mechanical strength of PU films. The crystalline nature of SNPs not only gives mechanical strength but also gives stiffness to the PU complex. However, at concentrations above the 25 % SNP, the stress resistance decreased. The force applied to the nanocomposite film develops a uniformly distributed stress along the cross section of the film. When uniformly distributed SNPs interact with each other at higher concentrations, they congregate and begin to agglomerate. These SNP agglomerates are formed in nanocomposites

during elongation. The stress distribution during the force applied to the nanocomposite films does not remain uniform due to the presence of agglomerated SNPs. The stress concentration region forms at the agglomeration site. This stress concentration region developed due to the resistance offered by the agglomerate during the elongation. This induces the breaking of the linkages between the SNPs and the PU solution. The action of separating SNP and PU reduces the overall value of tensile and flexural stress. [45,46]. At the higher concentration of 30 % SNP, the homogeneous SNP interactions within the matrix reduces the strength. As, the PU molecules interaction with SNP overcomes the ultrasound irradiation energy the resultant rise in agglomeration rate of SNP is dominant. This leads to the formation of lumps SNP in the polymer matrix as seen in Figure 5.5 SP4 composition [47].

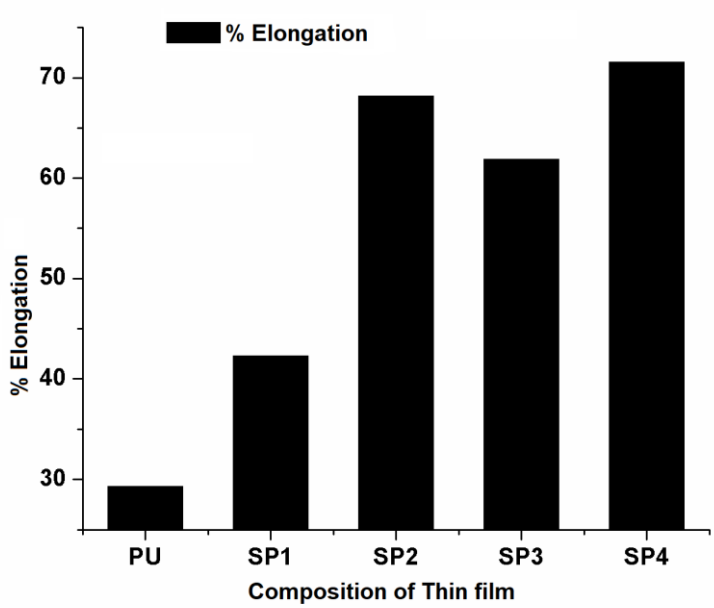

Figure 5.5 Mechanical performance of different SNP compositional thin film.

The lumps of SNP create the stress concentrated area across the polymer matrix under variable load. It can be observed in Figure 5.5 that the percent elongation of nanocomposite films decreases as the SNP composition increases in the film. The crystalline nature of the SNP produces stiffness in the PU film while, the interconnected bonds of the hydroxyl group and the sulphonic functional group offer rigidity to the PU matrix. The additional strength to the PU matrix shows significant variations in percent elongation at lower applied force. The results show that a rise in bond developed due to hydroxyl functional group between PU and SNP will help the nanocomposite matrix to regain its shape and size up to Young's module of elasticity. The rise in % elongation (%E) with increasing SNP concentration implies the increased

Young's modulus of elasticity with the higher SNP concentration until agglomeration starts. The enhancement in percent elongation of nanocomposite film is the function of uniform mixing also, as it helps to avoid the agglomerated lumps of SNP in the polymer matrix. These lumps will generate the stress concentrated area at a particular location which will reduce the film capacity to regain its original shape and size. Thus, the ultimate percent elongation value will be lower down for the nanocomposite film. The uniformly distributed SNP nanofiller connects to the surrounding polymer matrix with strong bond induced due to hydroxyl functional group and provides additional strength against the externally applied force.

A significant increase in mechanical characteristics is seen when substantial thermal blending is carried out, with both the TS and % E increasing, resulting in the formation of toughened films. The % E of the films ranged from 23 to 68 % on average. When the films were subjected to vigorous mixing, it was discovered that the tensile qualities of the films were changed in a variety of ways. As a general rule, films with the highest proportion of TS also had the lowest rate of % E. From Figure 5.5, it can be seen that when nanocomposite films are mixed intensively, they develop a significant degree of toughness as well as a high toughness-to-volume proportion [48]. The % E at the SP3 composition of SNP-PU nanocomposite shows lower value than that of SP4 in the Figure 5.5. The reason behind it could be that the elongation phenomenon in the virgin PU corresponds to the effect of polymeric interactions, i.e., all the monomeric units are linked by strong covalent bonds and show corresponding elongation properties [49]. The addition of SNP nanofiller will induce the directional secondary interactions in the SNP-PU polymer matrix, such as non-covalent bonds and hydrogen bonds. The overall % E of the SNP-PU nanocomposite film will be the cumulative effect of these intermolecular interactions. At lower concentrations of SNP, such as SP1 and SP2, the covalent bonds in the PU polymer complex will be dominant. However, at a higher concentration of SNP at SP4, the % E will be driven by the strength of directional secondary interactions of non-covalent bonds due to SNP nanofiller. At the critical concentration of SP3, the lower value of the % E in SNP-PU nanocomposite film will be due to a cumulative effect for which conventional covalent bonds and additional directional secondary interaction will be responsible [50].

5.4.4 Opacity of the SNP-PU thin film

Measurements of reflectance and transmittance over the visible spectrum are other important properties of these films. The opacity measurement is critical for packing items that are light sensitive. The ratio of light intensity that is incident on the surface of a thin film from a source

to the fraction of light transmitted is defined as the opacity of the film. The transmitted portion of the light will depend on the film thickness and film composition. The resistance to direct transmission of light through the packaging film needs to be optimal enough to maintain the bacterial growth in the packed material, besides the visual appearance. The optimal value of nanofillers is dependent on the required optical density for the packed material.

Transmittance value at a wavelength of 600 nm was noted for the different compositions of SNP-PU nanocomposite film. The baseline comparison was carried out with virgin PU thin film. The observed values of transmittance show a gradual decrease with an increase in SNP composition in the nanocomposite film. This decrease in the transmittance was due to the addition of crystalline SNP to the PU complex. The strong crystalline structure of SNP induces resistance to light traveling through the film. The portion of light incident on the crystalline structure was reflected that was recorded. This reflection increases as the number of SNP increases in the fixed surface area of the thin film, which is nevertheless the concentration of SNP. The optical density of the film is calculated by Equation 5.4. [51]. Table 5.2 shows that as the SNP concentration increases, the optical density of the film decreases significantly. As the increase in compactness of the film with SNP concentration results in a rise in optical density. The observations show clearly that, with the addition of 5 % SNP in pure PU complex, the rise in optical density was about 9 %, whereas, with the addition of 10 % SNP, it was 46 %. The rise in SNP by 20 % and 30 % show a rise in optical density of 69 % and 76 %, respectively. The relative increase from 5 % to 10 % SNP was significant as it showed an 80 % rise in optical density. However, addition above 10 % SNP enhances the optical density by 33 % and 9 %, respectively, for 20 % and 30 % SNP addition.

$$\text{Optical Density} = \text{Log}_{10}(\text{Opacity}) \qquad \text{(Eq. 5.4)}$$

Table 5.2 UV-Vis observations of the thin film [52]

Composition of nanocomposite thin film	Transmittance (T)	Absorbance (A)	Opacity of the thin film	Optical density of the thin film
PU	0.94	0.022	1.02	0.0086
5 % SNP + PU	0.87	0.060	1.23	0.091
10 % SNP + PU	0.73	0.137	2.91	0.464
20 % SNP + PU	0.61	0.215	4.99	0.698
30 % SNP + PU	0.53	0.276	5.87	0.768

5.4.5 Bacterial transmission across the nanocomposite films

The diluted culture after the absorption study was placed on the agar plate to measure the bacterial count. The number of bacteria growing on each plate was determined as discussed in the experimental section, and the total bacterial count in each flask was calculated. The absorbance at 600 nm of the cultures in conical flasks after exposure to the environment was measured and the results are shown in Figure 5.6. The absorbance values were high in the control flask when compared to the flasks sealed with polyurethane films. Though the results were conclusive, we still determined the bacterial count by serial dilution and plating. This might be due to the fact that the flasks sealed with polyurethane film allow bacteria to pass through them while the SNP-PU composite films filter the bacteria present in the external environment. Although the polyurethane film closed flask had bacterial growth, the bacterial count was significantly less than the control.

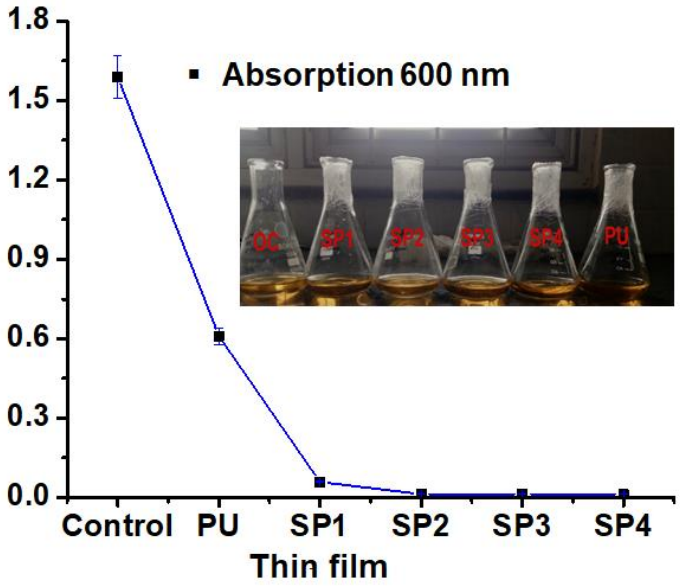

Figure 5.6 Bacterial density using UV spectroscopy

It was found that the control flask had a high bacterial count of 5 x 109, whereas the flask sealed with PU films had a bacterial count of 2.5 x 10^3. The conical flasks sealed with SP1, SP2, SP3, and SP4 did not have any bacteria growing in them. The commonly found E. coli was used for the experiments. The size of E. coli varied from 1.0 to 2.0 μm in length with a radius of about 0.5 μm [53]. However, the pore size of virgin PU synthesised by the casting method was reported to be between 50 to 100 μm [54]. From the experimental results in the Figure 5.6, it can be concluded that ultrasonically dispersed SNP gets occupied in the pore of the PU complex. The uniform distribution of SNP in the PU solution reduces the overall pore

size of nanocomposite thin film. This phenomenon of nanofilling helps to develop resistance to bacterial as well as air passages through the thin sheet [55,56].

The compact structures of the film were attributed to the ultrasonic irradiation during the blending of the SNP and PU. The rate of transmission of bacteria across the film from a bacteria-rich environment to a closed culture inside the flask was decreases due to the narrower pore size of the nanocomposite film [57,58]. The nanocomposite film shows higher resistance to even 24 h of continuous environmental exposure. Thus, bacterial resistance at the lower additional SNP in the PU matrix is positive for its packaging application. This again shows that the polyurethane films have the ability to filter microorganisms from the external environment, but the efficiency is far less than the SP films [52].

5.4.6 Barrier performance of nanocomposite thin film.

5.4.6.1 Water vapour permeability (WVP)

The transmission rate of water vapour through the micropores of the thin film is significant for packaging applications. The average 50 µm thick thin film with the 78.54 cm^2 area was used for the experimentations. The observed results are shown in Figure 5.7. The SNP was added uniformly in the PU complex producing a uniform PU-SNP film structure. The WVP varies with the surrounding temperatures and concentration of SNP in nanocomposite film.

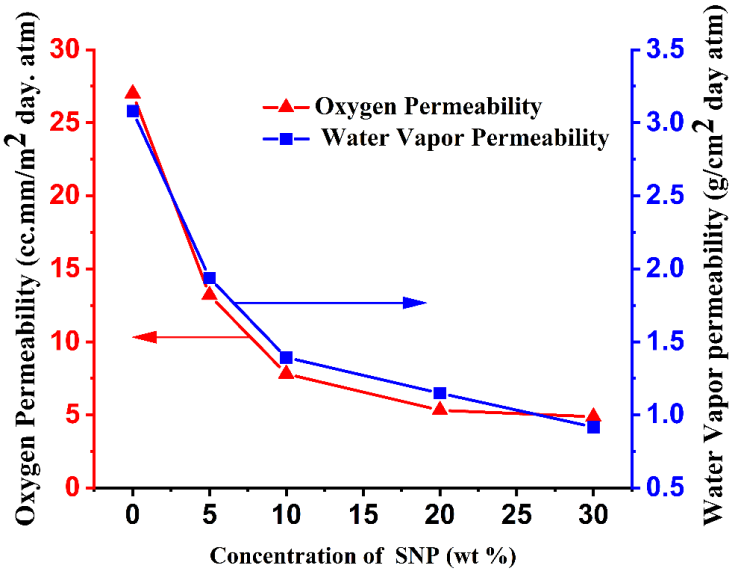

Figure 5.7 Water vapour and oxygen barrier performance of composite thin film

In the previous discussion from Figure 5.2, it was clear that as the SNP density increases the compactness in the composite film also increases. This phenomenon reduces the pore size of

SNP-PU composite film due to which the rate of transmission of vapours across the thickness of film reduces. The travel time of water vapours increases as the thickness of the film increases. At the higher thickness, the diffusion of water vapor across the plane of the film may also be the reason for the reduction of WVP across the film. Another important parameter is the surrounding temperature. The rise in the temperature directly affects the gross humidity across the film [21,59].

The humidity difference leads to the higher pressure gradient across the film which is the reason for the higher WVP. The observations from the experiments indicate that at the higher temperature the WVP increases. The higher concentration of SNP (30 %) shows the lowest WVP about 0.917 g pa^{-1} cm^{-2} day^{-1}, which is again increasing at higher temperatures. This may cause a higher diffusion rate of water vapor across the thin film at higher temperatures above 35 ^{o}C. At higher temperatures, the vapor pressure is overcome by the static pressure leading to a higher pressure drop across the film. The relative humidity inside the vessel increases with the rise in the temperature [60]. The higher difference in relative humidity across the film was the driving force for the higher molecular transformation. Similar results for the starch glycerol films were reported by Miranda et al. [61]. The film with the addition of 20 % concentration of SNP shows an effective reduction of 60 % WVP and above. At higher addition of SNP in the polymer complex, the formation of lumps was detected.

5.4.6.2. Oxygen barrier of nanocomposite thin film.

Figure 5.7 illustrates the effect of SNP concentration enhancement in the nanocomposite complex for the water vapor and oxygen transmission through the thin film. The specimen used for the analysis was with a uniform thickness of 200 µm. The synthesized thin film with the specific (dia. 50 mm) dimension was placed. The transmission rate of oxygen was reduced as the % SNP increased in the composite film. The addition of 5 % SNP in the composite thin film shows the drastic reduction in oxygen permeability. The results observed from the experiments show 44 % reduction in oxygen permeability with the addition of 5 % SNP. However, the permeability reduction rate was reduced after 5 % SNP. With the addition of 10 % SNP, a permeability reduction of 65 % was observed. The reduction of 75 % and 84 % were observed with the addition of 20 % and 30 % SNP respectively. The uniform distribution of SNP in the PU matrix will reduce the pore size at the lowest stage, this will make thin-film most impermeable.

The synthesized nanocomposite SNP-PU films shows a lower operating stress zone between tensile stress and flexural stress. The effective reduction in WVP to 60 to 85 %, makes the film

valuable for packaging applications at lower temperature conditions. At lower temperatures up to 40 ^{o}C, the film shows higher thermal stability, resistance against bacterial (99 %), water vapor transformation and higher mechanical properties make it suitable as a packaging material. The extent of acid hydrolysis with ultrasound assistance was enhanced significantly in the starch granules during the synthesis of SNP. The process is robust and produces a batch of SNPs with a nanoscale size. The SNP-based PU nanocomposite thin film shows enhanced mechanical and thermal moisture barrier performance. These films exhibit higher resistivity for water vapour and oxygen permeability. Further, significant improvement is observed barrier to the bacteria microbes which have prominent applications in food packing.

5.5 Conclusions

The synthesis of uniform distribution of starch nanoparticles in PU was achieved with ultrasound assistance. The rise in the concentration of starch nanofiller in the PU matrix enhanced the mechanical and thermal properties of the thin film. Ultrasound assisted acid hydrolysis showed lower particle size of SNPs compared to conventional synthesis process, hence there is improved performance due to increase in the local crystallinity. The synthesized nanocomposite films show 99 % resistance to bacterial transformation. The optimal value of the SNP to achieve the maximum bacterial transformation resistance is 5 %. The glass transition temperature of nanocomposite films shows an increasing pattern as the percentage of SNP increases in the PU complex. The increase in the glass transition temperature is due to increase in the overall crystallinity imparted by uniform dispersion of starch nanoparticles in the PU matrix. The uniform distribution of SNP in the polymer complex reduces the pore size of the film surface as compared to the plan PU film. The water vapour permeability (WVP) of the film was affected by the temperature of the surroundings and the concentration of SNPs in the film. Overall with the addition of 20 % SNP, the WVP reduced to 60 %, whereas oxygen permeability was reduced to 75 %. The opacity of the film decreased as the SNP concentration increased, the film became more rigid, and the flexural stress of the thin film showed a reduction with a rise in SNP concentration. The tensile strength of the film increased by the addition of SNP which implies the rise in young's modulus of the film. At lower temperatures up to 40 ^{o}C, the prepared SNP-PU nanocomposite film showed higher thermal stability, resistance against bacterial, water vapour transformation, and higher mechanical properties making it suitable as a packaging material.

References

[1] A. Pluta-Kubica, E. Jamroz, G. Khachatryan, A. Florkiewicz, P. Kopel, Application of Furcellaran Nanocomposite Film as Packaging of Cheese., Polymers (Basel). 13 (2021). https://doi.org/10.3390/polym13091428.

[2] M.R. Sharaby, E.A. Soliman, A.B. Abdel-Rahman, A. Osman, R. Khalil, Novel pectin-based nanocomposite film for active food packaging applications., Sci. Rep. 12 (2022) 20673. https://doi.org/10.1038/s41598-022-25192-4.

[3] L. Dai, C. Qiu, L. Xiong, Q. Sun, Characterisation of corn starch-based films reinforced with taro starch nanoparticles, Food Chem. 174 (2015) 82–88. https://doi.org/10.1016/j.foodchem.2014.11.005.

[4] S.S. Low, M. Yew, C.N. Lim, W.S. Chai, L.E. Low, S. Manickam, B.T. Tey, P.L. Show, Sonoproduction of nanobiomaterials – A critical review, Ultrason. Sonochem. 82 (2022) 105887. https://doi.org/10.1016/j.ultsonch.2021.105887.

[5] A. Rahaman, A. Kumari, X.A. Zeng, M. Adil Farooq, R. Siddique, I. Khalifa, A. Siddeeg, M. Ali, M. Faisal Manzoor, Ultrasound based modification and structural-functional analysis of corn and cassava starch, Ultrason. Sonochem. 80 (2021) 105795. https://doi.org/10.1016/j.ultsonch.2021.105795.

[6] M.A. Javaid, K.M. Zia, A. Iqbal, S. Ahmad, N. Akram, X. Liu, H. Nawaz, M.K. Khosa, M. Awais, Utilization of waxy corn starch as an efficient chain extender for the preparation of polyurethane elastomers, Int. J. Biol. Macromol. (2020) 116544. https://doi.org/10.1016/j.ijbiomac.2020.01.011.

[7] N. Zheng, L. Wang, Z. Sun, The effects of ultrasonication power and time on the dispersion stability of few-layer graphene nanofluids under the constant ultrasonic energy consumption condition, Ultrason. Sonochem. 80 (2021) 105816. https://doi.org/10.1016/j.ultsonch.2021.105816.

[8] E.A. Alenyorege, H. Ma, I. Ayim, F. Lu, C. Zhou, Efficacy of sweep ultrasound on natural microbiota reduction and quality preservation of Chinese cabbage during storage, Ultrason. Sonochem. 59 (2019) 104712. https://doi.org/10.1016/j.ultsonch.2019.104712.

[9] A. Inui, A. Honda, S. Yamanaka, T. Ikeno, K. Yamamoto, Effect of ultrasonic frequency and surfactant addition on microcapsule destruction, Ultrason. Sonochem. 70 (2021) 105308. https://doi.org/10.1016/j.ultsonch.2020.105308.

[10] S. Bel Haaj, A. Magnin, C. Petrier, S. Boufi, Starch nanoparticles formation via high

power ultrasonication, Carbohydr. Polym. 92 (2013) 1625–1632. https://doi.org/10.1016/j.carbpol.2012.11.022.

[11] L. Zhou, X. He, N. Ji, L. Dai, Y. Li, J. Yang, L. Xiong, Q. Sun, Preparation and characterization of waxy maize starch nanoparticles via hydrochloric acid vapor hydrolysis combined with ultrasonication treatment, Ultrason. Sonochem. 80 (2021). https://doi.org/10.1016/j.ultsonch.2021.105836.

[12] M. Girard, F. Bertrand, J.R. Tavares, M.-C. Heuzey, Rheological insights on the evolution of sonicated cellulose nanocrystal dispersions, Ultrason. Sonochem. 78 (2021) 105747. https://doi.org/10.1016/j.ultsonch.2021.105747.

[13] S. Sumitomo, H. Koizumi, M.A. Uddin, Y. Kato, Comparison of dispersion behavior of agglomerated particles in liquid between ultrasonic irradiation and mechanical stirring, Ultrason. Sonochem. 40 (2018) 822–831. https://doi.org/10.1016/j.ultsonch.2017.08.02.

[14] E.A. Serna-Galvis, J.F. Guateque-Londono, J. Silva-Agredo, J. Porras, Y. Avila-Torres, R.A. Torres-Palma, Superior selectivity of high-frequency ultrasound toward chorine containing-pharmaceuticals elimination in urine: A comparative study with other oxidation processes through the elucidation of the degradation pathways, Ultrason. Sonochem. 80 (2021). https://doi.org/10.1016/j.ultsonch.2021.105814.

[15] S. Kalia, A. Dufresne, B.M. Cherian, B.S. Kaith, L. Averous, J. Njuguna, E. Nassiopoulos, Cellulose-based bio- and nanocomposites: A review, Int. J. Polym. Sci. 2011 (2011). https://doi.org/10.1155/2011/837875.

[16] P. Kampeerapappun, D. Aht-ong, D. Pentrakoon, K. Srikulkit, Preparation of cassava starch/montmorillonite composite film, Carbohydr. Polym. 67 (2007) 155–163. https://doi.org/10.1016/j.carbpol.2006.05.012.

[17] P.G. Seligra, C. Medina Jaramillo, L. Fama, S. Goyanes, Biodegradable and non-retrogradable eco-films based on starch-glycerol with citric acid as crosslinking agent, Carbohydr. Polym. 138 (2016) 66–74. https://doi.org/10.1016/j.carbpol.2015.11.041.

[18] H. Dai, P.R. Chang, F. Geng, J. Yu, X. Ma, Preparation and properties of starch-based film using N,N-bis(2-hydroxyethyl)formamide as a new plasticizer, Carbohydr. Polym. 79 (2010) 306–311. https://doi.org/10.1016/j.carbpol.2009.08.012.

[19] M.C. Galdeano, S. Mali, M.V.E. Grossmann, F. Yamashita, M.A. Garcia, Effects of plasticizers on the properties of oat starch films, Mater. Sci. Eng. C. 29 (2009) 532–538. https://doi.org/10.1016/j.msec.2008.09.034.

[20] J.H. Jagannath, C. Nanjappa, D.K. Das Gupta, A.S. Bawa, Mechanical and barrier

properties of edible starch-protein-based films, J. Appl. Polym. Sci. 88 (2003) 64–71. https://doi.org/10.1002/app.11602.

[21] A.S. Abreu, M. Oliveira, A. De Sa, R.M. Rodrigues, M.A. Cerqueira, A.A. Vicente, A. V. Machado, Antimicrobial nanostructured starch based films for packaging, Carbohydr. Polym. 129 (2015). https://doi.org/10.1016/j.carbpol.2015.04.021.

[22] H. Angellier, S. Molina-Boisseau, A. Dufresne, Mechanical properties of waxy maize starch nanocrystal reinforced natural rubber, Macromolecules. 38 (2005) 9161–9170. https://doi.org/10.1021/ma0512399.

[23] B.B. Sanchez de la Concha, E. Agama-Acevedo, M.C. Nunez-Santiago, L.A. Bello-Perez, H.S. Garcia, J. Alvarez-Ramirez, Acid hydrolysis of waxy starches with different granule size for nanocrystal production, J. Cereal Sci. 79 (2018) 193–200. https://doi. org/10.1016/j.jcs.2017.10.018.

[24] P. Liu, W. Gao, X. Zhang, B. Wang, F. Zou, B. Yu, L. Lu, Y. Fang, Z. Wu, C. Yuan, B. Cui, Effects of ultrasonication on the properties of maize starch/stearic acid/ sodium carboxymethyl cellulose composite film, Ultrason. Sonochem. 72 (2021). https://doi.org /10.1016/j.ultsonch.2020.105447.

[25] Y. Shen, J. He, Z. Xie, X. Zhou, C. Fang, C. Zhang, Synthesis and characterization of vegetable oil based polyurethanes with tunable thermomechanical performance, Ind. Crops Prod. 140 (2019). https://doi.org/10.1016/j.indcrop.2019.111711.

[26] C.S. Wong, N.I. Hassan, M. Sukor, M.A.P. Serra, J. Alberto, M. Gonzalez, L. Angel, K. Haji, Photo-activated self-healing bio-based polyurethanes, Ind. Crop. Prod. 140 (2019) 111613. https://doi.org/10.1016/j.indcrop.2019.111613.

[27] J. Chen, Q. Wang, M. Luan, J. Mo, Y. Yan, X. Li, Polydopamine as reinforcement in the coating of nano-silver on polyurethane surface: Performance and mechanisms, Prog. Org. Coatings. 137 (2019). https://doi.org/10.1016/j.porgcoat.2019.105288.

[28] M.E. V. Hormaiztegui, B. Daga, M.I. Aranguren, V. Mucci, Bio-based waterborne polyurethanes reinforced with cellulose nanocrystals as coating films, Prog. Org. Coatings. 144 (2020) 105649. https://doi.org/10.1016/j.porgcoat.2020.105649.

[29] H.-C. Zhang, B. Kang, L.-S. Chen, X. Lu, Enhancing toughness of poly (lactic acid)/Thermoplastic polyurethane blends via increasing interface compatibility by polyurethane elastomer prepolymer and its toughening mechanism, Polym. Test. 87 (2020) 106521. https://doi.org/10.1016/j.polymertesting.2020.106521.

[30] H. Zhang, Y. She, S. Song, H. Chen, J. Pu, Improvements of mechanical properties and

specular gloss of polyurethane by modified nanocrystalline cellulose, BioResources. 7 (2012) 5190–5199. https://doi.org/10.15376/biores.7.4.5190-5199.

[31] Y. Lu, L. Tighzert, F. Berzin, S. Rondot, Innovative plasticized starch films modified with waterborne polyurethane from renewable resources, Carbohydr. Polym. 61 (2005) 174–182. https://doi.org/10.1016/j.carbpol.2005.04.013.

[32] M. Yazdi, V. Haddadi Asl, M. Pourmohammadi, H. Roghani-Mamaqani, Mechanical properties, crystallinity, and self-nucleation of carbon nanotube-polyurethane nano composites, Polym. Test. 79 (2019) 106011. https://doi.org/10.1016/j.polymertes ting. 2019.106011.

[33] V.S. Hakke, U.D. Bagale, S. Boufi, G.U.B. Babu, S.H. Sonawane, Ultrasound Assisted Synthesis of Starch Nanocrystals and It's Applications with Polyurethane for Packaging Film, J. Renew. Mater. 08 (2020) 239–250. https://doi.org/10.32604/jrm.2020.08449.

[34] C.A. International, S.T. Method, Standard Test Method for Tensile Properties of Thin Plastic Sheeting, ASTM. 08.01 (2017) 9. https://doi.org/10.1520/D0882-00.

[35] G. Sezonov, D. Joseleau-Petit, R. D'Ari, Escherichia coli physiology in Luria-Bertani broth, J. Bacteriol. 189 (2007) 8746–8749. https://doi.org/10.1128/JB.01368-07.

[36] H.-Y. Kim, S.S. Park, S.-T. Lim, Preparation, characterization and utilization of starch nanoparticles, Colloids Surfaces B Biointerfaces. 126 (2015) 607–620. https://doi.org /10.1016/j.colsurfb.2014.11.011.

[37] J.-L.L. Putaux, S. Molina-Boisseau, T. Momaur, A. Dufresne, Platelet Nanocrystals Resulting from the Disruption of Waxy Maize Starch Granules by Acid Hydrolysis, Biomacromolecules. 4 (2003) 1198–1202. https://doi.org/10.1021/bm0340422.

[38] C.A. International, S.T. Method, Standard Test Method for Oxygen Gas Transmission Rate Through Plastic Film and Sheeting Using a Coulometric Sensor, Cell. 15.10 (2017) 7. https://doi.org/0.1520/D3985-17.

[39] Z. Cherifi, B. Boukoussa, A. Zaoui, M. Belbachir, R. Meghabar, Structural, morphological and thermal properties of nanocomposites poly(GMA)/clay prepared by ultrasound and in-situ polymerization, Ultrason. Sonochem. 48 (2018) 188–198. https: //doi.org/10.1016/j.ultsonch.2018.05.027.

[40] R. Kumar, G. Ghoshal, M. Goyal, Synthesis and functional properties of gelatin/CA–starch composite film: excellent food packaging material, J. Food Sci. Technol. 56 (2019) 1954–1965. https://doi.org/10.1007/s13197-019-03662-4.

[41] M.M. Zerafat, S. Sabbaghi, A comparative study of gelatin and starch-based nano-

composite fi lms modi fi ed by nano-cellulose and chitosan for food packaging applications, Carbohydr. Polym. 189 (2018) 48–55. https://doi.org/10.1016/j.carbpol.2018.02.012.

[42] X. Cao, L. Zhang, J. Huang, G. Yang, Y. Wang, Structure-Properties Relationship of Starch/Waterborne Polyurethane Composites, J. Appl. Polym. Sci. 90 (2003) 3325–3332. https://doi.org/10.1002/app.13079.

[43] C. Medina Jaramillo, T.J. Gutiérrez, S. Goyanes, C. Bernal, L. Fama, Biodegradability and plasticizing effect of yerba mate extract on cassava starch edible films, Carbohydr. Polym. 151 (2016) 150–159. https://doi.org/10.1016/j.carbpol.2016.05.025.

[44] Y. Liu, L. Yang, C. Ma, Y. Zhang, Thermal behavior of sweet potato starch by non-isothermal thermogravimetric analysis, Materials (Basel). 12 (2019). https://doi.org/10.3390/ma12050699.

[45] Y.R. Lee, A. V. Raghu, H.M. Jeong, B.K. Kim, Properties of waterborne polyurethane/functionalized graphene sheet nanocomposites prepared by an in situ method, Macromol. Chem. Phys. 210 (2009) 1247–1254. https://doi.org/10.1002/macp.200900157.

[46] Y. Tang, X. Zhang, R. Zhao, D. Guo, J. Zhang, Preparation and properties of chitosan/guar gum/nanocrystalline cellulose nanocomposite films, Carbohydr. Polym. 197 (2018) 128–136. https://doi.org/10.1016/j.carbpol.2018.05.073.

[47] J. Li, Y. Li, Y. Song, S. Niu, N. Li, Ultrasonic-assisted synthesis of polyvinyl alcohol/phytic acid polymer film and its thermal stability, mechanical properties and surface resistivity, Ultrason. Sonochem. 39 (2017) 853–862. https://doi.org/10.1016/j.ultsonch.2017.06.017.

[48] M. Dick, T.M.H. Costa, A. Gomaa, M. Subirade, A.D.O. Rios, S.H. Flores, Edible film production from chia seed mucilage: Effect of glycerol concentration on its physicochemical and mechanical properties, Carbohydr. Polym. 130 (2015) 198–205. https://doi.org/10.1016/j.carbpol.2015.05.040.

[49] A. Hejna, P. Kosmela, M. Klein, K. Gosz, K. Formela, J. Haponiuk, L. Piszczyk, Rheological properties, oxidative and thermal stability, and potential application of biopolyols prepared via two-step process from crude glycerol, Polym. Degrad. Stab. 152 (2018) 29–42. https://doi.org/10.1016/j.polymdegradstab.2018.03.022.

[50] A. Kulshreshtha, K.J. Modica, A. Jayaraman, Impact of Hydrogen Bonding Interactions on Graft-Matrix Wetting and Structure in Polymer Nanocomposites, Macromolecules.

52 (2019) 2725–2735. https://doi.org/10.1021/acs.macromol.8b02666.

[51] S. Boufi, H. Kaddami, A. Dufresne, Mechanical performance and transparency of nanocellulose reinforced polymer nanocomposites, Macromol. Mater. Eng. 299 (2014) 560–568. https://doi.org/10.1002/mame.201300232.

[52] V.S. Hakke, V.K. Landge, S.H. Sonawane, G. Uday Bhaskar Babu, M. Ashokkumar, E. M. M. Flores, The physical, mechanical, thermal and barrier properties of starch nanoparticle (SNP)/polyurethane (PU) nanocomposite films synthesised by an ultrasound-assisted process, Ultrason. Sonochem. 88 (2022) 106069. https://doi.org/10.1016/j.ultsonch.2022.106069.

[53] N. Hilal, V. Kochkodan, L. Al-Khatib, T. Levadna, Surface modified polymeric membranes to reduce (bio)fouling: A microbiological study using E. coli, Desalination. 167 (2004) 293–300. https://doi.org/10.1016/j.desal.2004.06.138.

[54] M. Nayani, S. Gunashekar, N. Abu-Zahra, Synthesis and characterization of polyurethane-nanoclay composites, Int. J. Polym. Sci. 2013 (2013) 1–5. https://doi.org/10.1155/2013/717895.

[55] P.A. Charpentier, K. Burgess, L. Wang, R.R. Chowdhury, A.F. Lotus, G. Moula, Nano-TiO_2/polyurethane composites for antibacterial and self-cleaning coatings., Nanotechnology. 23 (2012) 425606. https://doi.org/10.1088/0957-4484/23/42/425606.

[56] P. Balakrishnan, M.S. Sreekala, V.G. Geethamma, N. Kalarikkal, V. Kokol, T. Volova, S. Thomas, Physicochemical, mechanical, barrier and antibacterial properties of starch nanocomposites crosslinked with pre-oxidised sucrose, Ind. Crops Prod. 130 (2019) 398–408. https://doi.org/10.1016/j.indcrop.2019.01.007.

[57] S.A. Madbouly, Waterborne Polyurethane Dispersions and Thin Films : Biodegradation and Antimicrobial Behaviors, Molecules. 26 (2021) 961.

[58] B. Sukkaneewat, S. Utara, Ultrasonic-assisted Dunlop method for natural rubber latex foam production: Effects of irradiation time on morphology and physico-mechanical properties of the foam, Ultrason. Sonochem. 82 (2022) 105873. https://doi.org/10.1016/j.ultsonch.2021.105873.

[59] M.S. Sarwar, M.B.K. Niazi, Z. Jahan, T. Ahmad, A. Hussain, Preparation and characterization of PVA/nanocellulose/Ag nanocomposite films for antimicrobial food packaging, Carbohydr. Polym. 184 (2018) 453–464. https://doi.org/10.1016/j.carbpol.2017.12.068.

[60] G. Bang, S.W. Kim, Biodegradable poly(lactic acid)-based hybrid coating materials for

food packaging films with gas barrier properties, J. Ind. Eng. Chem. 18 (2012) 1063–1068. https://doi.org/10.1016/j.jiec.2011.12.004.

[61] C.S. Miranda, M.S. Ferreira, M.T. Magalhaes, A.P.G. Bispo, J.C. Oliveira, J.B.A. Silva, N.M. Jose, Starch-based Films Plasticized with Glycerol and Lignin from Piassava Fiber Reinforced with Nanocrystals from Eucalyptus, Mater. Today Proc. 2 (2015) 134–140. https://doi.org/10.1016/j.matpr.2015.04.038.

Chapter 6. Cellulose nanocrystal: synthesis and functional properties and application in PU nanocomposite for thermal, mechanical and Barrier properties.

6.1 Introduction

Plastic packaging materials are a huge environmental hazard due to their inappropriate disposal and non-biodegradability. As a result, there is a need for environmentally friendly, safe, and nontoxic products [1]. Biopolymers have sparked substantial attention due to their biodegradability, potential as an alternative for synthetic plastic films, comparable cost, availability, and ability to reduce dependency on fossil fuels. Biopolymer-based nanocomposite packaging materials (such as polysaccharide, lipid, or protein) have advantageous mechanical, thermal, biodegradable, chemical-resistant, antibacterial, and gas barrier properties (toward oxygen, moisture, flavors, and lipids). These polymers have the potential to increase the shelf life of perishable foods while staying affordable and straightforward to prepare [2].

6.1.1 An overview of bio-nanocomposites

Cellulose is the most abundant biopolymer, and it plays a vital structural role in plant cell walls. Cellular walls include semicrystalline cellulose microfibrils. In addition, due to its biocompatibility, biodegradability, renewability, environmental friendliness and non-toxicity, cellulose has been attracted more and more attention in the field of biomedical materials. The natural cellulose fibers can be used for reinforcements. Natural cellulose fibers can be used to reinforce biodegradable polymer composites and have been increasingly used as an alternative to talcum and glass fibers for plastic reinforcement. However, the strengths of natural fiber composites are lower than those of the glass fiber composites. This is because of the incompatibility between the generally hydrophobic host polymer matrix and hydrophilic natural fibers, and the lower thermal resistance of the cellulosic material [3]. Furthermore, the mechanical properties of cellulose fibers deteriorate after moisture uptake. Structural modification of the cellulose fiber surfaces, e.g., by chemical grafting and physicochemical treatments, is therefore necessary. Such modifications can improve the interfacial adhesion between the two phases; they can also improve the mechanical properties, biodurability, and weathering ability of the corresponding surface. However, a strength and stiffness equal to or surpassing those of glass fibers cannot be obtained with unmodified cellulosic fibers. Such high strength and stiffness have been achieved by using regenerated cellulose fibers as one of the cellulose derivatives and nanoscale cellulose particles [4].

Bio-based composites have many advantages over inorganic composites due to their non-food agricultural economy foundations, specific strength and modulus, reactive surface that can be used to graft certain groups, high sound attenuation properties, combustibility, and flexibility to avoid fracture during production. Thermoplastic matrix composites are suitable for manufacturing complex things due to their low processing costs and flexible design. Because thermosetting polymers lack molecular mobility, they cannot be melted and recycled like thermoplastics. 20 years ago, Favier et al. [5] reported the first investigation on the reinforcing of composites using cellulose nanofibers. They reported that polysaccharides have piqued the interest of many researchers in polymer nanocomposites due to the excellent intrinsic properties of nanocrystals, including their nanosized dimensions, high surface area, biodegradability, nontoxicity, renewability, low density, and ease of modification provided by the large number of surface hydroxyl groups.

The compatibility of the cellulose nanoparticles with the base polymer plays an important role in the synthesis of bionanocomposites. Thermoplastics and thermosets are composed of long, chain-like molecules with varying molecular linkages. In thermoplastics, weak van der Waals forces hold long chain molecules together, whereas thermosetting requires strong covalent bonds [6]. Plastic reinforcing with suitable fillers increases the mechanical qualities and usefulness of the material. In this way, lignocellulosic resources outperform inorganic fillers and are critical to a sustainable global economy. Finally, because of their renewable nature, wide availability of fillers, lignocellulosic fibers offer many advantages over synthetic fibers [7]. Polyurethane (PU) elastomer's unique physical and chemical properties, as well as its widespread industrial applications in fields as diverse as biomedicine, transportation, coatings, water treatment membranes, electrical cables, furniture cushioning foams, and food packaging, have piqued the interest of researchers from a wide range of disciplines [8]. Because of its elastomer-plastic admixture, PU has both soft (linear long chains of diols) and stiff (diisocyanate and short-chain molecules) components in its backbone. All of these advantages added to the material's already exceptional strength, wear resistance, and machinability [9]. PU's main drawbacks are its combustibility, which causes a significant amount of smoke to be released, and its weak barrier properties, which restrict its application in both industrial and daily contexts [10].

6.1.2 Nanocomposite synthesis approaches available

The nanocomposite synthesis can be synthesised by several approaches. The major focus of all these methods to achieve the uniform distribution of filler material in the biopolymer. The uniform distribution possibly achieved with the approach. The widely used approach was solvent evaporation and casting process. In the approach for the synthesis of CNC-PU nanocomposite, the most cellulose nanocomposites are manufactured using the solvent casting process with Teflon or propylene dishes. To evaporate solid polymer nanocomposite films, combine adequate nanocellulose solution and dissolved polymer matrix. According to study reported by Arslan et al. [11], casting/evaporation produces the strongest materials. Because of increased CNC-to-CNC interactions and more uniform matrix filler dispersion. Cellulose nanoparticles must be equally dispersed throughout the polymer in cellulose nanocomposites [12]. Another approach was electrospinning spins which generally employed with cellulose nanofiber from a charged drop of liquid polymer using an electric current [13]. Continuous nanoscale material synthesis at low cost is made possible by electrostatic forces. Electrospinning can handle biopolymers without causing harm to sensitive molecules due to high pH, temperatures, or pressures [14]. Third approach was layer-by-layer assembly (LbL) is a thin-film manufacturing technique that layers materials with opposing charges. This technique enhances CNC interactions with polar polymeric matrices such as chitosan [15,16]. The multilayered films were formed by hydrogen bonding and electrostatic interactions between the negatively charged sulfate groups of the nanoparticles and the ammonium groups of the chitosan.

The highest mechanical reinforcement effect of CNCs is observed when using unmodified nanoparticles bearing hydroxyl groups and for materials processed by casting/evaporation from a liquid medium in which they are homogeneously dispersed. Asempour et al. [17] created TFN membranes by integrating cellulose nanocrystals (CNCs) into the polyamide active layer. Membranes were created using in situ interfacial polymerization of m-phenylenediamine (MPD) and trimesoyl chloride (TMC) with varying concentrations of CNCs. Aside from the high cost of manufacture and restricted availability of nanoparticles, increased environmental concerns caused by hazardous NP leakage into the permeate and retentate streams have been noted as a key hurdle to the commercialization of nanocomposite reverse osmosis membranes. To address these issues, we added cellulose nanocrysts to the polyamide active layer since they are non-toxic, biodegradable, and renewable. Cellulose nanocrystals were combined with an organic solution of trimesoyl chloride to form a membrane, which was subsequently solidified

via in-situ interfacial polymerization with m-phenylenediamine. A TFN membrane based on CNC technology improves desalination performance. Kang et al. [18] on the other hand utilized the gum arabica as base biopolymer and was well mixed with the CNCs to produce the nanocomposite film for the enhancement of life span of strawberry. The nanocomposite were prepared with solution casting approach and observed to have higher mechanical strength shows lower weight loss in the strawberry after the coating. Polyurethanes are now among the most widely made and used polymers. Coatings, adhesives, foams, rubbers, and fibers are just a few of the various applications. The advancement of PU coating technology has created an alternative approach for manufacturing surfaces that are both hygienic and resistant to microbial contamination. It is straightforward to deposit a thin polymeric top layer in a regulated liquid system, starting with an appropriate solution/dispersion of antibacterial components, and ensures that the coating is successfully charged. The fact that the antibacterial charge may be focused on the surface contributes to its efficacy. When compared to other methods of adding antibacterial compounds, melt compounding delivers greater antibacterial properties. Low density, excellent flexibility, shape memory, high abrasion resistance, corrosion resistance, high elongation at break, damping ability, weathering durability, high elasticity, antiaging, good processibility, high impact strength, excellent gloss, transparency, controllable hardness, high biocompatibility and bio stability, excellent blood compatibility, and good low temperature flexibility are all desirable properties of polyurethane composites. Polyurethane composites' molecular structures may be tweaked to better fulfill specific demands. PUC has a few notable drawbacks when used in high-temperature situations. While polyurethane composites offer many positive attributes, they can have a few drawbacks. These defects include a lack of tensile strength and thermal stability in high-temperature working settings, as well as an inability to resist corrosion. Under these conditions, polyurethane composites readily catch fire and do not adhere well to metal [19].

Polyurethane composite low tensile strength and poor heat resistance are well-known weaknesses. Other properties of polyurethane composites include low thermal and electrical conductivity (EC). By incorporating additional ingredients, nanocomposite materials were created [19] in response to the inadequacies of polyurethane composites. These are the main reasons why polyurethane was selected for this study. The purpose of this research is to enhance the CNC-PU nanocomposite and examine the impact of various CNC dosages incorporated into nanocomposite films. The extended study of cellulose nanocrystals (CNC) used as nanofiller for the polyurethane (PU) solution has been discussed in the present chapter. In terms

of tensile strength and Young modulus, CNC outperform glassfiber. Nanocellulose is a structural component of natural cellulose with several potential uses, including plastic reinforcing, gel formation, and thickening agents [20].

CNCs has improved properties including as crystallinity, tensile strength, and water-holding capacity. When combined with a good polymer matrix, CNCs show a great deal of potential as an efficient reinforcement for premium bio-based composites. The CNC was synthesized using the hydrodynamic cavitation-assisted acid hydrolysis process, and it was subsequently homogenized into the polymer solution using ultrasonic irradiation. To achieve the necessary uniform mixing, ultrasound irradiation was suggested to maximize the CNC uniform dispersion in the PU solution. The present chapter No. 6 discusses the benefits of CNCs quantitative mixing in the PU polymer matrix for nanocomposite production. These nanocomposite films' mechanical, thermal, and microbiological barrier capabilities have been studied and reported on. CNC-PU nanocomposite films may be utilized in packaging applications.

6.2 Methods for synthesis of CNC-PU nanocomposite films.

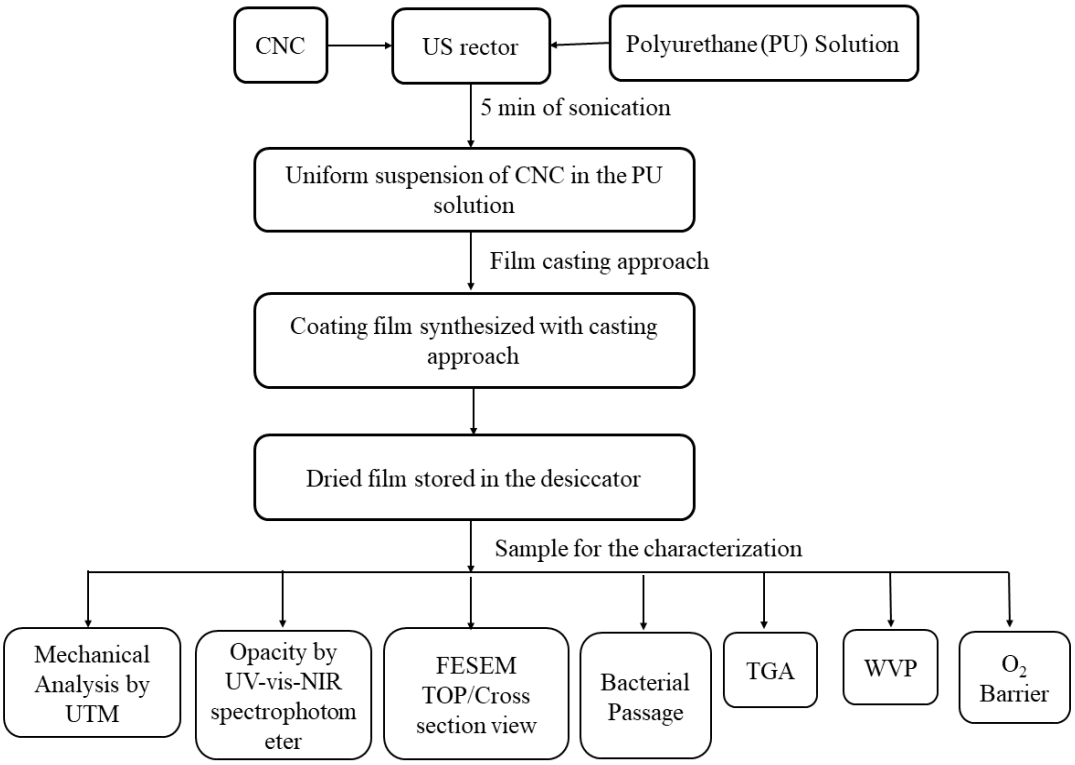

Figure 6.1 Block diagram for the synthesis of CNC-PU nanocomposite thin film

The block diagram illustrated in Figure 6.1 shows the overall process coating film synthesis and its major characterization involved. The dispersion of 205 mg of CNC in deionised water

(50 mL, 200 mL glass beaker) was achieved with the 5 min US irradiation in pulse mode (3 s, on and 2 s off). The pulse mode was utilized to control the temperature of suspension. To enhance the easy interaction and dispersion of CNC in PU solution, the CNC was initially dispersed in deionised water to adjust the viscosity for nanocomposite film preparation to apply on substrate. The dispersion of CNC in solution of PU was accomplished via 20 kHz sonication (5 minutes) at temperature of 20 ^{o}C. The well dispersed CNC-PU nanocomposite suspension than used for next process of thin sheet preparation.

6.2.1 Casting of nanocomposite film

The uniformly blended mixture of CNC and PU was exploited for the synthesis of films through the casting technique. The 200 µm thickness of the nanocomposite sheets of well dispersed CNCs in PU solution was achieved using stainless steel (SS) film applicator 9031 (Samriddhi International Inc, Mumbai India). The produced nanocomposite sheets were then dried with the help of vacuum oven (VT 6025, Thermo Fisher Scientific India Pvt. Ltd.). Films of PU with CNC of 5, 10, and 15 % (wt) were synthesized and examined for variations properties such as mechanical property, transmission resistance to bacteria, and water vapour permeability (WVP) at different temperatures. The 5 % (wt) CNC is blended with the PU solution with the help of ultrasonic irradiation. This suspension is used to synthesize the nanocomposite film denoted as CP1. The different amounts of CNC in the PU polymer matrix are prepared as 5 % (CP1), 10 % (CP2), and 15 % (CP3) to understand the CNC concentration effects on the properties of films. At the higher concentration of CNC in the polyurethane matrix, the lumps of CNC were observed predominantly, as shown in Figure 6.2.

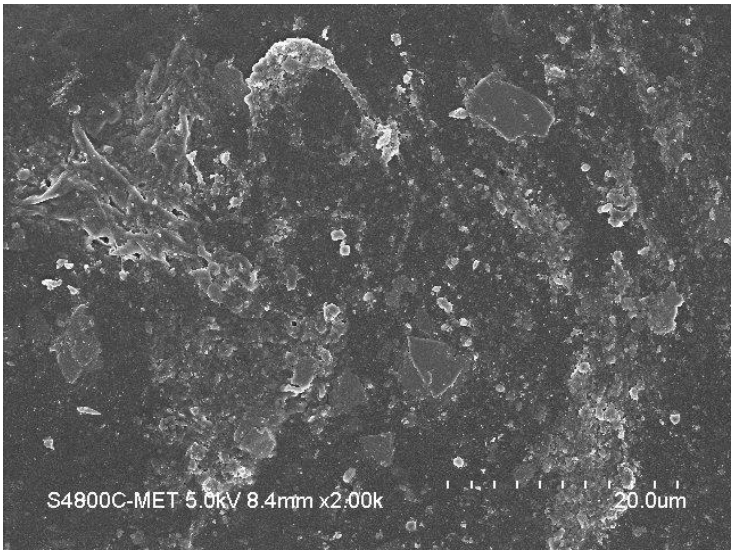

Figure 6.2 The surface image using SEM for 20% (wt %) CNC blended in PU polymer.

Figure 6.2 shows the surface morphology of the CNC (20 %) blend in the PU matrix. The observations from Figure 6.2 shows the difficulty in achieving CNC uniform distribution in the PU matrix. When the tiny structures of CNC interact with the PU polymer at higher concentrations, the possibility of inter-CNC interaction is much higher. These inter-CNC interactions develop the drag pull, due to which some portions of PU polymer and CNC get agglomerated and form lumps. However, at lower concentrations, these inter-CNC interactions are surpassed by the cavitation effect. During the experiments, it was observed that the highest concentration of CNC, which can be uniformly distributed in a PU polymer matrix with ultrasound assistance, is 15 %, which is much lower than that of SNP. Considering the higher concentration of CNC, which could be uniformly distributed in the PU matrix. The three concentrations were chosen as 5, 10, and 15 % of CNC for the blending in the polymer matrix. These different composition films were synthesized and stored in the desiccator to keep them from getting wet and contaminated by bacteria. The film applicator was used for the synthesis of uniform-thickness PU films. The thickness of the film was verified by the digital thickness measurement device from the coating thickness gauge PCE-CT 80 (PCE Instruments UK). The random checks at different points confirm that the film's thickness is 200 µm.

6.3 Characterization of CNC-PU nanocomposite films.

6.3.1 Morphological study of nanocomposite CNC-PU films

Field emission scanning electron microscope (FESEM) (FEI Quanta 200 F integrated with Oxford-EDS system IE 250 X Max 80, Netherlands) 50X to approx. 200,000X, 2 kV to 30 kV, was used to examine the morphology of films. FESEM cross-sectional views of the film verified a consistent distribution of SNPs. The 1X1 cm2 for films was used as sample specimen for the analysis.

6.2.2 Thermal-physical property analysis of films

Thermogravimetric analysis (TGA) was used to estimate the glass transition temperatures of the films and the perfect thermal resistance. The TGA studies were performed on the Perkin-Elmer instrument (TGA 8000, USA) under a nitrogen environment to demonstrate the thermo-physical behaviour of CNC-PU nanocomposite films. An automated Mettler balance was used to weigh 6 samples of the films with a weight of about 5 mg was introduced in the pans. A TA fast press was used to seal the pan after it was put on a spacer insert. The reference was an empty pan with a cover that was sealed to provide a sufficient heat capacity. The film was tested three times and TGA was carried out at a heating rate of 5 ^{o}C min^{-1} from 25 to 350 ^{o}C

with nitrogen gas flowing at a rate of 60 mL min^{-1}. The enthalpy change (H) was calculated using the weight of the film and represented as J g^{-1} of dry matter [21].

6.3.3 Mechanical property analysis of nanocomposite CNC- PU films

The mechanical characteristics of the film were determined using the Universal Testing Machine (UTM) T 150 tensile tester (KLA, India). The mechanical properties were performed using UTM machine as per the ASTM D 882 [22] standard test methods. The specimen (100 mm length x 3 mm thickness x 20 mm breadth) was taken in a tensile machine to determine the tensile strength (TS) for the film with the constant crosshead speed of 5 mm/min.

6.3.4 UV-visible spectrophotometry for the light transmittance and opacity

UV-vis-NIR spectrophotometer (Cary 5000, Agilent technologies, USA) was used to observe the UV-Vis response of the nanocomposite film. The transmission (% T) was noted for different samples considering virgin PU film as the baseline. The individual component transmittance at 600 nm wavelength was noted. Lambert-Beer's equation was used to convert transmittance observation in absorbance. The opacity of films was calculated as per mentioned in chapter 5.

$$\text{Opacity} = \frac{abs_{600}}{X} \qquad \text{(Eq.5.2)}$$

Where, X is the thickness of thin-film in mm [23].

6.3.5 Bacterial passage through nanocomposite CNC- PU thin films.

To understand whether the films allowed the passage of bacteria, the following experiment was carried out. Six sterilized conical flasks were taken and 20 ml sterilized Luria-Bertani broth media was added to each of them. The mouth of the conical flasks was tightly sealed using the films and exposed to the environment for 24 h. One flask was left unsealed to act as a control. After exposure for 24 h, the conical flasks were incubated at 37 ºC for 24 h at 180 rpm. Following this, the absorbance of the culture was measured at 600 nm using a spectrometer (UV-1800 model, Shimadzu Analytical Pvt. Ltd., India). The cultures were then diluted and spread plated on Luria-Bertani agar plates. These plates were maintained at 37 ºC for 12 h and the bacterial count in each agar plate was determined. The total bacterial count in each conical flask was calculated after considering the dilution factor. All experiments were performed in triplicate and the standard error of the mean was calculated.

6.3.6 Determination of water vapor permeability of nanocomposite film.

WVP tests were conducted using ASTM (1996) [26] method E96 with some modifications. Each film sample was sealed over a circular opening of a cylindrical vessel of an opening diameter of 6 cm. The cylindrical vessel was filled with water. The desiccator temperature was monitored by a water-heated thermostat (28 ^{o}C, 35 ^{o}C, 40 ^{o}C) and a temperature measuring indicator was placed inside the desiccator to monitor the temperature. To maintain the relative humidity (RH) across the film, anhydrous calcium chloride (75 % RH) was placed in the desiccator. The effect of temperature on the water vapour transmission from inside vessel to outside through the film was observed. The weight difference of vessel and cross-sectional area of film were used to calculate the water vapours permission rate (WVPR). After the attainment of steady-state (about 32 h), the WVP (g/Pa.s.m) was calculated as equation 5.3.

$$WVP = [WVPR/S(R_1 - R_2)]\ d, \qquad \text{(Eq. 5.3)}$$

Where, S is the saturation vapor pressure of water (Pa) at the test temperature, R_1 is the RH in the desiccator, R_2 is the RH in the permeation cell and d is the film thickness (m) [24].

6.3.7 Oxygen barrier performance of the composite film.

To measure the oxygen permeability of thin films, samples of thin films were examined using the ASTM 3985 standard test [25]. By inserting the test sample in one of the chambers, permeation cells were employed to create a barrier between two compartments. Both chambers were entirely decommissioned. Following that, one compartment was filled with nitrogen, while the other was filled with oxygen. Because of the barrier, oxygen may seep into the nitrogen carrier gas and be transported to the colorimetric detector, causing an electrical current to flow. The signal's strength was related to the quantity of oxygen flowing into the detector.

6.4. Result and discussion

The cellulose nanocrystals (CNC) are dispersed in the polyurethane (PU) polymer solution with the help of ultrasound irradiation for short time period. The cohesion forces were induced in the liquid to produce disruption in the liquid during the cavitation phenomenon. Ultrasonic irradiation creates cavities that collapse resulting in localized high pressures and temperatures, leading to the formation of radicals. Furthermore, the generation of shock waves during bubble collapse significantly improves mass transfer and emulsification processes, two critical factors that influence reaction rates and improve reactant de-agglomeration. Basically, PU has a soft segment matrix with hard domains strewn around. Its mechanical properties are affected by the

degree of nanophase separation. Some polyurethanes (PUs) decay faster than others, and this difference may be explained by looking at their chemical composition. The polyols are soft segment, was often an oligomeric macromonomer with a chain terminated by hydroxyl (-OH) groups and a low glass transition temperature (i.e. ≤ 25 °C).

The extent of the reinforcement is demonstrated to be dependent on factors such as nanofiller dispersion in the polymer matrix and interfacial adhesion between the nanofillers and the polymer matrix [26]. The CNC surface interaction with the polyurethane through the hydroxyl linkages results in the CNC-PU nanocomposite. When the CNC is distributed in the PU solution, it acts as a nucleate. The hydroxyl functional group from the extender associated with the di-isocyanate significantly interacts with the CNC basic structure. During interactions, there is a possibility of water molecule generation and removal with the solvent. The polyols may interact with the sulfate functional group. All of the surface interactions that can occur between CNC nanofiller and PU solution result in a stronger nanocomposite film with respect to the base polymer. The crystallinity of PU polymer films was enhance due to the addition of CNC. The present approach to the solvent evaporation casting method was to generate uniformly CNC distributed PU nanocomposite films. The analysis of the film was discussed in the next section.

6.4.1 Morphological studies of CNC-PU nanocomposite films.

The images are taken for top view and cross section in of the CNC-PU nanocomposite film. It is clearly shows from the cross section that with increase in the loading of CNCs from (5 to 15 % (wt %), all right hand side images) in PU matrix, this is clearly shows that using ultrasound irradiation, more number of entanglement of CNCs occurs in PU due to enhanced shearing effect.

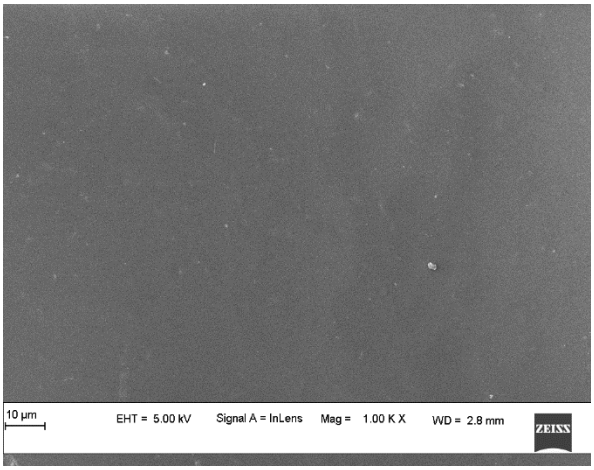

a) CP 1 (5 % CNC)

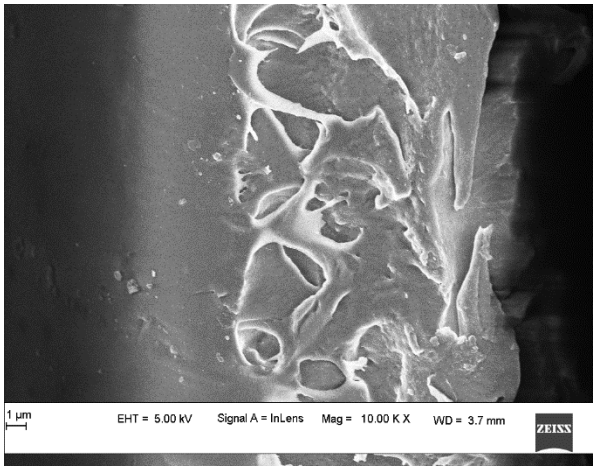

d) CP 1 (5 % CNC)

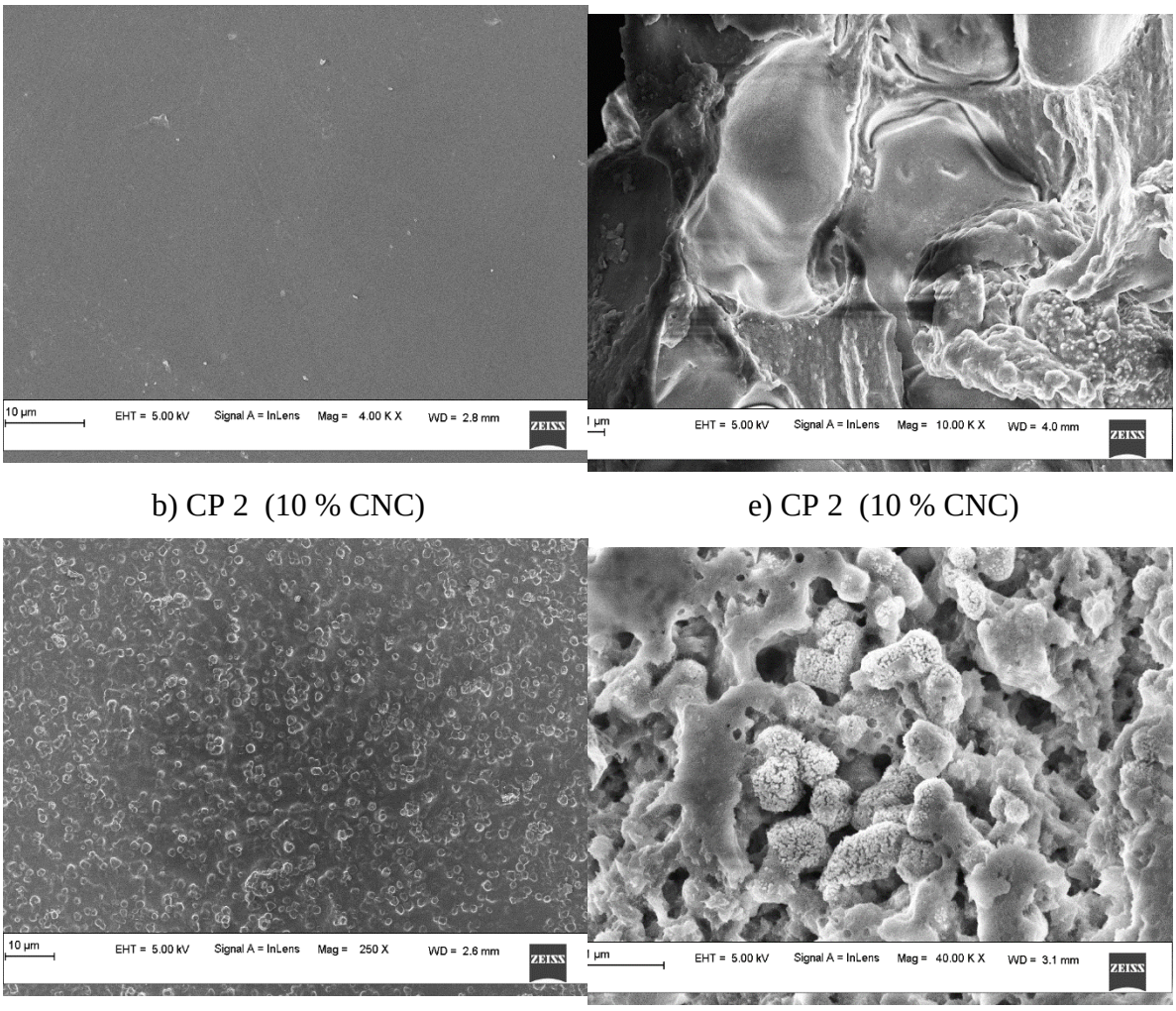

b) CP 2 (10 % CNC) e) CP 2 (10 % CNC)

c) CP 3 (15 % CNC) f) CP 3 (15 % CNC)

Figure 6.3 FESEM images of films a) CP1, b) CP2, and c) CP3 are the surface microstructure views, and d) CP1, e) CP2, and f) CP3 are the cross-sectional view of film.

FESEM images in Figure 6.3 show the top view and cross-sectional view of nanocomposite films with different compositions. Thus, the mechanical agitation is ineffective to achieve better dispersion over ultrasound assisted technique for CNCs loading into PU [31]. The Several factors affect the homogeneity of the nanocomposite film. Flocculation, coagulation, and clotting should be prevented during the homogenization of the CNC with the polymer matrix [32]. During the preparation of composites above 15 % CNC additions, these phenomena are very common, thus the synthesized films show lumps of CNC, and uneven distribution across the film surface. The uneven distribution of CNC is a major issue due to which the strength, barrier properties, and thermal properties of nanocomposite can be affected [27].

6.4.2 Thermophysical properties of the CNC-PU thin film

DSC was used to investigate the CNC-PU nanocomposite thin films. Increased heat resistance was observed in the thermosetting polyurethane in conjunction with CNCs as a nanofiller. The CNC addition in PU results in a wide thermogram from 48 ^{o}C to 104 ^{o}C. Table 6.1 shows effective Tg and Tm for the thin films of individual nanocomposite films. The significant difference in the Tg was observed for the nanocomposite film as the CNC concentration increased. The second order transition temperature Tg and melting point temperature Tm rise by a few degrees, which significantly increases the processability. At the 15% CNC addition, the (Tm-Tg) increases to 56 ^{o}C, but for PU film it was observed to have 31 ^{o}C only. This increasing temperature (Tg) from 33.6 ^{o}C to 48.2 ^{o}C will help to enhance the coating application temperature in various applications. The rise in the ΔH corresponds to the additional CNC mass in the polyurethane solution. The crystalline structure of the synthesized CNC blend with the PU solution develops the homogeneous suspension [33].

The thermal decomposition of composite film was studied using a first derivative plot of weight % with respect to temperature. Figure 6.4 illustrates the decomposition nature of different nanocomposite films against temperature. The interaction between the surface activated CNC granules and the PU solution is the prominent reason behind the rise in the ΔH observed during the DSC of nanocomposite film.

Table 6.1 DSC analysis of CNC-PU nanocomposites film.

	Film composition	T_g (^{o}C)	T_m (^{o}C)	-ΔH (J g^{-1})
PU	100 % PU	33.6	64.7	3.34
SP1	5% CNC + 95% PU	37.1	79.2	23.6
SP2	10% CNC + 90% PU	42.3	92.9	31.9
SP3	15% CNC + 85% PU	48.2	104.6	39.1

There is rise in the ΔH occurs, when cellulose nanocrystals are added into the PU composite. The phenomena responsible for it is the local nucleation and crystallinity. With more addition of the cellulose nanocrystals there will significant improvement occurs in the crystallization process i.e. the more number of polymeric changes are surrounded near the CNCs. Figure 6.3 shows that as the concentration of CNC in the PU solution increases, the compactness of the film increases significantly. The melting energy will be higher as the compactness of the film

increases [46,47]. The presence of CNC requires a significant amount of enthalpy, Table 6.1 illustrates that, as with a 5 % addition of CNC, the enthalpy rise is about 20 J g^{-1}.

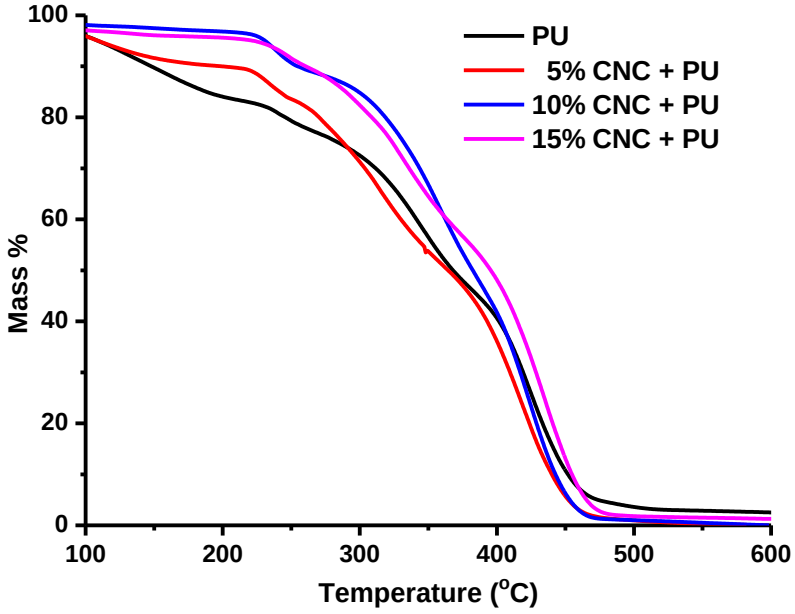

Figure 6.4 Thermal degradation of the nanocomposite films with different composition of CNC and PU

The additional energy at an initial 5 % CNC can be attributed to higher PU-CNC interaction. At lower concentrations of CNC, higher polymeric interaction requires more energy. At higher concentrations, CNC granules become closer together and surface interaction increases. This leads to a lowering of the energy requirement per g of CNC granule. Thermogravimetric analysis (TGA) and differential thermal analysis (DTA) of the thermoset composite thin sheets are shown in Figure 6.4. TGA was carried out to understand the thermal stability and weight loss when increasing from room temperature to 800 °C at a rate of 10 °C/min. Initial weight loss was 10% for the pure PU thin sheet, which was observed to be below 100 °C due to the loss of volatile components present in the solution and moisture. A major weight loss of 40 % occurred when the sample was heated from 200 to 300 °C. Both of the losses were due to the presence of low molecular weight components and amorphous components present in the PU. However, the addition of CNC to the PU solution shows higher resistance to degradation. The results show that the first weight loss of 10 % in the CNC added thin composite sheets occurred at a temperature of 250 to 300 °C, which is much more than basic PU thin films. In this first stage of mass loss was observed due to the amount of moisture present in thin sheet. As reported

by Tang et al. [34] cellulose shows the first degradation at about 110 ^{o}C, whereas second stage of degradation was observed around 340 ^{o}C. The CNC dispersed using US in the PU solution shows additional energy requirement for the degradation of complex with respect to virgin PU. As the weight percent of CNC in the PU solution increases, the resistance to thermal degradation also increases. The degradation window for the PU film was observed in between 100 to 330 ^{o}C.

However, the CNC added nanocomposite shows higher degradation window which is starts from 250 ^{o}C to more than 450 ^{o}C. It could be possible that, addition of CNC in the polymer matrix develops an ionic bond with the PU components. These electrostatic bonds develop heat resistance in the nanocomposite thin sheets. The degradation rate of thin sheets decreases as the quantity of CNC added more. The uniform mixing of the CNC in the PU matrix substantially increases the thermal resistance of the film up to certain limitations. The Multistage decomposition DTG curves also favour the same conclusion as the TGA output of thermal analysis.

6.4.3 Mechanical strength analysis

The uniform mixing is the key feature to get the effective physical, mechanical and thermal strength to the film. These films show the various structural changes when they are exposed to external force. The uniform distribution of the CNCs for each composition helps to strengthen the film through the cross-section. The distribution of force applied on the PU film was divided into the CNCs which provides additional strength to the structure. Figure 6.5 shows the mechanical strength characteristics. Figure 6.5 (a) gives the variation of tensile stress of the nanocomposite, whereas Figure 6.5 (b) gives a observations of the flexural stress variations in the nanocomposites thin film. It can be found that as the concentration of nanofiller increases the tensile stress resistance and flexural stress resistance of nanocomposite films rise. However, at concentrations above the 15 % CNC, the agglomeration of CNCs nanofillers dominates the consistency of the suspension. Thus the maximum concentration of CNCs that can uniformly distributed by the proposed ultrasonic approach was only 15 %. This is because of the agglomeration of CNC nanofiller during the elongation, these agglomerated lumps provide additional repulsive forces to the PU matrix. This action of separation of CNC and PU reduces the overall value of tensile stress as well as the flexural stress. The rise in the tensile stress shows enhancement in the mechanical strength of PU films significantly till 15 (wt %) of CNC concentration. The crystalline nature of CNCs not only gives mechanical strength but also gives stiffness to the PU complex.

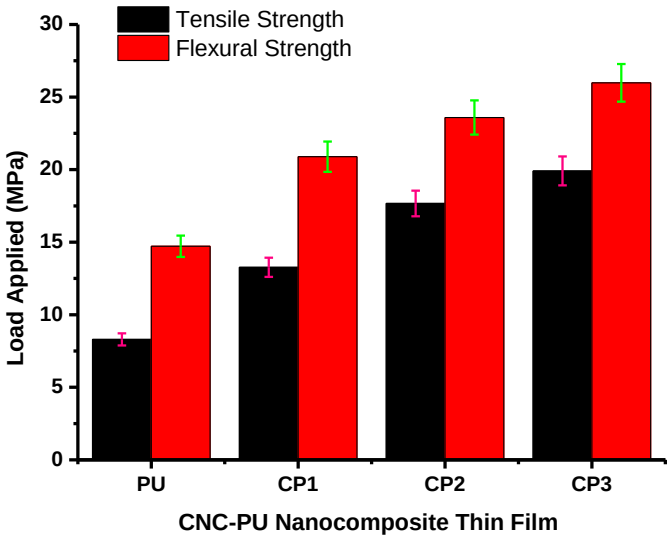

Figure 6.5 Mechanical characteristics of nanocomposite films: a) tensile strength (MPa) and b) flexural strength (MPa).

At the higher concentration of 15 % CNC, the homogeneous CNC interactions within the matrix reduces the strength. As, the PU molecules interaction with CNC overcomes the ultrasound irradiation energy the resultant rise in agglomeration rate of CNC is dominant. This leads to due to the formation of concentrated CNC area in the polymer matrix, at higher concentration as seen in Figure 6.3 [35]. The lumps of CNC create the stress concentrated area across the polymer matrix under variable load. The crystalline nature of the CNC produces stiffness in the PU film while, the interconnected bonds of the hydroxyl group and the sulphonic functional group offer rigidity to the PU matrix. The additional strength to the PU matrix shows significant variations in tensile stress at lower applied force. The results show that a rise in bond developed due to hydroxyl functional group between PU and CNC will help the nanocomposite matrix to regain its shape and size up to Young's module of elasticity. These lumps will generate the stress concentrated area at a particular location which will reduce the film capacity to regain its original shape and size. Thus, the ultimate percent tensile stress value will be lower down for the nanocomposite film. The uniformly distributed CNC nanofiller connects to the surrounding polymer matrix with strong bond induced due to hydroxyl functional group and provides additional strength against the externally applied force.

6.4.4 Opacity of the CNC-PU thin film

Measurements of reflectance and transmittance over the visible spectrum are other important properties of these films. The opacity measurement is critical for packing items that are light

sensitive. The ratio of light intensity that is incident on the surface of a thin film from a source to the fraction of light transmitted is defined as the opacity of the film. The transmitted portion of the light will depend on the film thickness and film composition. The resistance to direct transmission of light through the packaging film needs to be optimal enough to maintain the bacterial growth in the packed material, besides the visual appearance. The optimal value of nanofillers is dependent on the required optical density for the packed material.

Transmittance value at a wavelength of 600 nm was noted for the different compositions of CNC-PU nanocomposite film. The baseline comparison was carried out with virgin PU thin film. The observed values of transmittance show a gradual decrease with an increase in CNC composition in the nanocomposite film. This decrease in the transmittance was due to the addition of crystalline CNC to the PU complex. The strong crystalline structure of CNC induces resistance to light traveling through the film. The portion of light incident on the crystalline structure was reflected that was recorded. This reflection increases as the number of CNC increases in the fixed surface area of the thin film, which is nevertheless the concentration of CNC. The optical density of the film is calculated by equation 5.4. Table 6. 2 shows observations at the CNC concentration increases, the variations in the optical density of the film significantly. As the increase in compactness of the film with CNC concentration results in a decrease in the opacity of the nanocomposite films due to compact structure [36–38].

$$\text{Optical Density} = \text{Log}_{10}(\text{Opacity}). \qquad \text{(Eq. 5.4)}$$

Table 6.2 UV-Vis observations of the thin film

Composition of nanocomposite thin film	Transmittance (T)	Opacity of the thin film	Optical density of the thin film
PU	0.94	1.02	0.0086
5% CNC + PU	0.63	1.6	0.1989
10% CNC + PU	0.32	3.2	0.4972
15% CNC + PU	0.20	5.03	0.6981

The Transmitted light intensity observed to be lowered as CNC-PU interactions build and block the pathways of light transmittance. The observations show that, with the addition of 5 % CNC in pure PU complex, the rise in optical density was about 22 %, whereas, with the addition of 10 % CNC, it was 49 %. The relative increase from 5 % to 10 % CNC was significant as it

showed an 80 % rise in optical density. However, addition above 5 % CNC enhances the optical density significantly by the two fold and three fold respectively, for 10 % and 15 % CNC addition. These results are shows similar behaviour of cellulose as reported by Heredia-Guerrero et al. [39].

6.4.5 Bacterial barrier property analysis of nanocomposite films

The diluted culture after the absorption study was placed on the agar plate to measure the bacterial count. The number of bacteria growing on each plate was determined as discussed in the experimental section, and the total bacterial count in each flask was calculated. The absorbance at 600 nm of the cultures in conical flasks after exposure to the environment was measured and the results are shown in Figure 6.6.

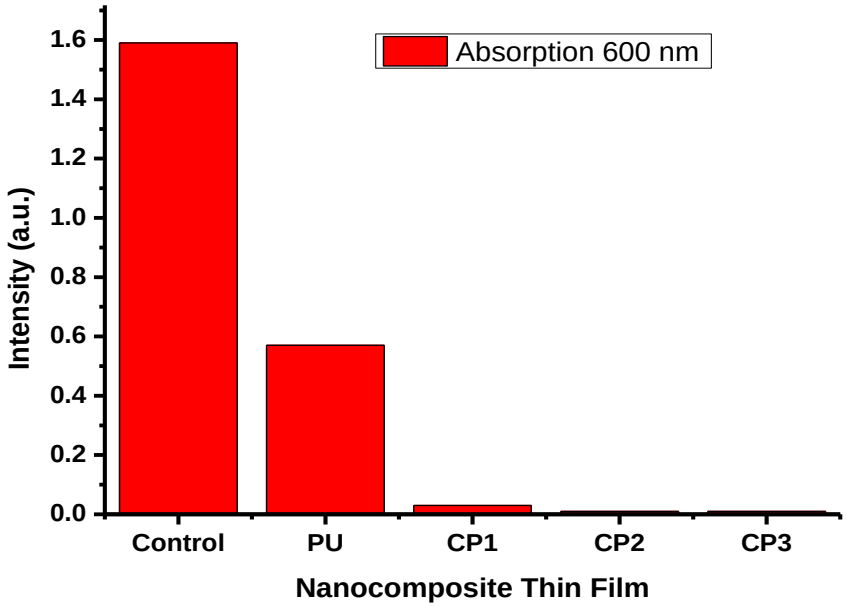

Figure 6.6 Bacterial density using UV spectroscopy

The absorbance values were high in the control flask when compared to the flasks sealed with polyurethane films. Though the results were conclusive, we still determined the bacterial count by serial dilution and plating. This might be due to the fact that the flasks sealed with polyurethane film allow bacteria to pass through them while the CNC-PU composite films filter the bacteria present in the external environment. Although the polyurethane film closed flask had bacterial growth, the bacterial count was significantly less than the control. It was found that the control flask had a high bacterial count of 5×10^9, whereas the flask sealed with PU films had a bacterial count of 2.5×10^3. The conical flasks sealed with CP1, CP2, and CP3, did

not have any bacteria growing in them. The commonly found E. coli was used for the experiments. The size of E. coli varied from 1.0 to 2.0 μm in length with a radius of about 0.5 μm [40]. However, the pore size of virgin PU synthesised by the casting method was reported to be between 50 to 100 μm [41].

From the experimental results, it can be concluded that ultrasonically dispersed CNC gets occupied in the pore of the PU complex. The uniform distribution of CNC in the PU solution reduces the overall pore size of nanocomposite thin film. This phenomenon of nanofilling helps to develop resistance to bacterial as well as air passages through the thin sheet [42]. The compact structures of the film were attributed to the ultrasonic irradiation during the blending of the CNC and PU. The rate of transmission of bacteria across the film from a bacteria-rich environment to a closed culture inside the flask was decreases due to the narrower pore size of the nanocomposite film [43,44]. The nanocomposite film shows higher resistance to even 24 h of continuous environmental exposure. Thus, bacterial resistance at the lower additional CNC in the PU matrix is positive for its packaging application. This again shows that the polyurethane films have the ability to filter microorganisms from the external environment, but the efficiency is far less than the CNC-PU nanocomposite films.

6.4.6 Water vapour permeability (WVP) performance of nanocomposite film

The transmission rate of water vapour through the micropores of the thin film is significant for packaging applications. The average 50 μm thick thin film with the 78.54 cm^2 area was used for the experimentations. The observed results are shown in Figure 6.7 The CNC was added uniformly in the PU complex producing a uniform PU-CNC film structure. The WVP varies with the surrounding temperatures and concentration of CNC in nanocomposite film. From Figure 6.3, it was clear that as the CNC density increases the compactness in the composite film also increases. This phenomenon reduces the pore size of CNC-PU composite film due to which the rate of transmission of vapours across the thickness of film reduces. The travel time of water vapours increases as the thickness of the film increases. At the higher thickness, the diffusion of water vapor across the plane of the film may also be the reason for the reduction of WVP across the film [42,45]. Another important parameter is the surrounding temperature. The rise in the temperature directly affects the gross humidity across the film. The humidity difference leads to the higher pressure gradient across the film which is the reason for the higher WVP. The observations from the experiments indicate that at the higher temperature the WVP increases [37].

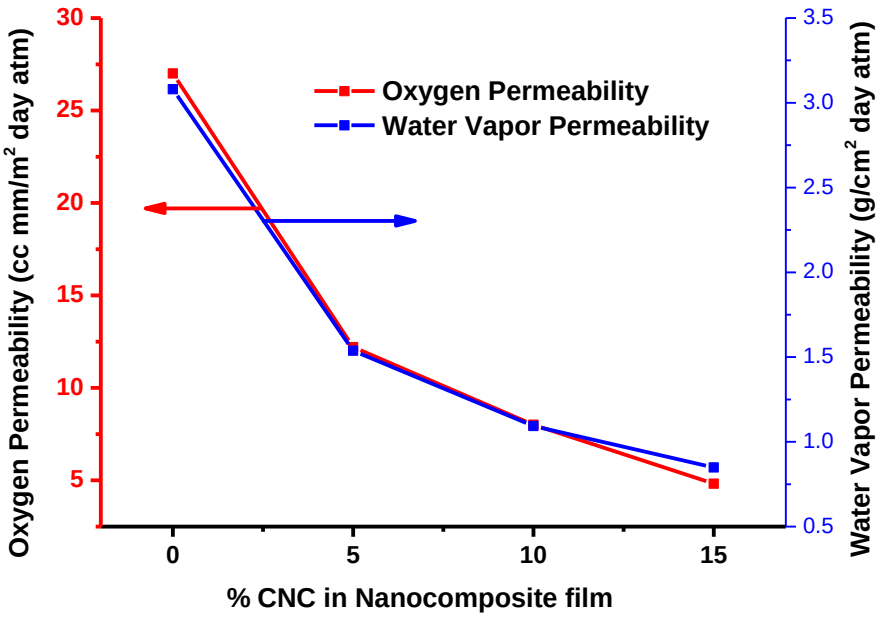

Figure 6.7 Water vapour and oxygen barrier performance of composite thin film

The higher concentration of CNC (15 %) shows the lowest WVP is 0.819 g pa^{-1} cm^{-2} day^{-1}, which is again increasing at higher temperatures. This may cause a higher diffusion rate of water vapor across the thin film at higher temperatures above 35 ^{o}C. At higher temperatures, the vapor pressure is overcome by the static pressure leading to a higher pressure drop across the film. The relative humidity inside the vessel increases with the rise in the temperature [46,47]. The higher difference in relative humidity across the film was the driving force for the higher molecular transformation. Similar results for the starch glycerol films were reported by Miranda et al. [48]. The film with the addition of 15 % concentration of CNC shows an effective reduction of 76 % WVP and above. At higher addition of CNC in the polymer complex, the formation of lumps was detected.

6.4.7 Oxygen barrier of nanocomposite thin film.

Figure 6.7 illustrates the effect of CNC concentration enhancement in the nanocomposite complex for the water vapor and oxygen transmission through the thin film. The specimen used for the analysis was with a uniform thickness of 200 µm. The synthesized thin film with the specific (dia. 50 mm) dimension was placed. The transmission rate of oxygen was reduced as the % CNC increased in the composite film. The addition of 5% CNC in the composite thin film shows the drastic reduction in oxygen permeability. The results observed from the experiments show 47 % reduction in oxygen permeability with the addition of 5% CNC.

However, the permeability reduction rate was reduced after 5% CNC. With the addition of 10% CNC, a permeability reduction of 65 % was observed. The reduction of 84% were observed with the addition of 15 % of CNCs. The uniform distribution of CNC in the PU matrix will reduce the pore size at the lowest stage, this will make thin-film most impermeable [49].

The synthesized nanocomposite CNC-PU films shows a lower operating stress zone between tensile stress and flexural stress. The effective reduction in WVP to 70 to 76 %, makes the film valuable for packaging applications at lower temperature conditions. At lower temperatures up to 40 ^{o}C, the film shows higher thermal stability, resistance against bacterial (99 %), water vapor transformation and higher mechanical properties make it suitable as a packaging material [28]. The extent of acid hydrolysis with ultrasound assistance was enhanced significantly in the microcrystalline cellulose (MCC) granules during the synthesis of CNCs. The process is robust and produces a batch of CNCs with a nanoscale size. The CNC-based PU nanocomposite thin film shows enhanced mechanical and thermal moisture barrier performance. These films exhibit higher resistivity for water vapour and oxygen permeability. Further, significant improvement is observed barrier to the bacteria microbes which have prominent applications in food packing.

6.5 Comparison between CNC based and SNP based PU nanocomposite thin films

6.5.1 Overview of the comparison

In this section, the mechanical, thermal, and barrier properties of the nanocomposite thin films synthesized with the different composites of biomass nanofillers are compared. The composition of starch nanoparticles (SNPs) or cellulose nanocrystals (CNCs) in the polyurethane (PU) polymer matrix shows significant effects on its performance during packaging applications. When used in packaging, thin films must have mechanical strength, thermal resistance, and, most importantly, low or zero water vapour, oxygen, and bacterial permeability across the thin film. The different techniques are reported by the researchers through which successful incorporation of bio nanoparticles as nanofillers into the polymer matrix was achieved. One such method is in situ polymerization, in which the nanofillers are processed along with the monomer to create a very intricate polymer structure. The method's sole downside is that the nanocomposites' molecular orientations are completely at random. Nanofillers in a polymer matrix may be distributed unevenly due to intermolecular forces. Sol-gel synthesis is another approach; it can produce high-quality films up to a micron in thickness and complements physical deposition methods. Sol-gel coatings on metallic subtracts have

their limitations, however. There are a number of limitations to this approach, such as crackability and maximum thickness [50]. It's possible that heat therapy is essential in certain cases as well. If the film thickness is more than a critical value, tensile stresses will build during drying, eventually causing cracks to occur. Self-healing aluminum pillared montmorillonite clay-based nanocomposite covering with increased corrosion resistance to preserve magnesium alloy was created by Adsul et al. [51] using the sol-gel process. The cold spray method [52] is a variant on the conventional hot spray technique, which uses a layer-by-layer strategy to create nanocomposite thin films [53]. A further method for fabricating the nanocomposite thin film is plasma-enhanced chemical vapour deposition [54]. This is a very power intensive set of procedures. In this research, ultrasound was used to disperse nanofillers throughout the polymer matrix. With the use of ultrasound, nanofillers in a polymer matrix are able to diffuse more deeply into the matrix, and the hot spots created by the ultrasound provide more energy for the polymer to interact with the nanofillers. The mechanical, thermal, and bacterial transmission resistance of polyurethane matrices containing varying concentrations of SNPs (wt %) were investigated. The present section the comparison between the effects due to SNPs and CNCs used as nanofillers in the polyurethane matrix.

6.5.2 Mechanical property comparison of CNC- and SNP- based PU nanocomposite films.

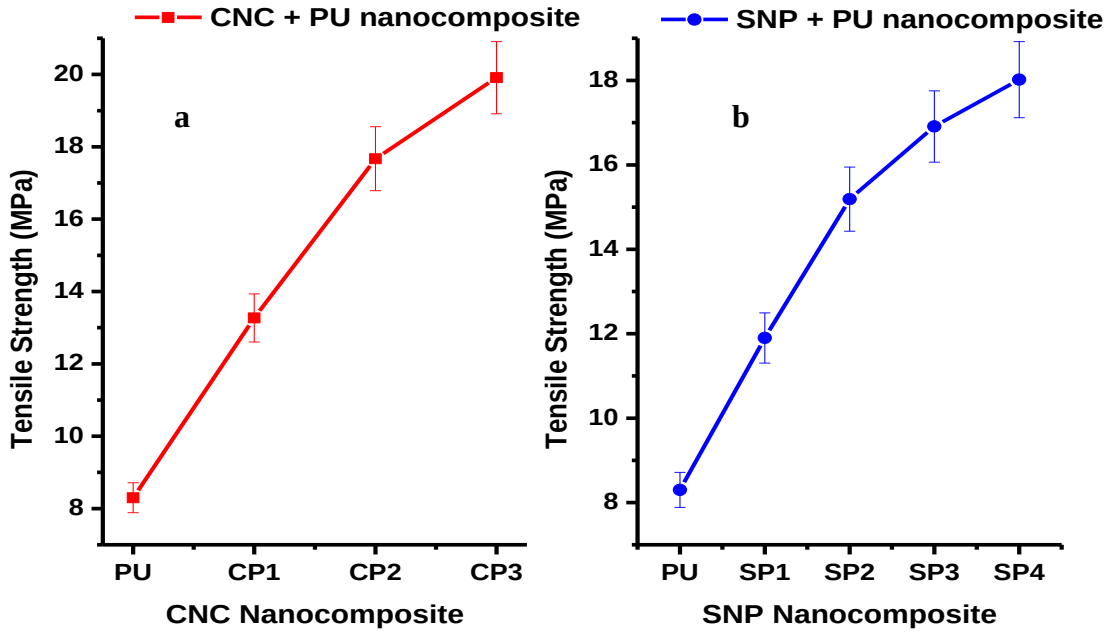

Figure 6.8 Comparison between the nanocomposite with the a) CNC and b) SNP additives Tensile Strength.

As mentioned in chapters 5 and 6, the mechanical properties of the nanocomposite were analysed with the conventional UTM. The tensile strength of the synthesized nanocomposite films of PU shows significant improvement with both the nanofillers CNCs and SNPs, which is shown in the following Figures 6.8 (a and b), respectively.

The tensile strength shows a difference of 25 % when the same quantity of CNCs and SNPs are added to the PU matrix. The results clearly show that higher surface interactions between CNCs and the PU polymer matrix make nanocomposite materials more compact and rigid. The constant load resistance of CNC-blend PU nanocomposite thin films was higher than that of SNP-blend nanocomposite thin films [47,55]. Bending ultimate stress is typically greater than tensile strength. The flexural strength of CNC-blended nanocomposite films is much higher than that of SNP-blended nanocomposite films. These combined results imply the conclusion that the surface interaction of CNC in the PU polymer matrix is much higher.

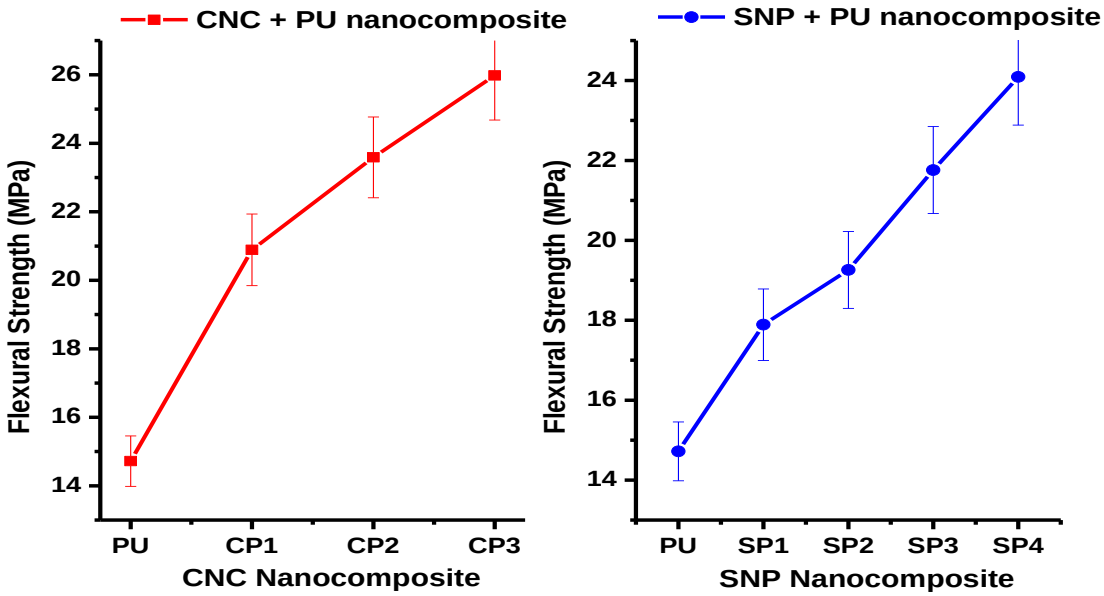

Figure 6.9 Comparison between the nanocomposite with the CNC and SNP additives Flexural Strength.

This could be attributed to the higher number of hydroxyl functional groups associated with the CNC structure as compared with SNPs. The two glucosidic (bi-molar) monomers of cellulose possess approximately twice the number of active hydroxyl functional groups on the surface (interacting end of cellulose). The physico-chemical interaction of CNC in the PU matrix developed during ultrasound assisted blending. The flexural strength comparison of nanocomposite films is illustrated in Figure 6.9.

Increased amounts of CNCs and SNPs in the corresponding bio-nanocomposites resulted in an expected increase in Young's modulus and strength values, as well as a decrease in strain at break [56–58]. The formation of a more connected cellulose network while increasing nanoparticle concentration is likely responsible for the increased tensile capabilities demonstrated in CNC-based nanocomposites compared to SNP-based nanocomposites. CNCs are well-suited for building such a network because to their wide aspect ratio and concomitant versatility. On the other hand, the contribution of the nanocomposite film crystalline domains to improving mechanical properties should be addressed, however this is of much less relevance in the current study could be consider for the future work. The crystallinity of the nanocomposite films developed in the study increased significantly. However, as shown by the FESEM Figure 6.3, the increased contact between the CNC and the PU hosting polymer is also an important element in explaining the better mechanical properties of the CNC-based nanocomposites. Because the polymer chains would not be able to move as freely, the host polymer Young modulus and strength would increase as a consequence of the interactions [59,60].

6.5.3 Thermal properties comparison of CNC- and SNP- based PU nanocomposite films.

The thermal degradation of nanocomposite films with both the nanofillers CNCs and SNPs shows significant rise in the first stage degradation. The Figures 6.10 a, and b shows the variation of thermal degradation ranges along with the addition of CNCs and SNPs in the PU matrix.

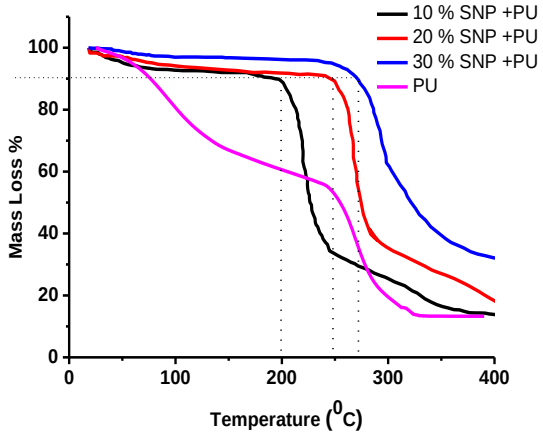

a) TGA analysis for the SNP based PU nanocomposite thin films

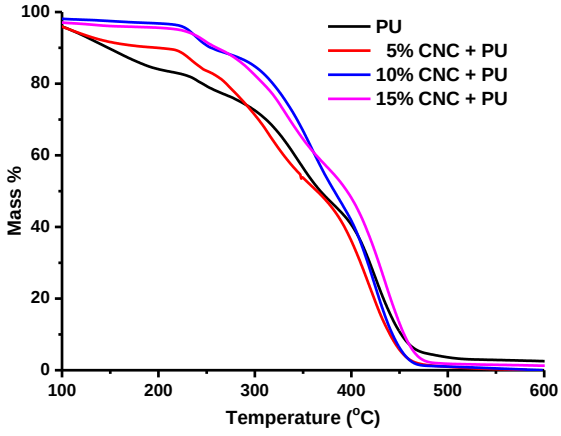

b) TGA analysis for the CNC based PU nanocomposite films

Figure 6.10 Thermal degradation analysis for the nanocomposite films with different composition.

Figure 6.10 clearly shows that heat resistance in CNC-based nanocomposite films was stronger even at lower concentrations of addition compared to SNPs in nanocomposite thin films. When comparing the initial stage of thermal degradation for comparable compositions of 10 %, the findings stated that for 10 % SNP-based Pu nanocomposite thin film, mass loss begins at 200 oC. At this temperature, the SNP-PU nanocomposite bounded moisture evaporates and the polyols bond begins to disintegrate [33,61,62]. Thermal stability was observed to rise significantly as the SNP content in the PU matrix increased. Thermal deterioration begins around 270 ^{o}C for 10 % CNC-based PU nanocomposite films, however there is no substantial variations as such with SNP additions in thermal degradation with increasing CNC concentration in the nanocomposite films. All nanocomposite films of SNP-based PU with varied compositions are stable above 200 ^{o}C, but this temperature is greater than 270 ^{o}C for CNC-based PU nanocomposite [63].

6.5.4 Water vapour and oxygen barrier properties comparison of CNC- and SNP- based PU nanocomposite films.

The nanofillers when blended with the PU solution with ultrasound assistance, the compact thin structure results due to the uniform blending of nanofillers. FESEM images of cross-sections of nanocomposite thin films, as indicated in chapters 5 and 6, support the compact structure and uniform distribution of nanofillers in the polyurethane solution. The amount of hydroxyl functional groups on the surface of SNPs and CNCs was shown to be the cause of the compact interaction. When these hydroxyl functional groups linked with the polyols in the PU polymer matrix, physico-chemically strong connections are formed [64]. The figure 6.11-illustrates the comparative analysis of water vapour permeability and oxygen permeability comparison of both CNC and SNP based nanocomposite thin films.

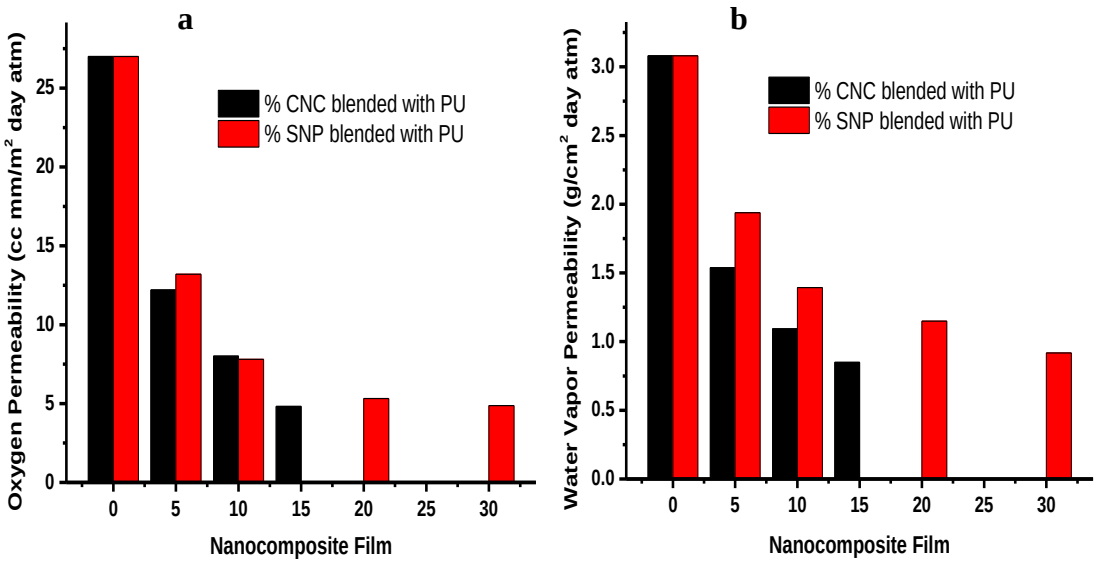

Figure 6.11 Comparison between CNC and SNP reinforcement in PU.

These active interactions will also contribute to the higher mechanical and thermal robustness of nanocomposite thin films. When the permeability of the overall generated nanocomposite thin films for water vapour, oxygen, and bacterial transmission was investigated, amazing results were observed [28,47,65]. The bacterial transmission rate of the nanocomposite thin films was significantly decreases by just addition of (5 %) SNPs or CNCs to the PU matrix. The minimal use of nanofillers inhibited 98 % of bacterial transmission over the whole thickness of the film. Water vapour permeability and oxygen permeability of thin films are critical for packaging applications [39]. The testing results reveal that CNC-based PU nanocomposite thin films outperform other materials due to higher water vapour and oxygen permeability at lower concentrations. CNCs nanofiller concentrations are nearly half as high as SNPs (wt %) and display more effective resistance to water vapour and bacterial transmissions.

6.6 commercial competency of the synthesized nanocomposite films

6.7 Conclusions

The uniform distribution of cellulose nanocrystals (CNC) in a polyurethane (PU) solution was achieved with ultrasound assistance. The increase in the concentration of CNC nanofiller in the PU matrix enhanced the mechanical and thermal properties of the thin film. Ultrasound assisted

intensified mixing increases the local crystallinity of the thin film with respect to the base polymer PU. The synthesized SNP-PU nanocomposite films show 99 % resistance to bacterial cell transmission. The optimal value of the CNC to achieve the maximum bacterial transformation resistance is 5 %. The glass transition temperature of nanocomposite films shows an increasing pattern as the concentration of CNC increases in the PU complex. The increase in the glass transition temperature is due to increase in the overall crystallinity imparted by uniform dispersion of CNCs in the PU matrix. The uniform distribution of CNC in the PU solution develops the strong hydrogen linkages and improves the local crystallinity of nanocomposite. The uniform distribution of CNC in the polymer complex reduces the pore size of the film surface as compared to the plan PU film. The water vapour permeability (WVP) of the film was affected by the temperature of the surroundings and the concentration of CNCs in the film. Overall with the addition of 15 % CNC, the WVP was reduced to 76 %, whereas oxygen permeability was reduced to 84 %. The optical density of the film increased as the CNC concentration increased, the film became more rigid, and the flexural stress of the thin film showed not much significant improvement with a rise in CNC concentration. The tensile strength of the film increased with the addition of CNC, which implies a rise in the young's modulus of the film. At lower temperatures up to 40 ^{o}C, the prepared CNC-PU nanocomposite film showed higher thermal stability, resistance against bacterial, water vapour and oxygen transformation, and mechanical properties, making it suitable as a packaging material.

The addition of nanofillers CNCs and SNPs to the PU matrix is proven to provide extra strength to the original PU. The uniform distribution of nanofillers was a major barrier in the manufacturing of nanocomposite films; however, ultrasound-assisted blending of nanoparticles into the polymer matrix addresses some of the challenges associated with non-uniform distributions. When the thermal and mechanical characteristics of the produced nanocomposite films were evaluated, it was discovered that CNC as a nanofiller outperformed SNP.

CNC-based nanocomposite thin films have substantially greater mechanical strength than SNP-based PU nanocomposite thin films. CNC with a larger amount of hydroxyl functional groups and an unbranched structure has a reduced barrier to the formation of physicochemical bonds. With the same concentration of CNCs and SNPs, there was a considerable increase in tensile and flexural strength. With the inclusion of nanofilles, the thermal breakdown rate of PU thin films is slowed. The biomass nanoparticle SNPs and CNCs exhibit inter-surface contacts, resulting in increased resistance to heat degradation of nanocomposite thin films. The hydroxyl functional group promotes the formation of physicochemical bonds between the CNC/SNP

surface and the polymer interactive ends. The dissolution of these physicochemical links necessitates the use of extra energy. The temperature working window of the polyurethane expands as the concentration of SNPs in it increases.

At lower concentrations (approximately 5 %) SNPs and CNCs, the produced nanocomposite films demonstrate greater resistance to bacterial cell transmission across the thickness. Furthermore, based on the overall observations, the CNCs-based PU nanocomposite films perform superiorly in terms of mechanical and thermal resistance. It also has a stronger resistance to bacterial transmission. All of these films are suitable for low shear stress operating zones in product packaging.

References

[1] C. Calvino, N. Macke, R. Kato, S.J. Rowan, Development, processing and applications of bio-sourced cellulose nanocrystal composites, Prog. Polym. Sci. 103 (2020). https://doi.org/10.1016/j.progpolymsci.2020.101221.

[2] B. Schumann, M. Schmid, Packaging concepts for fresh and processed meat – Recent progresses, Innov. Food Sci. Emerg. Technol. 47 (2018) 88–100. https://doi.org/10.1016/j.ifset.2018.02.005.

[3] S. Johnson, L. Kang, H.M. Akil, Mechanical behavior of jute hybrid bio-composites, Compos. Part B Eng. 91 (2016) 83–93. https://doi.org/10.1016/j.compositesb.2015.12.052.

[4] P. Phanthong, P. Reubroycharoen, X. Hao, G. Xu, A. Abudula, G. Guan, Nanocellulose: Extraction and application, Carbon Resour. Convers. 1 (2018) 32–43. https://doi.org/10.1016/j.crcon.2018.05.004.

[5] V. Favier, H. Chanzy, J.Y. Cavaille, Polymer Nanocomposites Reinforced by Cellulose Whiskers, Macromolecules. 28 (1995) 6365–6367. https://doi.org/10.1021/ma00122a053.

[6] B. Adak, M. Joshi, B.S. Butola, Polyurethane/functionalized-graphene nanocomposite films with enhanced weather resistance and gas barrier properties, Compos. Part B Eng. 176 (2019) 107303. https://doi.org/10.1016/j.compositesb.2019.107303.

[7] D. Trache, A.F. Tarchoun, M. Derradji, T.S. Hamidon, N. Masruchin, N. Brosse, M.H. Hussin, Nanocellulose: From Fundamentals to Advanced Applications, 2020. https://doi.org/10.3389/fchem.2020.00392.

[8] N. Athir, S.A.A. Shah, F.K. Shehzad, J. Cheng, J. Zhang, L. Shi, Rutile TiO2 integrated zwitterion polyurethane composite films as an efficient photostable food packaging material, React. Funct. Polym. 157 (2020) 104733. https://doi.org/10.1016/j.reactfunctpolym.2020.104733.

[9] M. Zahid, A.E. Del Río Castillo, S.B. Thorat, J.K. Panda, F. Bonaccorso, A. Athanassiou, Graphene morphology effect on the gas barrier, mechanical and thermal properties of thermoplastic polyurethane, Compos. Sci. Technol. 200 (2020) 108461. https://doi.org/https://doi.org/10.1016/j.compscitech.2020.108461.

[10] J.W. Yan, C. Hu, L.H. Tong, Z.X. Lei, Q.-B. Lin, Migration test and safety assessment of polyurethane adhesives used for food-contact laminated films, Food Packag. Shelf Life. 23 (2020) 100449. https://doi.org/https://doi.org/10.1016/j.fpsl.2019.100449.

[11] D. Arslan, E. Vatansever, D.S. Sarul, Y. Kahraman, G. Gunes, A. Durmus, M. Nofar, Effect of preparation method on the properties of polylactide/cellulose nanocrystal nanocomposites, Polym. Compos. 41 (2020) 4170–4180. https://doi.org/10.1002/pc.25701.

[12] T.T. Dele-Afolabi, A.H.M. Ariff, O.J. Ojo-Kupoluyi, E.O. Atoyebi, Chitosan Nanocomposites as Wound Healing Materials: Advances in Processing Techniques and Mechanical Properties, Pertanika J. Sci. Technol. 31 (2023) 543–575. https://doi.org/10.47836/pjst.31.1.32.

[13] C. Bavatharani, E. Muthusankar, S.M. Wabaidur, Z.A. Alothman, K.M. Alsheetan, M. mana AL-Anazy, D. Ragupathy, Electrospinning technique for production of polyaniline nanocomposites/nanofibres for multi-functional applications: A review, Synth. Met. 271 (2021) 116609. https://doi.org/10.1016/j.synthmet.2020.116609.

[14] P. Sagitha, C.R. Reshmi, O. Manaf, S.P. Sundaran, K. Juraij, A. Sujith, Development of nanocomposite membranes by electrospun nanofibrous materials, in: M. Sadrzadeh, T. Mohammadi (Eds.), Nanocomposite Membr. Water Gas Sep., Elsevier, 2020: pp. 199–218. https://doi.org/10.1016/B978-0-12-816710-6.00008-0.

[15] Y. Song, P. Tzeng, J.C. Grunlan, Super Oxygen and Improved Water Vapor Barrier of Polypropylene Film with Polyelectrolyte Multilayer Nanocoatings, Macromol. Rapid Commun. 37 (2016) 963–968. https://doi.org/10.1002/marc.201600140.

[16] C. Wang, M.J. Park, H. Yu, H. Matsuyama, E. Drioli, H.K. Shon, Recent advances of nanocomposite membranes using layer-by-layer assembly, J. Memb. Sci. 661 (2022) 120926. https://doi.org/https://doi.org/10.1016/j.memsci.2022.120926.

[17] F. Asempour, D. Emadzadeh, T. Matsuura, B. Kruczek, Synthesis and characterization of novel Cellulose Nanocrystals-based Thin Film Nanocomposite membranes for reverse osmosis applications, Desalination. 439 (2018) 179–187. https://doi.org/10.1016/j.desal.2018.04.009.

[18] S. Kang, Y. Xiao, X. Guo, A. Huang, H. Xu, Development of gum arabic-based nanocomposite films reinforced with cellulose nanocrystals for strawberry preservation, Food Chem. 350 (2021) 129199. https://doi.org/10.1016/j.foodchem.2021.129199.

[19] A.M. Palve, R.K. Gupta, Polyurethane-Based Nanocomposites and Their Applications, in: Polyurethane Chem. Renew. Polyols Isocyanates, American Chemical Society, 2021: pp. 225-255 SE–8. https://doi.org/10.1021/bk-2021-1380.ch008.

[20] S.J. Eichhorn, C.A. Baillie, N. Zafeiropoulos, L.Y. Mwaikambo, M.P. Ansell, A. Dufresne, K.M. Entwistle, P.J. Herrera-Franco, G.C. Escamilla, L. Groom, M. Hughes, C. Hill, T.G. Rials, P.M. Wild, Review: Current international research into cellulosic fibres and composites, J. Mater. Sci. 36 (2001) 2107–2131. https://doi.org/10.1023/A:1017512029696.

[21] A. Babaei-Ghazvini, I. Shahabi-Ghahfarrokhi, V. Goudarzi, Preparation of UV-protective starch/kefiran/ZnO nanocomposite as a packaging film: Characterization, Food Packag. Shelf Life. 16 (2018) 103–111. https://doi.org/10.1016/j.fpsl.2018.01.008.

[22] C.A. International, S.T. Method, Standard Test Method for Tensile Properties of Thin Plastic Sheeting, ASTM. 08.01 (2017) 9. https://doi.org/10.1520/D0882-00.

[23] J.T. Martins, M.A. Cerqueira, A.A. Vicente, Influence of α-tocopherol on physicochemical properties of chitosan-based films, Food Hydrocoll. 27 (2012) 220–227. https://doi.org/10.1016/j.foodhyd.2011.06.011.

[24] A.M. Slavutsky, M.A. Bertuzzi, M. Armada, Water barrier properties of starch-clay nanocomposite films, Brazilian J. Food Technol. 15 (2012) 208–218. https://doi.org/10.1590/s1981-67232012005000014.

[25] C.A. International, S.T. Method, Standard Test Method for Oxygen Gas Transmission Rate Through Plastic Film and Sheeting Using a Coulometric Sensor, Cell. 15.10 (2017) 7. https://doi.org/0.1520/D3985-17.

[26] A. Kamkar, E. Molaee-aghaee, A. Khanjari, A. Akhondzadeh-basti, B. Noudoost, N.

Shariatifar, M. Alizadeh Sani, M. Soleimani, Nanocomposite active packaging based on chitosan biopolymer loaded with nano-liposomal essential oil: Its characterizations and effects on microbial, and chemical properties of refrigerated chicken breast fillet, Int. J. Food Microbiol. 342 (2021) 109071. https://doi.org/10.1016/j.ijfoodmicro.2021.109071.

[27] M.M. Zerafat, S. Sabbaghi, A comparative study of gelatin and starch-based nano-composite fi lms modi fi ed by nano-cellulose and chitosan for food packaging applications, Carbohydr. Polym. 189 (2018) 48–55. https://doi.org/10.1016/j.carbpol.2018.02.012.

[28] C. Metzger, S. Sanahuja, L. Behrends, S. Sängerlaub, M. Lindner, H. Briesen, Efficiently extracted cellulose nanocrystals and starch nanoparticles and techno-functional properties of films made thereof, Coatings. 8 (2018) 1–19. https://doi.org/10.3390/coatings8040142.

[29] M. Salajkova, L. Valentini, Q. Zhou, L.A. Berglund, Tough nanopaper structures based on cellulose nanofibers and carbon nanotubes, Compos. Sci. Technol. 87 (2013) 103–110. https://doi.org/10.1016/j.compscitech.2013.06.014.

[30] N. Srikhao, P. Kasemsiri, A. Ounkaew, N. Lorwanishpaisarn, M. Okhawilai, U. Pongsa, S. Hiziroglu, P. Chindaprasirt, Bioactive Nanocomposite Film Based on Cassava Starch/Polyvinyl Alcohol Containing Green Synthesized Silver Nanoparticles, J. Polym. Environ. 29 (2021) 672–684. https://doi.org/10.1007/s10924-020-01909-2.

[31] Z. Cherifi, B. Boukoussa, A. Zaoui, M. Belbachir, R. Meghabar, Structural, morphological and thermal properties of nanocomposites poly(GMA) /clay prepared by ultrasound and in-situ polymerization, Ultrason. Sonochem. 48 (2018) 188–198. https://doi.org/10.1016/j.ultsonch.2018.05.027.

[32] R. Kumar, G. Ghoshal, M. Goyal, Synthesis and functional properties of gelatin/CA–starch composite film: excellent food packaging material, J. Food Sci. Technol. 56 (2019) 1954–1965. https://doi.org/10.1007/s13197-019-03662-4.

[33] J. Shojaeiarani, D.S. Bajwa, N.M. Stark, T.M. Bergholz, A.L. Kraft, Spin coating method improved the performance characteristics of films obtained from poly (lactic acid) and cellulose nanocrystals, Sustain. Mater. Technol. 26 (2020) e00212. https://doi.org/10.1016/j.susmat.2020.e00212.

[34] Y. Tang, X. Zhang, R. Zhao, D. Guo, J. Zhang, Preparation and properties of chitosan/guar gum/nanocrystalline cellulose nanocomposite films, Carbohydr. Polym.

197 (2018) 128–136. https://doi.org/10.1016/j.carbpol.2018.05.073.

[35] J. Li, Y. Li, Y. Song, S. Niu, N. Li, Ultrasonic-assisted synthesis of polyvinyl alcohol / phytic acid polymer film and its thermal stability, mechanical properties and surface resistivity, Ultrason. Sonochem. 39 (2017) 853–862. https://doi.org/10. 1016/j.ultsonch. 2017.06.017.

[36] G. Sezonov, D. Joseleau-Petit, R. D'Ari, Escherichia coli physiology in Luria-Bertani broth, J. Bacteriol. 189 (2007) 8746–8749. https://doi.org/10.1128/JB.01368-07.

[37] M. Li, X. Tian, R. Jin, D. Li, Preparation and characterization of nanocomposite films containing starch and cellulose nanofibers, Ind. Crops Prod. 123 (2018) 654–660. https://doi.org/10.1016/j.indcrop.2018.07.043.

[38] A.S. Abreu, M. Oliveira, A. De Sá, R.M. Rodrigues, M.A. Cerqueira, A.A. Vicente, A. V. Machado, Antimicrobial nanostructured starch based films for packaging, Carbohydr. Polym. 129 (2015). https://doi.org/10.1016/j.carbpol.2015.04.021.

[39] J.A. Heredia-Guerrero, L. Ceseracciu, S. Guzman-Puyol, U.C. Paul, A. Alfaro-Pulido, C. Grande, L. Vezzulli, T. Bandiera, R. Bertorelli, D. Russo, A. Athanassiou, I.S. Bayer, Antimicrobial, antioxidant, and waterproof RTV silicone-ethyl cellulose composites containing clove essential oil, Carbohydr. Polym. 192 (2018) 150–158. https://doi.org /10.1016/j.carbpol.2018.03.050.

[40] N. Hilal, V. Kochkodan, L. Al-Khatib, T. Levadna, Surface modified polymeric membranes to reduce (bio)fouling: A microbiological study using E. coli, Desalination. 167 (2004) 293–300. https://doi.org/10.1016/j.desal.2004.06.138.

[41] M. Nayani, S. Gunashekar, N. Abu-Zahra, Synthesis and characterization of polyurethane-nanoclay composites, Int. J. Polym. Sci. 2013 (2013) 1–5. https://doi.org/ 10.1155/2013/717895.

[42] P. Balakrishnan, M.S. Sreekala, V.G. Geethamma, N. Kalarikkal, V. Kokol, T. Volova, S. Thomas, Physicochemical, mechanical, barrier and antibacterial properties of starch nanocomposites crosslinked with pre-oxidised sucrose, Ind. Crops Prod. 130 (2019) 398–408. https://doi.org/10.1016/j.indcrop.2019.01.007.

[43] S.A. Madbouly, Waterborne Polyurethane Dispersions and Thin Films : Biodegradation and Antimicrobial Behaviors, Molecules. 26 (2021) 961.

[44] B. Sukkaneewat, S. Utara, Ultrasonic-assisted Dunlop method for natural rubber latex foam production: Effects of irradiation time on morphology and physico-mechanical properties of the foam, Ultrason. Sonochem. 82 (2022) 105873. https://doi.org/10.

1016/j.ultsonch.2021.105873.

[45] R.A. Carvalho, A.C.S. de Oliveira, T.A. Santos, M.V. Dias, M.I. Yoshida, S.V. Borges, WPI and Cellulose Nanofibres Bio-nanocomposites: Effect of Thyme Essential Oil on the Morphological, Mechanical, Barrier and Optical Properties, J. Polym. Environ. 28 (2020) 231–241. https://doi.org/10.1007/s10924-019-01598-6.

[46] X. Li, C. Qiu, N. Ji, C. Sun, L. Xiong, Q. Sun, Mechanical, barrier and morphological properties of starch nanocrystals-reinforced pea starch films, Carbohydr. Polym. 121 (2015) 155–162. https://doi.org/https://doi.org/10.1016/j.carbpol.2014.12.040.

[47] A. Ghadetaj, H. Almasi, L. Mehryar, Development and characterization of whey protein isolate active films containing nanoemulsions of Grammosciadium ptrocarpum Bioss. essential oil, Food Packag. Shelf Life. 16 (2018) 31–40. https://doi.org/10.1016/j.fpsl.2018.01.012.

[48] C.S. Miranda, M.S. Ferreira, M.T. Magalhães, A.P.G. Bispo, J.C. Oliveira, J.B.A. Silva, N.M. José, Starch-based Films Plasticized with Glycerol and Lignin from Piassava Fiber Reinforced with Nanocrystals from Eucalyptus, Mater. Today Proc. 2 (2015) 134–140. https://doi.org/10.1016/j.matpr.2015.04.038.

[49] K. Gonzalez, A. Retegi, A. Gonzalez, A. Eceiza, N. Gabilondo, Starch and cellulose nanocrystals together into thermoplastic starch bionanocomposites, Carbohydr. Polym. 117 (2015) 83–90. https://doi.org/10.1016/j.carbpol.2014.09.055.

[50] G. Bang, S.W. Kim, Biodegradable poly(lactic acid)-based hybrid coating materials for food packaging films with gas barrier properties, J. Ind. Eng. Chem. 18 (2012) 1063–1068. https://doi.org/10.1016/j.jiec.2011.12.004.

[51] S.H. Adsul, T. Siva, S. Sathiyanarayanan, S.H. Sonawane, R. Subasri, Aluminum pillared montmorillonite clay-based self-healing coatings for corrosion protection of magnesium alloy AZ91D, Surf. Coatings Technol. 352 (2018) 445–461. https://doi.org/10.1016/j.surfcoat.2018.08.034.

[52] F. Fanelli, A.M. Mastrangelo, F. Fracassi, Aerosol-Assisted Atmospheric Cold Plasma Deposition and Characterization of Superhydrophobic Organic–Inorganic Nanocomposite Thin Films, Langmuir. 30 (2014) 857–865. https://doi.org/10.1021/la404755n.

[53] D. Li, X. Chen, Y. Gong, B. Zhang, Y. Liu, P. Jin, H. Li, Synthesis and Vacuum Cold Spray Deposition of Biofunctionalized Nanodiamond/Hydroxyapatite Nanocomposite for Biomedical Applications, Adv. Eng. Mater. 19 (2017) 1700363. https://doi.org/10.

1002/adem.201700363.

[54] F.L. Heale, I.P. Parkin, C.J. Carmalt, Slippery Liquid Infused Porous TiO2/SnO2 Nanocomposite Thin Films via Aerosol Assisted Chemical Vapor Deposition with Anti-Icing and Fog Retardant Properties, ACS Appl. Mater. Interfaces. 11 (2019) 41804–41812. https://doi.org/10.1021/acsami.9b14160.

[55] A. Hejna, P. Kosmela, M. Klein, K. Gosz, K. Formela, J. Haponiuk, Ł. Piszczyk, Rheological properties, oxidative and thermal stability, and potential application of biopolyols prepared via two-step process from crude glycerol, Polym. Degrad. Stab. 152 (2018) 29–42. https://doi.org/10.1016/j.polymdegradstab.2018.03.022.

[56] L. Tang, B. Huang, Q. Lu, S. Wang, W. Ou, W. Lin, X. Chen, Ultrasonication-assisted manufacture of cellulose nanocrystals esterified with acetic acid, Bioresour. Technol. 127 (2013) 100–105. https://doi.org/10.1016/j.biortech.2012.09.133.

[57] B. Duan, P. Sun, X. Wang, C. Yang, Preparation and properties of starch nanocrystals/ carboxymethyl chitosan nanocomposite films, Starch - Starke. 63 (2011) 528–535. https://doi.org/10.1002/star.201000136.

[58] Y.R. Lee, A. V. Raghu, H.M. Jeong, B.K. Kim, Properties of waterborne polyurethane /functionalized graphene sheet nanocomposites prepared by an in situ method, Macromol. Chem. Phys. 210 (2009) 1247–1254. https://doi.org/10.1002/macp.200900157.

[59] S.-Y. Kang, Z. Ji, L.-F. Tseng, S.A. Turner, D.A. Villanueva, R. Johnson, A. Albano, R. Langer, Design and Synthesis of Waterborne Polyurethanes, Adv. Mater. 30 (2018) 1706237. https://doi.org/10.1002/adma.201706237.

[60] S.H. Othman, Bio-nanocomposite Materials for Food Packaging Applications: Types of Biopolymer and Nano-sized Filler, Agric. Agric. Sci. Procedia. 2 (2014) 296–303. https://doi.org/10.1016/j.aaspro.2014.11.042.

[61] F. Fathi, A. Dadkhah, H. Namazi, Characterisation and surface chemical modification of starch nanoparticles with lactid through ring opening polymerisation, Int. J. Nanoparticles. 7 (2014) 37–48. https://doi.org/10.1504/IJNP.2014.062012.

[62] M. Mahardika, H. Abral, A. Kasim, S. Arief, M. Asrofi, Production of nanocellulose from pineapple leaf fibers via high-shear homogenization and ultrasonication, Fibers. 6 (2018) 1–12. https://doi.org/10.3390/fib6020028.

[63] S. Boufi, H. Kaddami, A. Dufresne, Mechanical performance and transparency of nanocellulose reinforced polymer nanocomposites, Macromol. Mater. Eng. 299 (2014)

560–568. https://doi.org/10.1002/mame.201300232.

[64] M. Li, X. Qiang, W. Xu, H. Zhang, Synthesis, characterization and application of AFC-based waterborne polyurethane, Prog. Org. Coatings. 84 (2015) 35–41. https://doi.org/10.1016/j.porgcoat.2015.02.009.

[65] M.S. Sarwar, M.B.K. Niazi, Z. Jahan, T. Ahmad, A. Hussain, Preparation and characterization of PVA/nanocellulose/Ag nanocomposite films for antimicrobial food packaging, Carbohydr. Polym. 184 (2018) 453–464. https://doi.org/10.1016/j.carbpol.2017.12.068.

Chapter 7. SNP used as nanoadsorbent for the removal of Cu (II) ions from wastewater.

7.1 Introduction

Water is one of the many aspects that contribute to the survival of human civilization. Water covers 71% of the Earth's surface, but only around 1% is drinkable owing to uneven distribution and the fact that the majority of the water is salty (97 %) or frozen (2 %). Only 1 % of the water on Earth is suitable for human consumption, hygiene, and industry. The Earth is covered with water, but the supply of drinking water is not keeping up with the rising demand [1]. The world's escalating water issue is being exacerbated by the fast development of both human population and industrial productivity. The water crisis is a worldwide disaster that has just recently appeared. Several contaminants make using water collected directly from natural sources dangerous, especially for human consumption. Some of these pollutants are deadly, and their consequences on people and other creatures might be devastating. Water quality has deteriorated owing to pollution, and ecological balance has been disrupted, all as a result of human exploitation of natural resources and the environment to suit human wants and aspirations for energy production and a variety of other activities. Wastewater comprises a broad variety of compounds that are harmful to the environment. Phosphorus, nitrogen, and carbon contained in wastewater may encourage the growth of algae, mosquito larvae, and other pests in waterways. It contains dissolved inorganic constituents like as salt, calcium, suspended particles, biodegradable organics, pathogens, and heavy metals. Contaminants are often removed using traditional remediation processes. Physical repair solutions have significant downsides in terms of cost-effectiveness and environmental impact [2]. Table 7.1 gives overview on the commonly found heavy metals and their respective effects on the surroundings.

Table 7.1 Commonly found heavy metals and their respective effects on the surroundings.

S no.	Heavy metal	Major source	Effects	Ref.
1	Cadmium	Air, water, soil, and, sludge, sewage, Ni–Cd battery, plating	Nephrotoxicity, suppression of antioxidant enzyme activity, carcinogenicity in humans, and build-up in the kidney and liver are all potential side effects.	[3]

2	Arsenic	Found with other metals in trivalent atomic state. Found in soil, and water, pesticides, deep well water, mining sites, emission from coke oven	Children's CNS damage, oxidative stress, and a higher risk of diabetes, mellitus, and high blood pressure, as well as skin lesions, subjective neurological impairments, and oxidative stress.	[4]
3	Chromium	Road dust containing chromium, metal treatment use, wood preservative, oil drilling sites, burning fossil fuels, oxidative pigment	Lung, along with potential effects on the kidneys, liver, skin, and immune system cause digestive, hepatic, cardiovascular, and hematological problems	[5]
4	Copper	Food, drinking water	Cause acute gastrointestinal symptoms, liver toxicity, infants, can suffer from copper, tumor promoter	[6]
5	Cobalt	Naturally found in various forms and a part of numerous Anthropogenic sources. Occupational, dietary and medical, intake are some other sources of exposure	Hematological, endocrine dysfunctions and in extreme cases, malfunctioning MoM hip implants	[7]
6	Nickel	Found in abundance in the earth's crust and core. occurs in air, water, sediments, and soil	Respiratory cancer risks, Contact dermatitis; headaches; gastrointestinal manifestations; respiratory manifestations; lung cancer; epigenetic effect	[8]

Wastewater treatment is a multidisciplinary area that requires consideration of economic, ecological, and social concerns. The study of adsorption is of great importance from an environmental point of view, as it can be considered as an alternative technique for removing toxic pollutants from wastewaters. Therefore, there is a need for the search of low-cost and easily available materials, which can adsorb Cu (II). Undoubtedly, agricultural waste materials are presently the most challenging topics, which is gaining stern considerations during the past several decades. Table 7.2 summarizes heavy metal remediation options in wastewater. Microbiological methods, plant-based degradation, and the use of nanomaterials were among the innovative heavy metal remediation and wastewater treatment techniques. This table assists

in recognizing the difference and devising strategies to enhance existing techniques while allowing for the development of new ones [9].

Table 7.2 Overview on the conventional wastewater treatments.

Name of method	Mechanism	Advantages	Disadvantages	Ref
Conventional methods	Chemical precipitation, ion exchange, chemical oxidation, reduction, reverse osmosis, ultrafiltration, electrodialysis and adsorption	Good controllability and resilience to high amount of heavy metals present	Low metal removal efficiencies for high operational costs production of waste by products that are difficult to manage, high energy requirements, lead to secondary pollution.	[2]
Microbial treatment	Biosorption and Bioaccumulation, passive and active mechanisms	Reduces energy consumption and cost, inhibits pathogens, reduce odor and improves air quality	Low in process, limited due to presence of non-biodegradeable contaminant and may also cause toxicity of microbes	[10]
Nanomaterial based treatment	Single stage-treatment method, chelation, metal adsorption	Extraordinary adsorption capacity and reactivity due to surface and size effect, quantum effect, and macro quantum tunnel effect	Agglomeration, few real life applications, use of toxic chemicals lack of extensive study, experimentation and documentation	[11]
Non-conventional Biosorption	Adsorption	Green approach, lower chemical requirement, Energy requirement lower	Surface activation requirement for adsorbents, pretreatment such as particle size reduction, geletimization, thermal phase separation are required essentially	[12]

7.1.1 Heavy metal ions existence in wastewater.

Metal plating, mining, tannery, smelting, alloy, and battery manufacturing all emit dangerous metal ions into the environment, which ultimately accumulate in the food chain. Adsorption has been found in studies to effectively remove hazardous metals from wastewater. Natural and agricultural waste materials are appropriate absorbents for use in Bio-sorption technology,

which provides an economical alternative to standard effluent treatment procedures due to their cheap cost, extended lifetime, and high availability [13]. Chemically treated plant wastes have been reported to have higher adsorption capabilities than untreated equivalents. This is due to the widespread use of chemicals such as oxidizing agents, mineral and organic acids, bases, organic compounds, and so on. Heavy metal ions are very soluble in water and hence may be absorbed by living organisms. Heavy metal ions may enter the food chain and build up to harmful levels, causing a slew of health issues in people. Heavy-metal ion pollution in water may cause environmental problems even at low concentrations, emphasizing the need of materials capable of effectively complexing these metal ions. Some of the techniques for removing heavy metals from wastewater include membrane processing, chemical precipitation, ion exchange, filtration, reverse osmosis, electrochemical treatment, and adsorption. Adsorption has been found in investigations of effluent processing with heavy metal concentration to be an exceedingly efficient method of eliminating heavy metals from wastewater streams. Adsorption is a process for choosing, condensing, or keeping one or both components of a mixture on a solid surface. The word "adsorbent" refers to the material that is adsorbing, while "adsorbate" refers to the substance that is being absorbed. Despite competition from alternative commercial adsorbents such as silica gel and activated alumina, activated carbon is still widely used. Because of its widespread usage in the water and wastewater treatment industries, activated carbon remains a costly resource. Recent scientific studies underscore the need for simple, cost-effective solutions for removing heavy metals from polluted water systems, such as the utilization of economical agricultural waste products. Agricultural items containing functional groups that bind metal ions include proteins, polysaccharides, and lignin. Agricultural wastes, which include multiple favourable surface groups and occur naturally, may be utilized to replace manufactured adsorbents. In recent years, much research has been undertaken on the use of agricultural by-products such as ash, banana pith, pine bark, peanut, soybean hulls, eggs, rice husk, orange peel, hazelnut shell, sawdust, and compost to remove heavy metals from soil [6].

Nanotechnology is one feasible approach for removing heavy metals from polluted water systems. This subject is rapidly increasing in tandem with the major traditional strategies for removing heavy metals from wastewater [14]. Nanoparticles are particles with a surface area to volume ratio of 1 to 100 nm that give them unique properties. Pollutants and pollutants may cause these chemicals to react [15]. They can reach the source of the pollution, where their higher reactivity and subsequent removal effectiveness may be most beneficial. Industrial

effluents, surface water, ground water, drinking water, and so on may all be cleaned and decontaminated using a range of nanomaterials that have been created with certain properties and features in mind [16]. Many different types of nanomaterials are utilized to remove heavy metals. They have a better removal efficiency, are less expensive, and may be reused.

7.1.2 Biosorption: a non-conventional approach for heavy metal ion removal from wastewater

Plants, as agricultural waste materials and food industries discarded material have been used as biosorbents, it is a form of reusing and recycling those waste materials thus no significant costs are associated with using plant materials. The potential of plant biosorbents are mainly due to the presence of carboxylic and phenolic functional groups in the cellulosic matrix or components associated with cellulose such as lignin and hemicellulose [17]. Aloe vera wastes were used as biosorbent for the removal of uranium and cadmium from water, it was found that the carboxyl, carbonyl and hydroxyl groups facilitated metal binding [18]. Table 7.3 discuss some of reported biosorbents for the removal of heavy metal ions from the wastewater.

Table 7.3 Reported Biosorbents for the removal of heavy metal ions from wastewater.

Sr. n	Biosorbent	Metal ions separated	Adsorption capacity / Effectiveness	Ref
1	Sawdust of poplar tree	Copper	13.43 mg/g	[19]
2	Wheat shell	Copper	8.34 mg/g	[20]
3	Peanut hulls	Copper	9 (mg/g)	[21]
4	Peanut pellets	Copper	12 (mg/g)	[21]
5	Alkali treated Coconut coir	Copper	30 %	[22]
6	Coconut coir powder	Copper, Nickel, and Cadmium	12 %	[23]
7	Peanut husk	Copper	10.15 (mg/g)	[24]
8	Starch nanoparticles	Copper	43 mg/g	Present study

He et al. [25] developed a lead-ion-imprinted magnetic biosorbent to remove Pb (II). They found that the developed nano-biosorbent showed higher sensitivity even when the suspension had the lowest concentration of Pb (II). Further, Celekli et al. [26] explored the pumpkin husk's Cu (II) adsorption capacity. They have reported the removal of Cu from suspension using the

surface-modified (by KOH) pumpkin husk with maximum sorption of 73 mg/g. It exhibits the efficient application of biosorbent to remove Cu metal ions from the suspension. The dried orange peels were exploited to remove cupric ions from the waste, as demonstrated by Kumar et al. [27]. They noted that the monolayer adsorption of cupric ions was favourable during biosorption and the maximum cupric ions separation from the dried orange peels was 33.99 mg/g. Sayiter Yildiz [28] used almond shell to extract the Cu (II) ion from wastewater. The almond shell effectively removes the 86% of Cu (II) from the wastewater. In the similar context Xin et al. [29] modified cellulose via thermally induced phase separation followed by alkaline hydrolysis to create a functionalized cellulose-based monolith that was used as a highly efficient adsorbent to remove heavy metal ions. The cellulose-based monolith shows higher affinity for the cd (II) ions. The maximum adsorption capacity of the functionalized cellulose monolith was reported at 110 mg/g. Starch granules consist of a hydroxyl functional group on the surface. In the process of starch nanoparticle synthesis through intensified acid hydrolysis, the synthesized granules show the presence of a sulfate functional group. The additional presence of sulphate functional group on the SNP surface makes them available to interact with the charged species from the suspension [30].

In this section, the synthesize starch nanoparticles through intensified acid hydrolysis approach was explore for the adsorption ability. The surface charged SNPs synthesized in the intensified acid hydrolysis approach interact with the opposite charge species. The ability of this chemisorption could be useful for the extraction of heavy metal ions such as lead, copper, zinc, and many more [31]. The experiments were carried out with the copper contaminated wastewater for the evaluation of adsorption capacity of synthesized starch nanoparticles. The results were analysed and discussed in the present chapter.

7.2 Experimental procedure

7.2.1 Materials

The corn starch granules were purchased from Sigma Aldrich, India. The laboratory-grade sulfuric acid (H_2SO_4) and copper sulphate ($CuSO_4{\cdot}5H_2O$) were purchased from Thermo Fisher Scientific, India.

7.2.2 Synthesis and optimization of SNPs

The ultrasound-assisted acid hydrolysis was used to synthesize SNPs. For this, starch granules with the initial average granular size ranging from 5 to 9 μm, received from Sigma Aldrich, were used to reduce to the nanoscale size. The variations in the acid concentration were

examined with constant power input and irradiation time to obtain an optimal acid concentration for the minimal size of the starch granules. The desired acid concentration was prepared using the stock solution of H_2SO_4 (0.5 M). The SNP s were synthesized as per the previous approach of ultrasound assisted acid hydrolysis and used for the experimentations. The experiments were carried out in three sets for consistency.

7.2.3 Preparation of Cu (II) ions contaminated wastewater solution

The Cu (II) salt was dissolved in deionized water to obtain the stock solution. 24.97 g $CuSO_4.5H_2O$ was dissolved in 1000 ml of deionized water to produce a stock solution of fixed concentration [27]. The working solutions with initial Cu concentrations varied from 5 mg/L to 35 mg/L and were attained by diluting the stock suspension. The solution pH was attained to the required value using an appropriate buffer solution (acidic buffer with pH 2, 3, 4, 5 and 6; basic buffer of pH 8). The resultant stock solutions were sealed in an airtight container and kept in a refrigerator.

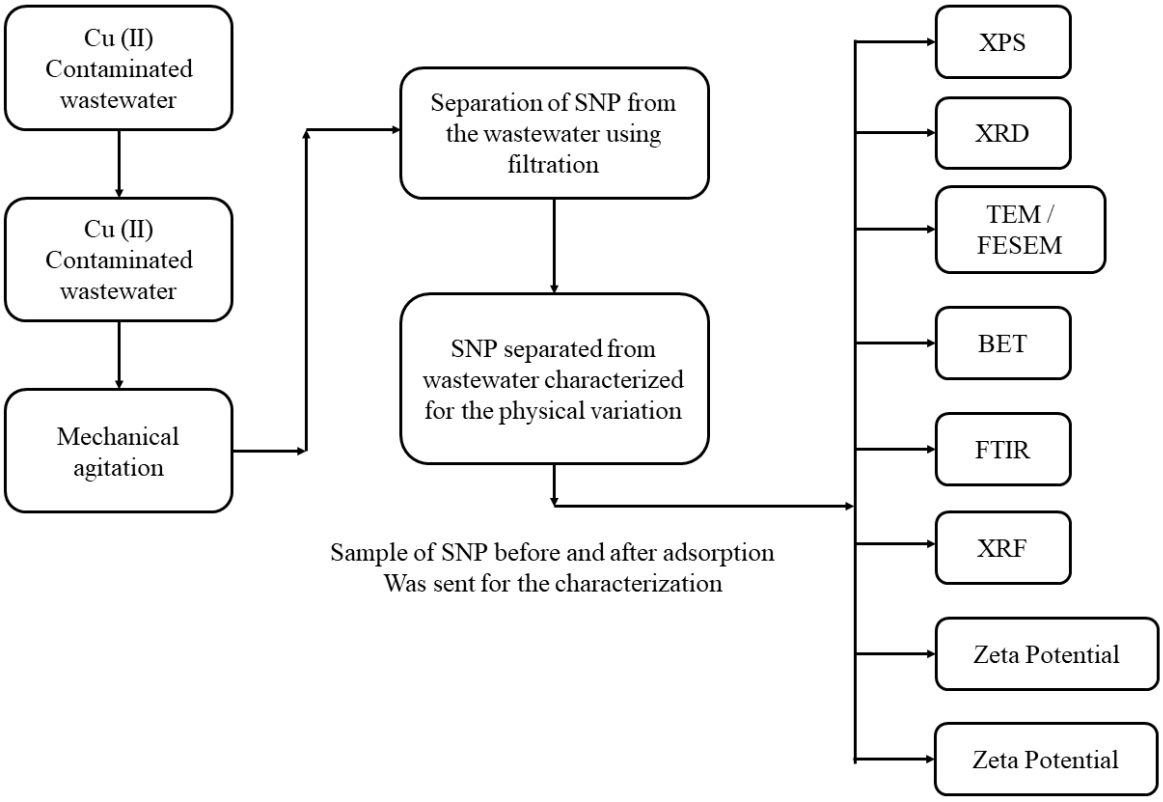

Figure 7.1 Block diagram of Cu (II) extraction process using SNP as nanoadsorbent

7.2.4. Experimental procedure and method of analysis

The adsorption experiments were performed in a batch mode with a working volume of 200 mL using a 250 mL flask. The primary aim is to find the concentration gradient of Cu (II) ions

in the suspension through the adsorption process. The concentration gradient is the number of Cu (II) ions removed from the solution. The fixed quantity of SNPs adsorbent was added into a 200 mL suspension of known Cu (II) ion concentration. The initial and final Cu (II) ion concentrations in the suspension were determined via a UV-visible spectrophotometer at 434 nm [32]. The adsorption capacity of SNP was estimated using the following equation 7.1.

$$Q_{Ad} = (C_{Cu_0} - C_{Cu_e}) \frac{V}{m} \quad \text{(Eq. 7.1)}$$

Where C_{Cu_0} and C_{Cu_e} denote the copper metal concentration at the start and equilibrium, correspondingly. V represents the solution volume, and m denotes the adsorbent mass. Q_{Ad} is the adsorption capacity of SNP in mg/g. The comparative extraction of Cu (II) from the suspension was calculated using equation 7.2.

$$\text{Cu removal (\%)} = \frac{(C_{Cu_0} - C_{Cu_e})}{C_{Cu_0}} \times 100 \quad \text{(Eq. 7.2)}$$

Copper removal efficiency (%) was calculated and compared under different operating conditions. The variation in the initial concentration of Cu (II) in the suspension, pH, and the added amount of SNPs were considered. The optimal conditions to achieve the maximum Cu (II) adsorption from the suspension were noted [33].

7.3 Characterization of biosorbent (SNP) before and after the use.

The dry powder of SNPs was kept in a desiccator to avoid moisture influence. To prepare a synthetic Cu (II) stock solution, an appropriate amount of copper sulphate ($CuSO_4.5H_2O$) was dissolved in deionized water. The solution pH was maintained in an acidic regime to generate the driving force for adsorption. The synthesized SNPs were introduced to the stock solution with the known initial Cu (II) ion concentration. After reaching the equilibrium, the SNP/Cu complex sediments were formed in the solution. Then, the solution was centrifuged (Eppendorf® Centrifuge, 5430R, Germany) at 6500 rpm for 15 min at 10 ºC to separate the SNP/Cu complex from the solution. The SNP-Cu complex was then vacuum dried at 40 ºC and stored in a desiccator until further characterization.

FTIR was used to determine the existence of active functional groups in the SNPs. TEM (transmission electron microscopy, Vitrobot Mark IV 200 kV, USA) was employed to examine the SNPs adsorbent capacity to metal particles. The Cu adsorption on the starch surface was confirmed from the X-ray fluorescence (XRF) (ED-XRF) (EPSILON-1 PANalytical,

Netherlands) diffraction. The biosorbent was analyzed for metal components through XRF. The effect of pH, initial concentration of Cu, and the SNPs dosage on the overall removal efficiency was investigated. The SNPs before and after Cu adsorption were characterized by XRD (PANalytical XPERT-PRO, Netherlands) to find crystallinity changes due to the sorption of Cu on the SNPs granules. XRD was performed at 30 mA and 40 kV with a scan range (2θ) of 10 to 80o at a scan rate of 0.02 s^{-1}. The shift in the diffraction pattern could be because of the functional group attachment with the Cu ions from the suspension. The field emission scanning electron microscope (FE-SEM) (ZEISS Sigma 500 VP, Germany) and X-ray photoelectron spectroscopy (XPS) (PHI Versaprobe III, Canada) were used to analyze the surface modification and binding energy variations in the SNP before and after Cu adsorption. The zeta potential was measured at the equilibrium pH of the suspension using a Malvern zetameter (Zetasizer Nano Z, PANalytical, Netherlands). The surface area analysis was carried out using Brunauer–Emmet–Teller (BET) analysis with nitrogen adsorption isotherm employing surface analyzer Belsorp mini II (Microtrac, Japan).

7.4 Results and Discussion

The starch nanoparticles are synthesized during the intensified acid hydrolysis can be exposed for the various applications. In the process of acid hydrolysis of starch the amorphous section in which the amylose and amylopectin are randomly oriented due to higher proportion of unbranched amylose. These sections shows higher affinity towards the acid and undergoes complete hydrolysis. The complete hydrolysis of amylose or amylopectin leads its transformation in the linear monomers such as glucose or fructose. The complete hydrolysis of amorphous section leading for the first stage synthesis of SNP. The negative charge on the surface of crystalline residue after the hydrolysis was attributed to the sulphate (-OSO_2-) functional group attachment from the H_2SO_4 during the hydrolysis. This is significant phenomenon of hydrolysis process with the sulphuric acid. Other mineral acids such as hydrochloric acid, nitric acid are not able to generate this effect due to limitation on the hydroxyl groups. The attachment of sulphate group to the surface of starch nanoparticles was observed to be through the formation of chemical bonded. Due to this the negatively charge SNP could be a good carrier material for the species with the opposite charge. During the experiments with the synthetic wastewater for the initial trials, the positively charge Cu (II) ions were attached with the SNP show meaningful variation of Cu (II) ions in the contaminated wastewater. The synthesized SNPs where directly blended with the contaminated wastewater

without any pre-treatment. The observations from the experiment analysed and confirmed by using various analytical methods.

7.4.1 TEM and FESEM of the SNPs before and after adsorption

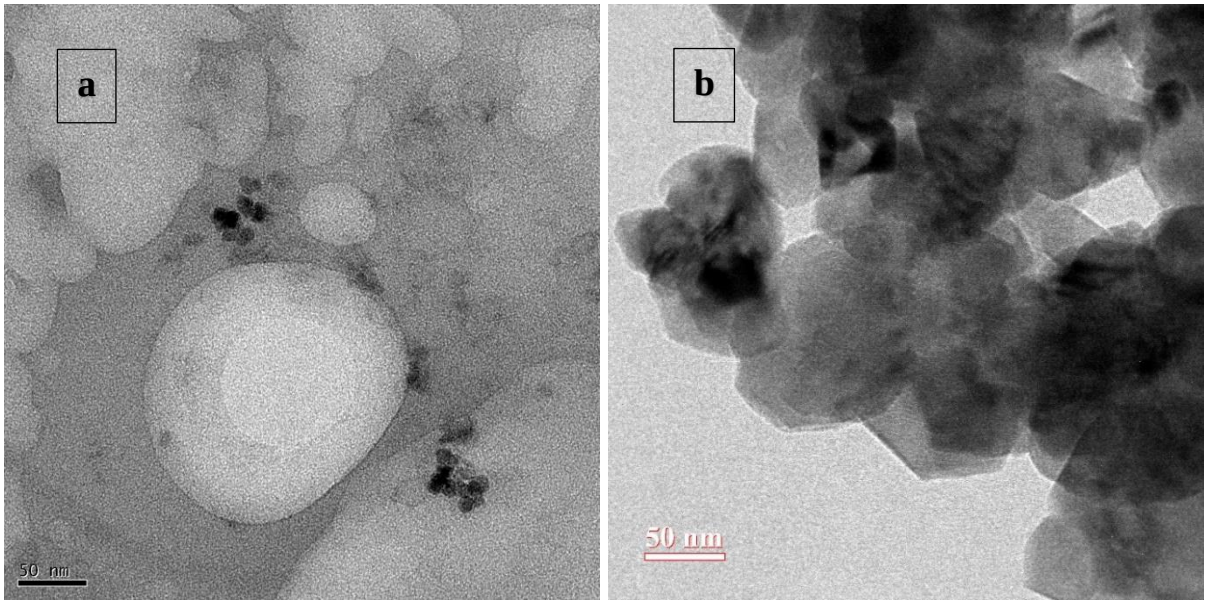

Figure 7.2 TEM of SNPs (a) before b) after Cu (II) adsorption.

The transmission electron microscopical images show particle size differences in figure 7.2 (a) and (b). The difference in the particle size was due to the presence of Cu ions on the surface after the adsorption. Figure 7.2 (b) illustrates the larger particle size compared to the SNP in figure 7.2 (a). The Cu ions present on the SNP surface are stable. The field emission scanning microscopy gives a clear morphological difference between the SNP before and after adsorption.

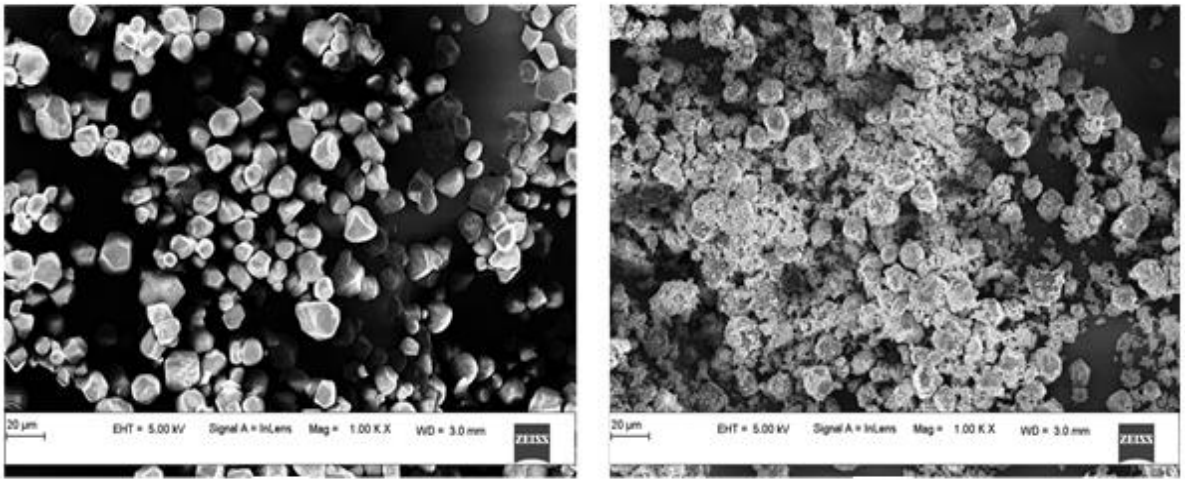

a b

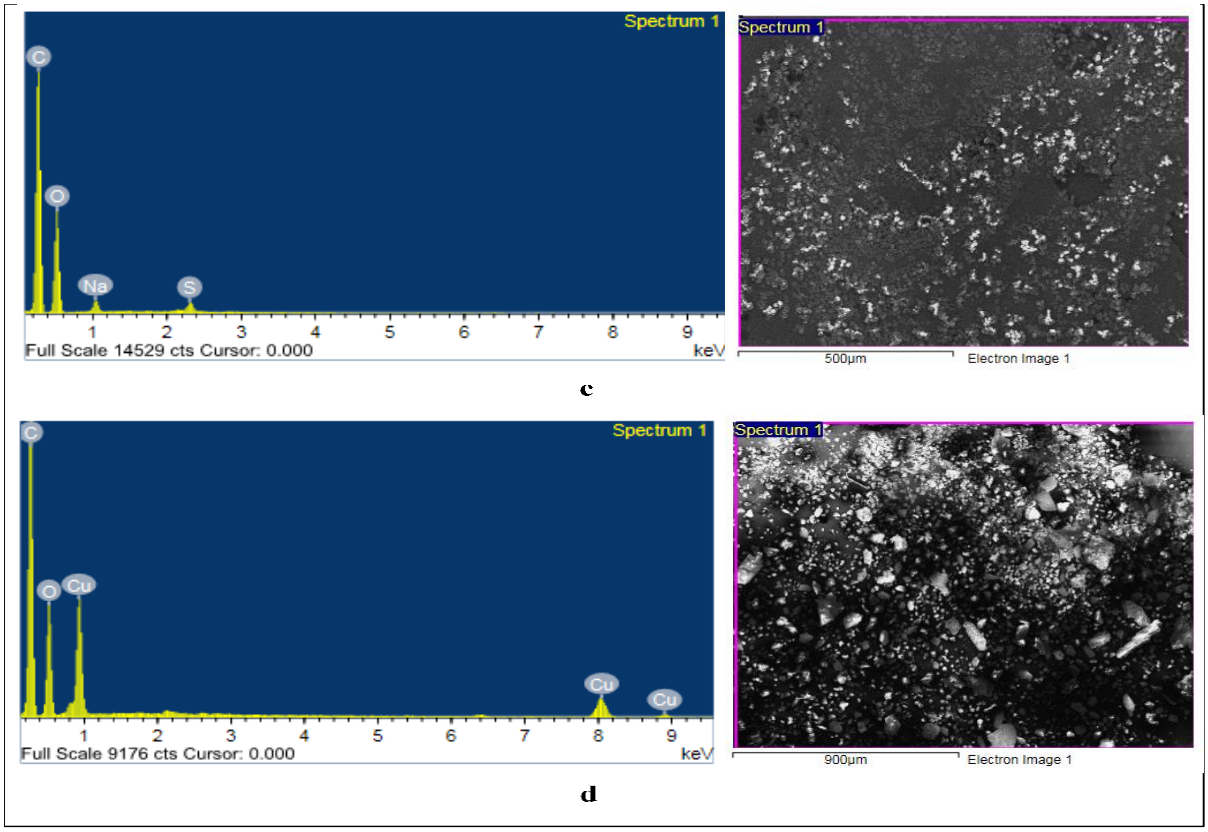

Figure 7.3 FE-SEM of SNPs before (a) and after (b) the adsorption process, the corresponding energy-dispersive X-ray spectroscopy (EDS) for SNPs before (c) and after (d) adsorption.

The Cu ions interact with the sulphonic functional group on the surface of SNP. This interaction can be confirmed from the energy-dispersive X-ray spectroscopy (EDS) observations. The weak chemical bond between the sulfonic group and Cu (II) metal ions leads to agglomeration in the surface-active SNPs. The XRF and energy dispersive X-ray spectroscopy (EDS) spectra confirm that the sediments separated from the stock solution after 60 minutes contained starch as well as Cu metal ion. The FESEM characterization was carried out to obtain information about the surface morphology of both the SNPs before and after the adsorption of Cu. The FESEM of the SNPs before and after the adsorption process is illustrated in figure 7.3, along with corresponding energy-dispersive X-ray spectroscopy (EDS) observations. The microscopic images in figure 7.3 (a, b) confirm the surface attachment of Cu ions on the SNPs granules. The EDS confirms the presence of sulphur from the sulfonic functional group on the surface of SNPs before the adsorption process, which was overcome due to its interaction with the Cu ions during the adsorption process. The presence of Cu ions in different oxidation states at different energies on the SNPs surface after the adsorption process indicates its electrostatic

interaction with the SNPs surface. Figure 7.3 (b) shows that SNPs-Cu agglomerates are more likely after drying than SNPs adsorbent, possibly due to intermolecular interactions between Cu ions in the complex [34]. The figure 7.3 (c and d) shows the energy dispersive X-ray spectroscopy (EDS) for the starch nanoparticles before and after the adsorption. The presence of Cu ions in different energy state was found in SNP after the adsorption process. The EDS analysis of starch confirmers the presence of Cu on the SNP surface. The different energy states of Cu attributed due to its interaction with hydroxyl functional group and sulphate functional group.

7.4.2 Brunauer-Emmett-Teller (BET) Characterization of SNPs before and after adsorption

The nitrogen gas adsorption isotherms was depict in figure 7.4, exhibiting similarities with the typical IV type adsorption behaviour [17]. Also, the N_2 isotherms exhibit a well-known sharp modulation of adsorption/desorption limbs where the adsorption branches are significantly shift toward lower relative pressure (P/P_o). Based on the N_2 isothermal results, the mesoporous SNPs adsorbent illustrates appreciable specific surface area, mesoporous volume (V_m), and tuneable mesoporous diameters (D_m). The SNPs show a higher surface area after the adsorption process due to the adsorption of Cu on the surface.

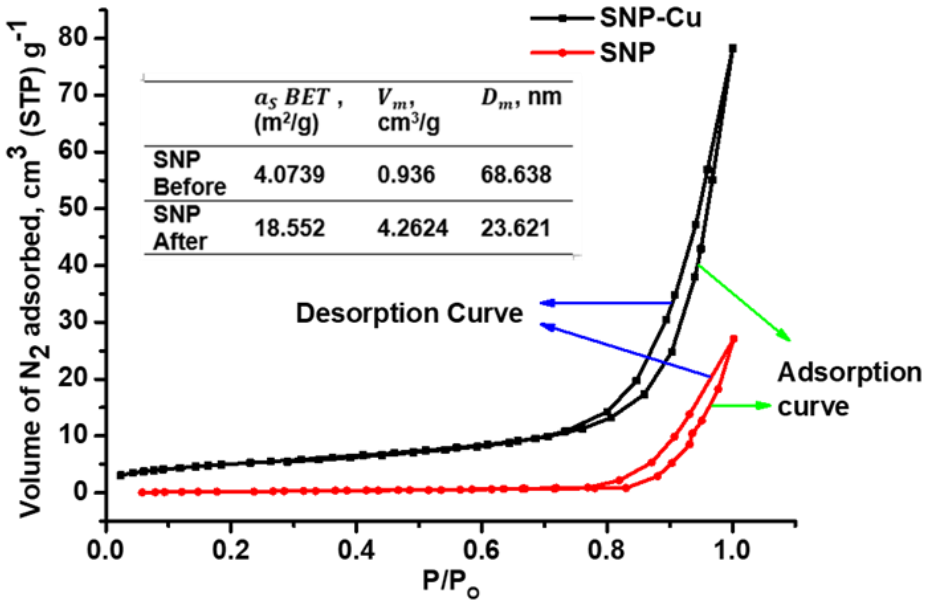

Figure 7.4 N_2 adsorption/desorption isotherms for the SNPs before and after adsorption of Cu (II)

7.4.3 FTIR analysis of SNPs

FTIR is an essential tool to examine the functional groups capable of adsorbing Cu (II) metal ions. The sulphonic group (-$OHSO_2$) on the SNPs surface was confirmed through a band at 1019 cm^{-1}.

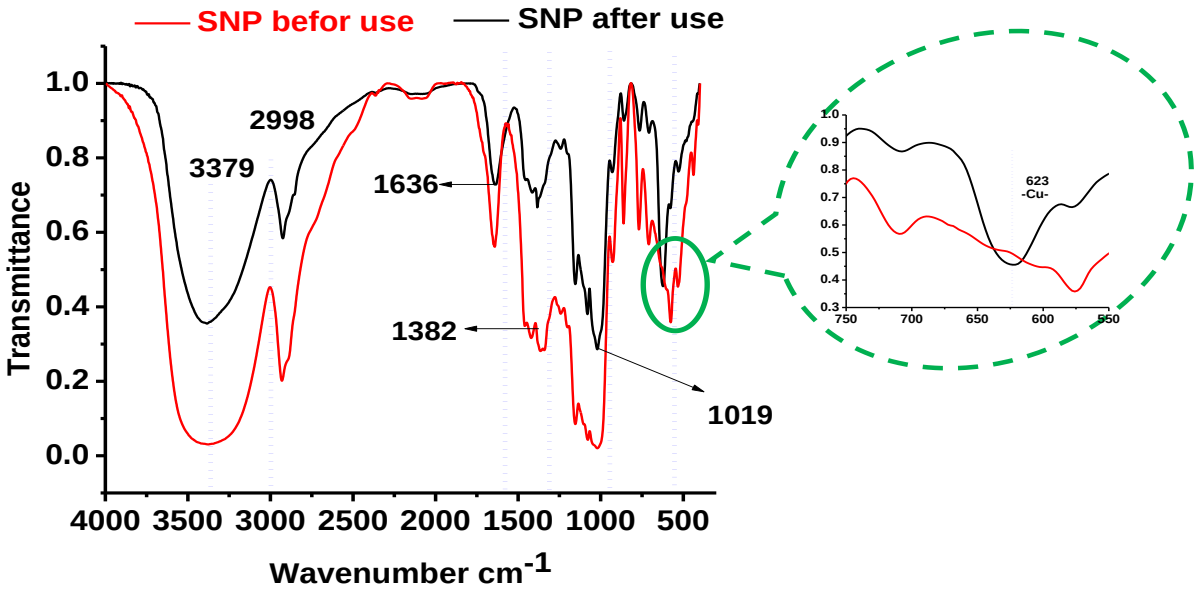

Figure 7.5 Comparative Fourier transform infrared (FTIR) spectra of SNPs before and after adsorption.

The broad band at 3329 cm^{-1} illustrates the stretching vibrations of the hydroxyl group. The stretching energy of the hydroxyl group indicates the adsorption of moisture by the SNPs during analysis. The carbonyl functional groups were found at 1075 cm^{-1} on the starch surface. The stretching of the bond between C-O was observed due to the vibration in the range of 1636-1382 cm^{-1}. Figure 7.5 shows the FTIR spectrum of SNPs before and after Cu (II) adsorption, illustrating a shift in the intensity of the -OH and carbonyl bands after sorption, demonstrating their participation in adsorption [35,36]. Surface -OH group is one of the active functional groups responsible for Cu (II) adsorption as the wavenumber shifts from 1650 cm^{-1} to 1729 cm^{-1}. The characteristic sulphone (S=O) stretching vibrations band for SNPs at 447 cm^{-1} disappears significantly after the adsorption of Cu (II). This indicates its involvement in the adsorption of Cu ions. The band at 629 cm^{-1} reveals the presence of a -Cu- bond associated with the surface of SNPs. The characteristic band of the sulphonyl (-S=O-) functional group present at 547 cm^{-1} in SNPs shifted to 629 cm^{-1} after adsorption. This shift confirms that it is strongly involved in the adsorption of Cu(II) ions through bonds from the hydroxyl functional

group. The band shift between 600 and 750 cm^{-1} in the SNPs after adsorption implies the presence of Cu metal ions. The -Cu bond energy is significantly observed between 550 and 750 cm^{-1}.

7.4.4 XPS and XRF spectra of SNPs before and after adsorption

X-ray photoelectron spectroscopy (XPS) was use for the chemical analysis of SNPs before and after adsorption. The surface chemical species analysis for the starch granules before and after the adsorption process was achieved at a depth of 5 nm. The surface depth analysis for the SNPs before and after adsorption was also achieved.

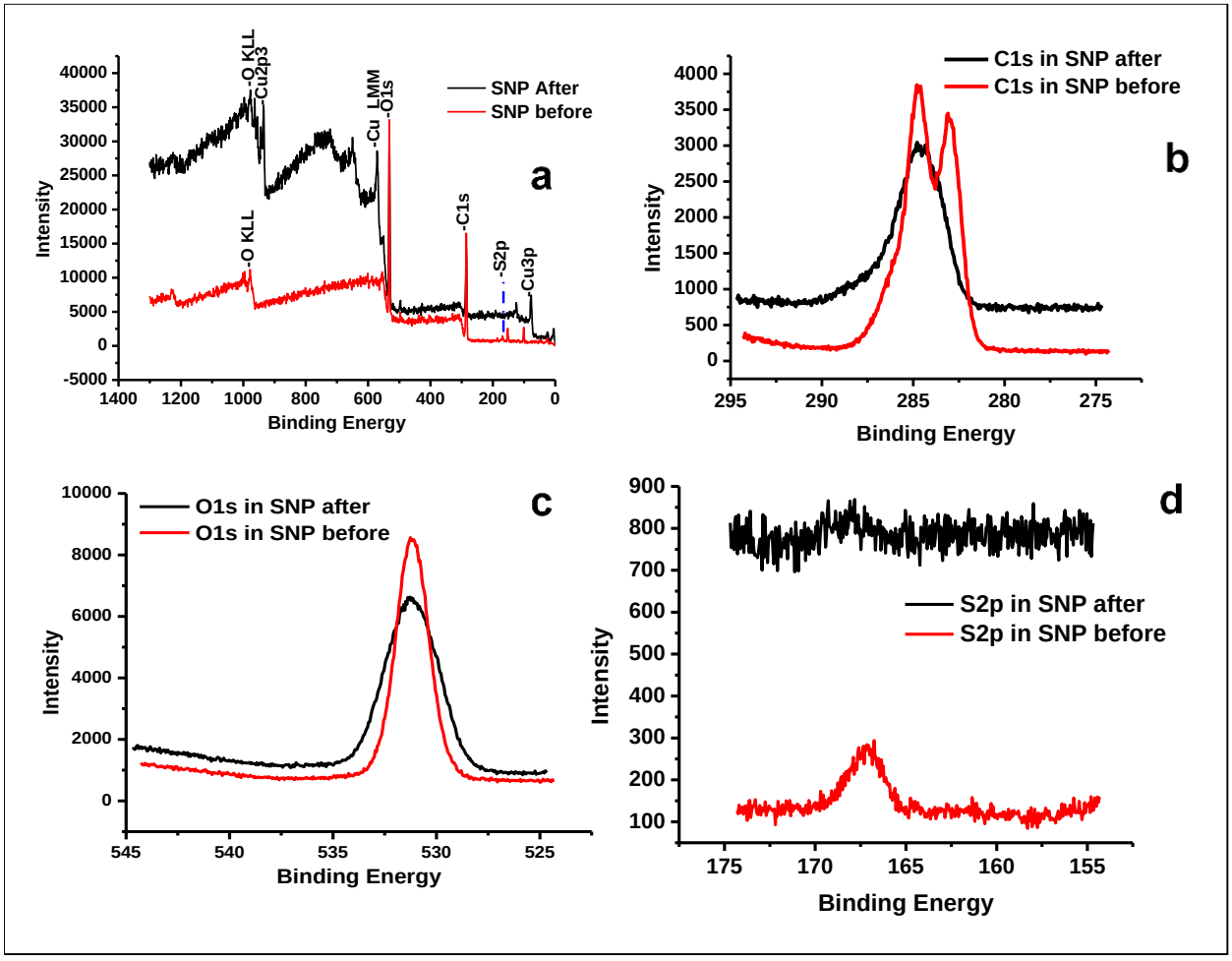

Figure 7.6 (a) High-resolution XPS spectrum of the surface activated SNPs before and after adsorption; (b) for C1s (c) for O1s, and (d) for S1s

The X-ray photoelectron spectrometer used characteristic Al Kα radiation as an excitation source and a constant pass energy of 40 eV. The binding energy (BE) of C 1s was shift to 284.6 eV as an internal reference. In figure 7.5, the XPS inspection spectra of SNPs, SNPs-Cu and high-resolution XPS spectra of C1s, O1s and S1s have been shown for the changes in surface

elements and their bond energies. The main elements in the SNPs adsorbent are C1s, O1s and S1s. The hydroxyl and sulphonic functional groups on the surface of SNPs could be confirmed (figure 7.6 (b), (c) and (d)). After Cu ion adsorption on the surface of SNPs, Cu appears in the XPS spectrum of SNPs-Cu nanocomposite. Further, the chemical environment changes of the surface elements were analysed by the high-resolution spectra of C1s, O1s and Cu 1s in XPS. In the spectrum of C1s (figure 7.6(b)), the starch nanoparticles present a single peak of 284.6 eV, corresponding to stable carbon bonds. These are attribute to the C1s in the glucose monomers. The new peaks at 284.72 eV and 282.99 eV show the interaction of C1s with the Cu ions after adsorption. In the spectrum of O 1s (figure 7.6 (c)), the peak at 531.62 eV can be attributed to the C-O bond, unaffected by the adsorption process. The variation in the intensity of the peak was attribute to OH radical interactions at the surface with the Cu ions and surroundings [37,38].

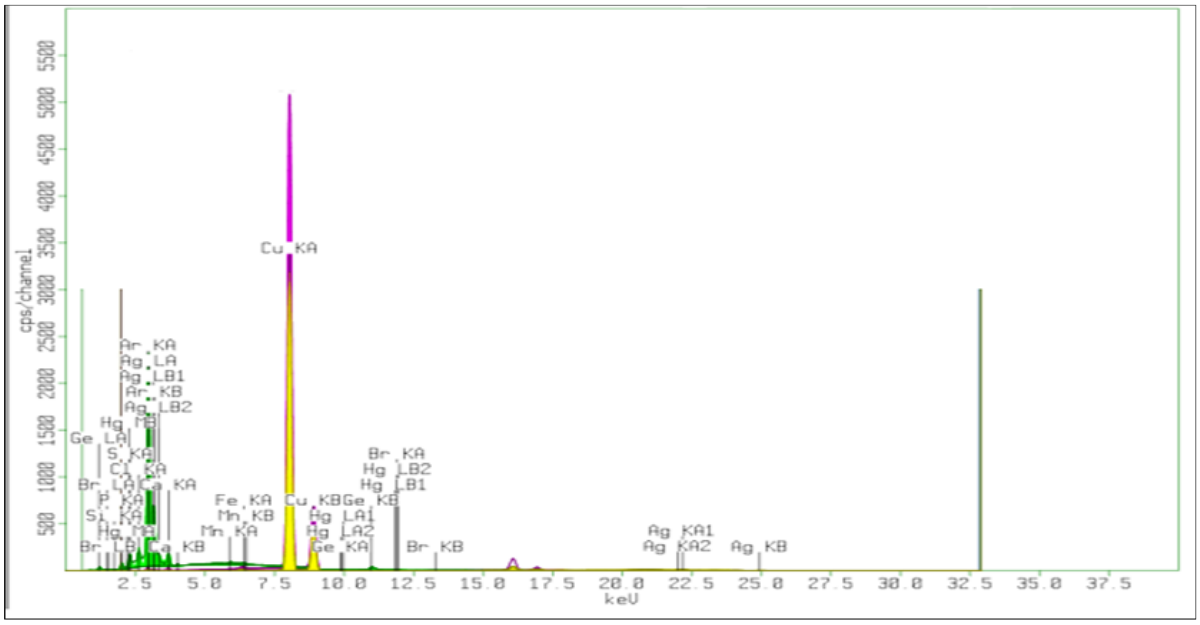

Figure 7.7 XRF spectrum of the surface activated SNPs after adsorption

The new linkages develop between hydroxyl or carboxyl groups on the surface of starch nanoparticles due to acid hydrolysis during the size reduction increasing the intensity at 531.62 eV. The sulfonic functional group interaction with the Cu ions was illustrate in figure 7.5 (d) for all S 1s at 167.29 eV. The intensity variation is due to the electrostatic interaction of S 1s. The new peaks at 934.74 eV, 572.03 eV, and 77.29 eV was attributed to Cu (II), Cu and Cu (III) interactions of Cu with the SNPs surface. The peak strength of S 1s were decrease after Cu (II) adsorption, indicating that Cu (II) is involved in the adsorption process [39].

XRF is an elemental analysis method that detects the presence of specific elements using secondary X-rays generated by individual atoms. The XRF spectrum for the SNPs after the adsorption process were illustrate in figure 7.7. The Cu component in the spectrum is significantly higher than other metal components. Other metal components are due to the contamination of impurities during sample handling. The adsorption of Cu on the SNPs surface is prominent due to the interaction with the hydroxyl group. This is why the concentration of Cu on the surface of SNPs is more prominent. Cu metal ions on the SNPs surface are seen in figure 7.7, where they attract surfaces more strongly than other metal ions [40].

7.4.5 Zeta potential of SNPs after adsorption

The figure 7.8 illustrates the zeta potential of SNPs-Cu after adsorption. After 60 min of adsorption equilibrium, the dried SNPs were analysed for the potential charges along the surfaces. The higher negative charge (-68 mV) of the colloidal solution of SNP-Cu shows higher stability. The additional potential in SNP granules after the adsorption confirms the presence of attached Cu ions on the surface [41].

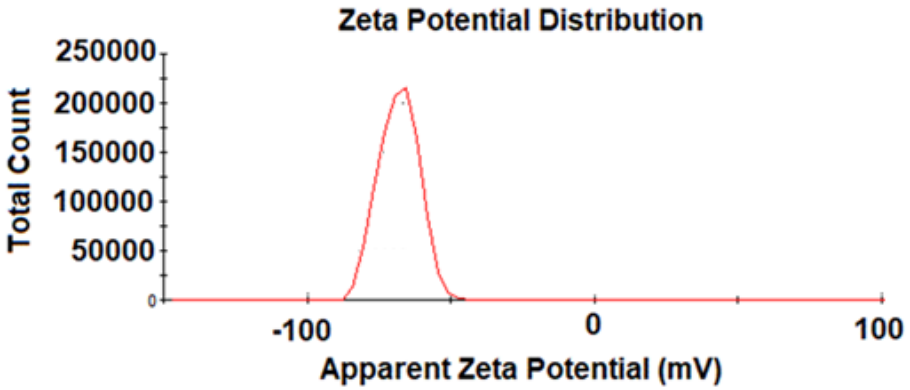

Figure 7.8 Zeta potential of SNPs after adsorption

7.4.6 XRD of SNPs before and after adsorption

The SNPs possess a semi-crystalline structure as observed in the figure 7.9. Ultrasonic cavitation destroys the natural starch particles, elucidating a high impact of the resultant cavities collapse. The critical peak of Cu is predominant on the surface of starch by comparing the SNPs before and after adsorption. The XRD diffraction of SNPs-Cu shows significant variations. The prominent peak of Cu is found at 36.65^{o} and 42.47^{o}. The diffraction supports the adsorption of Cu on the surface of SNPs. The significant variation in the SNP-Cu XRD spectrum was observed as compared with the SNP spectrum.

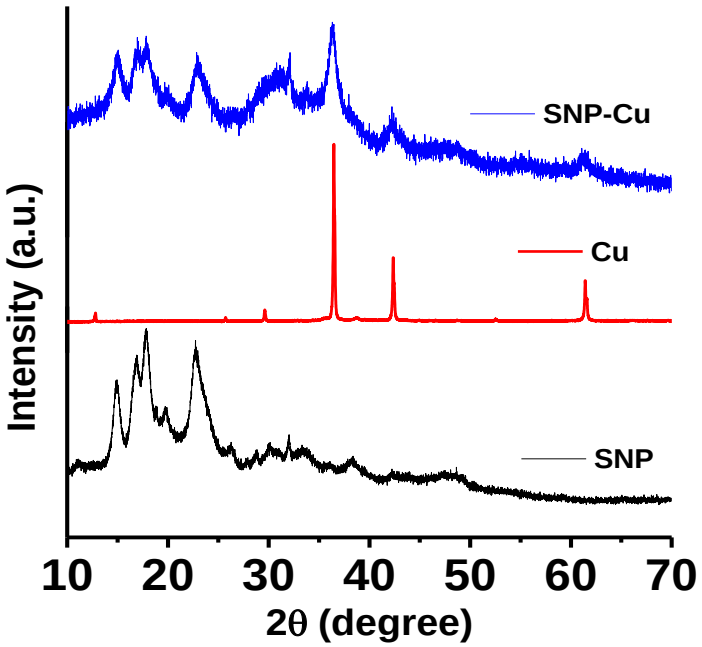

Figure 7.9 XRD spectrum of SNPs before and after adsorption compared with Cu NPs.

The Significant peaks of Cu 36^{o} (111), 42^{o} (200) and 61^{o} (211) was dominantly observed in the SNP-Cu composite indicates the presence of Cu in the composite. The amorphous SNPs shows higher crystallinity as peaks gets sharpen and width gets narrower in SNP-Cu composite.

7.4.7 Effect of adsorbent dosage and pH variation on the removal efficiency of Cu.

Adsorption is a surface phenomenon. The higher quantity of SNPs gives a larger surface area for the adsorption process. At the fixed initial concentration, the effect of dosage on the adsorption efficiency of Cu (II) metal ions was studied. The adsorption efficacy depends upon the available surface area on SNPs. As the dosage of SNPs increases, adsorption sites and hence the effective surface area available for adsorption increases several folds, leading to higher extraction efficiency of Cu (II) ions from the suspension. However, the increase in removal efficiency was up to a certain critical limit with increasing dosage. After this critical limit, the actual enhancement in Cu (II) adsorption with respect to the increasing amount of SNPs was much lower. Thus, a further increase in the dosage after the critical limit does not significantly enhance the removal efficiency of SNPs. This phenomenon was ascribed to the occupancy of all the active sites on the surface of SNPs followed by equilibrium achievement in the multilayer formation. Figure 7.10 illustrate the effect of adsorbent dosage and pH of initial solution on the Cu (II) removal efficiency during adsorption process.

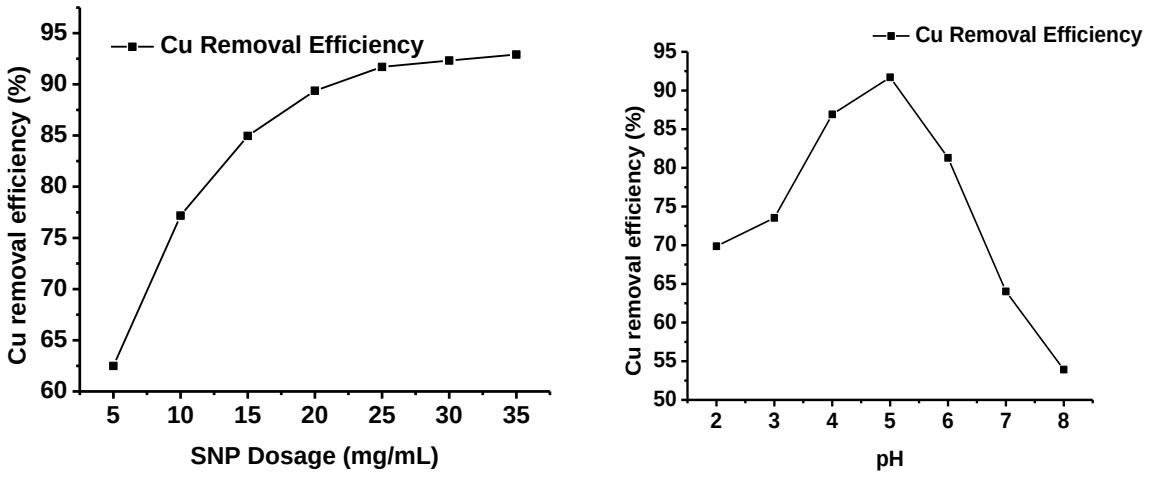

(a) (b)

Figure 7.10 Effect of a) SNPs dosage b) pH on the removal efficiency of Cu (II) ions

The Cu (II) ions might be assembled in a multilayer on the SNPs surface. The progress of such a multilayer formation could depend on the adsorption forces arising from SNPs. At the critical dosage of SNPs (25 mg/mL), the strength of adsorption forces was balance by the maximum number of Cu (II) molecules. Due to this, after the critical dosage limit, the actual Cu (II) ion adsorption rate is much lower, and the actual Cu (II) absorbed on the SNPs is much lower. Thus, excess dosage after the critical limit is not economical. Another reason for the lower adsorption rate might be the agglomeration of SNPs. The intermolecular interaction between SNPs molecules will be higher at a higher dosage. Such a higher interaction may lead to agglomeration of SNPs which diminishes the overall available surface active sites for adsorption. As the accessibility to the number of active sites reduces at a higher dosage, the removal efficacy after a critical limit is lower.

Thus, the addition of SNPs after the critical dosage does not have any significance. The uniform mixing of SNPs directly affects the removal of Cu (II) ions. The interaction of Cu (II) ions with SNPs enhances the adsorption rate. The removal efficiency of Cu (II) is almost constant beyond the optimal dosage of SNPs. As shown in figure 7.10 (a), the maximum removal of 93 % was obtained at a 25 mg/mL dosage. A similar reduction in the adsorption capacity of Cu (II) ions has been reported by Kumar et al. [27]. Additionally, the results indicate that the critical limit of the dose may not be constant for all the adsorbents, which depends on the surface area of the adsorbent and the number of adsorbates. Intermolecular forces are crucial in determining the amount of critical dose. The adsorption of Cu (II) ions on the adsorbent surface of SNPs is due to the interaction between the charged surfaces. The surface charges on the SNPs and Cu

(II) metal ions play a significant role in the overall removal efficiency. A change in the pH varies the concentration of H^+ ions in the suspension, which is in direct contact with both the adsorbent as well as the adsorbate. The effect of pH on the surface charges of the absorbent and adsorbate during the adsorption process was studied by varying pH values. The removal efficiency of Cu (II) ions on the surface of SNPs was studied in the range of pH from 2 to 8.

Figure 7.10 (b) illustrates the removal efficiency of Cu (II) ions with changes in pH. At an optimal pH of 5, the maximum removal efficiency of 93 % was achieved. Also, the removal efficiency increases with an increase in the pH from 2 to 5. The lower is the pH value; the larger is the number of H+ ions present in the suspension. This higher number of H+ ions directly affects the affinity of Cu (II) towards the surface of the SNPs adsorbent. In comparison to Cu (II), positively charged hydrogen ions interact more strongly with the active sites of SNPs at lower pH values. This results in an overall lower adsorption efficiency of Cu (II) ions. However, with an increasing pH value of suspension, the number of H^+ ions decreases in the suspension, increasing SNPs adsorption efficiency for Cu (II). The increase in Cu (II) removal efficiency was noticed up to the optimal pH of the suspension. Similar results were observed by Kubra et al. [42] using functionalized lignin-based complex for the adsorption of Cu (II).

A further increase of pH above the optimum value decreases the Cu (II) removal efficacy of the as-produced SNPs. The higher pH suspension contains a higher concentration of HO- ions, which interact with Cu (II) ions and results in a complex structure that includes forming a stable CuO structure in the suspension. CuO has a lower affinity for the active sites of the SNPs surface. As a result, the Cu (II) removal efficiency of as-produced SNPs at higher pH values is low. At a pH greater than 5, the removal efficacy of Cu (II) on the SNPs decreases. The optimal pH depends on the surface interactions between the adsorbent and the targeted adsorbate.

7.4.8 Effect of initial concentration of Cu ions in solution

The interaction between the active sites on the surface of the adsorbent and the moving Cu (II) ions in the suspension affects the adsorption mechanism. The impact of the initial concentration of Cu (II) ions on the available active sites of the adsorbent is significant. The effect of initial Cu (II) ions on the removal efficacy was studied with a fixed amount of SNPs. The activation sites on the adsorbent are constant at the constant amount of SNPs.

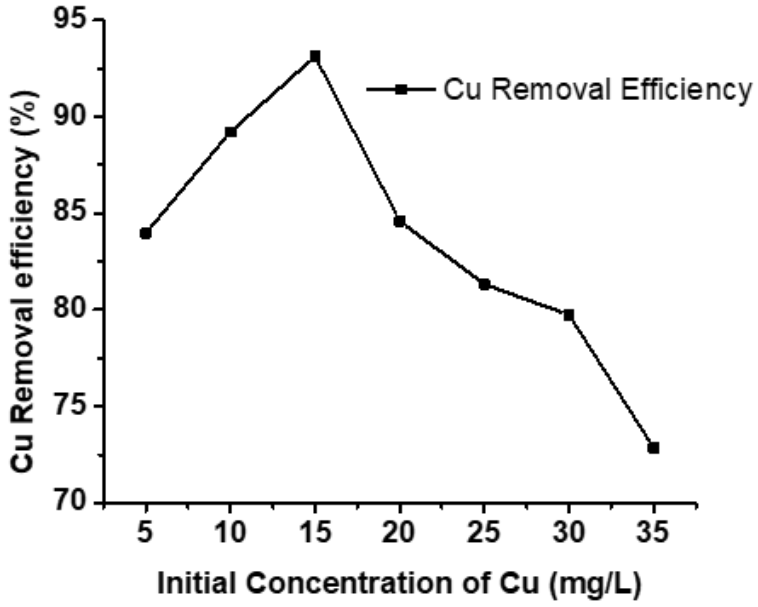

Figure 7.11 Effect of initial concentration of Cu (II) ions on the adsorption capacity of SNPs.

The interaction between active sites of SNPs and Cu (II) ions separates Cu (II) ions from the suspension. Thus, the limiting component of the process is the availability of active sites on the SNPs surface. With the increase in the initial concentration, the removal efficiency of Cu (II) ions increases, which is up to an optimal concentration. The removal efficiency decreased drastically with an increase in the initial concentration. The concentration changes were observe from 5 to 35 mg/mL of cupric ions, keeping the pH and the amount of SNPs constant. Figure 7.11 shows the removal efficacy of cupric ions with an increase in the initial quantity of cupric ions per mL of suspension at constant pH (5) and SNPs loading (25 mg/mL). The volume of cupric ions present in the suspension illustrates the significant effect on the extraction efficiency of SNPs. At the volume fraction of Cu (II) ions in the suspension, the availability of active sites is higher; also, the binding affinity between the surface of the adsorbent and adsorbate is high. This results in a higher rate of adsorption of Cu (II) ions on the SNPs surface. The heat of adsorption released during adsorption is much lower than the heat of desorption, favourable for the higher adsorption rate. Thus, at a lower concentration, higher removal efficacy is observed. The decrease in the removal efficiency may occur due to the higher lateral interaction between adsorbate molecules. The lateral interactions between the adsorbate Cu (II) molecules involve higher energy exchanges through the Brownian motion, the force of attraction and repulsion, making them unstable on the surface of adsorbent SNPs.

This increases the desorption rate compared to the adsorption rate of Cu (II) adsorbates on the surface of SNPs.

The formation of a monolayer on the active sites of SNPs was observed at higher initial concentrations of Cu (II) ions. The lateral interaction of Cu (II) ions in the suspension prevent further propagation of Cu (II) adsorption beyond the monolayer. The local mass transfer coefficient values of individual Cu (II) molecules are affected by lateral interaction at higher concentrations of Cu (II). This results in a lower rate of Cu (II) transfer from the suspension to the actual active site of the SNPs adsorbent. As a result, the removal efficiency of Cu (II) from the suspension is reduced. Thus, adsorption at a higher initial concentration of Cu (II) follows the Langmuir isotherm, reducing the removal efficacy of Cu (II) ions compared to its lower initial concentration.

7.4.9 Mechanism of Copper ions adsorption on SNPs

The mass transfer-driven adsorption involves the sedimentation of copper metal particles on the surface of SNPs. The interface interaction between the SNPs and Cu ions could be in two ways, one goes with bioaccumulation, and another is biosorption. The accumulation of Cu ions on the surface of SNP does not offer any physical or chemical interactions. However, Cu will be bounded with the physicochemical bond with the SNP surface in the biosorption. The possible adsorption mechanisms of metal ions onto biosorbents include physical adsorption, chemisorption, electrostatic interactions, hydrogen bonding, pi-pi interactions, and precipitation. The representation of a possible mechanism is illustrated in figure 7.12.

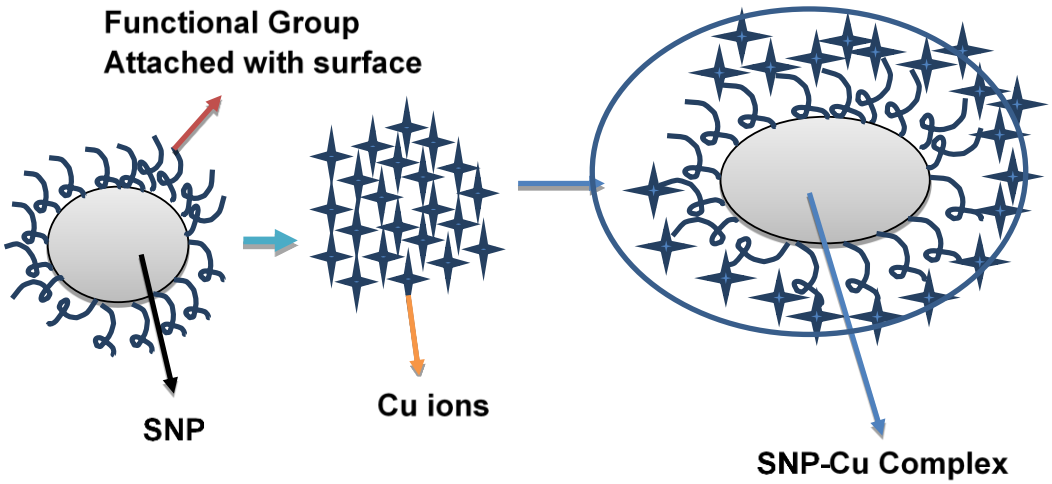

Figure 7.12 Mechanism of the adsorption of Cu ions on the SNPs surface

The FTIR analysis of SNPs confirms the presence of functional groups such as carbonyl, carboxyl, and hydroxyl groups on the surface of SNPs granules, which are most often negatively charged. Besides, the metal ions can be adsorbed onto the pores and cavities on the surface of SNPs. The microporous SNPs surface is verified with the BET analysis of SNPs before the adsorption process. The higher adsorption amount of N_2 molecules on the surface of the SNPs-Cu cloud may be because of the higher pore density associated with the complex. The adsorption of Cu (II) ions from wastewater involve the diffusion of Cu (II) ions and their binding to the SNPs surface via electrostatic attractions [43,44]. It can be suggested that the electrostatic attractions between positively charged metal ions and the negatively charged functional groups of the SNPs could successfully promote the adsorption capacity. Other attractive forces, such as Van der Waal forces, hydrogen bonding, and concentration gradients, may be involved in Cu (II) ion adsorption on the surface of SNPs [18].

The experimental findings for the removal efficiency of Cu ions employing generated SNPs must also be compared to conventional copper removal techniques. Table 7.4 compares the findings of the reported research with those of the present set of trials in order to better understand the effectiveness of the suggested strategies.

Table 7.4 Overview of the reported bio-adsorbents for the removal of Cu ions from wastewater.

Biosorbent used for adsorption	Sorbent	Maximum efficiency (mg/g)	Optimal conditions	Isotherm Validated	Mechanism	Ref.
Calcined animal bone	Zn (II), Cu (II)	Zn(II): 26.93 Cu(II): 22.98	pH: 4.5; Et: 180 min; D: 2-16 g/L; Ci:100 mg/L	Pseudo-second order kinetics	Electrostatic attraction and surface adsorption	[45]
Calcite modification of agri-cultural waste	Cu(II)	21.3	pH: 5.5; Et:100 min D: 0.05 g/L; Ci:100 mg/L	Pseudo-second order, Langmuir model	Monolayer chemisorption	[46]
Pectin based composite hydrogel from grape fruit peel	Cu(II)	80.6	pH: 6; Et: 100 min; D: 25 %; Ci:100 mg/L	Pseudo-second order, Langmuir model	Electrostatic attraction, ion exchange and physical adsorption	[47]
Gundelia Tournefortii	Cu(II)	38.8	pH: 3; Et: 50 min; D: 5 g/L; Ci:200 mg/L	Pseudo-second order and Langmuir model	Weak electrostatic interaction	[48]

Green vegetable waste	Cu(II)	75	pH: 3.5; Et: 120 min; D: 0.6 g/L; Ci: 1.5 mg/L	pseudo-second order, Langmuir isotherm	Physical adsorption	[49]
low cost natural/agricultural waste biomasses	Cu(II)	75	pH: 6; Et: 180 min; D: 0.6 g/L; Ci: 25 mg/L	Pseudo-second order, Dubinin-Radushkevich isotherm	Monolayer adsorption and physicochemical adsorption	[50]
SNP (present work)	Cu(II)	93	pH: 5; Et: 60 min; D:25 mg/L Ci: 15 mg/L	pseudo-second order, Langmuir isotherm	Monolayer adsorption and Physi-chemical adsorption	-

* Et: Equilibrium time (min); Ci: Initial concentration of adsorbate (mg/L); D: Dosage (g)

7.4.9.1 Copper ions adsorption on SNPs: kinetics analysis

The adsorption process depends on the overall contact time between the adsorbent's surface and the number of adsorbates in the suspension. With a longer time, a higher quantity of Cu (II) ions could interact with the SNPs and hence a higher separation. The adsorption kinetics shows a certain optimal value where desorption balances all the adsorptive forces from the SNPs granules. No further significant Cu (II) ion adsorption on the SNPs surface. This optimum is the equilibrium condition, and the time to reach this condition is the minimum time or equilibrium time [50].

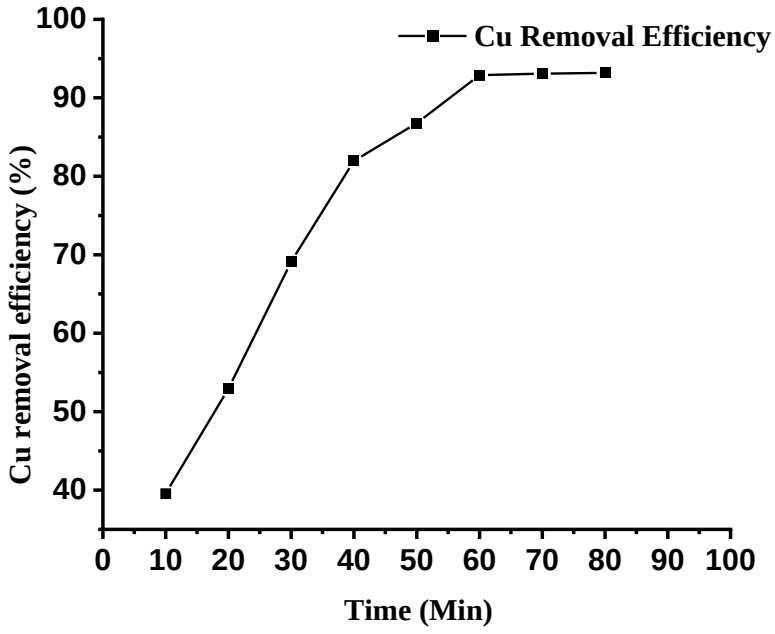

Figure 7.13 Effect of contact time on the removal efficiency of Cu (II) ions from the solution.

The figure 7.13 gives the adsorption capacity of SNP with respective to the time. The maximum adsorption efficiency of 93 % of the initial concentration was observed to be achieved with in 60 min. The adsorption was not significantly increases after 93 % after 60 min, thus the time 60 min was conclude to be equilibrium time for the adsorption of Cu (II) ions on the SNPs. The kinetics of Cu (II) adsorption was studied with changes in the removal efficiency with respect to time. Two pseudo-first order and pseudo-second order kinetics were utilized to verify the adsorption kinetics.

The pseudo-first order adsorption kinetics was evaluated using the following equation 7.3.

$$\log(Q_e - Q_t) = \log(Q_e) - \frac{k_1}{2.303} t \qquad \text{(Eq. 7.3)}$$

Where k1 is the constant. The graph of $\log(Q_e - Q_t)$Vs t (Figure 7.14 (a)) gives an overview of the pseudo-first- order adsorption kinetics. The overall linear regression value (R2) for the pseudo-first order kinetics is 94 %. The intercept and slope of the regression were calculated, and then k1 and intercept $\log(Q_e)$ were obtained.

Pseudo-second order adsorption kinetics was evaluated by the following equation 7.4.

$$\frac{t}{Q_t} = \frac{1}{k_2 (Q_e)^2} + \frac{1}{Q_e}(t) \qquad \text{(Eq. 7.4)}$$

Figure 7.14 (b) illustrates the kinetics of $\frac{t}{Q_t}$Vs t. The slope and intercept provide the values of second order, constant k_2 and the equilibrium quantity (Q_e) of Cu (II) ions adsorbed per gram of SNPs, respectively.

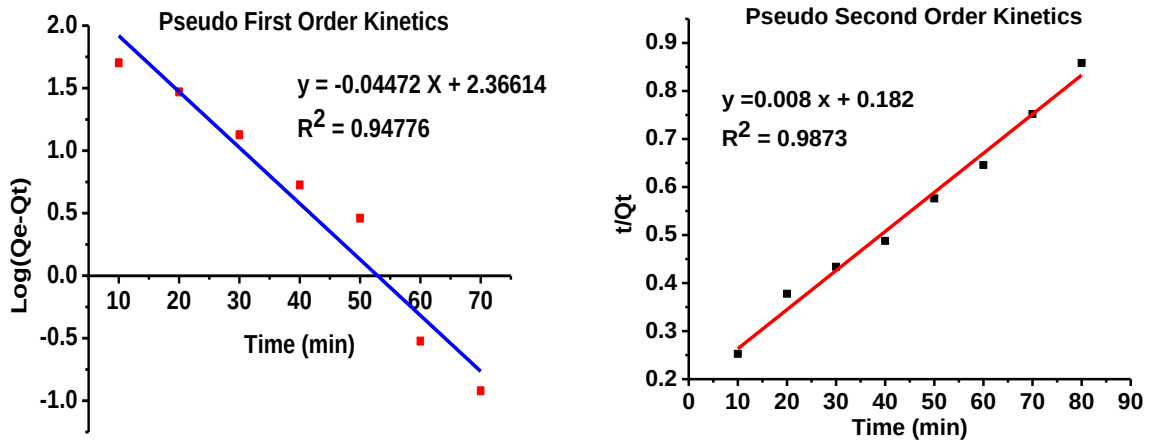

(a) (b)

Figure 7.14 (a) Pseudo-first order adsorption kinetics (b) Pseudo-second order adsorption kinetics of Cu (II) ions on the surface of SNPs.

The regression value of second order kinetics is 0.9873, higher than the pseudo-first order kinetics. These observations exhibit that the pseudo-second order adsorption kinetics is the more suitable for this adsorption [51].

7.4.9.2 Adsorption isotherm

The basic operation principles for Cu (II) adsorption are the mass transfer and physicochemical interaction between adsorbate (Cu) and adsorbent (SNPs). The adsorption process could be understood through various isotherms. These isotherms are equilibrium correlations amongst the various process parameters. The isotherm helps to define the mechanism through which the progress of the adsorption process occurs. The Langmuir adsorption isotherm and Freundlich isotherm are commonly used primary mechanisms of the adsorption processes. The monolayer adsorption is associated with the Langmuir isotherm, whereas the multilayer adsorption isotherm validates the Freundlich isotherm. The quantitative distribution of adsorbate in the two distinguished phases as solid-phase adsorbent and liquid phase suspension at equilibrium conditions can be estimated using the isotherm. The monolayer formation of adsorbate on the adsorbent surface can be explained using the Langmuir isotherm. The number of active sites available for adsorption on the adsorbent surface will only be occupied by the equivalent number of adsorbates. The multilayer formation of adsorbate on the adsorbent surface is not considered by the Langmuir adsorption isotherm. The Langmuir isotherm should have been treated as an ideal condition for adsorption [48].

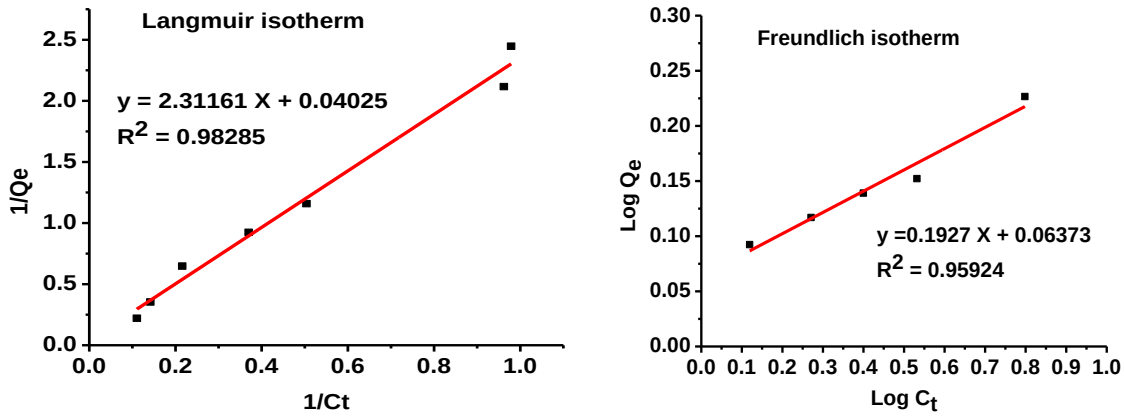

(a) (b)

Figure 7.15 (a) Langmuir adsorption mechanism (b) Freundlich isotherm mechanism.

In comparison, the specialty of the isotherm is the value of RL. The RL calculated from the Langmuir isotherm verifies the feasibility of the adsorption process. If the value of RL is greater

than 1, the adsorption is not favourable; however, when 0<RL<1, the adsorption is favourable. The adsorption process is irreversible in the case of RL =0 [52]. The affinity of Cu (II) ions towards SNPs in the suspension was validated from these isotherms. Following equations of Langmuir isotherm (equation 7.5) and Freundlich isotherm (equation 7.6) were used to plot figure 7.15 (a) and (b), respectively. The value of RL is calculated from the slope and intercept of figure 7.15 (a) (equation 7.7).

$$Q_e = \frac{X}{M} = \frac{Q_{max} * b\ C}{1+bC}$$

$$\frac{1}{X/M} = \frac{1}{Q_{max}} + \frac{1}{Q_{max} b} \quad \frac{1}{C_t} \qquad \text{(Eq. 7.5)}$$

$$\log Q_e = \log K + \frac{1}{n} \log C \qquad \text{(Eq. 7.6)}$$

$$R_L = \frac{1}{1+bC_o} \qquad \text{(Eq. 7.7)}$$

Where b is the Langmuir constant, while K and n are the Freundlich constants for the adsorbent and adsorbate pair, respectively.

From the Langmuir isotherm, the value of RL= 0.017 tends towards the irreversible behaviour of the process. The R_2 value of the Langmuir isotherm is 98 % which is higher than the value of the Freundlich isotherm. Thus, adsorption follows Langmuir adsorption behaviour. The maximum value of Cu (II) separated from the solution is 43 mg/g of SNPs, indicating good applicability of the developed adsorbent for real case scenarios [48].

7.5 Conclusions

SNPs were synthesized through the robust ultrasound assisted acid hydrolysis process. By process optimization, the synthesised SNPs show smaller particle size distribution at a low acid concentration (0.25 M) (50-80 nm). As-synthesized SNPs are the surface activated entities, and the anionic functional groups are present on the SNPs surface. These SNP were utilized for the extraction of cupric ions. The process was favourable and confirmed by the characteristic value of RL in the Langmuir isotherm (RL= 0.017). It exhibits pseudo-second-order adsorption kinetics and follows the Langmuir adsorption isotherm. The various parameters for the adsorption were studied. The additional specific surface area in SNPs after adsorption is attributed to the presence of Cu (II) ions on the surface. The XPS analysis of the SNPs-Cu composite confirms the interaction of Cu (II) with the surface sulfonic functional group. This weak electrostatic interaction keeps the Cu (II) ions on the surface of SNPs. The optimal values of different parameters were: initial concentration of Cu (II) ion 15 mg/mL, pH 5, and SNPs

dosage 25 mg/mL, resulting in the maximum Cu (II) ion removal of 93 % from the suspension. The RL value of the adsorption process is close to zero, indicating its irreversibility. The biosorption of Cu with the abundantly found SNPs is an economical and eco-friendly process. The results may benefit industrial wastewater treatment. The advantage of this process is that it does not require any functionalization of biosorbent. The maximum value of Cu (II) ions separated from the solution was 43 mg/g of SNPs, was observed which is much higher than that of reported in the literature at lower initial concentration.

References

[1] V.O. Abramov, A. V. Abramova, G. Cravotto, R. V. Nikonov, I.S. Fedulov, V.K. Ivanov, Flow-mode water treatment under simultaneous hydrodynamic cavitation and plasma, Ultrason. Sonochem. 70 (2021) 105323. https://doi.org/10.1016/j.ultsonch.2020.105323.

[2] W. Rongwong, K. Goh, Resource recovery from industrial wastewaters by hydrophobic membrane contactors: A review, J. Environ. Chem. Eng. 8 (2020) 104242. https://doi.org/10.1016/j.jece.2020.104242.

[3] R.-X. Wu, G.-F. Zheng, W.-W. Li, L.-B. Zhong, Y.-M. Zheng, Electrospun Chitosan Nanofiber Membrane for Adsorption of Cu(II) from Aqueous Solution: Fabrication,

Characterization and Performance, J. Nanosci. Nanotechnol. 18 (2018) 5624–5635. https://doi.org/10.1166/jnn.2018.15433.

[4] R.M. Puthusseri, H.P. Nair, T.K. Johny, S.G. Bhat, Insights into the response of mangrove sediment microbiomes to heavy metal pollution: Ecological risk assessment and metagenomics perspectives, J. Environ. Manage. 298 (2021) 113492. https://doi.org /10.1016/j.jenvman.2021.113492.

[5] S. Lal, A. Singhal, P. Kumari, Exploring carbonaceous nanomaterials for arsenic and chromium removal from wastewater, J. Water Process Eng. 36 (2020) 101276. https://doi.org/10.1016/j.jwpe.2020.101276.

[6] X. Zhang, Y. Liu, Concurrent removal of Cu(II), Co(II) and Ni(II) from wastewater by nanostructured layered sodium vanadosilicate: Competitive adsorption kinetics and mechanisms, J. Environ. Chem. Eng. 9 (2021) 105945. https://doi.org/10.1016/j.jece. 2021.105945.

[7] H. Tounsadi, A. Khalidi, M. Abdennouri, N. Barka, Activated carbon from Diplotaxis Harra biomass: Optimization of preparation conditions and heavy metal removal, J. Taiwan Inst. Chem. Eng. 59 (2016) 348–358. https://doi.org/10.1016/j.jtice.2015.08.01.

[8] P. Bartczak, M. Norman, Ł. Klapiszewski, N. Karwańska, M. Kawalec, M. Baczyńska, M. Wysokowski, J. Zdarta, F. Ciesielczyk, T. Jesionowski, Removal of nickel(II) and lead(II) ions from aqueous solution using peat as a low-cost adsorbent: A kinetic and equilibrium study, Arab. J. Chem. 11 (2018) 1209–1222. https://doi.org/10.1016 /j.arabjc.2015.07.018.

[9] S.A. Al-Saydeh, M.H. El-Naas, S.J. Zaidi, Copper removal from industrial wastewater: A comprehensive review, J. Ind. Eng. Chem. 56 (2017) 35–44. https://doi.org/10.1016 /j.jiec.2017.07.026.

[10] P. Murugesan, V. Evanjalin Monica, J.A. Moses, C. Anandharamakrishnan, Water decontamination using non-thermal plasma: Concepts, applications, and prospects, J. Environ. Chem. Eng. 8 (2020) 104377. https://doi.org/10.1016/j.jece.2020.104377.

[11] S. Khan, M. Naushad, A. Al-Gheethi, J. Iqbal, Engineered nanoparticles for removal of pollutants from wastewater: Current status and future prospects of nanotechnology for remediation strategies, J. Environ. Chem. Eng. 9 (2021). https://doi.org/10.1016/j.jece. 2021.106160.

[12] N. Kim, D. Park, Biosorptive treatment of acid mine drainage: a review, Int. J. Environ. Sci. Technol. 19 (2022) 9115–9128. https://doi.org/10.1007/s13762-021-03631-5.

[13] F.R. Kurzemann, M. Fernández-Delgado Juárez, M. Probst, M. Gómez-Brandón, C. Partl, H. Insam, Effect of biomass fly ashes from fast pyrolysis bio-oil production on soil properties and plant yield, J. Environ. Manage. 298 (2021). https://doi.org/10. 1016/j.jenvman.2021.113479.

[14] Y. Wang, Y. Liu, K. Zheng, L. Xie, Q. Ren, Z. Yang, Q. Liao, Y. Wang, R. Chen, The role of extracellular polymeric substances (EPS) in the reduction of Cr(VI) by Pannonibacter phragmitetus BB, J. Environ. Chem. Eng. 9 (2021) 106163. https://doi. org/10.1016/j.jece.2021.106163.

[15] S.M.D. Niaki, A. Takdastan, M.H. Bazafkan, M.A. Zazouli, Survey of Nanofiltration Technology In Removing Heavy Metals (Ni , Cu and Zn) From Industrial Waste Water, (2015) 45–50.

[16] J.M. Jacob, R. Ravindran, M. Narayanan, S.M. Samuel, A. Pugazhendhi, G. Kumar,

Microalgae: A prospective low cost green alternative for nanoparticle synthesis, Curr. Opin. Environ. Sci. Heal. (2020) 1–5. https://doi.org/10.1016/j.coesh.2019.12.005.

[17] D.S. Malik, C.K. Jain, A.K. Yadav, Removal of heavy metals from emerging cellulosic low-cost adsorbents: a review, Appl. Water Sci. 7 (2017) 2113–2136. https://doi.org /10.1007/s13201-016-0401-8.

[18] M.A. Renu, K. Singh, S. Upadhyaya, R.K. Dohare, Removal of heavy metals from wastewater using modified agricultural adsorbents, Mater. Today Proc. 4 (2017) 10534–10538. https://doi.org/10.1016/j.matpr.2017.06.415.

[19] F.N. Acar, Z. Eren, Removal of Cu(II) ions by activated poplar sawdust (Samsun clone) from aqueous solutions., J. Hazard. Mater. 137 (2006) 909–914. https://doi.org/10. 1016/j.jhazmat.2006.03.014.

[20] N. Basci, E. Kocadagistan, B. Kocadagistan, Biosorption of copper (II) from aqueous solutions by wheat shell, Desalination. 164 (2004) 135–140. https://doi.org/10.1016/S0 011-9164(04)00172-9.

[21] P.D. Johnson, M.A. Watson, J. Brown, I.A. Jefcoat, Peanut hull pellets as a single use sorbent for the capture of Cu(II) from wastewater., Waste Manag. 22 (2002) 471–480. https://doi.org/10.1016/s0956-053x(01)00036-8.

[22] N. Asim, M.H. Amin, N.A. Samsudin, M. Badiei, H. Razali, M. Akhtaruzzaman, N. Amin, K. Sopian, Development of effective and sustainable adsorbent biomaterial from an agricultural waste material: Cu(II) removal, Mater. Chem. Phys. 249 (2020) 123128. https://doi.org/10.1016/j.matchemphys.2020.123128.

[23] C. Aravind, K. Chanakya, K. Mahindra, Removal of heavy metals from industrial waste water using coconut coir, Int. J. Civ. Eng. Technol. 8 (2017) 1869–1871.

[24] Q. Li, J. Zhai, W. Zhang, M. Wang, J. Zhou, Kinetic studies of adsorption of Pb(II), Cr(III) and Cu(II) from aqueous solution by sawdust and modified peanut husk., J. Hazard. Mater. 141 (2007) 163–167. https://doi.org/10.1016/j.jhazmat.2006.06.109.

[25] Y. He, W. Xiao, G. Li, F. Yang, P. Wu, T. Yang, C. Chen, P. Ding, A novel lead-ion-imprinted magnetic biosorbent: preparation, optimization and characterization, Environ. Technol. (United Kingdom). 40 (2019) 499–507. https://doi.org/10.1080/09593330. 2017.1397762.

[26] A. Celekli, B. Bozkus, H. Bozkurt, Development of a new adsorbent from pumpkin husk by KOH-modification to remove copper ions, Environ. Sci. Pollut. Res. 26 (2019) 11514–11523. https://doi.org/10.1007/s11356-017-1160-2.

[27] K. Kumar, S.S. Patavardhan, S. Lobo, R. Gonsalves, Equilibrium study of dried orange peel for its efficiency in removal of cupric ions from water, Int. J. Phytoremediation. 20 (2018) 593–598. https://doi.org/10.1080/15226514.2017.1405379.

[28] S. Yildiz, Kinetic and Isotherm Analysis of Cu(II) Adsorption onto Almond Shell (Prunus Dulcis), Ecol. Chem. Eng. S. 24 (2017) 87–106. https://doi.org/10.1515/eces-2017-0007.

[29] Y. Xin, S. Ma, G. Chen, L. Huang, Z. Xie, Highly efficient removal of cadmium (II) ions using cellulose-based monolith with a hierarchically porous structure fabricated through phase separation method, J. Water Process Eng. 48 (2022) 102901. https://doi.org/10.1016/j.jwpe.2022.102901.

[30] V.S. Hakke, V.K. Landge, S.H. Sonawane, G. Uday Bhaskar Babu, M. Ashokkumar, E. M. M. Flores, The physical, mechanical, thermal and barrier properties of starch

nanoparticle (SNP)/polyurethane (PU) nanocomposite films synthesised by an ultrasound-assisted process, Ultrason. Sonochem. 88 (2022) 106069. https://doi.org/10.1016/j.ultsonch.2022.106069.

[31] A. Meringer, A.S. Liffourrena, R.M. Heredia, G.I. Lucchesi, P.S. Boeris, Removal of copper and/or zinc ions from synthetic solutions by immobilized, non-viable bacterial biomass: Batch and fixed-bed column lab-scale study, J. Biotechnol. 328 (2021) 87–94. https://doi.org/10.1016/j.jbiotec.2021.01.011.

[32] O.E. Abdel Salam, N.A. Reiad, M.M. ElShafei, A study of the removal characteristics of heavy metals from wastewater by low-cost adsorbents, J. Adv. Res. 2 (2011) 297–303. https://doi.org/10.1016/j.jare.2011.01.008.

[33] C. Fonseka, S. Ryu, G. Naidu, J. Kandasamy, S. Vigneswaran, Recovery of water and valuable metals using low pressure nanofiltration and sequential adsorption from acid mine drainage, Environ. Technol. Innov. 28 (2022) 102753. https://doi.org/10.1016/j.eti.2022.102753.

[34] H. Sadegh, G.A.M. Ali, V.K. Gupta, A.S.H. Makhlouf, R. Shahryari-ghoshekandi, M.N. Nadagouda, M. Sillanpaa, E. Megiel, The role of nanomaterials as effective adsorbents and their applications in wastewater treatment, J. Nanostructure Chem. 7 (2017) 1–14. https://doi.org/10.1007/s40097-017-0219-4.

[35] F. Fathi, A. Dadkhah, H. Namazi, Characterisation and surface chemical modification of starch nanoparticles with lactid through ring opening polymerisation, Int. J. Nanoparticles. 7 (2014) 37–48. https://doi.org/10.1504/IJNP.2014.062012.

[36] M. Ahmad, A. Gani, I. Hassan, Q. Huang, H. Shabbir, Production and characterization of starch nanoparticles by mild alkali hydrolysis and ultra-sonication process, Sci. Rep. 10 (2020) 3533. https://doi.org/10.1038/s41598-020-60380-0.

[37] Y. Chen, Y. Liu, Y. Li, Y. Chen, Y. Wu, H. Li, S. Wang, Z. Peng, R. Xu, Z. Zeng, Novel Magnetic Pomelo Peel Biochar for Enhancing Pb(II) And Cu(II) Adsorption: Performance and Mechanism, Water, Air, Soil Pollut. 231 (2020) 404. https://doi.org/10.1007/s11270-020-04788-4.

[38] C. Ding, W. Cheng, X. Wang, Z.-Y. Wu, Y. Sun, C. Chen, X. Wang, S.-H. Yu, Competitive sorption of Pb(II), Cu(II) and Ni(II) on carbonaceous nanofibers: A spectroscopic and modeling approach, J. Hazard. Mater. 313 (2016) 253—261. https://doi.org/10.1016/j.jhazmat.2016.04.002.

[39] M. Fronczak, Adsorption performance of graphitic carbon nitride-based materials: Current state of the art, J. Environ. Chem. Eng. 8 (2020) 104411. https://doi.org/10.1016/j.jece.2020.104411.

[40] L. Brinza, K. Geraki, I.G. Breaban, M. Neamtu, Zn adsorption onto Irish Fucus vesiculosus: Biosorbent uptake capacity and atomistic mechanism insights, J. Hazard. Mater. 365 (2019) 252–260. https://doi.org/10.1016/j.jhazmat.2018.11.009.

[41] D. Beyene, M. Chae, J. Dai, C. Danumah, F. Tosto, A.G. Demesa, D.C. Bressler, Characterization of cellulase-treated fibers and resulting cellulose nanocrystals generated through acid hydrolysis, Materials (Basel). 11 (2018). https://doi.org/10.3390/ma11081272.

[42] K.T. Kubra, M.S. Salman, M.N. Hasan, A. Islam, M.M. Hasan, M.R. Awual, Utilizing an alternative composite material for effective copper(II) ion capturing from wastewater, J. Mol. Liq. 336 (2021) 116325. https://doi.org/10.1016/j.molliq.2021.116325.

[43] S. Muthusaravanan, N. Sivarajasekar, J.S. Vivek, T. Paramasivan, M. Naushad, J. Prakashmaran, V. Gayathri, O.K. Al-Duaij, Phytoremediation of heavy metals: mechanisms, methods and enhancements, Environ. Chem. Lett. 16 (2018) 1339–1359. https://doi.org/10.1007/s10311-018-0762-3.

[44] D. Bozic, M. Gorgievski, V. Stanković, N. Strbac, S. Serbula, N. Petrovic, D. Bozic, M. Gorgievski, V. Stankovic, N. Strbac, S. Serbula, N. Petrovic, Adsorption of heavy metal ions by beech sawdust - Kinetics, mechanism and equilibrium of the process, Ecol. Eng. 58 (2013) 202–206. https://doi.org/10.1016/j.ecoleng.2013.06.033.

[45] R. Slimani, I. El Ouahabi, A. Elmchaouri, B. Cagnon, S. El Antri, S. Lazar, Adsorption of copper (II) and zinc (II) onto calcined animal bone meal. Part I: Kinetic and thermodynamic parameters, Chem. Data Collect. 9–10 (2017) 184–196. https://doi.org/10.1016/j.cdc.2017.06.006.

[46] S. Wang, S. Zhong, X. Zheng, D. Xiao, L. Zheng, Y. Yang, H. Zhang, B. Ai, Z. Sheng, Calcite modification of agricultural waste biochar highly improves the adsorption of Cu(II) from aqueous solutions, J. Environ. Chem. Eng. 9 (2021) 106215. https://doi.org/10.1016/j.jece.2021.106215.

[47] W. Zhang, J. Song, Q. He, H. Wang, W. Lyu, H. Feng, W. Xiong, W. Guo, J. Wu, L. Chen, Novel pectin based composite hydrogel derived from grapefruit peel for enhanced Cu(II) removal, J. Hazard. Mater. 384 (2020) 121445. https://doi.org/10.1016/j.jhazmat.2019.121445.

[48] S. Golshan Shandi, F. Doulati Ardejani, F. Sharifi, Assessment of Cu (II) removal from an aqueous solution by raw Gundelia tournefortii as a new low-cost biosorbent: Experiments and modelling, Chinese J. Chem. Eng. 27 (2019) 1945–1955. https://doi.org/10.1016/j.cjche.2018.12.027.

[49] M.I. Sabela, K. Kunene, S. Kanchi, N.M. Xhakaza, A. Bathinapatla, P. Mdluli, D. Sharma, K. Bisetty, Removal of copper (II) from wastewater using green vegetable waste derived activated carbon: An approach to equilibrium and kinetic study, Arab. J. Chem. 12 (2019) 4331–4339. https://doi.org/10.1016/j.arabjc.2016.06.001.

[50] B. Singha, S.K. Das, Adsorptive removal of Cu(II) from aqueous solution and industrial effluent using natural/agricultural wastes, Colloids Surfaces B Biointerfaces. 107 (2013) 97–106. https://doi.org/10.1016/j.colsurfb.2013.01.060.

[51] M. Naushad, A. Mittal, M. Rathore, V. Gupta, Ion-exchange kinetic studies for Cd(II), Co(II), Cu(II), and Pb(II) metal ions over a composite cation exchanger, Desalin. Water Treat. 54 (2015) 2883–2890. https://doi.org/10.1080/19443994.2014.904823.

[52] G.R. Belton, Langmuir adsorption, the Gibbs adsorption isotherm, and interfacial kinetics in liquid metal systems, Metall. Mater. Trans. B. 7 (1976) 35–42. https://doi.org/10.1007/BF02652817.

Chapter 8. Overall Conclusions

8.1 Conclusions for the present study.

The current research investigates the benefits of bio nanoparticles as a nanofiller in polymer matrix for packaging applications and as a nanoadsorbent for wastewater treatment. The objective of the present work is to develop an improved acid hydrolysis process for manufacturing starch and cellulose nanoparticles and to assess their performance as a nanofiller and nanoadsorbent. To accomplish the objective of the present task, it was accomplish in four stages.

The initial step of the project was the manufacture of starch nanoparticles using traditional acid hydrolysis. The use of H_2SO_4 and ultrasound assistance was exploit for the intensification of conventional acid hydrolysis approach. The cavitation in the acidic suspension of native starch was produced using high frequency ultrasound sonication (frequency = 20 kHz). Conventional acid hydrolysis took at least 48 hours to convert 12-15 micron size native starch granules to the nanoscale of 500-600 nm. The conversion time for the accelerated acid hydrolysis strategy with the same starting native granular size is just 40 minutes when the nanoscale size is less than 100 nm. The cavitation impact during acid interactions was relate to the faster hydrolysis rate. Cavitation causes a greater mass transfer rate, whereas shear stress causes physical disintegration of native starch granules. Because of the physical degradation of the top surface of the starch granules, the impingement rate of acid in the starch granules rises. The produced starch nanoparticles (SNPs) have a particle size range of 70-90 nm, an 87 % crystallinity, and a better heat resistance and water absorption capability. The maximum duration for ultrasonic irradiation (0.5 M acid concentration) to obtain the gelatinization condition for the native starch solution is 60 minutes. The precipitation technique for starch granule reconstruction might generate SNPs, but it has poorer crystallinity and is more amorphous.

The numerous experiment was perform for the optimization of acid concentration during the intensified acid hydrolysis. The results revealed that when the acid content increased throughout the SNP production process, the final particle size increased with a narrower particle size distribution. Particle size of minimal with broad particle size dispersion at lower acid concentration (0.5 M). The SEM and TEM image analysis techniques was used to synthesize and validate the oval shape of SNPs. The enhanced strategy was used to synthesize SNPs, which were discovered to be an association of sulfonic (-OSO_2-) functional on the surface of SNP granules. The technique is robust and environmentally friendly since the acid used in the process was recover with about 10 % loss. The intensification of traditional acid

hydrolysis was accomplish at the expense of extra energy for cavitation formation, with a considerable decrease in conversion time, reduced particle size, and greater yield to 42 %, where it is not more than 16 % in the conventional process.

The second step was the manufacture of cellulose nanofibers (CNF) from cotton cellulose using an intensified acid hydrolysis method. SEM image examination validated the synthesized CNF. The crystalline structure of the CNF was confirm by XRD investigation. The elimination of cellulose's amorphous area during enhanced acid hydrolysis resulted in greater crystallinity. Microcrystalline cellulose (MCC) with starting particle sizes ranging from 7-9 μm was used in the same phase for the manufacture of cellulose nanocrystals (CNC). Using a close loop hydrodynamic cavitation technique, where the cavities was generates in an acidic solution of microcrystalline cellulose grains. The procedure is being run constantly and has been discovered to create the CNC with a greater yield of 47 %. During the enhanced acid hydrolysis process, CNCs was produce with a spherical shaped nanocrystalline structure. The procedure was conducted continuously for 15 minutes, and substantial alterations in the MCC were found. The crystallinity of CNC synthesized is greater than that of MCC. FESEM was used to examine the morphology of synthesized CNCs, which confirmed their spherical form. The significant economic analysis of synthesis approach for the synthesis cellulose nanoparticles (CNF and CNC) observed that continuous cavitation assisted acid hydrolysis was best approach for the synthesis of cellulose nanoparticles as it required lower cost per unit as well as it is safer to operate. However, the acoustic cavitation assisted acid hydrolysis was also effective in comparison with the conventional acid hydrolysis approach for synthesis of cellulose nanoparticles. The hydrodynamic cavitation assisted acid hydrolysis are influenced by various parameters such as, flow condition of suspension, cavitation number, the orifice plate opening to pipe diameter ratio, pressure gradient across the orifice plate, and most importantly initial granular size of cellulose.

In the third portion, biomass nanoparticles were used as nanofillers (SNPs and CNCs) and polyurethane (PU) polymer as the foundation material to create nanocomposite thin films. The process's main bottleneck was the uniform dispersion of biomass nanoparticles in the polymer solution. The ultrasound-assisted blending of SNP or CNC nanofillers in the PU matrix provided a partial solution, as the energy produced during the cavitation process provided additional exergy to activate and induce the hydroxyl physicochemical interactions between polyols from PU and hydroxyl functional groups from nanoparticles. For the manufacture of nanocomposite thin films, the simple casing approach was adopted. The film applicator was

used to keep the thickness of the film under control. The mechanical and thermal characteristics, water vapour permeability, and bacterial cell transmission through the film were all investigated in the nanocomposite films. When compared to PU thin films, the crystallinity, mechanical, and thermal characteristics of the synthesized nanocomposite films were found to be greater. The incorporation of nanofillers CNCs or SNPs into the PU matrix results in the formation of a compact structure of nanocomposite thin film. Thin film compactness gives greater resistance to the transition of water vapour, oxygen, and bacterial cells. At lower concentrations of nanofiller additions, the water vapour permeability of CNC-based nanocomposite film was found to be higher than that of SNP-based nanocomposite film. When 5 % CNC or SNP nanofillers were added to the thin films, bacterial cell transmission was decreased to 97 % when compared to the PU thin film. Significantly, the bacterial transmission rate is identical for both nanofillers at the same dose. The addition of SNP or CNC to the PU polymer matrix adds extra strength to the PU thin film. The mechanical properties of thin films were tested and found to be more concerning CNCs, resulting in increased performance when compared to CNCs nanofillers.

Surface-charged entities are the produced SNP using an enhanced acid hydrolysis method. The FTIR research proved that SNPs have a sulfonic functional group on their surface. As a result of their electrical charge, these nanoparticles were used to filter out copper (II) ions from synthetic wastewater. A preliminary test was performed to see whether SNP was successful in removing Cu (II) ions from the polluted water supply. Only a small number of studies have attempted to use SNP for this purpose. It was determined that 93 % of Cu (II) ions could be eliminated by using SNPs. Its adsorption kinetics are pseudo-second-order and it fits the Langmuir isotherm. Several adsorption parameters were investigated. The presence of Cu (II) ions on the surface of SNPs after adsorption is responsible for the increase in specific surface area. X-ray photoelectron spectroscopy (XPS) of the SNPs-Cu composite provides further evidence that Cu (II) interacts with the surface sulfonic functional group. For maximal Cu (II) ion removal from the solution, the ideal values of these parameters were 15 mg/mL, pH 5, and 25 mg/mL of SNPs. Biosorption of Cu using naturally occurring SNPs is a resource- and cost-efficient option. Potentially useful for improving the treatment of wastewater from industrial sources. This technique has the advantage that no biosorbent functionalization is required.

8.2 Future prospective

The commercially used petroleum based packaging materials are basic source for the pollutant generation and it retained for longer time due to larger time requirement of its degradation in

the environment. The strong chemical linkages in the petroleum based polymers such as polyethylene, polypropylene which required large energy for the degradation as well as the products after the decomposition are cause of NO_x and SO_x in the surroundings. All these are the new generation problem required a solution. The bio-degradable or the polymers which could have their degradation within some considerable day, could be used as packaging material. The reported studied are available for the successful synthesis of biodegradable polymers using natural polymers such as cellulose, starch, glycerol, protein, and chitosan. The major drawback of these synthesized films was it could not reach to the required mechanical and thermal resistance as well as good enough barrier to the water vapours, oxygen and bacterial cell. The present study focuses on the synthesis of starch and cellulose nanoparticles with the intensified acid hydrolysis methods, through which these nanoparticles are synthesized with greener approach. The process was cost effective, robust and safer for the production of nanoparticles with higher yield in lower consumption of time. The nanoparticles were used as nanofiller for the synthesis of nanocomposite films for the packaging applications. Simultaneously, they also exploited for the adsorption role for the removal of Cu (II) ions from synthetic wastewater.

After the first foot step study of these huge topic some of future prospective studies could be possible as

1. The SNP and CNC could be also included in the polymer with more concentration with help of In-situ polymerization approach.
2. The biomedical application of SNP and CNC could be exposure.
2. The surface charged SNPs or CNCs could be used for another metal ion leaching from the wastewater. The nanoparticles are can be utilized as nanoadsorbates for the wastewater treatment.
3. As, the robust method for the synthesis of biomass starch and cellulose nanoparticles were proven in the present work, the more applications could be exposed such as thickeners, organic material carrier etc.

Research Outcomes

Patent Filled

Indian Patent

1. Shirish H. Sonawane, **Vikas S. Hakke**, Narsimha. P, P. Dilip Kumar, Bhaskar Bethi, "Low cost hybrid system based on hydrodynamic cavitation and hydrogel adsorption for textile dye waste" Application No.202141007302A, Publication Date : 26/02/2021.

2. Shirish H. Sonawane, **Vikas S. Hakke**, Vividha K Landge, P. Dilip Kumar, "Time, and productive method for the production of cellulose nanocrystals and its use thereof", submitted on 18.09.2022. Application No.202241064456, Publication Date: 18/11/2022.

Articles in Journals

1. **Vikas S. Hakke**, Vividha Landge, Shirish H Sonawane, G Uday Bhaskar Babu, Muthupandian Ashokkumar, Erico MM Flores, The physical, mechanical, thermal and barrier properties of starch nanoparticle (SNP)/polyurethane (PU) nanocomposite films synthesized by an ultrasound-assisted process Ultrasonics Sonochemistry, Vol. 88, 2022,106069, ISSN 1350-4177, https://doi.org/10.1016/j.ultsonch.2022.106069. **(I.F. 9.336)**

2. **Vikas S. Hakke**, Vividha Landge, Shirish Sonawane, G. Uday Bhaskar Babu, Sivakumar Manickam, Grzegorz Boczkaj, Cu (II) ions removal from wastewater using starch nanoparticles (SNPs): An Eco-sustainable approach, Canadian Journal of Chemical Engineering, 2022. https://doi.org/10.1002/cjce.24588. **(I.F. 2.5)**

3. **Vikas S. Hakke**, Shirish Sonawane, Sambandam Anandan, Shriram Sonawane, Muthupandian Ashokkumar, "Process Intensification Approach Using Microreactors for Synthesizing Nanomaterials - A Critical Review", Nanomaterials 2021, 11(1), 98. https://doi.org/10.3390/nano11010098. **(I.F. 5.719)**

4. **Vikas S. Hakke**, Bagale, U. D., Boufi, S., Uday, G., Sonawane, S. H. (2020). Ultrasound assisted synthesis of starch nanocrystals and its applications with polyurethane for packaging film. Journal of renewable materials, 8(3), 239–250. https://doi.org/10.32604/jrm.2020.08449. **(I.F. 2.115)**

5. Vividha K Landge, **Vikas S. Hakke**, Manohar Kakunuri, G Uday B Babu, Grzegorz Boczkaj, Shirish H Sonawane, Synthesis of bimetallic Co–Pt/cellulose nanocomposites for catalytic reduction of p-nitrophenol, Reaction Chemistry & Engineering, https://doi.org/10.1039 /D1RE00422K, 2022. (**I.F. 5.2**).

International Conference:-

1. **Vikas S. Hakke**, P. Dilipkumar, Yogesh Patil, Shirish H Sonawane, Grzegorz Boczkaj, on "Cost effective Industrial Wastewater treatment using hybrid hydrodynamic cavitation technique" during 14-16 April 2022. **Awarded with "Best Paper & Presentation"** in International Conference on Advances in Chemical and Materials Sciences (ACMS-2022) Organized by: Indian Institute of Chemical Engineers, Headquarters.

2. **Vikas S. Hakke**, Vividha K Landge, Shirish H Sonawane, Effect of starch nanofillers on physical, mechanical, thermal and barrier property of polyurethane coating film, (2021) International Chemical Congress of Pacific Basin Societies (PACIFICHEM), Virtual Congress during December 16 – 21, 2021.

3. **Vikas S. Hakke**, R.W. Gaikwad, Shirish H Sonawane, V. A. Sapkal, "Modeling of ion exchange process for Cu (II) eradication from acid mine drainage using artificial neural network (ANN) in the 1st international conference on water, energy & environment [WEECON 2021] conducted on 23rd & 24th December 2021, organized by ISET research India in association with IEI Vietnam.

4. **Vikas S. Hakke**, Vividha Landge, S. B. Dethe, "Combustion studies of saw dust in fluidised bed Reactor," Technological Advances in climate-smart agriculture and sustainability Proceedings of international conference on TACSAS-2017, Page No. 308-311.

Book Chapter

1. **Vikas S. Hakke**, Shailesh Ghodke, Dilipkumar P, M. Surya Teja, Shirish Sonawane, Ravindra Gaikwad, Shriram Sonawane, Ultra sonication based wastewater treatment, Novel Approaches Towards Wastewater Treatment and Resource Recovery Technologies, Edited by Arvind Kumar Mungray, Alka A. Mungray, Shriram Sonawane, Shrirish Sonawane, Elsevier, August 1, 2022. ISBN: 9780323906272. https://doi.org/10.1016/B978-0-323-90627-2.00017-4.

2. Sneha A. Korpe, Vividha K. Landge, **Vikas S. Hakke**, Shirish H. Sonawane, P. V. Rao and, Shriram S. Sonawane, AOPs for Petrochemical/Textile/Tannery industry wastewater treatment, Novel Approaches Towards Wastewater Treatment and Resource Recovery Technologies, Edited by Arvind Kumar Mungray, Alka A. Mungray, Shriram Sonawane, Shirish Sonawane, Elsevier, August 1, 2022. ISBN: 9780323906272. https://doi.org/10.1016/B978-0-323-90627-2.00002-2.

3. Vividha K. Landge, **Vikas S. Hakke**, Sneha A. Korpe, P. Venkateswara Rao, and, Shirish Sonawane, Hybrid systems using hydrodynamic cavitation / ultrasound / Fenton processes for effective treatment of wastewater, Novel Approaches Towards Wastewater Treatment and Resource Recovery Technologies, Edited by Arvind Kumar Mungray, Alka A. Mungray, Shriram Sonawane, Shirish Sonawane, Elsevier, August 1, 2022. ISBN: 9780323906272. http:// doi.org/10.1016/B978-0-323-90627-2.00003-4.

4. **Vikas S. Hakke**, Vividha K. Landge, and Shirish Sonawane, R. W Gaikwad. Mathematical, numerical and experimental investigations of metal extraction processes, Applications of Nanofluids in Chemical and Bio-medical Process Industry, Edited by Shriram Sonawane, Hussein A. Mohammed, Arvind Kumar Mungray, Shirish Sonawane Elsevier, June 1, 2022. ISBN: 9780323905640. https://doi.org/10.1016/B978-0-323-90564-0.00012-X.

5. Yogesh Patil, Surya Teja, **Vikas S. Hakke**, P Dilipkumar, P Narsimha, Tomy Joseph, P. R. Manoj, Shirish Sonawane, G. Boczkaj, "Zero liquid discharge strategies for industrial wastewater treatment reuse and resource recovery", in "Resource Recovery in Industrial Waste waters" edited by Mika Sillanpaa, Ali Khadir, Khum Gurung, Elsevier

6. **Hakke, V. S**., Seepana, M. M., Sonawane, S. H., Kola, A. K., Vooradi, R. (2021), Shirish H Sonawane. Hybrid Treatment Technologies for the Treatment of Industrial Wastewater. In: Inamuddin, Ahamed, M.I., Lichtfouse, E. (eds) Water Pollution and Remediation: Heavy Metals. Environmental Chemistry for a Sustainable World, vol 53. Springer, Cham. https://doi.org/10.1007/978-3-030-52421-0_8.

7. **Vikas S. Hakke**, Shirish H. Sonawane, Irina Potoroko and Irina Kalinina "Applications of Biodegradable Nanocomposites Films for Food Packaging. In: Recent Trends in Nanobiotechnology: Food and Biomedical Applications, Central West Publishing, springer 2019. ISBN: 1925823709.

8. **Vikas S. Hakke**, Uday D. Bagale, Shirish H. Sonawane, Dipak Pinjari, S. Manigandan, Shriram Sonawane, Chapter 16 - Self-healing polymeric coating for corrosion inhibition and fatigue repair, Editor(s): Sabu Thomas, Anu Surendran, Self-Healing Polymer-Based Systems, Elsevier, 2020, Pages 473-493, ISBN 9780128184509, https://doi.org/10.1016/B978-0-12-818450-9.00022-2.

9. Uday B. Bagale, Shirish H. Sonawane, Bharat Bhanvase, **Vikas S. Hakke**, Manohar Kakunuri, Sivakumar Manickam, Shriram S. Sonawane, " Multifunctional coatings based on smart nanocontainers, Editor(s): Abdel Salam Hamdy Makhlouf, Nedal Y. Abu-Thabit,

Advances in Smart Coatings and Thin Films for Future Industrial and Biomedical Engineering Applications, Elsevier, 2020, Pages 135-162, ISBN 9780128498705, https://doi.org/10.1016/B978-0-12-849870-5.00014-8.